

ABSTRACT

Title of Document: DEVELOPMENT AND ANALYSIS OF MICRO
POLYGENERATION SYSTEMS AND
ADSORPTION CHILLERS

Kyle Gluesenkamp, 2012

Directed By: Prof. Reinhard Radermacher, Mechanical
Engineering

About a fifth of all primary energy in the US is consumed by residential buildings, mostly for cooling, heating and to provide electricity. Furthermore, retrofits are essential to reducing this consumption, since the buildings that exist today will comprise over half of those in use in 2050. Residential combined heat and power (or micro CHP, defined by <5 kW electrical generation capacity) has been identified as a retrofit technology which can reduce energy consumption in existing homes during the heating season by 5-30%. This thesis investigates the addition of a thermally-driven chiller/heat pump to a CHP system (to form a trigeneration system) to additionally provide savings during the cooling season, and enhance heating season savings. Scenarios are identified in which adding thermally-driven equipment to a micro CHP system reduces primary energy consumption, through analytical and experimental investigations. The experimental focus is on adsorption heat pump systems, which are capable of being used with the CHP engines (prime movers) that are already widely deployed. The analytical analysis identifies energy saving

potential off-grid for today's prime movers, with potential on-grid for various fuel cell technologies.

A novel dynamic test facility was developed to measure real-world residential trigeneration system performance using a prototype adsorption chiller. The chiller was designed and constructed for this thesis and was driven by waste heat from a commercially available natural gas-fueled 4 kW (electric) CHP engine. A control strategy for the chiller was developed, enabling a 5-day experiment to be run using a thermal load profile based on moderate Maryland summer air conditioning loads and typical single-family domestic hot water demand, with experimental results in agreement with models. In this summer mode, depending on electrical loads, the trigeneration system used up to 36% less fuel than off-grid separate generation and up to 29% less fuel than off-grid CHP without thermally driven cooling. However, compared to on-grid separate generation, the experimental facility used 16% more primary energy. Despite high chiller performance relative to its thermodynamic limit, this result is primarily due to the electrical efficiency of the prime mover being lower than the grid. A residential trigeneration system utilizing a high temperature fuel cell is predicted to save up to 42% primary energy relative to the grid.

DEVELOPMENT AND ANALYSIS OF MICRO-POLYGENERATION SYSTEMS
AND ADSORPTION CHILLERS

by

Kyle Gluesenkamp

Dissertation submitted to the Faculty of the Graduate School of the
University of Maryland, College Park, in partial fulfillment
of the requirements for the degree of
Doctor of Philosophy
2012

Advisory Committee:

Professor Reinhard Radermacher, Chair
Associate Professor Christopher Cadou, Dean's representative
Research Associate Professor Yunho Hwang
Professor Gregory Jackson
Professor Kenneth Kiger

© Copyright by
Kyle Gluesenkamp
2012

DEDICATION

To Caitlin

ACKNOWLEDGEMENTS

This thesis is an outcome of my work in the Center for Environmental Energy Engineering. In carrying out the thesis, and in my career in general, I have benefited tremendously from the support and example of my advisor Professor Reinhard Radermacher. I have perused and pursued many thoughts he thought before me. I am also very appreciative of the efforts of all the members of my committee.

In roughly chronological order, I would also like to acknowledge the following people: my parents Bobbye and Cary for expecting the best from me; my brother Dean for showing me the power of detailed mechanical understanding; my wife Caitlin for her encouragement and hard work; Dick and Joan for their boundless support; Nick Fernandez and Ethan Lust for getting me started in the CEEE; Jan Muehlbauer for his incredible patience and forward momentum, and priceless help with countless details; Professor Yunho Hwang for his expansive efforts and dedication every day; Professor Travis Horton for his advice and example; Gilad Sharon for perspective; Amir Mortazavi and Abdullah Al-Abdulkarem for their questions, Timothy Fitzgerald, Omar Abdelaziz, Varun Singh, Vikrant Aute and Professor Ken Kiger for inspiration; Magnus Eisele, Jon Jones, Andrew Mueller, Hoseong Lee, Chris Horvath, Song Li and Cong Peng for their office companionship; Professor Greg Jackson for helping me to see the value of my work; Professor David Bigio for his energy and guidance; John Bush, Daniel Leighton, Bracha Mandel, Danielle Khoo and especially Suxin Qian for helping me complete this dissertation; and my daughters Eugenie and Louisa for helping propel me towards graduation.

TABLE OF CONTENTS

LIST OF TABLES	vii
LIST OF FIGURES	ix
ABBREVIATIONS, SYMBOLS AND SUBSCRIPTS	xv
Chapter 1: Introduction and Literature Review	1
1.1 Motivation.....	1
1.1.1 The residential sector	1
1.1.2 The importance of the residential retrofit market	2
1.2 Literature Review.....	3
1.2.1 Conventional residential CHP.....	3
1.2.2 Unconventional residential CHP.....	6
1.2.3 Residential CCHP	6
1.2.4 Adsorption heat pumps	9
1.2.5 Proposed system enhancements relevant to residential adsorption systems....	10
1.2.6 Carnot efficiency for heat-activated cycles.....	12
1.3 Objectives and Approach.....	17
1.4 Dissertation Organization	18
Chapter 2: Residential Energy Systems – Inventory and Analysis.....	20
2.1 T-Q analysis of feasibility of residential trigeneration	21
2.2 Inventory of residential energy systems	25
2.3 Trigeneration device matching – prime movers and thermally-driven chillers.....	31
2.4 Analytical expressions for polygeneration systems (cooling season).....	43
2.4.1 Expressions for primary energy ratio.....	46
2.4.2 Carnot systems at inherent cooling load ratio.....	59
2.4.3 Ideal systems at inherent cooling load ratio.....	63
2.4.4 Realistic system comparisons at inherent cooling load ratio	67
2.4.5 System comparisons for variable cooling load fraction.....	72
2.4.6 Sensitivity analysis.....	76
2.5 Conclusions based on first-order comparisons	78
Chapter 3: Separate Sensible and Latent Cooling Strategies for Trigeneration	80
3.1 Past approaches to the crystallization limit.....	80
3.1.1 Working fluid modifications.....	82
3.1.2 Absorption pressurization	82
3.1.3 Cascaded absorption/VCS system	84
3.2 SSLC approach	85
3.2.1 Description of SSLC and conventional system models.....	87
3.2.2 Available heat from engine.....	89
3.2.3 Duct burner	89
3.2.4 Modeling assumptions	90

3.2.5 Results.....	91
3.2.5 Conclusions.....	93
Chapter 4: Development of Dynamic CCHP Test Facility.....	94
4.1 Integration of CHP engine with simulated loads	94
4.1.1 Test facility	94
4.2 Adsorption chiller: design, construction and CCHP integration	99
4.2.1 Adsorption cycle: working principle and operational phases	100
4.2.2 Piping and instrumentation of prototype.....	103
4.2.3 Sizing of adsorption chiller components – equilibrium thermodynamic model	109
4.2.4 Fabrication of adsorption chiller.....	117
4.2.5 Integration of adsorption chiller into CCHP test facility	129
4.3 Residential load profiles	130
4.3.1 Space heating	134
4.3.2 Domestic hot water	135
4.4 Engine instrumentation energy balance with uncertainty.....	137
4.4.1 Fuel input	140
4.4.2 Electricity output.....	145
4.4.3 Hot water output	147
4.4.4 Exhaust heat losses	149
4.4.5 Convective losses from cabinet walls	161
4.4.6 Radiative losses from cabinet walls.....	161
4.4.7 Parasitic losses	164
4.5 Heat pump energy balance.....	166
4.5.1 Overall energy balance	167
4.5.1 Chilled water energy balance.....	171
4.6 Buffer tank energy balance	172
4.6 Other energy balances.....	175
Chapter 5: Experimental Results and Control Strategies.....	176
5.1 Steady state experimental results for engine.....	176
5.1.1 Performance metrics	176
5.1.2 Performance maps.....	177
5.1.3 Allocation of measured outputs	182
5.1.4 Engine instrumentation energy balance	183
5.1.5 Comparison with others’ data	185
5.1.6 Proposed improvements to heat recovery	188
5.2 CHP: dynamic load-following results.....	197
5.2.1 Representative detailed results.....	197
5.2.1 Comparison of load profiles.....	199
5.3 Adsorption heat pump: cyclic steady state results	201
5.4 Adsorption heat pump: control strategy and empirical model.....	209
5.5 CCHP: dynamic load-following experimental results	221
5.5.1 CCHP load profiles and SSLC strategy	222
5.5.2 CCHP load-following results.....	226

Chapter 6: Model Development and Validation	235
6.1 CHP: dynamic model development and validation	235
6.2 Adsorption heat pump: analytical models and validation.....	239
6.3 Adsorption heat pump: graphical approaches.....	264
6.4 Adsorption heat pump: detailed equilibrium thermodynamic model	269
6.5 Adsorption heat pump: empirical model and validation.....	273
Chapter 7: Conclusions	279
7.1 Contributions.....	280
Chapter 8: Recommendations for Future Work.....	283
Appendices.....	287
Alternate fuel energy calculation for instrumentation energy balance	287
Glossary of key terminology.....	290
References.....	291
Bibliography	294

LIST OF TABLES

Table 1: Summary of gaps in published literature on small and micro trigeneration.....	8
Table 2: Baseline (non-CHP) systems	26
Table 3: CHP and CCHP systems.....	27
Table 4: Parameters used in calculations for micro-scale devices ($\sim 25 \text{ kW}_{\text{elec}}$ for MT and $\sim 5 \text{ kW}_{\text{elec}}$ for all others)	35
Table 5: Work produced and saved by trigeneration systems	41
Table 6: EIA average primary energy electric grid efficiencies in the US.....	46
Table 7: Carnot efficiency of heat engines and chillers.....	60
Table 8: Inherent cooling fractions for various ideal and non-ideal systems	71
Table 9: Summary of expressions for PER of systems operating at their inherent cooling load fractions	72
Table 10: Summary of expressions for fuel consumption as a function of cooling load fraction (f_{clg}) for six cooling systems.....	73
Table 11: VCS specifications and requirements for cooling	88
Table 12: Performance data for 3.0 kW engine	89
Table 13: Absorption system heat exchanger data	90
Table 14: Key VCS modeling assumptions	91
Table 15: Fuel consumption at the design conditions of 49°C and 35 g/kg humidity ratio.	92
Table 16: Heat loads of absorption system heat exchangers	92
Table 17: Valve settings for the two operating modes and the draining/charging and de- aerating modes (O=open; X=closed).....	95
Table 18: Systematic uncertainties of all instrumentation	99
Table 19: Systematic uncertainties of selected values that were not measured directly ..	99
Table 20: Valve settings for conducting various procedures on AHP	108
Table 21: Correlations for nucleate pool boiling heat transfer	111
Table 22: Specifications of adsorption chiller	119
Table 23: Load profiles summary	131
Table 24: Natural gas composition data.....	143
Table 25: Grundfos water pump power consumption.....	146
Table 26: Comparison of exhaust enthalpies calculated from ASHRAE moist air correlation and EES	152
Table 27: Average composition of natural gas	153
Table 28: List of parasitic loads for laboratory Ecopower unit	165
Table 29: Test matrix for steady state prime mover performance mapping	178
Table 30: Variables and functional forms resulting in best fits for each dependent variable	180
Table 31: Coefficient values for Table 30	181
Table 32: Full load comparison of results between CEEE and B. Thomas	186
Table 33: Part load comparison of results between CEEE and B. Thomas	186
Table 34: Coefficients for curve fits for Q_{min} and Q_{max}	221
Table 35: Coefficients for curve fits for COP, t_{ads} and t_{HR}	221
Table 36: Cumulative totals for CCHP 5-day profile	227
Table 37: Trigeneration savings vs. three baseline scenarios	228

Table 38: List of all variables involved in determination of Ecopower part load ratio ..	236
Table 39: Conditions used in sample evaluation of Equation (84)	247
Table 40: Summary of Dühring diagram visual interpretations	269

LIST OF FIGURES

Figure 1: Illustration of the primary energy savings of using conventional onsite CHP compared with a baseline system.....	5
Figure 2: Carnot cooling efficiency ($COP_{clg,Ct}$) for an ideal heat-activated cooling device providing cooling at 10°C.....	12
Figure 3: Carnot heating efficiency ($COP_{htg,Ct}$) for an ideal heat-activated heat pump device providing heating at 30°C.....	13
Figure 4: Approximate residential thermal loads for the entire US.....	22
Figure 5: Hot and cold composite curves for aggregated annual residential thermal loads – includes both space heating and space cooling.....	23
Figure 6: T-Q match between SI-ICE engine waste heat and residential winter heating requirements.....	23
Figure 7: T-Q match for SI-ICE engine and residential summer cooling with heat-activated air conditioning device.....	24
Figure 8: COP_{th} vs. regeneration temperature of heat activated cooling technologies.....	32
Figure 9: Water dewpoint of combustion exhaust as function of AFR and ambient humidity ratio.....	34
Figure 10: Water dewpoint of combustion exhaust typical of four prime mover types ...	35
Figure 11: T-Q diagram for micro prime movers (temperature vs. fraction of fuel energy).....	36
Figure 12: T-Q diagram for micro prime movers (temperature vs. fraction of waste heat).....	37
Figure 13: Matching of micro prime movers and heat activated cooling devices.....	38
Figure 14: Exergy factor vs. fuel energy for nine micro prime movers.....	39
Figure 15: Practically realizable work or work equivalent vs. fuel energy for nine micro prime movers in combined cooling and power mode (no heating).....	41
Figure 16: Sankey diagram for grid-driven VCS.....	47
Figure 17: Sankey diagram for direct-fired HACD.....	49
Figure 18: Sankey diagram for CCHP without auxiliary burner.....	50
Figure 19: Sankey diagram for trigeneration system with auxiliary burner.....	53
Figure 20: Sankey diagram of trigeneration system with VCS backup cooling.....	55
Figure 21: Example setup for derivation of fuel consumption.....	56
Figure 22: Sankey diagram for trigeneration system with backup VCS and backup auxiliary burner.....	57
Figure 23: Comparison of PER^{-1} for trigeneration and separate generation at Carnot efficiencies and at $f_{Ct} = 40\%$	61
Figure 24: Contours of fractional energy savings for trigeneration as a function of cooling load fraction and fraction of Carnot performance.....	62
Figure 25: Inherent cooling load fraction ($f_{clg,inh}$) as function of prime mover efficiency and thermal COP, for $\lambda=\kappa=0$	64
Figure 26: Energetic suitability of various trigeneration possibilities compared to the conventional grid-driven VCS option. Grid efficiency is assumed to be 33.3%.	66
Figure 27: Effect of heat losses from prime mover on energetic suitability of trigeneration.....	67

Figure 28: Effect of parasitic electrical loads of thermally driven equipment on energetic suitability of trigeneration.....	68
Figure 29: Inherent cooling load fraction as function of prime mover electrical efficiency and chiller COP, for $\lambda=0.1$ and $\kappa=0.02$	69
Figure 30: Effect of both parasitic loads and heat losses.....	70
Figure 31: Full range of suitability possible based on optimistic assumptions (green) and pessimistic assumptions (gray).....	71
Figure 32: Comparison of grid-VCS and HTPEMFC-based systems.....	74
Figure 33: PER^{-1} vs. f_{clg} for various PM-based systems and grid-VCS.....	76
Figure 34: Sensitivity of PER to each variable affecting a SI-ICE-based trigeneration system without auxiliary burner.....	77
Figure 35: Sensitivity of PER to each variable affecting a SI-ICE-based trigeneration system with an auxiliary burner.....	77
Figure 36: Effect of changing independent operating variables on the shape of the Dühring plot.....	81
Figure 37: Dühring plots of the absorption cycle showing the effect of the pressurized absorber.....	83
Figure 38: Air flow schematic of the separate sensible and latent cooling (SSLC) system.....	86
Figure 39: Psychrometric chart of SSLC system at design point.....	87
Figure 40: Schematic of conventional system with VCS for cooling.....	88
Figure 41: Schematic of SSLC system model with LiBr absorption system and supplemental VCS.....	88
Figure 42: Schematic of test facility hydronics and hydronic instrumentation.....	94
Figure 43: Vertical locations of in-stream and external thermocouples on tank.....	96
Figure 44: Schematic of heat recovery loop within prime mover cabinet.....	98
Figure 45: Photo of Ecopower cabinet interior with labeled heat recovery components.....	98
Figure 46: Adsorption heat pump temperature nomenclature.....	100
Figure 47: Illustration of a simple adsorption chiller.....	101
Figure 48: Process and instrumentation diagram focusing on HTF plumbing.....	104
Figure 49: Process and instrumentation diagram focusing on instrumentation and vapor plumbing.....	105
Figure 50: Chilled water schematic.....	106
Figure 51: Recirculated refrigerant loop schematic.....	107
Figure 52: Illustration of temperatures associated with condenser.....	110
Figure 53: Relationship among condenser tube diameter, tube length, and ΔT_{cond}	110
Figure 54: Correlations for falling film heat transfer coefficient.....	113
Figure 55: Illustration of 9 components of pressure drop between two reservoirs, grouped into ΔP_{pipe} and ΔP_{valve}	115
Figure 56: Effect of pipe diameter on ΔP and ΔT_{sat} (38 mm valve ID).....	115
Figure 57: Effect of pipe diameter on ΔP and ΔT_{sat} (51 mm valve ID).....	116
Figure 58: Effect of ΔP on COP (solid lines) and SCP (dotted lines) at various heat rejection temperatures.....	117
Figure 59: Prototype adsorption chiller near final configuration.....	118
Figure 60: Adsorber heat exchanger used in prototype chiller.....	120
Figure 61: Close-up of adsorber heat exchanger coated fins.....	120

Figure 62: CAD drawing of vacuum chambers with flanges and locations of feedthroughs	121
Figure 63: Two vacuum chambers as received from PPI	122
Figure 64: Chiller aluminum frame with one chamber and adsorber	122
Figure 65: Vacuum chambers ready for heat exchanger installation, plumbing and instrumentation	123
Figure 66: Adsorber heat exchanger (left) and condenser (right) plumbed to chamber feedthroughs.....	124
Figure 67: Falling film evaporator plumbed to chamber feedthroughs	125
Figure 68: Falling film distributor in operation, close up.....	126
Figure 69: Falling film distributor in operation, zoomed out	126
Figure 70: Initial wettability of sanded and solvent-cleaned copper tubes.....	127
Figure 71: Filters used in refrigerant recirculation line	128
Figure 72: Inlet screen (230 micron) and magnet for refrigerant recirculation line	129
Figure 73: Residential shoulder season load profile	132
Figure 74: Residential summer season (DHW-only) load profile	132
Figure 75: Synthetic commercial load profile	133
Figure 76: Synthetic ramp-down and ramp-up profiles.....	133
Figure 77: System assumed for developing commercial load profile.....	134
Figure 78: Basic control volume view of prime mover cabinet.....	138
Figure 79: Decision tree depiction of logic programmed into LabVIEW to interpret the 0-5 V analog signals from the gas meter pulser	142
Figure 80: Sample output from gas meter logic routine	142
Figure 81: Raw calorimeter data taken at NIST	144
Figure 82: Comparison of three sources of HHV data	145
Figure 83: Transformer efficiency as a function of its part load ratio	146
Figure 84: Transformer losses as a function of transformer load	147
Figure 85: Relative uncertainty [%] in a heat flow based on ΔT and the absolute uncertainty in temperature measurement	148
Figure 86: Flowchart of measurements and calculation involved in determining the exhaust mass flow rate	150
Figure 87: Location of exhaust temperature measurement.....	151
Figure 88: Exhaust humidity ratio as a function of inlet humidity ratio for non-condensing exhaust	153
Figure 89: Engine air intake vacuum as a function of engine speed	155
Figure 90: Heat capacity of exhaust gas as a function of temperature, for three inlet humidities.....	158
Figure 91: Measured volumetric efficiency of the engine with error bars and linear curve fits	160
Figure 92: Example surface temperature grid (one out of six used) for purpose of radiative loss calculation.....	162
Figure 93: Maximum possible variation in radiation heat losses for different ambient temperatures.....	163
Figure 94: Detailed CHP view showing four control volumes (dotted lines).....	164
Figure 95: Overall chiller energy balance for steady state tests	168
Figure 96: Overall chiller energy balance during a steady state test	168

Figure 97: Overall chiller energy balance for 5-day load-profile test	169
Figure 98: Temperature profile of two heat recovery events.....	170
Figure 99: CHW energy balance for steady state tests	171
Figure 100: CHW dimensional energy balance vs. T_{CHW} and Q_{CHW}	172
Figure 101: Tank heat losses as function of difference in temperature between average tank temperature and surrounding air temperature.....	173
Figure 102: Contours of electrical efficiency [%HHV] as a function of engine speed and return water temperature	181
Figure 103: Contours of heat recovery efficiency [%HHV] as a function of engine speed and supply temperature	182
Figure 104: Allocation of fuel input (HHV) for various speeds.....	183
Figure 105: Energy balance plotted against engine speed for all 92 steady state tests...	184
Figure 106: Comparison of CEEE results with B. Thomas' results for two part load ratios	186
Figure 107: Comparison of CEEE results with B. Thomas' results for supply temperature	188
Figure 108: Current heat recovery scheme for Ecopower	189
Figure 109: First proposed modification to Ecopower heat recovery.....	190
Figure 110: Second proposed modification to Ecopower heat recovery	192
Figure 111: T-Q diagrams for current and two proposed heat recovery configurations	193
Figure 112: Maximum supply temperature configuration for ICE heat recovery	195
Figure 113: "Complexity no concern" configuration for ICE heat recovery.....	195
Figure 114: Comparison of relative merits of heat recovery configurations	196
Figure 115: Energy flows into and out of the tank for the residential shoulder season test	197
Figure 116: Tank temperatures for residential shoulder season test.....	198
Figure 117: Prime mover energy balance for residential shoulder season test.....	198
Figure 118: Tank energy balance for residential shoulder season test	199
Figure 119: Average outputs for all CHP profiles	200
Figure 120: Allocation of outputs for all CHP profiles	200
Figure 121: Comparison of PM to system control volume approach	201
Figure 122: Nomenclature for heat pump operation and control.....	202
Figure 123: Overview of adsorption chiller test methodology	204
Figure 124: All experimental tests in performance-space	204
Figure 125: All experimental tests in external condition-space.....	205
Figure 126: All experiments in internal condition-space.....	205
Figure 127: Fraction of Carnot performance achieved by all 145 experiments	206
Figure 128: Differential loading (equilibrium and actual) of all experimental tests	206
Figure 129: Experimental COP results for parametric study of t_{ads} , T_{evap} , and T_{cond}	208
Figure 130: Experimental capacity results for parametric study of t_{ads} , T_{evap} , and T_{cond}	208
Figure 131: Schematic of control strategy evaluation	210
Figure 132: Overview of control strategy and empirical model development	211
Figure 133: Kriging predictions vs. 145 experimental points using LOO method.....	213
Figure 134: Pareto sets in response-space for operation at 25 external conditions	214
Figure 135: External conditions with COP>0.1 and capacity>0.1 kW	214
Figure 136: Solutions circled in green from previous figure in performance-space	215

Figure 137: Performance as a function of cycle times for condition circled in red in previous two figures	216
Figure 138: Comparison of curve fitted and Kriging-predicted COP for 1,525 Pareto points	217
Figure 139: External conditions of 10 validation points.....	218
Figure 140: Curve-fitted vs. experimental COP for 10 experimental validation points.	218
Figure 141: Validation experiments in external condition-space	219
Figure 142: Validation experiments in internal condition-space.....	219
Figure 143: Validation experiments in response-space	220
Figure 144: Curve fit vs. experimental COP for validation experiments	220
Figure 145: VCS-based dehumidification configuration.....	223
Figure 146: Weather profile for Stirling, VA for late July (TMY data).....	223
Figure 147: Load profile for building in Stirling, VA	224
Figure 148: Required supply temperature for sensible cooling for three different air flow rates	224
Figure 149: Building sensible load and chiller minimum and maximum capacity for 300 cfm supply air flow rate.....	225
Figure 150: Building sensible load and chiller minimum and maximum capacity for 500 cfm supply air flow rate.....	225
Figure 151: Profile of capacity and chilled water supply temperature for adsorption chiller.....	226
Figure 152: Cumulative fuel energy allocation measured for 5-day experimental trigeneration experiment.....	227
Figure 153: Inputs and outputs of trigeneration system during profile test.....	229
Figure 154: Heat into tank	230
Figure 155: Thermal energy stored in 800 L tank	230
Figure 156: Temperature profile in 800 L tank	231
Figure 157: Profile and experimental results for condenser HTF inlet temperature	232
Figure 158: Zoom-in on profile of condenser HTF inlet temperature	232
Figure 159: Profile and experimental results for chilled water capacity	233
Figure 160: Profile and experimental results for chilled water supply temperature.....	233
Figure 161: Profile and experimental results for DHW.....	234
Figure 162: Zoom-in on DHW profile.....	234
Figure 163: Ecopower control strategy depicted as a decision tree, part 1 of 3	237
Figure 164: Ecopower control strategy depicted as a decision tree, part 2 of 3	238
Figure 165: Ecopower control strategy depicted as a decision tree, part 3 of 3	239
Figure 166: COP as a function of heat recovery effectiveness.....	254
Figure 167: Relative contributions of heat exchanger constituents to mass and thermal mass of heat exchanger in isolation.....	258
Figure 168: HX-only and extended control volumes for adsorber HX	259
Figure 169: Relative contributions to mass and thermal mass of extended control volume	260
Figure 170: Analytical COP expression without heat recovery compared to all experimental results.....	261
Figure 171: Analytical COP expression without heat recovery compared to experimental results without heat recovery.....	262

Figure 172: Analytical COP expression with 40% isosteric heat recovery effectiveness	262
Figure 173: Analytical COP expression with 40% isosteric heat recovery effectiveness vs. 170 experimental results	263
Figure 174: Analytical prediction error using the equilibrium assumption vs. adsorption duration	264
Figure 175: Analytical COP using the equilibrium assumption vs. measured COP	264
Figure 176: Dühring diagram for AQSOA FAM Z01 zeolite	265
Figure 177: $\Delta T_{wet,sat}$ and $\Delta T_{dry,wet}$ on the Dühring diagram of Z01	266
Figure 178: Equilibrium Dühring diagram for Z01 for $T_{CHW}/T_{rej}/T_{src} = 10/30/70^{\circ}\text{C}$	270
Figure 179: Effect of T_{CHW} on performance predicted by equilibrium model	271
Figure 180: Effect of T_{rej} on performance predicted by equilibrium model	271
Figure 181: Effect of T_{src} on performance predicted by equilibrium model	272
Figure 182: Illustration of state points (in time) for cycle with heat and pressure recovery	273
Figure 183: Empirical model results for $T_{CHW} = 7^{\circ}\text{C}$	274
Figure 184: Empirical model results for $T_{CHW} = 13^{\circ}\text{C}$	274
Figure 185: Empirical model results for $T_{CHW} = 19^{\circ}\text{C}$	275
Figure 186: Heat recovery duration for maximum and minimum capacity from control strategy/empirical model	276
Figure 187: Adsorption duration for maximum and minimum capacity from control strategy/empirical model	277
Figure 188: T-Q heating value diagram for stoichiometric complete combustion products of methane and dry air	288

ABBREVIATIONS, SYMBOLS AND SUBSCRIPTS

Abbreviations

Abs or ABs	absorption
Ads or ADs	adsorption
AB	auxiliary burner
A/C	air conditioner (for space cooling)
AFR	air:fuel ratio [$\text{kg}_{\text{air}}/\text{kg}_{\text{fuel}}$] <i>or</i> air flow rate [m^3/s] or [L/s]
AHP	adsorption or absorption heat pump
B	burner
B/F	boiler or furnace (i.e. a simple fuel-fired space heating device)
CCHP	combined cooling, heating and power
CHP	combined heating and power
COP	coefficient of performance
c.v.	control volume
DAQ	data acquisition
DF	direct fired
DHW	domestic hot water
DOE	US Department of Energy <i>or</i> design of experiments
DMR	dead mass ratio
DTMR	dead thermal mass ratio
EC	external combustion
ECOP	electric coefficient of performance ($\text{ECOP} = \kappa^{-1}$)
EERE	DOE's Office of Energy Efficiency and Renewable Energy
EJ	exajoule ($1.055 \text{ EJ} = 1 \text{ quadrillion Btu}$)
ER	electric resistance
ERWH	electric resistance water heater
EXV	electronic expansion valve
f	fuel consumption per unit load (where $\text{load} = \text{Load}_{\text{clg}} + \text{Load}_{\text{elec}}$), the same as PER^{-1}
f_{clg}	cooling load fraction: $f_{\text{clg}} = \text{Load}_{\text{clg}}/(\text{Load}_{\text{clg}} + \text{Load}_{\text{elec}})$
$f_{\text{clg,inh}}$	inherent cooling load fraction
f_{clt}	fraction of waste heat present in coolant
f_{Ct}	fraction of Carnot performance
f_{exhaust}	fraction of waste heat present in the exhaust
f_{VCS}	fraction of cooling provided by VCS
FC	fuel cell
GF	gas fired
GFWH	gas fired water heater
h	heat transfer coefficient [$\text{W}^1\text{m}^{-2}\text{K}^{-1}$]
HACD	heat-activated cooling device
HACT	heat-activated cooling technology/ies
HAHD	heat-activated heating device
HAHT	heat-activated heating technology/ies
HHV	higher heating value

HP	heat pump
HPWH	heat pump water heater
HR	heat recovery <i>or</i> heat recuperation
HTC	heat transfer coefficient [$\text{W}^1\text{m}^{-2}\text{K}^{-1}$]
HTF	heat transfer fluid
HV	heat transfer fluid valve
HX	heat exchanger
IC	internal combustion
ICE	internal combustion engine (reciprocating)
LHV	lower heating value
LOO	leave-one-out method
M	mixer <i>or</i> molecular weight
ODC	outdoor chiller
P	pressure [kPa] <i>or</i> [bar]
PHX	plate heat exchanger
PR	pressure ratio <i>or</i> pressure recovery
Q	heat transfer [kW]
q	heat flux [W/m^2]
ref	refrigerant
refrig	refrigerator
RH	relative humidity [%]
RIC	reciprocating internal combustion
RMSE	root mean squared error
SH	space heating
SHX	solution heat exchanger
T	temperature [$^{\circ}\text{C}$ <i>or</i> K]
TDC	thermally-driven chiller (equivalent to HACD)
V	valve <i>or</i> volume [m^3 <i>or</i> L]
VCS	vapor compression system
VV	vapor valve
w_i	mass fraction of species i [$\text{kg}_i/\text{kg}_{\text{tot}}$]
x	vapor quality (vapor mass fraction) [$\text{kg}_{\text{vap}}/\text{kg}_{\text{tot}}$]
X_i	molar fraction of species i [$\text{mol}_i/\text{mol}_{\text{tot}}$]
Y	loading [$\text{kg}_{\text{ref}}/\text{kg}_{\text{ads}}$]
Y_i	mass ratio of species i [$\text{kg}_i/\text{kg}_{\text{non-}i \text{ species}}$], <i>or</i> , where noted, mass fraction of species i [$\text{kg}_i/\text{kg}_{\text{tot}}$]
Z01	Mitsubishi Plastic AQSOA FAM-Z01 zeolite

Greek Symbols

α	heat transfer coefficient
β	normalized temperature difference
Δ	change <i>or</i> difference
ε	heat exchanger effectiveness
η	efficiency
κ	parasitic electrical load per unit cooling ($\kappa = \text{ECOP}^{-1}$)
λ	fractional heat losses from prime mover ($\lambda \equiv 1 - \eta_{\text{elec}} - \eta_{\text{HR}}$)

λ_{pinch}	pinch penalty – fraction of available heat not recovered due to being lower than the desired utilization temperature
τ	half cycle time ($\tau \equiv t_{ads} + t_{HR} + t_{PR}$)
τ_R	residence time (V/\dot{V})
ψ	relative heat of sorption ($\psi \equiv L_{des}/L_{evap}$)
ω	absolute uncertainty

Subscripts

abs	absorbent
ads	adsorbent
appr	approach (temperature)
b	bottom
calc	temporary number used in intermediate or internal calculation
clg	cooling
cond	condenser
Ct	Carnot
D	driving temperature <i>or</i> desorber
des	desorption
desup	desuperheater – device that uses the refrigerant superheat from a space heating heat pump compressor discharge to preheat DHW
elec	electrical
evap	evaporator
eq	equilibrium
ff	falling film
FCC	fuel chargeable to cooling
htg	heating
H	high temperature
HR	heat recovery (for prime mover or adsorption chiller)
in	the mass flow inlet to a component
inh	inherent
isob	isobaric
isost	isosteric (constant mass ratio)
L	lift <i>or</i> low temperature <i>or</i> length
LTH	lower threshold
m	middle
out	heat flow out of a system <i>or</i> the fluid outlet of a component
PM	prime mover
PR	pressure recovery (also known as mass recovery in the literature)
r	reduced (i.e. relative to critical)
ref	refrigerant <i>or</i> reference
rej	heat rejection
sat	saturation
sh	superheat
space	the space inside a building occupied by conditioned air
src	heat source (high temperature, unless noted)
src,H	high temperature heat source (typically at desorber)
src,L	low temperature heat source (typically at evaporator)

stoich	stoichiometric
th	thermal
TH	threshold
UTH	upper threshold
vp	vertical pitch

Chapter 1: Introduction and Literature Review

1.1 Motivation

In summary, this work is motivated by the fundamental question, “what is the most efficient use of fossil fuels to provide cooling?” Since cooling is often present with some electrical load, there may be benefits to simultaneously producing electricity and cooling. In particular, the focus is on energy system retrofits for existing buildings, as opposed to new construction where load reduction measures are often more cost effective.

1.1.1 The residential sector

As justification for this approach, consider the current energy consumption in the US. According to the DOE EERE 2009 Buildings Energy Data Book (DOE 2009), about 40% of US primary energy consumption (38.8 Quads) was by the buildings sector. About half of that (20.8 Quads) was in the residential sector. Thus it can be loosely said that one fifth of all energy consumed in the US is consumed in residences. Furthermore, over half of this residential primary energy is thermal, i.e. space heating (26.4%), space cooling (13.0%), and water heating (12.5%). Although refrigeration (7.2%), cooking (4.7%) and clothes drying (4.2%) are generally provided by electrical or directly-fuel-fired appliances, these are fundamentally thermal loads as well, so that 64% of residential primary energy consumption is attributable to thermal loads, and 36% is attributable to loads that must be met by electricity (mostly lighting and electronics). This ~2:1

ratio of thermal to electrical loads is similar to the ratio of thermal to electrical output from typical thermodynamic cycles used to produce electricity (Rankine, Brayton, Diesel and Otto cycles). This begs the question, what gains can be realized by producing electricity in a distributed way, thereby allowing the waste heat to be utilized?

1.1.2 The importance of the residential retrofit market

The residential energy sector has been clearly demonstrated to be important to reducing primary energy usage. Furthermore, the majority of the market for residential energy systems is in retrofits.

Consider data from the EIA Annual Energy Outlook (EIA 2011). By 2030, there are projected to be 141.2 million households in the US. Of these, only 23% will be constructed between 2010 and 2030, with the rest already existing today. Thus it is clear that making major reductions in primary energy usage in the residential sector will require retrofits.

The most cost effective retrofits begin with energy efficiency measures such as minimizing infiltration and conduction losses.

In general, a building's energy consumption for space heating (or cooling) is proportional to heat losses (or gains) and the space conditioning equipment efficiency. In new construction, an enhanced building envelope (i.e. reducing gains and losses) generally represents a greater opportunity for energy savings than enhancing the energy systems. For existing buildings, since the envelope is already built, the conditioning equipment efficiency is generally the only opportunity for significant savings.

1.2 Literature Review

The literature review first covers conventional residential CHP, which is the provision of space heating, DHW and electricity (but no cooling) with a boiler or furnace as backup. The “unconventional” residential CHP is covered, meaning the use of a VCS as backup heat source rather than a boiler. Next adsorption heat pumps are covered, and enhancements to the adsorption cycle that have been proposed in the literature. Finally an overview of the existing work on the efficiency of thermally driven cycles is discussed.

1.2.1 Conventional residential CHP

Extensive literature exists concerning “conventional” residential CHP. A conventional residential CHP system consists of a cogeneration engine, a grid connection for electrical import and export, and a backup boiler to handle heating during the colder days of the year.

CHP has two fundamental benefits to offer: reduced primary energy (fuel) use, and reduced utility costs. In addition, it tends to have CO₂ savings even greater than its primary energy savings by running on natural gas and possibly biofuels.

The fuel-saving principle of CHP lies in the ability to utilize waste heat from an engine, in contrast to centralized power plants which dump all their waste heat to the environment. Figure 1 uses round numbers to illustrate this: to supply the same electrical (1 unit) and thermal (3 units) loads, the CHP system uses only

5 units of fuel, compared to 7 units for the baseline system of a Rankine cycle electric grid and an onsite fuel-burning furnace, representing a reduction of nearly 30% over the baseline. Despite the higher fuel-to-power conversion rate of the large centralized electric utility plants compared to a small onsite engine (in this case, 33% compared with 20%), the ability to use the waste heat on site allows the smaller, lower efficiency engine to substantially reduce overall fuel consumption.

Figure 1 can also be used to illustrate the financial benefit of CHP.

Fundamentally, a unit of electricity is always more valuable than a unit of fuel, since more than one unit of fuel is required to produce a unit of electricity. With this in mind, note what the residence is actually purchasing in each case: for the baseline system, 1 unit of electricity and 4 units of fuel; while in the CHP case, 5 units of fuel. The same amount of site energy is bought in each case, but with CHP, 1 unit of expensive electricity is replaced by a unit of inexpensive fuel. If the electricity-to-fuel price ratio is taken as 3:1 (e.g. 12 cents/kWh for electricity; \$12 per thousand cubic feet of natural gas), then this also represents a reduction of nearly 30% in utility costs.

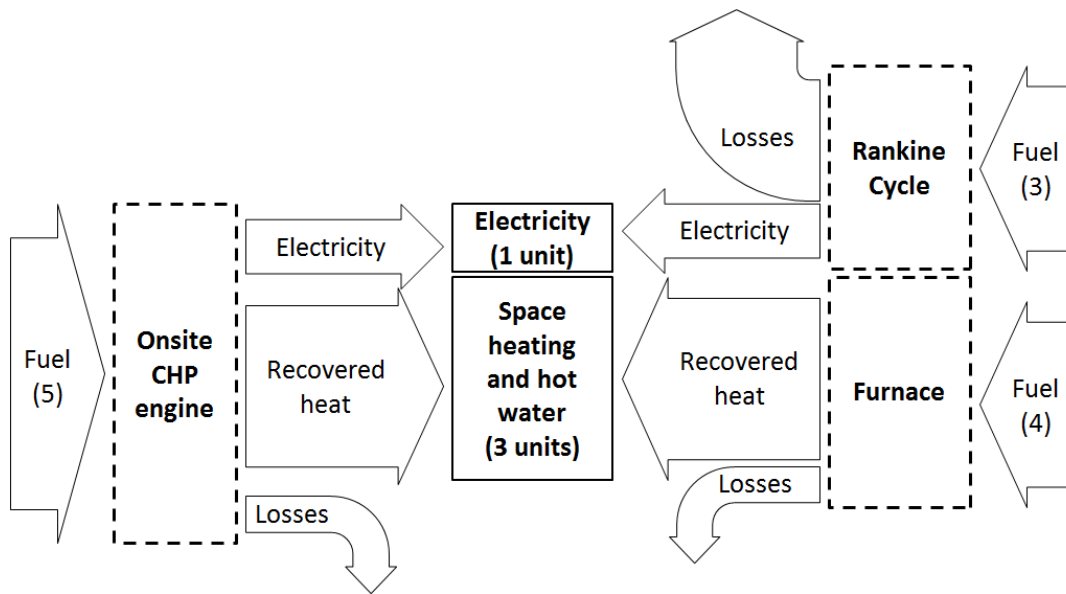


Figure 1: Illustration of the primary energy savings of using conventional onsite CHP compared with a baseline system

The simple analysis presented in Figure 1 does have some problems. For one, the 3:1 ratio of heating to electrical loads, which corresponds to the ratio of outputs of a typical small IC cogeneration engine, is only present for a few hours per year. Most of the year, the ratio of thermal to electrical loads will be greater or less than this value, and of course undergoes substantial diurnal fluctuations as well. Thus, in order to reduce capital cost and increase the average part load ratio of the CHP engine, conventional residential CHP systems generally include (1) a hot water thermal buffer storage tank of 350 to 1000 liters (about 100 to 300 gallons) and (2) an auxiliary fuel burner (boiler or furnace) to handle peak heating loads. Furthermore, during the cooling season, the only heating load is for DHW, and a CHP engine sized for winter will be grossly oversized for providing DHW alone, resulting in poor efficiency and low utilization during roughly half the year. In general, a conventional CHP engine will be utilized about half the hours in a

year, and the auxiliary burner will consume about as much fuel as the CHP engine.

The actual fuel savings realized by CHP installations in the field have been well characterized by a number of studies, notably by the UK Carbon Trust (2007). In a field study of 72 homes, it was found that appropriate residential installations (using Stirling engines with only 6% electrical efficiency) saved 4-14% on primary energy, while some inappropriate sites actually saw an increase in primary energy use with CHP.

1.2.2 Unconventional residential CHP

A fuel-burning furnace or boiler is not the only option for auxiliary heating. Several researchers have looked at using a VCS as backup.

Miguez et al. (2004) and Smith and Few (2001) discussed packaging a CHP engine with a vapor compression heat pump (in heating mode). In general, using a VCS instead of a boiler enhances the annual performance of the system, although it may be more difficult to package. Whereas a boiler connects directly to the thermal buffer tank already in place for the engine, the VCS needs to be installed separately. On the other hand, most homes in the US already have ductwork for air conditioning which can be used for a heat pump.

1.2.3 Residential CCHP








To date, no experimental data has been published on residential-scale (<5 kW_{elec}) micro CCHP for space cooling.

Ge et al. (2009) performed experimental and simulation studies on an 80 kW_{elec} gas turbine-based trigeneration system utilizing ammonia/water absorption chiller. Li and Wu (2009) performed experimental work on trigeneration system using a 16 kW_{elec} gas engine and adsorption heat pump. Table 1 summarizes the most closely related experimental work.

All of the work summarized in Table 1 used commercial reciprocating engines, and the majority also utilized commercial cooling equipment. In this dissertation work, a prototype chiller was constructed. The capacity of the prototype chiller was limited by the availability of sizes in desiccant-coated heat exchangers which were donated by the desiccant manufacturer. Had any size been available from the manufacturer, the chiller could have been about 6 kW for a 4 kW_{elec} engine. The engine was chosen from very limited commercial options in the US. The most optimum combination of sizes for an average US single-family residence may be a 1-2 kW_{elec} engine with a 2-3 kW chiller.

Table 1 demonstrates the literature gaps that are addressed by this dissertation. This dissertation work is the first research on fossil fuel powered trigeneration using driving temperature of less than 75°C, to use coolant heat as well as exhaust heat from a small prime mover.

Table 1: Summary of gaps in published literature on small and micro trigeneration

	Gluesenkamp (2012)	Khatri et al. (2010)	Angrisani et al. (2012)	Lin et al. (2007)	Li and Wu (2009)
Prime mover description	4 kW SI-ICE	3.7 kW CI-ICE	6 kW SI-ICE	9.5 kW CI-ICE	16 kW ICE
Chiller description and T_{regeneration}	3 kW zeolite A/C 70°C	0.04 kW NH ₃ refrig. 115°C	10 kW LiCl A/C >80°C	0.04 kW NH ₃ refrig. >200°C	10 kW silica gel A/C 80°C
Prime mover <5 kW	yes 	yes 	no	no	no
“Large” chiller*	yes 	no	yes 	no	yes 
Coolant waste heat utilized	yes 	no	no	no	no
Driving temperature <75°C	yes 	no	no	no	no

* Here “large” is defined as a cooling capacity more than 25% the PM electrical capacity

A heat-activated heat pump can, in general, provide either heating or cooling. In cooling mode, it will convert high temperature heat into low temperature cooling, rejecting both of these energy inputs at an intermediate temperature just above the ambient. In heating mode, it will accept heat both from the high temperature source and from the low temperature ambient, and provide both of these energy inputs at an intermediate temperature for space heating. In practice, heat-activated systems have mostly been explored for cooling, and this section summarizes some of these studies.

Li and Wu (2009) discuss packaging a water/silica gel adsorption heat pump (in cooling mode) with a CHP engine (16 kW electrical capacity).

Huangfu et al. (2007) experimentally evaluated an adsorption chiller for CCHP operation. They also discussed the control strategies of how to operate the

adsorption heat pump at part load: 1) varying the temperature supplied for desorption 2) varying the mass flow rate of heating water supplied for desorption 3) varying cycle time and 4) varying mass recovery pattern.

1.2.4 Adsorption heat pumps

The adsorption refrigerator was first developed more than 150 years ago, and due to the advantage of not requiring electricity, it was popular in railcars and other applications in an era without an electric grid. The technology all but disappeared following the popularity of the vapor compression cycle.

In recent decades, adsorption chillers and heat pumps have been explored by several researchers. Research in the technology underwent a revival in the 1990s, with a large number of papers being published since then.

Chen et al. (2010) proposed an adsorption heat pump design without valves.

Alefeld and Radermacher (1994) and Herold et al. (1996) defined the COPs achievable by ideal absorption heat pumps and refrigerators, and Meunier et al. (1997) used this as a starting point to establish the fundamental efficiency limits of adsorptive refrigeration cycles. While the theoretical performance limit of absorption cycles is equal to the Carnot limit, the theoretical performance limit for adsorption cycles is always less. This is due to the alternating nature of the adsorption and desorption processes, meaning that the adsorbent beds must be sensibly heated and cooled in transition between adsorbing and desorbing modes. Even if the heat used to heat the “dead mass” of the system is fully recuperated, for at least some portion of the cycle a finite temperature gap must exist between

the effective cycle temperatures and the heat reservoir temperatures, no matter the device design.

To quantify this performance degradation due to adsorber/desorber temperature swings, it is necessary to assign a finite heat capacity value to the adsorber beds.

Meunier et al. (1997) defined a basic adsorption cycle as having a single-bed, which is incapable of regenerative heating, and the condenser and adsorber temperatures are assumed to be equal. For this cycle, a typical COP will be one fifth of the Carnot COP.

However, it is important to note that, despite this difference in theoretical performance limits, practical devices may not follow the same trend. In particular, performance limits can be defined based on fluid properties rather than simply temperatures. From Alefeld and Rademacher (1994), the COP of absorption systems is limited by Equation (1).

$$COP = \frac{h_{fg}}{h_{fg} + \Delta h_{mix}} \quad (1)$$

1.2.5 Proposed system enhancements relevant to residential adsorption systems

Zogg et al. (2005) discussed ways to improve absorption systems, and some of their suggestions can also apply to adsorption systems. In particular, using a direct expansion (DX) evaporator to directly cool the building air would lower the overall temperature lift required of the heat pump. However, a DX evaporator would require a new evaporator design, as conventional evaporators

for vapor compression systems would not be suitable to the very low working pressure and higher sensitivity to pressure drop of adsorption heat pumps. As also noted by Zogg et al. (2005), a falling film design could be effective and practical as a DX evaporator for this application.

For the present experimental study, a chilled water loop was selected as the heat source for the evaporator for ease of measurement, control, and installation in the lab. However, it is expected that a commercially available residential adsorption system would likely utilize a DX evaporator of novel design. Compared with a chilled water secondary loop, this would minimize the overall temperature lift, reduce system complexity, and be more compatible with existing air conditioning ductwork.

Another cycle modification proposed by Zogg et al. (2005) is to boost the adsorber pressure (or reduce the desorber pressure) utilizing a small pressure ratio axial fan. This was proposed primarily as a means of avoiding crystallization in water-LiBr absorption systems, and it does of course incur a parasitic penalty by requiring electricity to run a fan. However, the fan could potentially be used in an adsorption system to boost the system performance during the extremes of ambient conditions, in order to allow the overall system to be sized slightly smaller, potentially mitigating capital costs and raising the seasonal average part load utilization ratio. In the adsorption cycle context, it is possible that a control strategy which utilizes mechanical pressure boosting for a short period at the end of the desorption/adsorption process might enhance capacity with a minimal COP penalty. Further study would be required to evaluate these potential benefits and

weigh them against the additional parasitic load and system complexity. In addition, this idea would not apply to systems which use water as a refrigerant, since no compressor exists at the appropriate scale to pressurize saturated water vapor at evaporator conditions (with a density one-hundredth that of atmospheric air).

1.2.6 Carnot efficiency for heat-activated cycles

For reference, contour plots are created here for the Carnot COP of heat-activated cooling and heating devices, as shown in Equations (2) and (3) and Figure 2 and Figure 3.

$$COP_{HACD} = \frac{T_2 - T_1}{T_2} \frac{T_0}{T_1 - T_0} \quad (2)$$

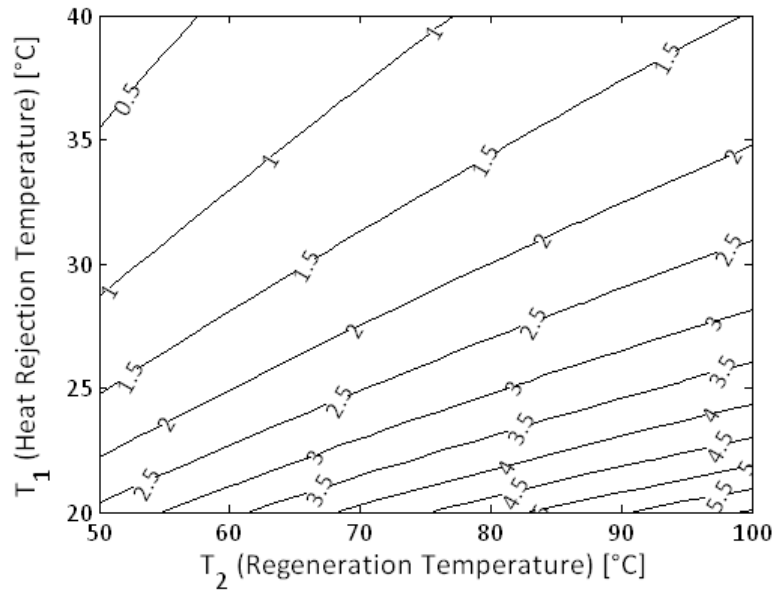


Figure 2: Carnot cooling efficiency ($COP_{clg,Ct}$) for an ideal heat-activated cooling device providing cooling at 10°C.

$$COP_{HAHD} = \frac{T_2 - T_0}{T_2} \frac{T_1}{T_1 - T_0} \quad (3)$$

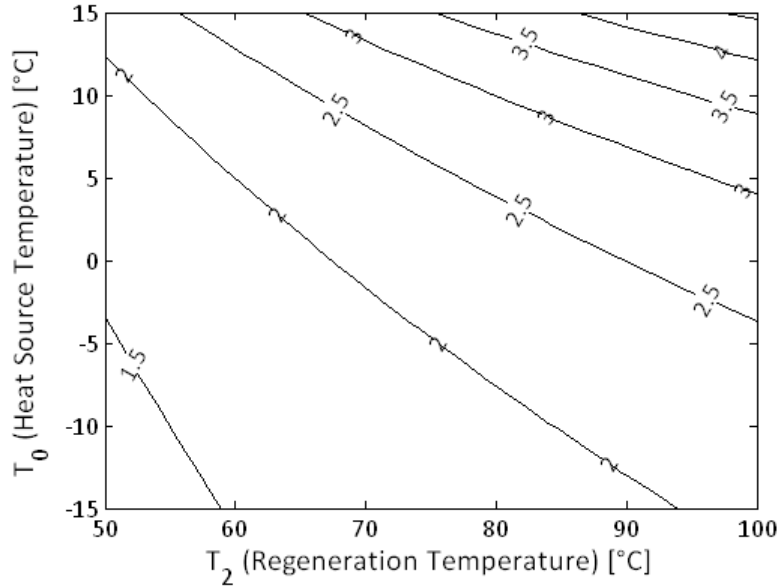


Figure 3: Carnot heating efficiency ($COP_{htg,Ct}$) for an ideal heat-activated heat pump device providing heating at 30°C .

In practice, most heat-activated cooling devices do not qualitatively follow the Carnot efficiency trend of increasing COP with increasing regeneration temperature. Typically there is some minimum regeneration temperature for proper operation, and as the regeneration temperature increases above that minimum, the device COP does not change appreciably (unless the cycle is fundamentally changed to better exploit a higher temperature, such as going from a single- to double-effect chiller). Thus it can be said, for a particular device, that the fraction of Carnot (also known as the Second Law efficiency) defined in Equation (4) tends to drop with increasing regeneration temperature.

$$f_{Ct} = \frac{COP}{COP_{Ct}} \quad (4)$$

In a Carnot cycle, all heat transfers occur across infinitely small temperature differentials, and all mass and momentum transfers (e.g. pumping, expansion, pipe flow) are reversible. In order to precisely quantify the deviation

of a cycle from the Carnot ideal, it would be necessary to know the finite driving potentials and corresponding flows for all heat, mass and momentum flows in a system. Further, in a system such as an adsorption cycle which has no true steady state, these potentials and flows must be integrated in time as well as space.

To pinpoint the areas in which design changes can have the largest impact on COP, the sources of entropy generation within the cycle can be analyzed. This is because the degree to which a system's COP approaches the Carnot limit depends on reducing irreversibilities, which are proportional to entropy generation, as discussed by Bejan (1982). For analysis of heat conversion systems, it is convenient to classify the various sources of entropy generation into three categories. External thermal coupling covers any heat transfer across a finite temperature difference between the cycle and a reservoir with which it communicates. Internal thermal coupling covers heat transfers among components within the system. Finally, the "other" category captures entropy generation due to phenomena such as viscous friction, chemical mixing, turbulent expansion, etc.

In vapor compression systems, it turns out that the most important entropy generation generally occurs within the compressor (due to heat transfer to and from the refrigerant during compression) and expansion valve (unrestrained expansion). In absorption cycles, the compressor is eliminated, but expansion losses still occur, and mixing of different fluids also contributes. For a well-designed absorption machine, the main irreversibilities occur in internal thermal transfers (solution heat exchanger) and external thermal transfers (in the condenser, evaporator, and generator) (Herold et al. 1996).

Adsorption cycles, by their very nature, require periodic heating and cooling of the adsorbent. Thus external thermal coupling entropy generation is very significant in adsorption cycles. Indeed, Meunier et al. (1996) calculate that, for a basic cycle (a single adsorber without regeneration), 97% of the overall entropy generation is attributable to external thermal coupling, and the COP is only one fifth of the Carnot COP. Regeneration (using two uniform-temperature adsorbers) improves the cycle COP by 50%, with external thermal coupling then contributing 70% of the irreversibilities, and internal thermal coupling (i.e. regeneration) contributing 22%. Further gains can be realized by increasing the number of adsorbers, or using a better regeneration process such as thermal wave regeneration rather than the uniform temperature process.

It is important to remember the role of fluid and mixture properties in determining system performance. While absorption systems are basically limited to two working pairs, adsorption systems have a much wider variety of possible working pairs, with many being developed. Thus, despite the inherent penalties involved in cyclic heating and cooling, adsorption systems could theoretically perform better than absorption with suitable working pair and design for heat and mass transfer.

An opportunity exists to improve adsorption system performance by reducing the “dead thermal mass” of the adsorber heat exchangers. This would benefit adsorption cycles independent of working pair selection. Current adsorption devices face a compromise between efficiency and power: on one hand, a packed bed of adsorbent pellets can be used, yielding a very low amount

of dead mass and high COP, but with poor heat transfer characteristics and therefore long cycle times required, resulting in low specific cooling power (SCP). On the other hand, a thin coating of adsorbent can be placed on a fin-and-tube heat exchanger, yielding excellent heat transfer characteristics (short cycle time; high SCP) with the penalty of a very high dead thermal mass ratio (and thus lower COP and more need for regeneration).

If a coated heat exchanger can be developed that reduced dead thermal mass while maintaining good heat transfer characteristics, it would advance the Pareto front of SCP vs COP for adsorption machines. Additional contributions would be making the system more compact, or increasing volumetric cooling power (VCP).

For stationary (e.g. residential) applications, the development of a heat exchanger with lower dead mass and better heat transfer characteristics can improve the achievable temperature lift. This translates into less degradation of capacity and COP at extreme environmental conditions, allowing the system to be sized smaller and therefore be less expensive.

For conventional automotive applications, the available waste heat is generally greater than the required cooling load. This means that there is some threshold value for thermal COP above which additional COP gains do not improve system efficiency. On the other hand, increases in SCP and VCP always return benefits by reducing the parasitic weight and volume that the vehicle must carry. If the dead mass is reduced enough, the potential exists to create a device

with sufficient efficiency that does not require regeneration, greatly simplifying the plumbing required.

1.3 Objectives and Approach

This thesis has two main objectives. The first is to determine and investigate the performance limitations of trigeneration systems, both analytically and experimentally. Since dynamic (load-following) operation is an important aspect of actual system performance, the experimental work involved multi-day experiments that followed realistic residential load profiles. Furthermore, development of a control strategy for novel prototype equipment was a critical enabling step for this load-following experimental approach. The analytical work allowed this objective to be addressed for ideal systems, a range of commercially available systems, and a range of technologically feasible systems.

The second main objective is to enhance trigeneration system performance by developing cooling strategies for high ambient temperatures. Operation in high ambient temperature conditions is one of the primary technical barriers for many thermally-driven cooling systems. This second objective was addressed through a modeling-based approach.

A further note is warranted on the first objective. This first objective is closely related to determining the energy-saving potential of micro trigeneration. This potential can be evaluated on economic or energetic terms, and this thesis focuses on the energetic evaluation since the benefits of a technology need to be identified before investment would be justified. However, since high initial cost is a primary practical barrier for polygeneration systems, the costs of components,

manufacturing, and installation are always kept in mind. In this thesis, the working definition of “energetic suitability” is that a micro-trigeneration system should result in a reduction in primary energy consumption to meet a given set of loads, when compared to the conventional methods of meeting those loads. Suitability thus depends on (1) trigeneration technologies (prime movers and thermally driven heat pumps), (2) the loads to be met and (3) assumptions made about the baseline system. The various combinations of these three elements are practically infinite, so an implicit additional objective is to develop meaningful evaluation criteria that lead to helpful results.

1.4 Dissertation Organization

Chapter 1 describes the background behind the dissertation, and a review of available literature, with gaps identified to support the contributions of the dissertation. Chapter 2 contains an analysis of trigeneration systems that justifies the experimental and simulation work described in subsequent chapters. It also provides insights into the most promising directions for trigeneration research and development and the performance potential of such systems. Next, novel applications of separate sensible and latent cooling (SSLC) to trigeneration are described in Chapter 3, since these SSLC strategies play a role in subsequent chapters. Chapter 4 describes the development of the experimental test facility, with experimental results presented in Chapter 5. Component and system models are described in Chapter 6, including analytical, thermodynamic, and empirical models of the adsorption cycle. Experimental results are used to validate the

various models. Finally, conclusions and recommendations for future work are provided in Chapters 7 and 8.

Chapter 2: Residential Energy Systems – Inventory and Analysis

Do polygeneration systems save energy? At first glance, there are arguments for both sides. In favor of distributed small trigeneration systems, heat energy is utilized that would otherwise be wasted. In favor of centralized generation with distributed vapor compression systems, centralized power stations have the economies of scale to maximize electrical generation efficiency. Numerous other relevant factors can be identified, such as the type of prime mover technology, the efficiency and parasitic electrical consumption of thermally driven equipment, and more. The question quickly becomes a complex one to answer.

This chapter addresses this central question in five sections. First, “temperature-cumulative heat load” analysis (or T-Q analysis) establishes whether residential loads are feasible candidates for trigeneration at all. Next an inventory of possible residential systems is presented for perspective on the issue. These possibilities are narrowed in the third section, which addresses the matching of prime movers with appropriate thermally-driven equipment. Finally, the fourth and fifth sections address the original question directly with an analytical treatment based on simple models of the most relevant systems, and chapter conclusions are summarized in a sixth section.

2.1 T-Q analysis of feasibility of residential trigeneration

Figure 4 depicts U.S. residential loads in a T-Q diagram, a central tool of pinch analysis (Kemp, 2007) (also called pinch technology or process integration). This diagram plots the various heat loads as lines where the width corresponds to the heat required [kW] and the height corresponds to the temperature change required. The slope thus corresponds to the inverse of heat capacity flowrate (i.e. [K/kW]), or the temperature change for a unit of heat extraction, of the streams. The units of heat load used here are Quads of site energy per year (according to the DOE EERE Energy Data Book [1]). The four loads requiring heat addition have been laid out one after the other horizontally, and similarly for the three loads requiring heat removal.

Three insights can be gained from this residential T-Q diagram: (1) the limited opportunities for recuperative heating can be identified, (2) the exergetic waste involved in furnaces and boilers can be seen, and (3) the potential for matching on-site polygeneration system to residential loads can be seen.

The T-Q diagram in Figure 4 can be redrawn as a “composite curve,” shown in Figure 5, in which the heating loads have been combined, and the cooling loads have been combined. In general, inspection of the composite curve reveals opportunities for recuperative heating: wherever a temperature-overlap occurs between heating curves (curves with positive slope) and cooling curves (with negative slope). Thus it can be seen that there is very little opportunity for recuperative heat transfer in residential systems – the only opportunity appears to be using DHW as a heat sink for space cooling over a small temperature overlap

(about 15 to 25°C). Air-to-air recuperation of ventilation air (i.e. “energy recovery ventilators,” or ERVs) is another opportunity. Additional opportunities, not shown here, emerge when the actual component temperatures of vapor compression units are depicted. This would show the possibility of using a desuperheater on a heat pump or air conditioner to heat DHW.

Another instructive aspect of Figure 4 is to consider the combustion temperature of fossil fuels typically used for heating. Burning fossil fuels at thousands of degrees is clearly not necessary for any typical residential loads, particularly for the largest residential heating loads of space heating and hot water heating.

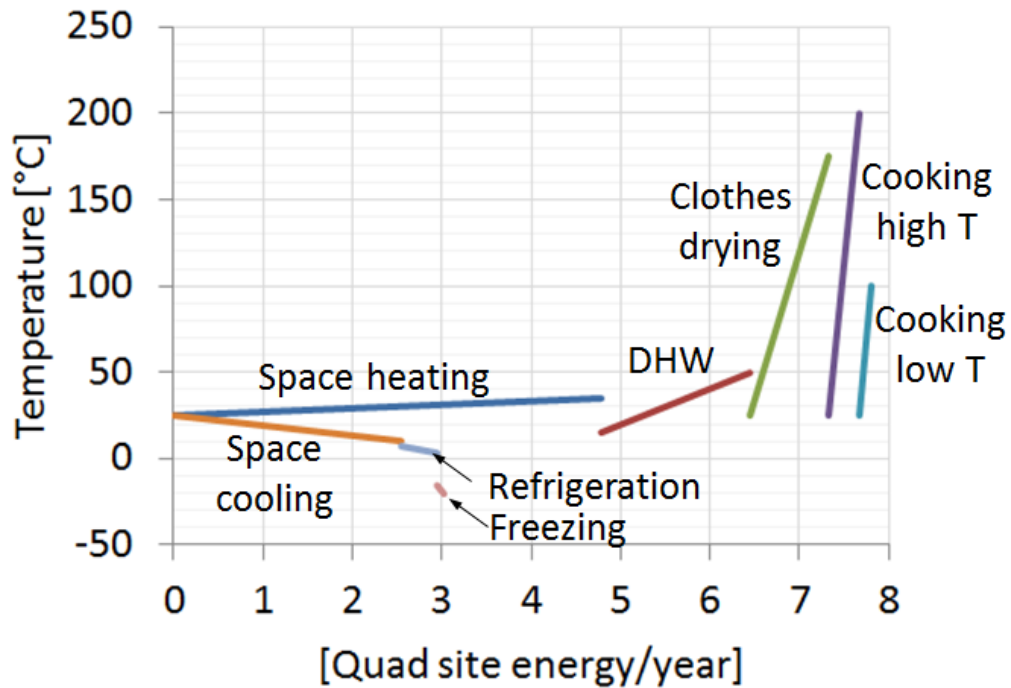


Figure 4: Approximate residential thermal loads for the entire US

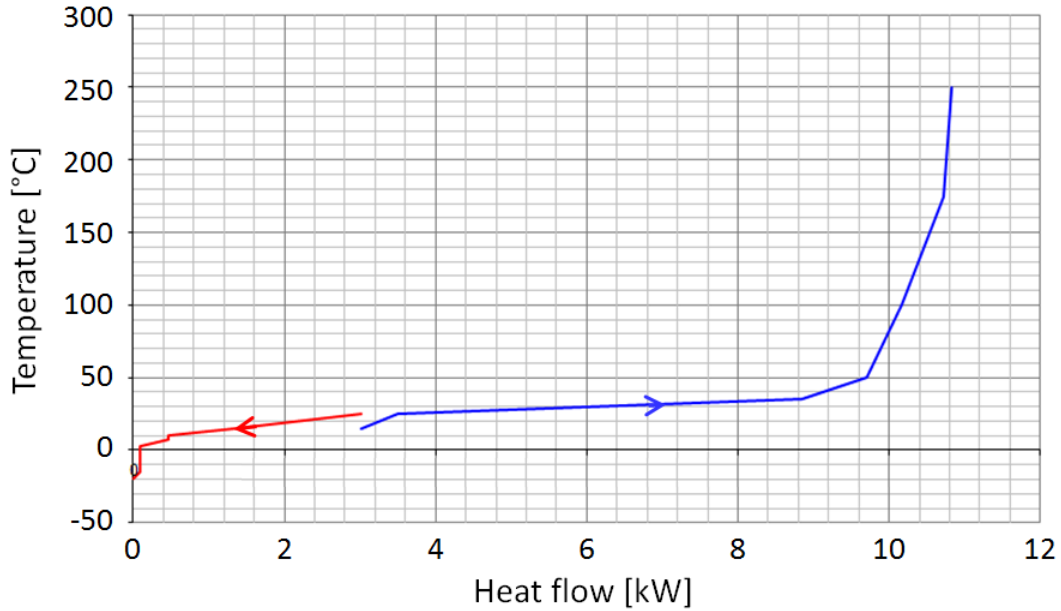


Figure 5: Hot and cold composite curves for aggregated annual residential thermal loads – includes both space heating and space cooling

Finally, the third insight comes from comparing the loads to the waste heat available from an engine. Figure 6 shows the case for winter, in which engine waste heat is well suited to the DHW and space heating loads of a residence.

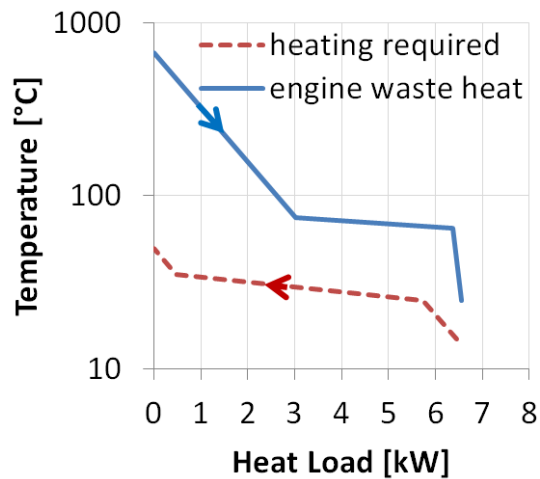


Figure 6: T-Q match between SI-ICE engine waste heat and residential winter heating requirements

Figure 7 depicts the case for summer, during which there are average space cooling and DHW loads. The DHW load is met directly by engine waste heat, while the cooling load is met by the evaporator of an adsorption heat pump.

Since the adsorption heat pump COP is assumed as 0.5, the width of the desorber line is twice the width of the evaporator line. The engine waste heat is again well-suited to the loads, and importantly, this engine is of similar capacity to the engine used in the summer case (7 kW waste heat in summer, 6.5 kW waste heat in winter).

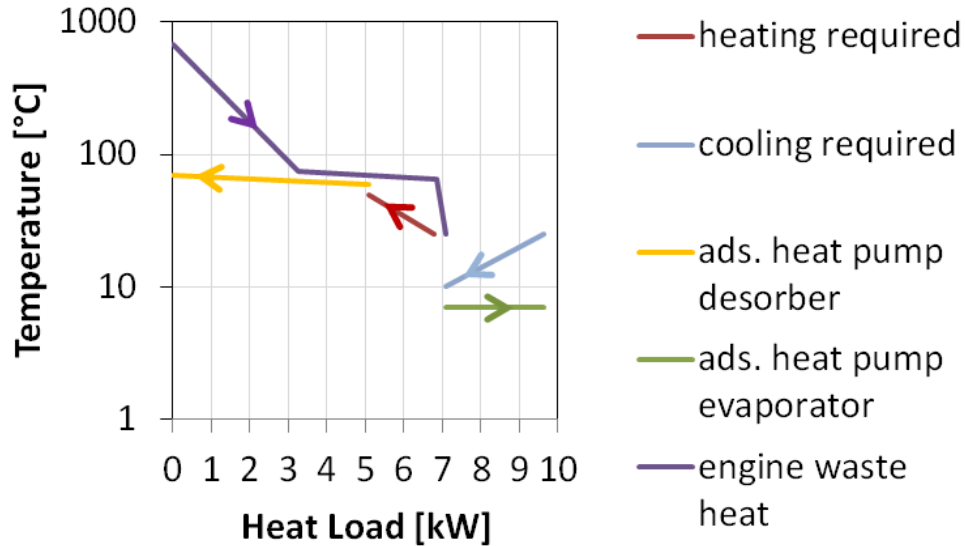


Figure 7: T-Q match for SI-ICE engine and residential summer cooling with heat-activated air conditioning device

This initial T-Q analysis shows that there is potential for using residential cogeneration engines as waste heat sources for thermally-driven residential cooling.

In practice, a storage tank would generally exist between the heat source and the loads. This means that a third line, representing the tank temperature, would lie in between the source and loads in the T-Q diagram. This line would be at best horizontal when thermal stratification is used to maintain constant high temperature availability.

2.2 Inventory of residential energy systems

In this section some perspective is offered by providing an inventory of (1) non-CHP residential energy systems, (2) CHP residential energy systems and (3) polygeneration systems.

In most residential energy systems today, each load is met by a sub-system which is completely independent of all other sub-systems. For example, a water heater provides hot water, a furnace provides heating, and a VCS provides air conditioning. Yet, it is very common for both natural gas and electrical grid connections to be present in typical US homes, and thus no infrastructural reason that each home can not act as a small cogeneration facility, importing gas and importing or exporting electricity.

Table 2 shows 30 possibilities for providing electricity, space heating, space cooling, and domestic hot water to a residence without CHP. It is assumed the residence requires both space heating and cooling during a typical year. Each possibility is characterized by the equipment present on site. Systems are distinguished by the following:

- the source of heating, whether boiler/furnace (BF), VCS, or electric resistance (ER)
- the method used for water heating: gas fired (GF), electric resistance (ER), or heat pump (HP)
- the presence or absence of a desuperheater on the main VCS for pre-heating domestic hot water
- if a VCS is used for heating, the presence or absence of backup heat, whether gas fired (GF) or electric resistance (ER) backup

Each “X” in Table 2 represents a physical device installed. When a VCS is present for space heating, it is assumed that VCS will also be used for cooling.

Table 2: Baseline (non-CHP) systems

Systems		Space heating and cooling component(s)					DHW components	
# of systems in row	Description	VCS cooling	VCS heating	Boiler/furnace	ER heating	Backup for VCS _{htg}	Primary water heater	Desuperheater
6	Baseline – gas heat	X		X			GF/ER/HP	y/n
18	Baseline – VCS heat		X			BF/ER/none	GF/ER/HP	y/n
6	Baseline – ER heat	X			X		GF/ER/HP	y/n

Table 3: CHP and CCHP systems

Systems		Onsite prime mover	Space heating and cooling component(s)					DHW components	
# in category	Description	Engine with HR	VCS cooling	VCS heating	AHP cooling	AHP heating	Backup heating	Primary water heater	Desuperheater
4	CHP-VCS _{clg}	X	X				BF/ER	PM	y/n
6	CHP-VCS _{htg}	X	X				BF/ER/ none	PM	y/n
2	CCHP-AHP _{clg}	X			X		BF/ER	PM	
6	CCHP-AHP _{clg} -VCS _{htg}	X	X		X		BF/ER/ none	PM	y/n
6	CCHP-AHP _{c/h} -VCS _{c/h}	X	X		X		BF/ER/ none	PM	y/n

Table 3 shows a comprehensive list of 24 possible polygeneration systems. It includes adsorption/absorption heat pumps (AHP), heating and cooling VCSs, and assumes that the prime mover will serve as the primary heat source (for both space heating and DHW). It is also assumed that a backup heat source is required; and if a VCS heat pump is the backup, an additional backup may also be required. Additional assumptions are listed in the following page.

In a simplified model, the number of possible systems scales as k^n , where k is the number of possible devices that could provide each amenity (e.g. electric heater, gas heater, desuperheater, etc) and n is the number of amenities (e.g. domestic hot water) to be provided. For example, if electricity, hot water and space cooling are required, and each could be provided by 2 possible devices, there would be $3^2 = 9$ possible systems. Changing the number of possible devices thus very rapidly increases the number of possible systems, with, for example, $5^3 = 125$ systems possible if each of three amenities has five possibilities.

In reality, each service does not have the same number of possibilities as the others, and certain possibilities preclude others. For example, if a home is to be heated with a vapor compression heat pump, then that heat pump will also be available for cooling duty in the summer via a 4-way valve. Another example is that, if no heat pump is used, then a desuperheater for DHW pre-heating is not possible.

Despite the expectation of possibilities increasing exponentially as additional component possibilities are considered, there are fewer possibilities with an onsite engine than without. This is due to the assumption that the onsite engine will always be the

source of DHW, whereas for all cases without an onsite engine there are three possibilities of DHW devices.

Table 3 contains 24 possibilities with an onsite engine (compared to the 30 baseline possibilities in Table 2).

Assumptions used in Table 3:

- Grid power is available
- If a CHP system exists onsite, it is the source of DHW
- The use of a cogeneration engine for DHW does not require backup, but use for space heating does
- A CHP system is always packaged with a backup space heating source – a boiler, furnace, or VCS.
- Since the capacity of a VCS for heating can be severely reduced at very cold ambient temperatures, it is common practice for standalone VCS units for heating to be packaged with a backup heating source (electric resistance or boiler/furnace). This may be required even if the VCS itself is a backup for a cogeneration engine.
- If a VCS heating system is in place, it includes a 4-way valve allowing cooling operation as well
- Direct-fired thermally-driven devices are not considered

Some possible devices not considered in Table 3:

- Solar space heating
- Solar hot water
- Biomass space heating (e.g. wood stove or pellet stove)
- Backup generator for grid power outages

Some possible loads not considered in Table 3:

- Pool heating
- Refrigeration

In the following sections, these multitudinous system possibilities are reduced to four: (1) grid-driven VCS, (2) direct-fired heat-driven chiller (3) engine heat-driven chiller, and (4) engine driven chiller and VCS.

Although not considered in subsequent analysis, it is important to make note of heat-driven heating devices. A heat-activated heat pump can operate in heating mode, drawing in heat from the low temperature ambient (e.g. 5°C) and providing this heat at the required space heating temperature (e.g. 30°C). Since the high temperature driving heat will all exit the device at useful space heating temperature, the thermal COP of these devices in heating mode always exceeds 1, and a general rule of thumb is for the COP to be about 1.5.

A COP of 1.5 means that every kW recovered from the CHP engine at high temperature can be used to deliver 1.5 kW at the space heating temperature. This provides a significant boost in heating capacity, but has significant limitations.

Consider that a typical auxiliary furnace or boiler, packaged with a CHP system, will have a heating capacity several times the maximum heating output from the engine. Thus, even with a HAHD, another auxiliary heating device will likely be required to avoid having to over-size the CHP engine. This auxiliary device could be a boiler, furnace or VCS, just like in the case without a HAHD.

A second limitation of using a HAHD for heating is that water is a common working fluid for these systems. Since pure water will freeze at 0°C, and since an approach temperature exists in the outdoor evaporator, the HAHD would only be utilizable down to an ambient air temperature of perhaps 5°C, unless it has a ground-source heat exchange loop or cascade arrangement with a VCS.

A third limitation is that evaporator and condenser designs for heat-activated systems are generally quite different – in contrast to a VCS, where the condenser and evaporator have relatively similar designs. Thus reversing operation of the heat pump between summer and winter is more problematic for heat-activated devices than it is for vapor compression devices.

A final limitation is with the heat rejection temperature of HAHDs. Conventional heating systems have supply temperatures around 40-50°C. However, common HAHDs suffer from performance degradation at temperatures about about 35°C. Thus using thermally-driven systems for heating may require novel approaches, whether low-temperature heating (e.g. underfloor radiant heating, or designing for high air flow rates), cascaded systems for reduced temperature lift, or thermally-driven system strategies for elevated temperature lift.

Currently, several European manufacturers are looking into commercializing gas-fired, adsorption-based HAHD as boiler replacements.

2.3 Trigeneration device matching – prime movers and thermally-driven chillers

A survey of thermally-driven cooling options was carried out, with the results shown in Figure 8, which was published in Gluesenkamp and Radermacher (2011).

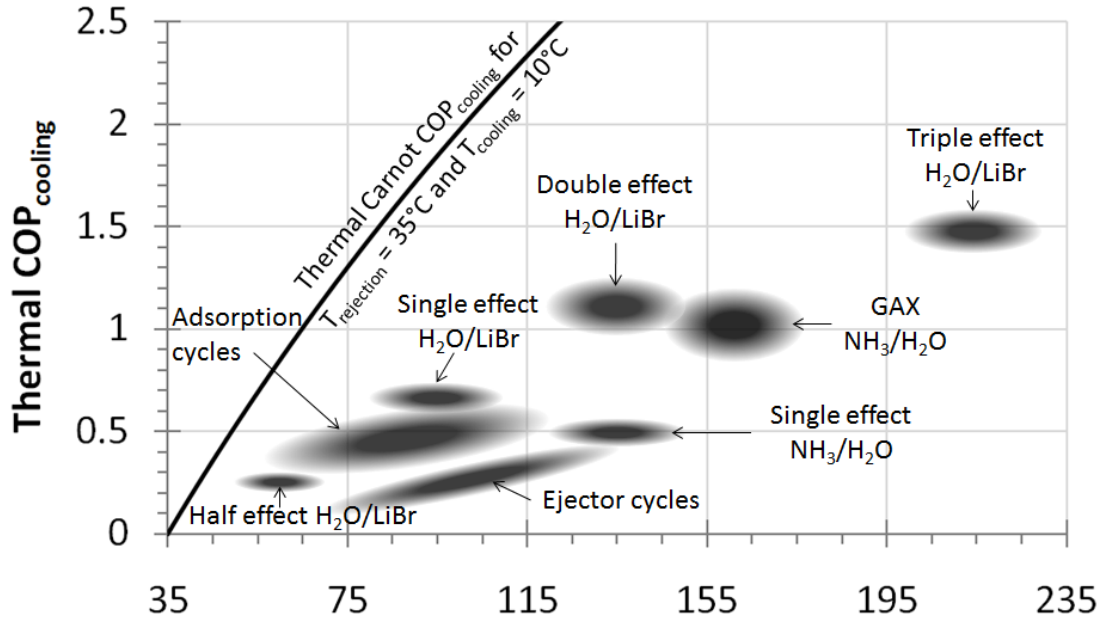


Figure 8: COP_{th} vs. regeneration temperature of heat activated cooling technologies (Gluesenkamp and Radermacher, 2011)

As shown in Figure 8, higher heat recovery temperatures generally allow better thermal COPs. However, at residential scales, only ICE, Stirling, and PEMFC based CHP units have been commercialized, which have heat recovery temperatures of only up to about 75°C. This limits the possibilities for residential trigeneration to adsorption and half-effect absorption technologies.

Regarding prime movers, it is important to consider the type and quality of waste heat available from each type. An analysis of the temperature versus cumulative heat transfer (T-Q analysis), a tool of pinch analysis (Kemp, 2007) is indispensable for making these comparisons of waste heat available from various prime movers.

From a system-perspective, the fuel energy that enters a prime mover exits in four ways: as electricity, exhaust/flue gas enthalpy, coolant heat, and “other” losses (including convection and radiation from the surfaces of the device, cyclic heating of components, etc.) In the analysis that follows, it is important to note that representative values are used

in this work to highlight the major differences among prime movers, and the particulars for each prime mover type can vary considerably depending on the design.

In the interest of a self-contained analysis, a reasonable estimate of the initial exhaust temperature can be obtained from an energy balance around the prime mover. One simple expression of this balance, shown in Equation (5), is possible with the following assumptions:

- constant specific heat of exhaust gases
- exhaust gas is not cooled below its dewpoint
- waste heat is defined as all fuel energy not converted to electricity
- values for AFR , $f_{exhaust}$, and η_{elec} are empirically known

$$T_{exhaust} \cong T_{ambient} + \left(\frac{1}{1 + AFR} \right) (LHV) (f_{exhaust}) (1 - \eta_{elec}) \left(\frac{1}{c_{P,exhaust}} \right) \quad (5)$$

Evaluation of this equation requires three empirical system-level values: the air-fuel ratio used by the device (AFR , mass basis), the electrical conversion efficiency (η_{elec}), and the fraction of waste heat rejected in the exhaust ($f_{exhaust}$). Here, waste heat is defined as fuel energy not converted to electricity (i.e. waste heat is proportional to $1 - \eta_{elec}$).

The water vapor content of combustion exhaust is generally quite high compared to normal air, due to the water formed in combustion. The mass fraction of water in the exhaust will depend primarily on AFR and ambient humidity. For a uniform, equilibrium cooling process, the exhaust dewpoint is the temperature at which water vapor will begin to condense. The exhaust dewpoint is equal to the saturation temperature of water at the water vapor partial pressure in the exhaust. Figure 9 shows the effect of AFR and ambient humidity ratio on the exhaust dewpoint. The graph has been generated by assuming

complete combustion of methane and air (all fuel is converted to CO_2 and H_2O), and that the exhaust gas cools in a quasi-steady equilibrium process at standard atmospheric pressure without any post-combustion dilution.

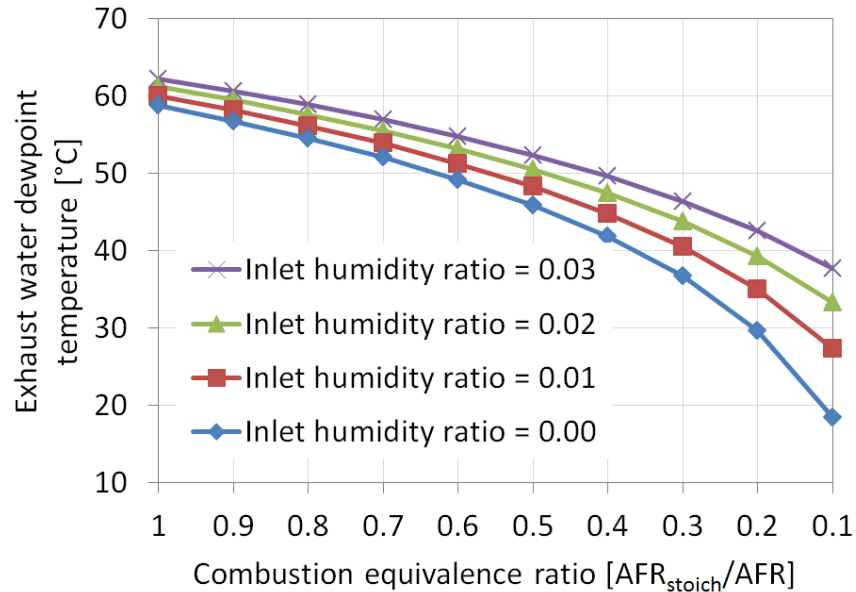


Figure 9: Water dewpoint of combustion exhaust as function of AFR and ambient humidity ratio

Figure 10 shows what this means for the four prime movers that reject a large fraction of their fuel energy in the exhaust, assuming the AFR values shown in Table 4 (note that equivalence ratio, $\text{AFR}_{\text{stoich}}/\text{AFR}$, is denoted ϕ). Prime movers with higher exhaust dewpoint have more potential to extract heat of condensation from the exhaust stream given a suitably low-temperature thermal load and/or suitably large temperature glide in their thermal load. This possibility is explored later (see Figure 108 to Figure 110).

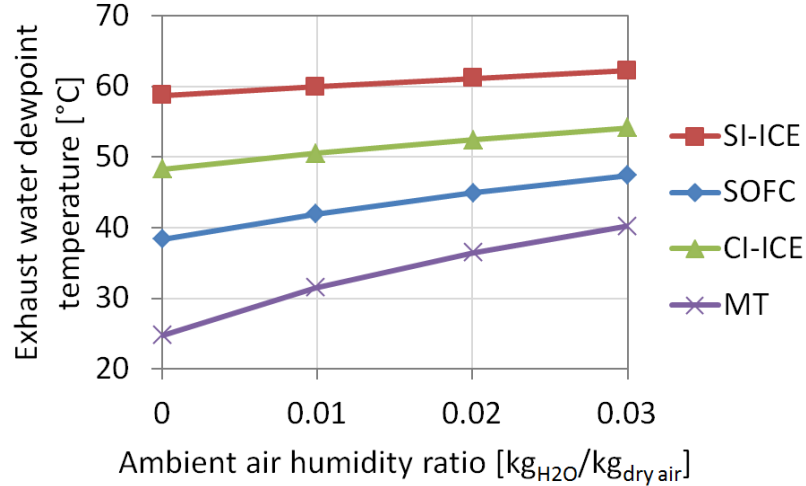


Figure 10: Water dewpoint of combustion exhaust typical of four prime mover types

Table 4: Parameters used in calculations for micro-scale devices ($\sim 25 \text{ kW}_{\text{elec}}$ for MT and $\sim 5 \text{ kW}_{\text{elec}}$ for all others)

Device	AFR [kg _{air} / kg _{fuel}]	$Y_{\text{H}_2\text{O,exh}}$ [kg _{H2O} / kg _{exh}] [†]	ϕ [-]	Fuel LHV [kJ/kg]	$\eta_{\text{elec,LHV}}$ [kW _{elec} / kW _{fuel}]	f_{exhaust} [kW _{exh} / kW _{wh}]	f_{clt} [kW _{clt} / kW _{wh}]	$T_{\text{clt,hi}}/T_{\text{clt,lo}}$ [°C]
SOFC	52	0.052	0.33	48,700	0.50	0.70	0.00	(no coolant)
SI-ICE	17.2	0.132	1.00	48,700	0.20	0.35	0.46	75 / 65
CI-ICE	30	0.082	0.57	48,700	0.24	0.33	0.47	85 / 75
MT	115	0.029	0.15	48,700	0.25	0.80	0.00	(no coolant)
SE/ORC	30	0.082	0.57	48,700	0.15	0.15	0.67	45 / 35
LTPEMFC	(N/A)*	(N/A)*	(N/A)*	121,000	0.40	0.00*	0.75	65 / 55
HTPEMFC	(N/A)*	(N/A)*	(N/A)*	121,000	0.40	0.00*	0.75	125 / 115

*it is assumed that PEMFC exhaust exits stack at coolant temperature and is cooled by intake air, thereby leaving control boundary near ambient temperature.

† for inlet air at 25°C and 50% RH (humidity ratio = 0.01) [kg_{H2O}/ kg_{dry air}]

For consideration of the heat available in the coolant as well, empirical knowledge of the fraction of waste heat rejected in the coolant (f_{clt}) and the coolant temperatures ($T_{\text{clt,hi}}$ and $T_{\text{clt,lo}}$) is also required. To create Figure 11, a T_{ambient} of 25°C and a constant $c_{P,\text{exhaust}}$ of 1.2 kJ/kg-K were assumed, along with the values in Table 4 for each prime mover. Most devices are assumed to run on natural gas, which has a stoichiometric AFR of 17.2 [kg_{air}/kg_{fuel}]. Regarding PEMFCs, only those running on pure hydrogen are considered in this work.

Figure 11 shows the available waste heat for eight prime movers of interest to micro polygeneration. Although not available at micro scales, the molten carbonate fuel cell (MCFC) is also included for comparison. All prime movers have been assumed to lose 15% of their fuel energy as un-captured heat dissipated to the ambient. Each line for exhaust heat assumed constant specific heat and extends down to the dewpoint temperature of the exhaust (corresponding to the water mass fraction shown in Table 4), which very closely approximates the heat released by the LHV of the fuel. Figure 11 has many uses for comparisons among prime movers and order-of-magnitude analyses. For example, by visual inspection of Figure 11, one can determine how much heat is available at a certain temperature from each prime mover.

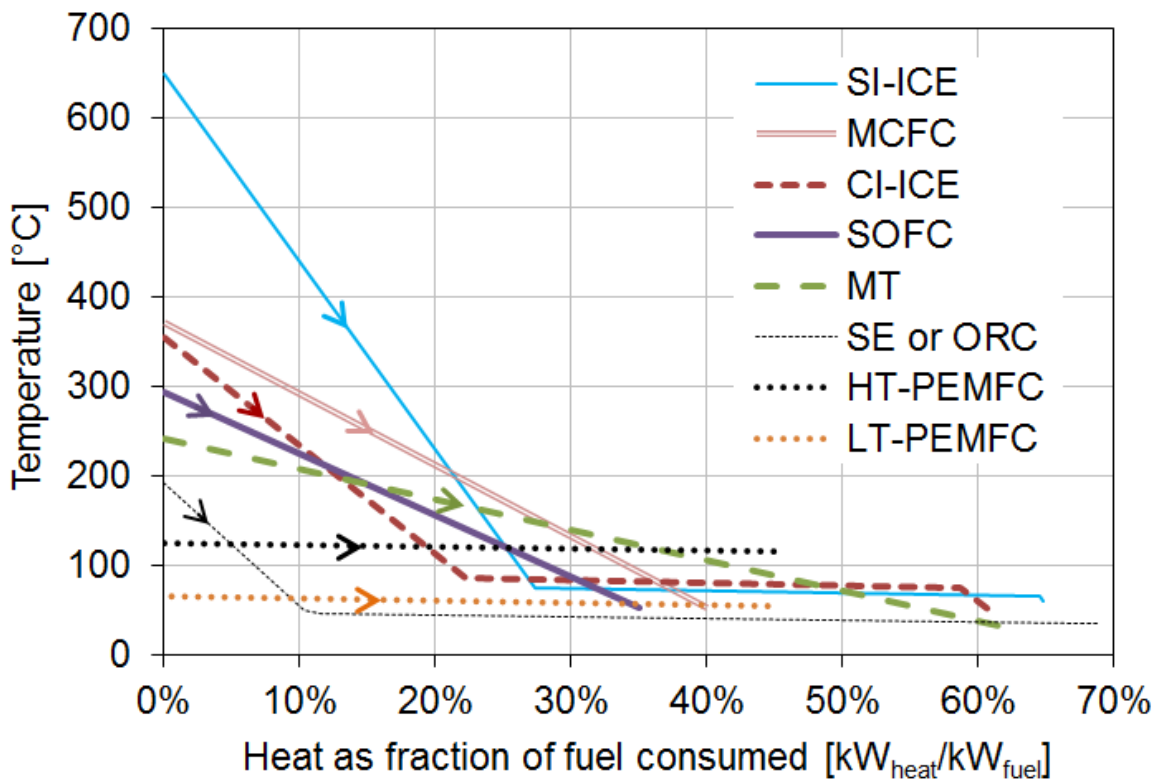


Figure 11: T-Q diagram for micro prime movers (temperature vs. fraction of fuel energy)

In addition, Figure 12 shows the T-Q diagram with heat depicted as the fraction of total waste heat rather than fraction of fuel energy.

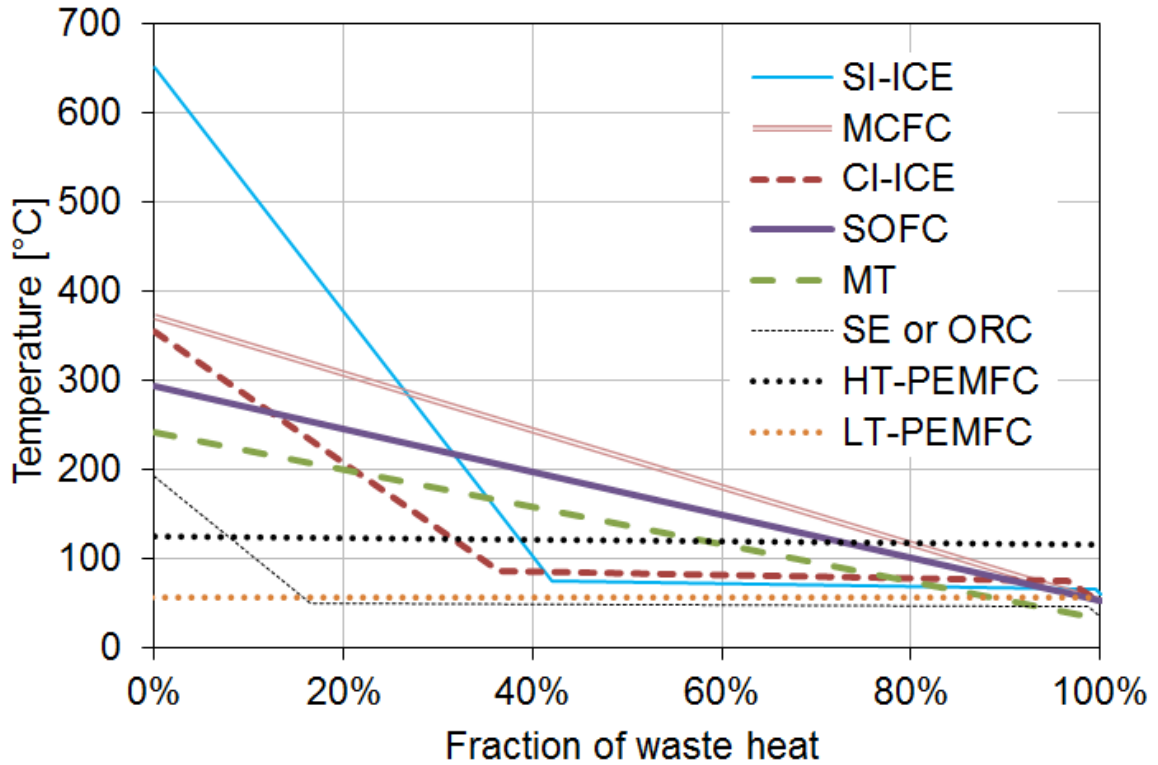


Figure 12: T-Q diagram for micro prime movers (temperature vs. fraction of waste heat)

Once the available waste heat (“heat source”) has been plotted (as in Figure 11 or Figure 12), the next step is to “match” it to a load, by determining how much available heat can actually be used by a given load. The line for a constant-specific-heat load consists of two points at the starting and ending temperatures (e.g. 25°C and 60°C for DHW). A restriction on the location of this line is that all points of the load line must lie below the source line, and be separated at every location by a minimum feasible local internal temperature difference, denoted ΔT_{min} . In these examples, $\Delta T_{min} = 10$ K was chosen. The location of a ΔT_{min} is called a “pinch point.”

Using the information contained in Figure 8 and Figure 11, each prime mover can be matched with a HACD technology. In many cases, more than one HACD technology is possible for a given prime mover. In these cases, a match is chosen that has the highest overall efficiency, given by the product of utilizable waste heat (Q_{util}) and COP_{th} . For

example, by inspection of Figure 11, for SI-ICE, adsorption can utilize 0.5 units of waste heat, so that $Q_{util} * COP_{th} = 0.5 * 0.5 = 0.25$ units of cooling. On the other hand, SI-ICE with SE-Abs can only utilize 0.21 units of waste heat, so that $Q_{util} * COP_{th} = 0.21 * 0.7 = 0.15$ units of cooling. Thus SI-ICE is matched with adsorption. The same procedure was applied to each prime mover technology individually.

This matching procedure results in Figure 13, which characterizes each trigeneration system by two values (electrical efficiency and thermal COP).

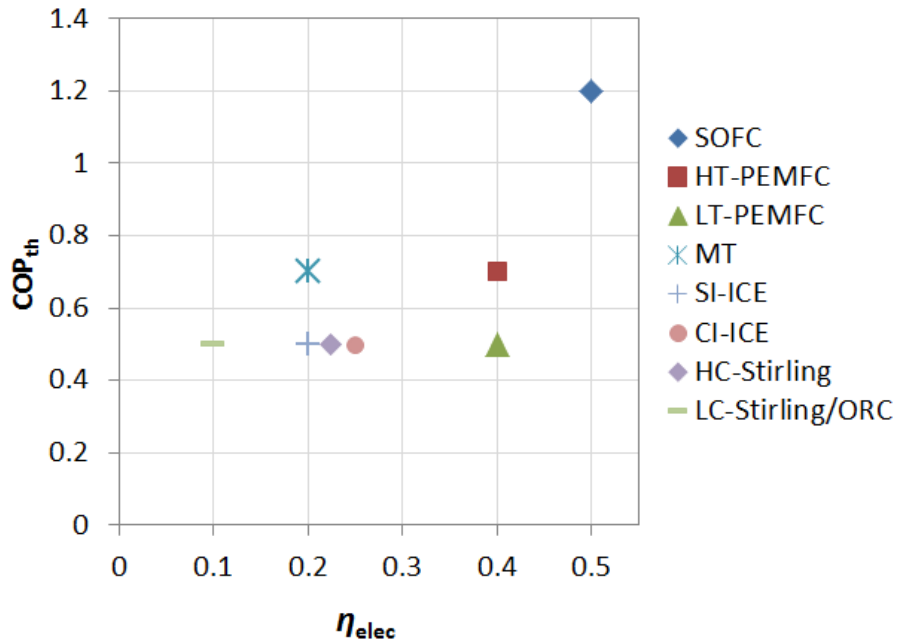


Figure 13: Matching of micro prime movers and heat activated cooling devices

Figure 13 serves as a description of the micro trigeneration systems that are possible. It will be adapted in the next section to account for the fuel consumption of trigeneration relative to conventional systems.

One drawback of Figure 11 and Figure 12 is that they do not capture the benefit of the electricity produced by the prime mover, since they only look at the waste heat. One way to capture the total benefit of all the products from the prime mover is shown in Figure 14. In this view, the “exergy factor” is defined as the theoretical potential for

prime mover outputs to produce work in a Carnot cycle (or infinite series of Carnot cycles at various temperatures), and this exergy factor is plotted against the fuel energy that entered the prime mover. Since electrical outputs are already a form of work, they have a value of 1. Exhaust and/or coolant waste heat has an exergy factor according to the efficiency of a Carnot engine operating at its temperature. Fuel energy lost via low temperature dissipation to the environment has an exergy factor of zero since it is effectively heat lost at ambient temperature. The area under such a curve thus represents the maximum possible work that could be produced by a prime mover, given a realistic characterization of its electrical efficiency and waste heat resources, and reversible utilization of all waste heat to produce further work.

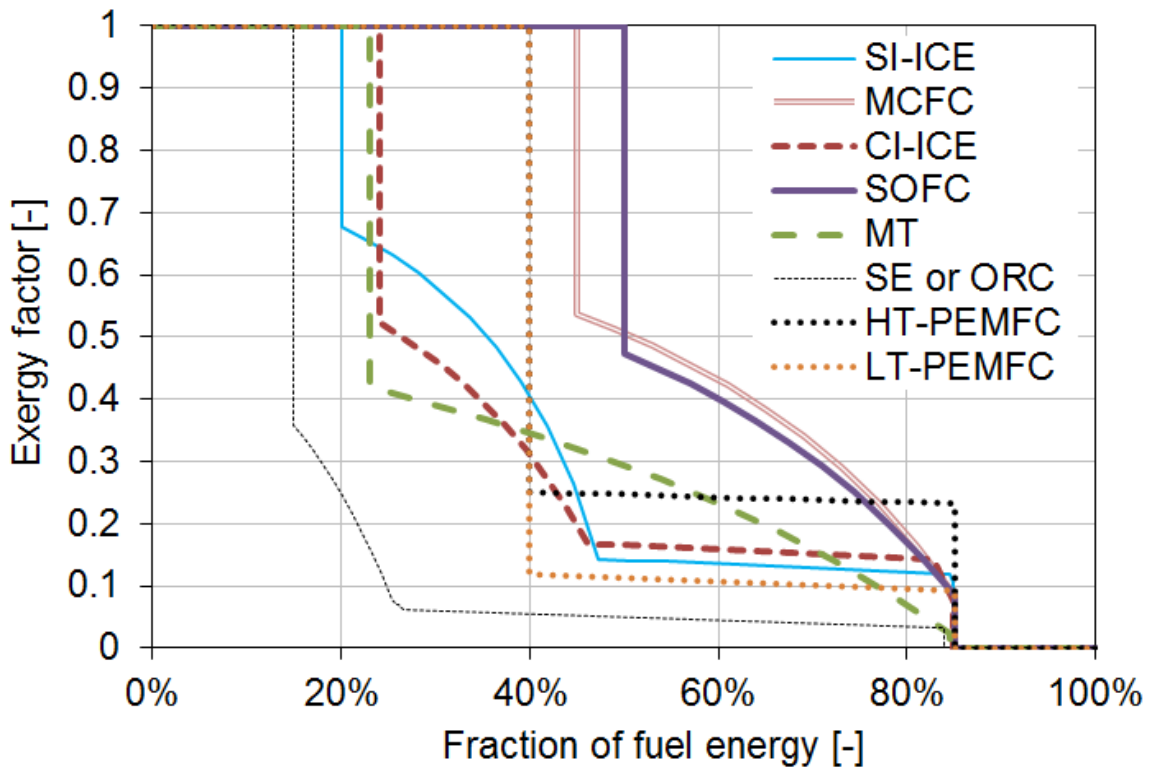


Figure 14: Exergy factor vs. fuel energy for nine micro prime movers

Of course, in CCHP, the waste heat is utilized to produce cooling. Furthermore, it is typically utilized over some narrow temperature range rather than over the full

temperature glide of the waste heat resource. In addition, there are discrete choices of utilization temperature ranges corresponding to available thermally-driven technologies (e.g. 140°C for double effect absorption, 100°C for single effect absorption, and 70°C for FAM-Z01-based adsorption).

To capture a more realistic picture of the benefit realized from waste heat utilization in CCHP, Figure 15 has a y-axis representing the work produced by the prime mover and the work which, in the absence of waste heat utilization by an available thermally-driven cooling technology, would have otherwise been consumed by a work-driven VCS (assuming a COP_{VCS} of 3.0). Since a comparison is now being made to a non-Carnot VCS, the values for waste heat utilization can be greater than the values for exergy factor shown in Figure 14 (if the f_{Ct} of the thermally driven cycle is greater than the f_{Ct} of the grid-VCS system). In Figure 15, the SE/ORC drops directly to zero after the electricity segment, since the waste heat amount is too small to utilize for micro scale prime movers. Also note that the horizontal extents of three prime movers (MCFC, SOFC, and MT) are subject to pinch limitations. This is because only some of the exhaust temperature lies above the utilization temperature. The fraction of available heat which is made unavailable by not being above the utilization temperature is referred to as the “pinch penalty” in Table 5, and is also denoted λ_{pinch} . On the other hand, for the remaining four prime movers (SI-ICE, CI-ICE, HTPEMFC and LTPEMFC), the utilization temperature is below the waste heat temperature everywhere, and the nonzero y-extent still reaches the value of $(1 - \lambda)$, where λ is the fraction of fuel energy lost to ambient in the prime mover itself.

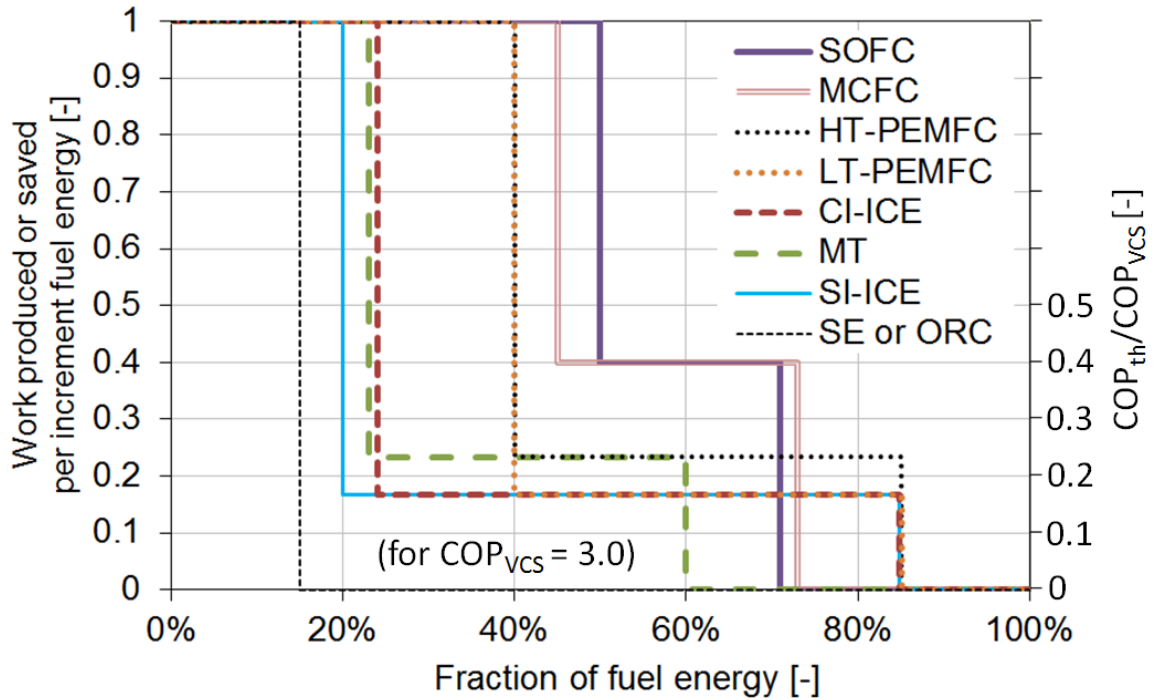


Figure 15: Practically realizable work or work equivalent vs. fuel energy for nine micro prime movers in combined cooling and power mode (no heating)

In Figure 15, the area under each curve represents the sum of work produced and work saved, per unit of fuel consumed. The numerical value of this area is shown for each prime mover in the last column of Table 5. Note that this analysis assumes a baseline VCS COP of 3, and the work saved would be reduced in proportion to any increase in baseline COP.

Table 5: Work produced and saved by trigeneration systems

PM type	Prime mover / η_{elec}	HACD / COP_{th}	Exhaust heat pinch penalty (λ_{pinch})	Work produced per unit fuel energy	Work saved per unit fuel energy	Total area in Figure 15
FC	SOFC / 50%	DE-Abs. / 1.2	37%	0.50	0.07	0.57
FC	MCFC / 45%	DE-Abs. / 1.2	28%	0.45	0.10	0.55
FC	HTPEMFC / 40%	SE-Abs. / 0.7	N/A	0.40	0.11	0.51
FC	LTPEMFC / 40%	Ads. / 0.5	N/A	0.40	0.08	0.48
IC	CI-ICE / 24%	Ads. / 0.5	0%	0.24	0.09	0.33
IC	MT / 23%	SE-Abs. / 0.7	32%	0.23	0.07	0.30
IC	SI-ICE / 20%	Ads. / 0.5	0%	0.20	0.10	0.30
EC	SE/ORC / 15%	Ads. / 0.5	0%	0.15	0.00	0.15

Based on this analysis, the SOFC and MCFC have the best performance, followed closely by the PEMFCs. Addition of thermally-driven cooling boosts the performance of an MCFC more than an SOFC. This is due to the MCFC's slightly lower electrical efficiency (more available heat) and slightly higher exhaust temperature (made possible by utilizing internal reforming for stack cooling, which in turn allows a lower excess air ratio). Among combustion-based prime movers, internal combustion devices (including MT) have better performance than external combustion, which stems from the lower electrical efficiency of external combustion (due to fluid property limitations when utilizing a closed fluid loop in external combustion cycles) and poor waste heat resources (due to the need to reject heat near ambient temperature for optimal electrical efficiency). Among internal combustion technologies, the SI-ICE receives the biggest improvement from adding thermally-driven cooling due to its lower electrical efficiency (more waste heat is available). The higher exhaust temperature of SI-ICE vs. CI-ICE does not help in this instance, since it is assumed that an adsorption chiller is utilizing exhaust and coolant heat at the coolant temperature. The MT, despite being coupled with a higher COP_{th} chiller than the ICEs, suffers from pinch limitations, so that it ends up with similar trigeneration performance to the ICEs. However the MT may have better performance if used in a true trigeneration mode that utilizes DHW while simultaneously driving a chiller, where the heat below the chiller utilization temperature could still be used for DHW (in contrast, any heat for DHW taken from an ICE is no longer available for cooling). The MT may also have a cost advantage due to fewer moving parts and availability of significant waste heat above 100°C (which makes chiller selection more flexible).

A final note concerns the application of this analysis to MW-scale systems. At that much larger scale, the electrical efficiencies of fuel cells and Stirling engines would not change significantly, while there would be dramatic increases in efficiency for internal combustion engines compared with their micro counterparts, for large axial gas turbines compared with radial micro turbines, and with the supercritical steam Rankine cycle over the organic Rankine cycle. For most prime movers, increasing capacity by two to four orders of magnitude would not significantly change the waste heat temperatures as a function of total waste heat available (Figure 12) (although gas turbines would have a higher exhaust temperature and reciprocating ICEs would have less heat in the coolant), but all would have less waste heat per unit of fuel consumed due to the higher electrical efficiencies. Thus although the overall performance of the system (work produced plus work saved) would be better, the theoretical marginal benefit of adding thermally-driven cooling would be smaller. Nevertheless, some practical considerations such as reduced heat losses through interconnecting plumbing and lower capital costs per unit capacity would benefit larger systems.

2.4 Analytical expressions for polygeneration systems (cooling season)

When is a trigeneration system a suitable tool for achieving energy savings? To help answer this question, this section proposes a simple set of parameters to describe a selection of energy systems, and derives analytical expressions for the energy consumption of each. These expressions are generally applicable to trigeneration on any scale, although when they are numerically evaluated in this chapter a focus is placed on micro scale systems. Using these expressions, the following issues are addressed:

- Energy consumption of polygeneration vs. conventional generation

- Grid-connected systems
- Grid independent systems
- Fuel cost savings of polygeneration vs. conventional generation
 - Grid-connected systems
 - Grid independent systems
- Sensitivity of polygeneration to non-idealities
 - Heat losses
 - Parasitic electricity consumption of thermally-driven heat pumps
 - Auxiliary burner efficiency
- Accuracy of the predictions of these simple analytical models (see section 6.6.4)

Initially, each energy system under consideration is described by only two parameters, leading to instructive and tractable equations and figures that display essential trends. The models are then expanded by relaxing some assumptions and introducing some non-idealities. This leads to more complicated but more accurate analytical expressions that characterize the fuel consumption of each system with 2 to 6 parameters. Evaluation of these expressions requires the substitution of empirical values for the parameters, but the expressions themselves remain analytical and generally applicable to any choice of empirical values relevant to any size system.

To enable these first-order comparisons of energy systems, the following assumptions are made in this chapter:

- Steady state: the expressions are derived from steady state analysis

- Bin-weighting: the values for efficiency and COP are taken to be the bin-weighted average values over an entire year
- Capacity independence: the chiller capacity is only limited by heat available from the prime mover
- Turndown ratio: the chiller and prime mover are capable of any PLR from 0 to 1

All of these assumptions are rather restrictive. One goal of this work is to demonstrate how much they deviate from more detailed simulations or experimental evaluations.

One relevant metric for energy consumption is the primary energy ratio (PER), which is the ratio of a useful product produced to the fuel consumed in its production. PER is typically defined based on a single product (electricity, cooling or heating). However, for polygeneration systems this definition is problematic since it does not capture the benefits of producing multiple outputs sequentially. A “mixed” PER can be defined as shown in Equation (6). However, this mixed PER is problematic for conventional separate generation of electricity, heating, and cooling. This is because the PER will depend on the ratio of loads to each other. For example, grid-driven VCS cooling may have a cooling PER of 1, with grid electricity having an electric PER of 1/3. Depending the ratio of cooling and electricity provided to a building, the mixed PER will have a value between 1/3 and 1. This problem is addressed in this thesis by taking advantage of the fact that the mixed PER of trigeneration systems will also vary with loads. As long as two systems’ PERs are being compared with each other at the same cooling load fraction, the absolute PER value is not important.

$$PER = \frac{Q_{clg} + Q_{htg} + W_{elec}}{Q_f} \quad (6)$$

The mixed PER as defined in Equation (6) is used throughout this work, except where fuel-chargeable-to cooling efficiency (η_{FCC}) is used, as will be explained later.

Fuel consumption may occur on-site or off-site. For computations in this chapter involving grid electricity, the average grid efficiency is taken to be 1/3 (33.3%). The EIA figures and projections for the average grid efficiency are given in Table 6. For night-time electricity, the grid efficiency tends to be slightly higher, and it tends to be slightly lower during times of peak usage (this is due to the less efficient “peaker” plants running when demand is high). In the winter, a conventional CHP engine offsets grid electricity at all hours, while in the summer, a trigeneration system offsets grid electricity most during the peak hours when grid efficiency is worst. For simplicity, and given all the uncertainties involved, a constant value of 1/3 is taken to be a good approximation.

Table 6: EIA average primary energy electric grid efficiencies in the US

Year	Average grid efficiency
2006	31.4%
2010	31.8%
2020	32.2%
2030	32.6%

2.4.1 Expressions for primary energy ratio

In this section, six system configurations are defined for which primary energy ratio (PER) expressions are derived. Each configuration is generic, i.e. any prime mover or any type of chiller or VCS could be used.

The expressions for PER are divided into “Carnot,” “ideal” and “realistic” categories. A “Carnot system” is ideal with respect to the First and Second Laws of Thermodynamics. An “ideal system” uses realistic Second Law efficiencies, but remains ideal with respect to the First Law: all fuel entering a device ends up as either electricity

or usable heat, and thermally-driven equipment has zero parasitic electrical consumption. A “realistic system” uses realistic First and Second Law efficiencies.

The baseline system is the grid-driven vapor compression system, shown in Figure 16.

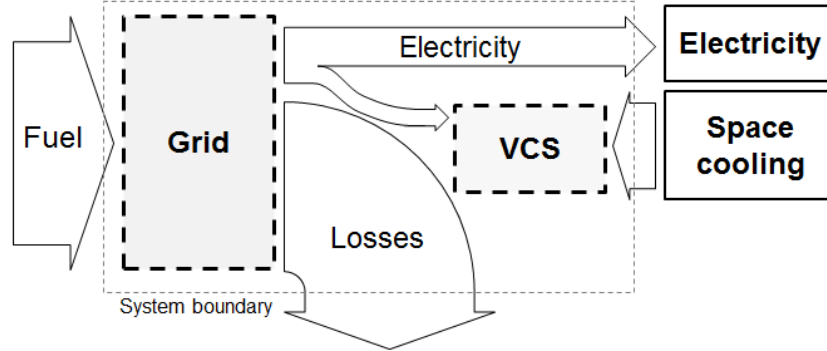


Figure 16: Sankey diagram for grid-driven VCS

To capture the relative amount of cooling and electrical loads required by the load (e.g. a building), the “cooling load fraction” (f_{clg}) is defined as in Equation (7).

$$f_{clg} = \frac{Load_{clg}}{Load_{clg} + Load_{elec}} \quad (7)$$

Since the cooling and electricity are produced independently of each other in the conventional system, it is possible to define single-output PER_{clg} and PER_{elec} in addition to the mixed PER. These three PERs are given in Equations (8), (9) and (10), respectively. Note that the mixed PER depends on the cooling load fraction, f_{clg} . In the limiting cases where $f_{clg} = 0$ and $f_{clg} = 1$, the mixed PER reduces to the appropriate single-output PER. Also note that the inverse of the mixed PER (the fuel consumption per unit of mixed loads) is linear with respect to f_{clg} , as expected for a system that produces electricity and cooling by independent processes.

$$PER_{clg} = \eta_{grid} COP_{VCS} \quad (8)$$

$$PER_{elec} = \eta_{grid} \quad (9)$$

$$PER = \frac{\eta_{grid}}{f_{c\lg} (COP_{VCS}^{-1} - 1) + 1} \quad (10)$$

In both ideal and non-ideal cases defined in this analysis, the grid-driven VCS system is the same. This is because the centralized grid is defined as wasting all heat, and the COP of VCSs is defined as including all forms of electrical consumption such as fans and pumps. In thermally driven systems, these electrical loads are considered “parasitic.”

Note that the PER of a PM-driven VCS system is obtained by simply replacing η_{grid} with η_{PM} , resulting in Equation (11).

$$PER = \frac{\eta_{PM}}{f_{c\lg} (COP_{VCS}^{-1} - 1) + 1} \quad (11)$$

Next, the following thermally-activated cooling possibilities are considered:

1. direct-fired thermally-activated chiller
2. engine-driven thermally-activated chiller without auxiliary burner
3. engine-driven thermally-activated chiller with auxiliary burner
4. engine-driven thermally-activated chiller with VCS and without auxiliary burner
5. engine-driven thermally-activated chiller with VCS and auxiliary burner

Each of these systems is illustrated by a Sankey diagram in Figure 17 through Figure 22.

(1) Direct-fired heat activated cooling device

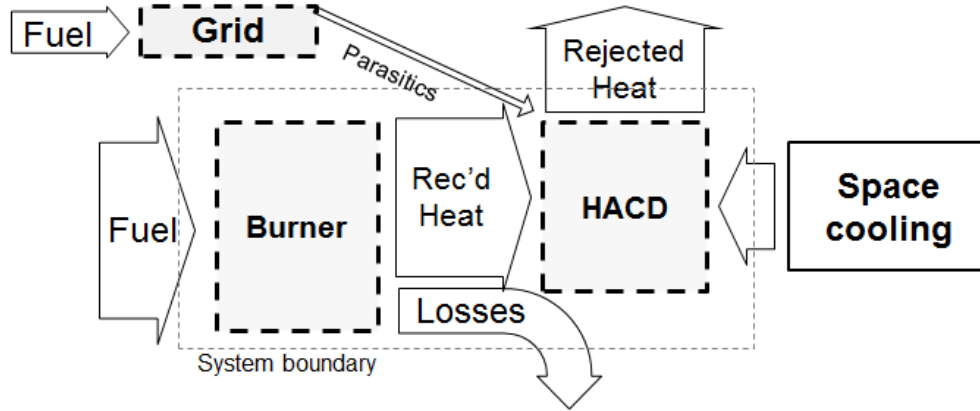


Figure 17: Sankey diagram for direct-fired HACD

The PER of an ideal direct-fired heat-activated cooling device is given in Equation (12).

$$PER_{DF-HACD} = COP_{th} \quad (12)$$

For a more realistic direct-fired heat-activated cooling device which has non-zero parasitic electric loads, the PER is given by Equation (13). The symbol κ represents the parasitic electrical loads of the chiller per unit of cooling produced.

$$PER^{-1} = \frac{1}{\eta_B COP_{th}} + \frac{\kappa}{\eta_{elec}} \quad (13)$$

(2) Engine-driven heat activated cooling device without auxiliary burner

The Sankey diagram for the most basic trigeneration system, an engine-driven heat-activated cooling device without auxiliary burner backup, is shown in Figure 18.

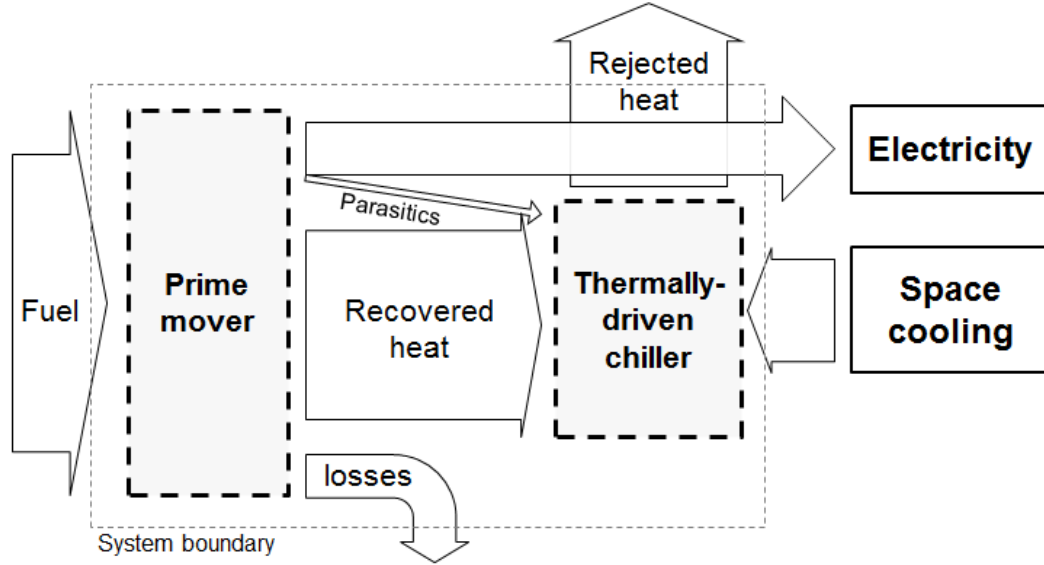


Figure 18: Sankey diagram for CCHP without auxiliary burner

With all components running at full load, this basic trigeneration system will produce a fixed or “inherent” cooling load fraction, denoted $f_{clg,inh}$. The value of this inherent fraction is given by Equation (14).

$$f_{clg,inh} = \frac{COP_{th}(1 - \eta_{elec} - \lambda)}{\eta_{elec} + COP_{th}(1 - \eta_{elec} - \lambda)(1 - \kappa)} \quad (14)$$

where λ represents heat losses. Precisely, λ is the fraction of fuel energy entering the prime mover which is not recovered as either electricity or utilizable heat. Note that, if a thermally-driven chiller were to use only exhaust heat from an ICE, then λ would include all coolant heat dumped to ambient.

It is possible for the system to operate at values of $f_{clg} \neq f_{clg,inh}$. When $f_{clg} \leq f_{clg,inh}$, excess cooling is available. The amount of heat sent to the chiller can be reduced, with the balance dumped to ambient. The PER under this condition is given by Equation (15).

$$PER = \frac{\eta_{PM}}{1 - f_{clg}(1 - \kappa)} \quad (15)$$

This expression lacks any term involving heat, such as COP_{th} or the quantity $(1 - \eta_{PM} - \lambda)$. This makes sense, since under the condition $f_{clg} \leq f_{clg,inh}$ the system is effectively running to meet electric loads, with cooling produced as a free byproduct. The limiting case of $f_{clg} = 0$ reduces to the pure PER_{elec} of a generator. The limiting case of $f_{clg} = 1$ cannot be evaluated here, since Equation (15) only applies when $f_{clg} \leq f_{clg,inh}$, and $f_{clg,inh}$ is always between 0 and 1.

When $f_{clg} \geq f_{clg,inh}$, and no backup form of cooling exists, excess electricity is produced. An off-grid system must either dump or store the excess. In the case of dumping excess electricity, Equation (16) gives the PER.

$$PER = \frac{COP_{th} (1 - \eta_{PM} - \lambda)}{f_{clg}} \quad (16)$$

This expression lacks any terms relating to electrical energy (η_{PM} or κ), since the system is effectively running to meet the cooling load, with electricity produced as a free byproduct.

The electricity produced in excess of the requirements of the load is given by Equation (17).

$$elec_{excess} = f_{clg} \left[\frac{\eta_{PM}}{COP_{th} (1 - \eta_{PM} - \lambda)} + (1 - \kappa) \right] - 1 \quad (17)$$

If the system is grid connected, that excess electricity can be exported, offsetting fuel. Accounting for this offset using the PER is problematic, however, since the PER can take on a non-physical negative value when the prime mover efficiency is greater than the grid efficiency. However, it works well according to the concept of “fuel chargeable to

cooling” for prime movers with efficiency lower than grid. Bearing this limitation in mind, the PER accounting for electricity offset is given by Equation (18).

$$PER^{-1} = f_{clg} \left(\frac{\eta_{grid} - \eta_{PM}}{\eta_{grid} COP_{th} (1 - \eta_{PM} - \lambda)} - \frac{1 - \kappa}{\eta_{grid}} \right) + \frac{1}{\eta_{grid}} \quad (18)$$

If $\eta_{grid} = \eta_{PM}$, as would be the case when comparing an off-grid system to a conventional system with the same prime mover efficiency, Equation (18) reduces to Equation (15). Note that the above equations can readily be transformed for an ideal case in which κ and λ are zero.

Finally, if a trigeneration system operates precisely at $f_{clg,inh}$, then its PER can be obtained by substituting $f_{clg,inh}$, Equation (14), for f_{clg} in either Equation (15) or Equation (16). The resulting expression for PER at $f_{clg,inh}$ is given in Equation (19).

$$PER^{-1} = \frac{1 + \kappa COP_{th} \left(1 - \frac{1 - \lambda}{\eta_{PM}} \right)}{\frac{\eta_{PM}}{1 - \kappa} + COP_{th} (1 - \eta_{PM} - \lambda)} \quad (19)$$

Equation (19) involves all the terms that are associated with every PM-HACD system (η_{PM} , COP_{th} , λ and κ). It applies to all PM-HACD-based systems operating at their respective $f_{clg,inh}$, regardless of the presence or absence of a VCS and/or an auxiliary burner.

(3) Engine-driven heat activated cooling device with auxiliary burner

A simple improvement to the previous basic trigeneration system is to add an auxiliary burner (AB) that can provide extra heat for the condition when $f_{clg} > f_{clg,inh}$. This prevents the wastage of electricity and expands the range of f_{clg} that the system can

handle. A qualitative Sankey diagram for this type of system is shown in Figure 19. Note that AB (auxiliary burner) is not to be confused with Abs (absorption chiller).

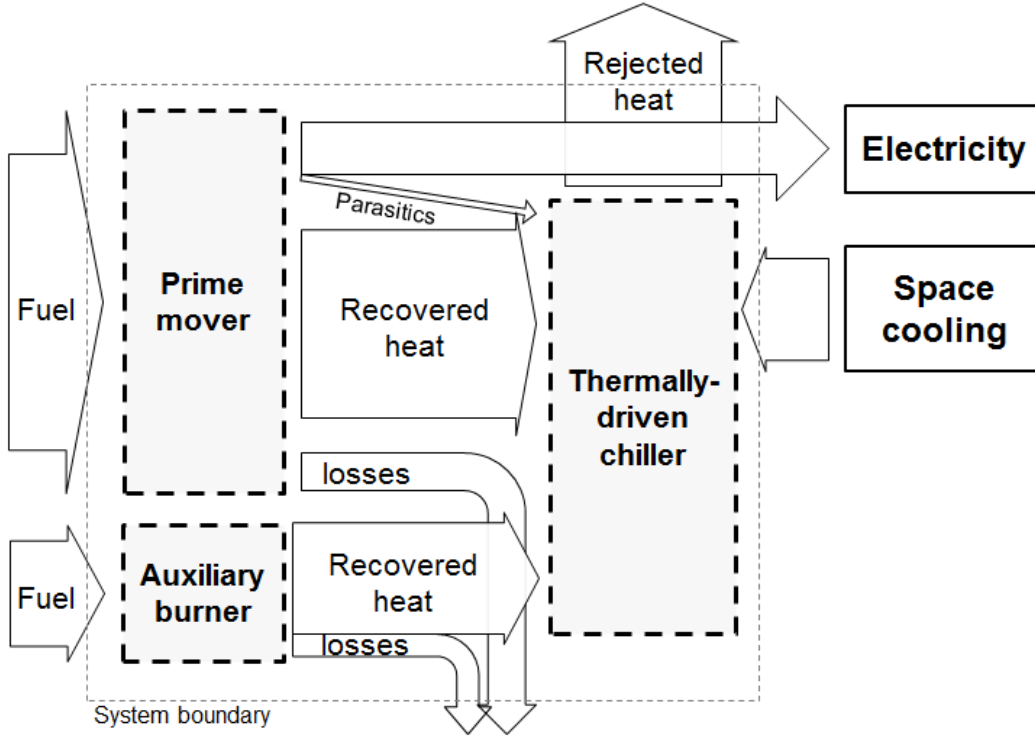


Figure 19: Sankey diagram for trigeneration system with auxiliary burner

The inherent cooling load fraction for this system is the same as for a system without the AB backup – see Equation (14). Under the condition that $f_{clg} \leq f_{clg,inh}$ (excess cooling is available), the PER is also the same – see Equation (15) and Equation (19). However, the PER differs when $f_{clg} > f_{clg,inh}$. When there was no AB backup, excess electricity had to be produced; the benefit of the AB is that it can be used to avoid wasting electricity. With the AB active, the PER is given by Equation (20).

$$PER = \left[\frac{f_{clg}}{COP_{th}\eta_{AB}} + \frac{[1 - f_{clg}(1 - \kappa)](\eta_{PM} + \eta_{AB} + \lambda - 1)}{\eta_{PM}\eta_{AB}} \right]^{-1} \quad (20)$$

For the limiting case of $f_{clg} = 1$, this equation becomes close to $PER = COP_{th}\eta_{AB}$.

This makes sense because the ratio of cooling to electricity is infinite at $f_{clg} = 1$, so

effectively all the cooling is driven by heat from the auxiliary burner. Furthermore, it is sensible that the PER does not precisely equal $COP_{th}\eta_{AB}$ because there is still a small contribution from the right-hand quotient, proportional to κ , which accounts for the fuel still being used by the prime mover to produce electricity for the parasitic loads of the thermally-driven device.

Under the current set of assumptions, this configuration does not export electricity, since the situation of $f_{clg} > f_{clg,inh}$ is handled by decreasing prime mover outputs and increasing the auxiliary burner heat output.

(4) Engine-driven heat activated cooling device with VCS and no auxiliary burner

Another component that can be added to a trigeneration system to improve the energy efficiency under high cooling load fractions is a VCS. At first this may seem an odd choice, since the VCS is supposed to be the incumbent technology that trigeneration would displace. However, the energy efficiency of trigeneration systems suffers when heat must be wasted or auxiliary burner options must be used, and the VCS offers a more efficient alternative method of backup cooling for trigeneration systems. A Sankey diagram of such a system is shown in Figure 20. For clarity, not all of the rejected heat is shown.

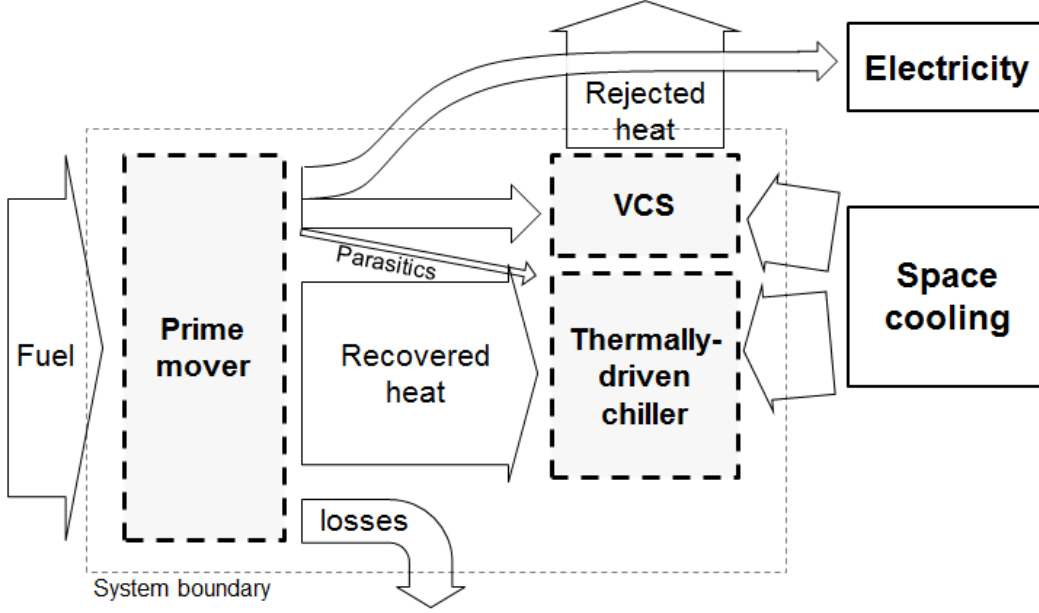


Figure 20: Sankey diagram of trigeneration system with VCS backup cooling

Once again, the inherent cooling load fraction for this system is the same as the other trigeneration systems previously introduced – see Equation (14). Also, the PER is the same as in Equation (15) or Equation (19) when $f_{clg} \leq f_{clg,inh}$ (excess cooling is available) – under this condition the VCS is inactive.

When when $f_{clg} > f_{clg,inh}$, the VCS becomes active, and the PER is given by Equation (21).

$$PER = \frac{\eta_{elec} (COP_{th}^{-1} - COP_{VCS}^{-1} + \kappa) - (1 - \lambda)(\kappa - COP_{VCS}^{-1})}{COP_{th}^{-1} [f_{clg} (COP_{VCS}^{-1} - 1) + 1]} \quad (21)$$

Under the current set of assumptions, this PM-HACD-VCS-noAB configuration does not export electricity, since the situation of $f_{clg} > f_{clg,inh}$ is handled by sending more electricity to the HACD.

To illustrate the method used in deriving the analytical expressions in this section, this HACD-VCS system is expanded as an example. Figure 21 shows how each independent energy flow in the Sankey diagram can be assigned a value, denoted by the 8

green letters a-h. The desired outcome is an expression relating the fuel consumption to the six parameters, denoted by the six familiar symbols shown in red. From a mathematical perspective, there are now $6+8=14$ variables. By writing an appropriate set of 8 equations, the undesired green variables can be eliminated, yielding an expression for fuel consumption in terms of only the six parameters. The appropriate equations can be developed as follows: each of the six parameters is defined as a function only of the variables to be eliminated (a-h), the total loads are normalized to be equal to unity (i.e. $1=c+d$), and an energy balance on the prime mover is expressed in terms of variables to be eliminated (i.e. $f=e+b+h+a+g$). The resulting system of equations was then solved in terms of the six parameters using the “solve” function in MATLAB. Starting from the MATLAB results, manual algebraic manipulation was carried out to achieve algebraic forms with the highest possible engineering significance and tractability.

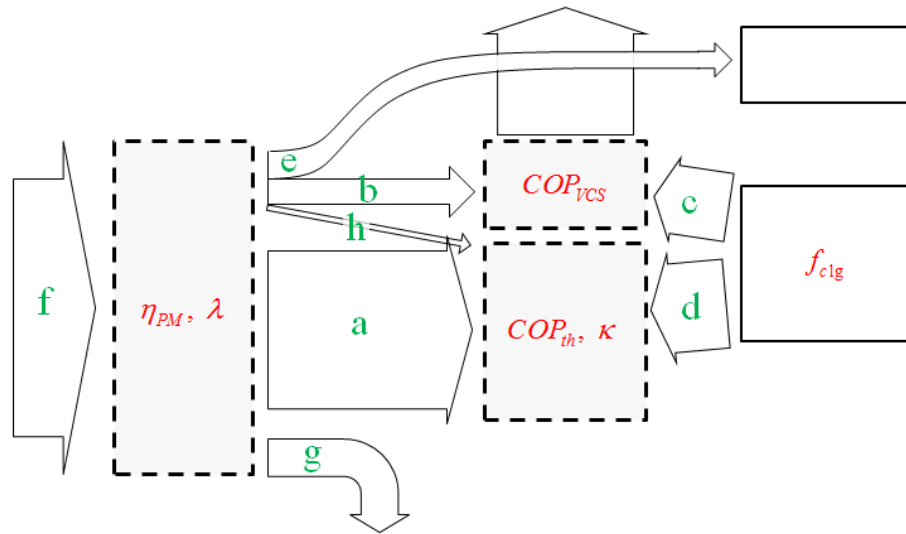


Figure 21: Example setup for derivation of fuel consumption

The system of 8 equations for this example is:

1. $f = e+b+h+a+g$ (energy balance on prime mover)
2. $1 = c+d$ (normalization of total loads)
3. $f_{clg} = c$ (definition of parameter f_{clg})
4. $\eta_{PM} * f = e+b+h$ (definition of parameter η_{PM})

5. $\lambda = g/f$ (definition of parameter λ)
6. $COP_{th} = d/a$ (definition of parameter COP_{th})
7. $\kappa = h/d$ (definition of parameter κ)
8. $COP_{VCS} = c/b$ (definition of parameter COP_{VCS})

(5) Engine-driven heat activated cooling device with VCS and auxiliary burner

It is also possible to configure a trigeneration system with both a backup VCS and a backup auxiliary burner (AB). This may improve the versatility of the system, expanding the range of f_{clg} it can efficiently provide. A Sankey diagram of such a system is shown in Figure 22. For clarity, heat rejection from the VCS and HACD are not shown.

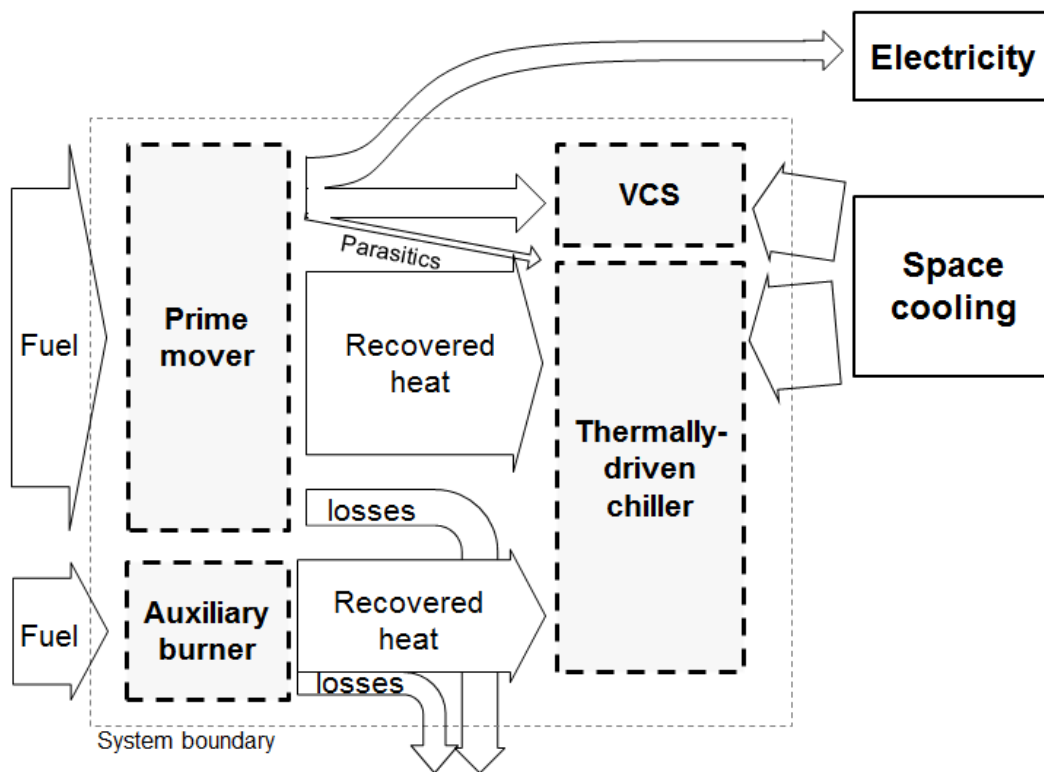


Figure 22: Sankey diagram for trigeneration system with backup VCS and backup auxiliary burner

This system has an additional degree of freedom not present in the previously introduced systems. For the same f_{clg} , it can vary the relative amounts of cooling produced by the VCS and the HACD. If such a system were built, this VCS/HACD

cooling fraction would be a decision variable in an optimization of the control strategy. For the present analysis, the fraction of cooling provided by the VCS is simply treated as another parameter in the system, denoted f_{VCS} , having a range of possible values from 0 to 1.

For $f_{clg} \geq f_{clg,inh}$, the expressions for this system are again given by Equations (15) and (19). When $f_{clg} \geq f_{clg,inh}$, the full expression becomes relatively cumbersome, so first an idealized form is shown in Equation (22), in which the idealizations are made that $\lambda=\kappa=0$ and $\eta_{AB}=1$. Due to the assumption that there are no parasitic loads and that the system is running in thermally-driven mode (i.e. $f_{clg} > f_{clg,inh}$), the η_{PM} term drops out completely.

$$PER^{-1} = 1 + f_{clg} \left(COP_{th}^{-1} - 1 + f_{VCS} \left(\frac{COP_{th} - COP_{VCS}}{COP_{th} COP_{VCS}} \right) \right) \quad (22)$$

When $f_{VCS} = 0$ (the VCS is disabled), this reduces to Equation (23).

$$PER^{-1} = 1 + f_{clg} (COP_{th}^{-1} - 1) \quad (23)$$

As expected, Equation (23) is the same as the result for the HACD-AB system, Equation (20), when the same assumption are applied that $\kappa=0$, $\lambda=0$ and $\eta_{AB}=1$.

A value of $f_{VCS}=1$ cannot be substituted into Equation (22), since it would violate the assumption that recovered heat from the engine be fully utilized, as was assumed in the derivation for this system in the case of $f_{clg} > f_{clg,inh}$. In other words, the option of dumping heat under the condition of $f_{clg} > f_{clg,inh}$ would introduce an additional degree of freedom into the system, which would require a new, more general, derivation with a new parameter representing the amount of heat being dumped. Since this is not a normally

desirable operating condition, and since the expression is already cumbersome without an additional parameter, this more general derivation is not pursued.

Reintroducing a non-unity η_{AB} , but keeping $\kappa=\lambda=0$, results in the expression shown in Equation (24).

$$PER^{-1} = f_{clg} \left[\frac{\eta_{PM} (COP_{VCS} (1 - f_{VCS} - COP_{th}) + f_{VCS} COP_{th}) + \dots}{\eta_{PM} COP_{th} COP_{VCS} \eta_{AB}} \right] - \frac{1 - \eta_{PM} - \eta_{AB}}{\eta_{PM} \eta_{AB}} \quad (24)$$

Finally, Equation (25) shows the most general form for the engine-driven HACD with backup VCS and backup auxiliary burner (AB). As with Equation (22) and Equation (24), evaluation for a set of component efficiencies would require optimizing PER with respect to f_{VCS} for each value of f_{clg} .

$$PER^{-1} = f_{clg} \left[\frac{\frac{\kappa(1 - f_{VCS}) - 1}{\eta_{AB}} + \frac{1 - f_{VCS}}{COP_{th} \eta_{AB}} - \frac{f_{VCS} (1 - \eta_{PM} - \eta_{AB} - \lambda)}{\eta_{PM} COP_{VCS} \eta_{AB}} + \dots}{\frac{\lambda(\kappa(1 - f_{VCS}) - 1) + \kappa(\eta_{AB} + f_{VCS} (1 - \eta_{AB}) - 1) + 1}{\eta_{PM} \eta_{AB}}} \right] + \frac{1}{\eta_{AB}} - \frac{1 - \eta_{AB} - \lambda}{\eta_{PM} \lambda} \quad (25)$$

2.4.2 Carnot systems at inherent cooling load ratio

An instructive comparison can be made by comparing trigeneration to separate generation under the assumption that all heat conversion devices operate without irreversibilities, i.e. at the Carnot limit. This analysis will use the PER expression for conventional separate electricity and cooling production, Equation (10), and the expressions for a basic trigeneration system with auxiliary burner (PM-HACD-AB), Equations (15) and (20). It will be assumed that all components – heat engines, work-

driven heat pumps, and heat-driven heat pumps – operate at their Carnot limit. Table 7 shows the equations and temperatures that have been assumed in the calculations of Carnot efficiencies.

Table 7: Carnot efficiency of heat engines and chillers

Device	Carnot equation	$T_{src,L}$ [K]/[°C]	T_{rej} [K]/[°C]	$T_{src,H}$ [K]/[°C]	Carnot value
heat engine	$\eta_{Ct} = \frac{T_{src,H} - T_{out}}{T_{src,H}}$	–	298.15/ 25	1273.15/ 1000	0.754
work-driven chiller	$COP_{Ct,clg} = \frac{T_{src,L}}{T_{out} - T_{src,L}}$	283.15/ 10	313.15/ 40	–	9.44
heat-driven chiller	$COP_{Ct,clg} = \frac{T_{src,L} (T_{src,H} - T_{out})}{(T_{out} - T_{src,L}) T_{src,H}}$	283.15/ 10	313.15/ 40	373.15/ 100	1.52

Inserting the Carnot values from Table 7 for the proper terms in the PER equations, the inverse PER of conventional and trigeneration are plotted with respect to f_{clg} in the left plot of Figure 23.

Next, the term f_{Ct} (fraction of Carnot efficiency) is defined for engines and heat pumps as in Equation (26).

$$\eta_{actual} = f_{Ct} \eta_{Ct} \quad \text{or} \quad COP_{actual} = f_{Ct} COP_{Ct} \quad (26)$$

In Figure 23, $f_{Ct} = 1$ for all devices in the left plot and $f_{Ct} = 0.40$ in the right plot.

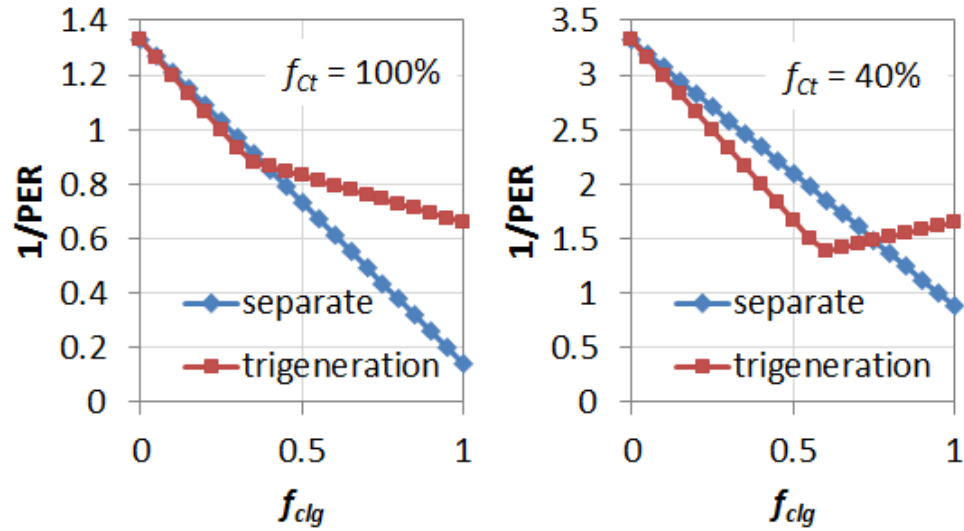


Figure 23: Comparison of PER^{-1} for trigeneration and separate generation at Carnot efficiencies and at $f_{Ct} = 40\%$

Next, f_{Ct} is allowed to vary in Figure 24, in which contours of primary energy savings are shown for trigeneration. Positive values represent savings, while negative values mean the trigeneration system is using more energy than separate generation. This is similar to the data shown in Figure 23, but with f_{Ct} added as an additional independent variable, the dependent variables (PER_{trigen} and $PER_{separate}$) converted to a single dependent variable (fractional energy savings), and that dependent variable shown as contours. In other words, Figure 23 is represented in Figure 24 by vertical slices at $f_{Ct} = 0.4$ and 1. For purposes of this figure, f_{Ct} is assumed to apply equally to all components. This is not necessarily realistic but reveals interesting trends.

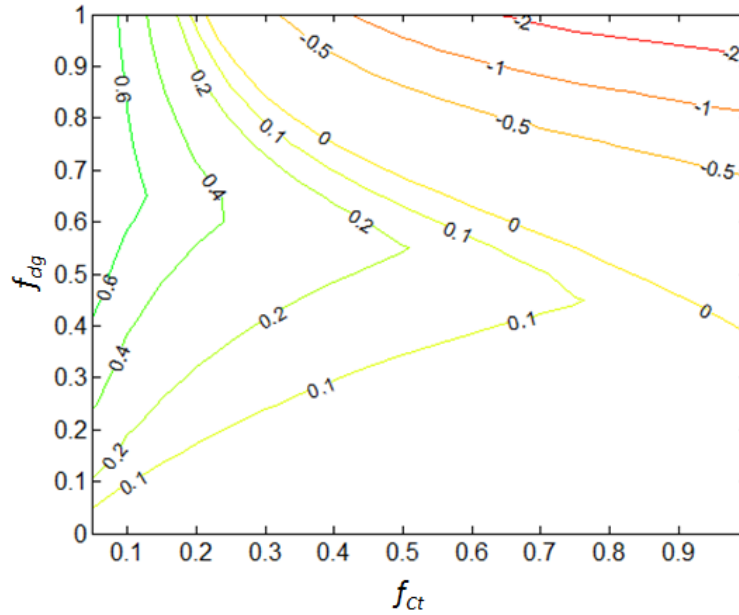


Figure 24: Contours of fractional energy savings for trigeneration as a function of cooling load fraction and fraction of Carnot performance

The discontinuities in some contours are related to the switch from $f_{clg} < f_{clg,inh}$ to $f_{clg} > f_{clg,inh}$. Drawing a line through the discontinuities would produce a plot of $f_{clg,inh}$ as a function of f_{Ct} .

Figure 24 highlights an interesting aspect of trigeneration. There is a clear general trend that, for a given f_{clg} , trigeneration saves more energy with lower values of f_{Ct} . That is, when energy conversion equipment is inefficient, the relative benefits of trigeneration are greater. This represents a long term challenge for trigeneration, since, as power generation and vapor compression systems are continually made more efficient, the potential benefits of trigeneration are reduced – even as the efficiency of trigeneration components keeps pace. On the other hand, an advantage in favor of trigeneration is that its components generally have more gains available, since they have been under development for less time.

Another observation is that, for a given value of f_{Ct} , trigeneration savings are greatest at $f_{clg,inh}$. The savings drop away steeply as f_{clg} increases, but in this example

approach zero as $f_{clg} \rightarrow 0$, since both trigeneration and separate generation are assumed to produce electricity at the same efficiency.

2.4.3 Ideal systems at inherent cooling load ratio

Here, “ideal” means there are no heat losses and no parasitic loads, while realistic electrical efficiencies and COPs are used.

This section compares trigeneration systems to conventional systems using pair-wise comparisons. Each pair-wise comparison is evaluated at the “inherent cooling load ratio,” a concept explained presently.

“Cooling load fraction” is defined in this thesis as the amount of cooling consumed divided by the sum of cooling and electricity consumed. For a building, this ratio can take on any value from zero to one, but a basic trigeneration configuration in which a prime mover drives a thermally driven chiller (shown in Figure 18) is characterized by production of a fixed (or “inherent”) cooling load fraction. If more cooling is desired, more electricity must also be produced (this situation can be mitigated with an auxiliary burner that provides supplemental heat to the chiller). Likewise, if more electricity is desired, the prime mover will also produce more heat, which can either go towards excess cooling or be dumped. Clearly, such a trigeneration system has the best performance at its inherent load ratio.

It should be noted that this is a simplification. Most prime movers, at least in theory if not in their implementation, are able to vary the ratio of heating to electricity while keeping fixed one of those outputs (for example, by independently regulating RPM and throttle in a spark ignition engine); thermally-driven chiller controls can adjust

cooling capacity at fixed heat input (for example, varying solution pump speed in an absorption chiller); and the temperature at which heat is transferred from prime mover to thermally-driven device can be regulated to vary cooling output for a given heat source. However, all of these means of regulating cooling load ratio are restricted within a narrow range, and all involve tradeoffs (typically, some component or heat transfer efficiency must be sacrificed to increase capacity). Thus, the simplified model of a fixed inherent cooling load ratio has considerable merit.

Figure 25 shows a contour plot of the inherent cooling fraction for trigeneration systems characterized by the two parameters of η_{PM} and COP_{th} , with $\kappa=\lambda=0$. Note that this is a visualization of Equation (14).

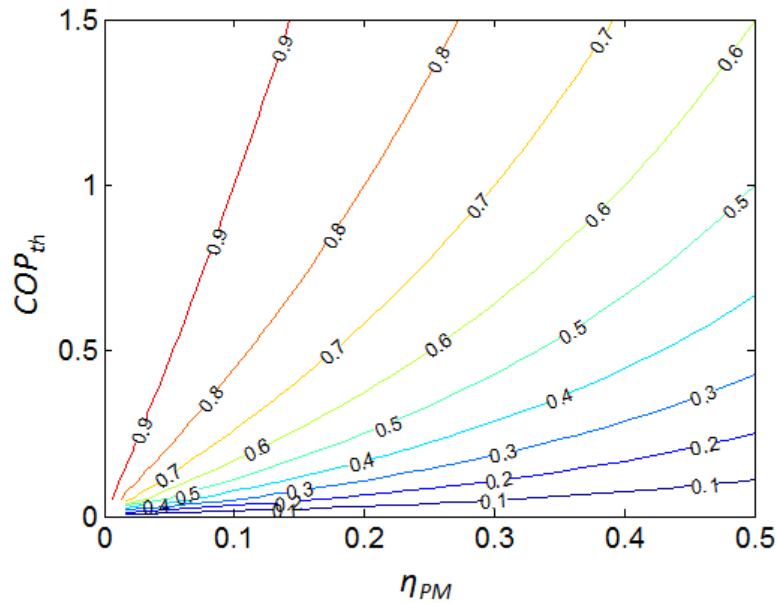


Figure 25: Inherent cooling load fraction ($f_{clg,inh}$) as function of prime mover efficiency and thermal COP, for $\lambda=\kappa=0$

Analysis of the 2-parameter ideal systems is profitable since it yields a very tractable expression for the suitability of trigeneration systems. If the absolute value of the fuel consumption of a system is desired with high accuracy, more sophisticated methods should be used. But this analysis reveals the essential trends in suitability of

trigeneration with the four most important parameters: grid efficiency, VCS COP, prime mover efficiency, and HACD COP_{th}.

The systems just discussed can all be compared pair-wise. A “break-even condition” can be defined by setting the PERs of two systems equal as in equation (27). This defines a relationship among component efficiencies in order for the two systems to have the same PER.

$$PER_{grid-VCS} = PER_{trigen} \quad (27)$$

Inserting the expressions for the grid-driven VCS and the engine waste heat-driven chiller, the expression shown in Equation (28) can be derived.

$$\eta_1 = \left(\frac{COP_{VCS}}{COP_{VCS} - COP_{th}} \right) \eta_2 - \left(\frac{COP_{th}}{COP_{VCS} - COP_{th}} \right) \quad (28)$$

This algebraic form was chosen such that, given assumptions of thermally-driven technology and COP of VCS systems, the equation is a linear expression for the prime mover efficiency required as a function of grid efficiency. In this linear formulation, the slope of the required prime mover efficiency with respect to grid efficiency is expressed by a ratio of COPs (typical value = $3/(3-0.5) \sim 1.2$); and the y-intercept is expressed by another ratio of COPs (typical value = $-0.5/(3-0.5) \sim -0.2$). The y-intercept is not particularly meaningful on its own, since it corresponds to a 0% grid efficiency.

This expression can also be used to answer such key questions as:

- For given grid, VCS and HACD performance, how efficient does an engine need to be?
- For given grid, VCS and engine performance, how efficient does a HACD need to be?

A graphical representation of the Equation (27) is shown in Figure 26 as a contour plot. In this figure, the contour lines represent the threshold of suitability of trigeneration for the given value of COP_{VCS} . Any trigeneration system characterized by η_{PM} and COP_{th} that lies above the contour line will save energy relative to the conventional system represented by the line.

Using the results from the trigeneration device matching section above, representative micro trigeneration systems have been plotted for various existing and proposed prime mover technologies. It can be seen that all combustion-based micro prime movers are marginally suitable, depending on the assumption of COP_{VCS} for conventional systems against which they are being compared. The fuel cell-based prime movers all display a comfortable margin of savings compared with the conventional system.

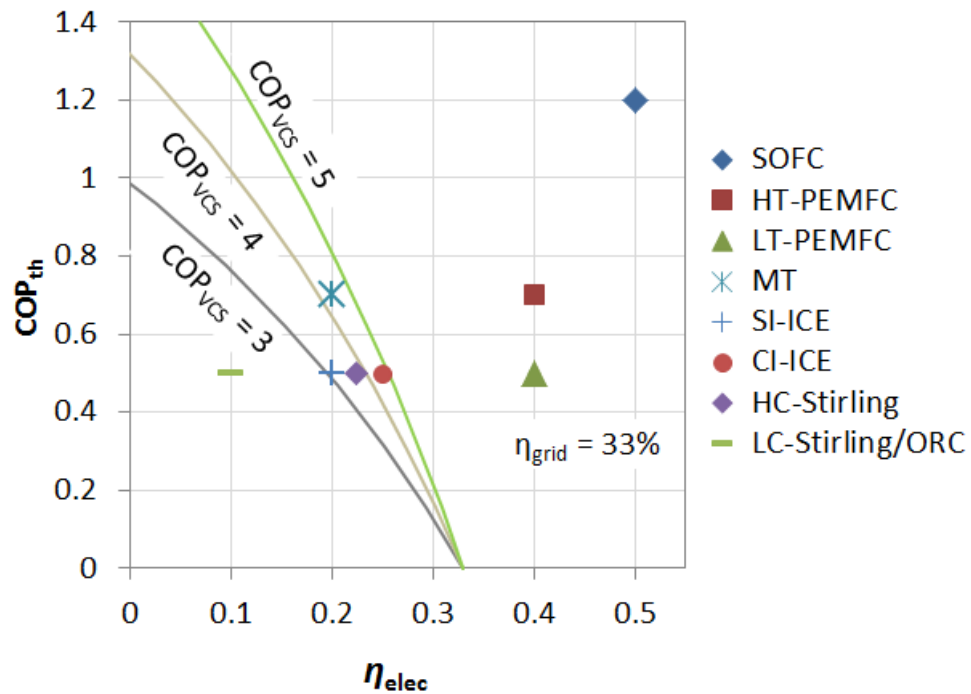


Figure 26: Energetic suitability of various trigeneration possibilities compared to the conventional grid-driven VCS option. Grid efficiency is assumed to be 33.3%.

2.4.4 Realistic system comparisons at inherent cooling load ratio

In real trigeneration systems, not all of the fuel energy goes to electricity or recovered heat. The lost fraction of fuel energy is defined as λ , and this parameter is varied in Figure 27 to visualize its impact on trigeneration energetic suitability. It can be seen that λ has the effect of increasing the y-intercept, with no change in the x-intercept. This makes sense since, by its definition, λ has no bearing on electrical efficiency, but decreases the efficiency of chilling.

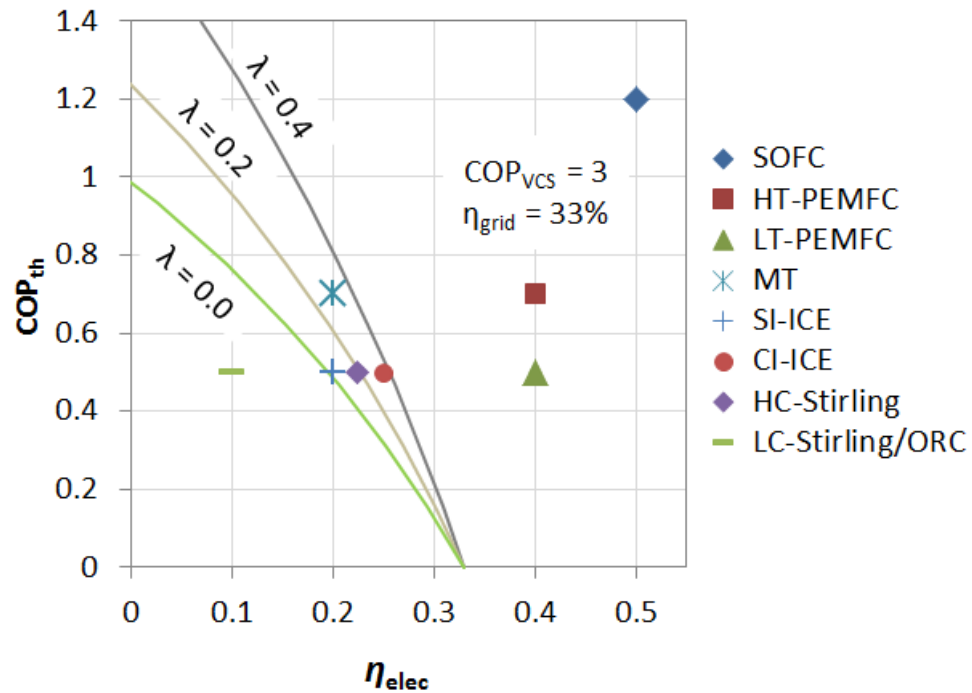


Figure 27: Effect of heat losses from prime mover on energetic suitability of trigeneration

Another non-ideality present in real systems is the parasitic electricity requirement of the thermally-driven cooling component. To capture this effect, κ is defined as the kW of electrical power required per kW of cooling provided. This is the same as the inverse of the more familiar ECOP, but defining parasitic loads based on κ instead of ECOP leads to tidier algebraic forms of the analytical expressions. This parameter κ is varied in Figure 28, with COP_{VCS} fixed at 3, to visualize the effect of

parasitic loads. The range of κ shown, from 0 to 0.08, corresponds to ECOPs of infinity to 12.5. The majority of commercial devices will fall somewhere in the middle of this range of κ .

A slightly more accurate approach might be to define the parasitic electricity per unit of rejected heat, since heat rejection often dominates the parasitic loads of thermally driven heat pumps. However, this analysis would not lend itself to neat analytical equations, and ECOP ($= \kappa^{-1}$) is the conventional way to define parasitic loads.

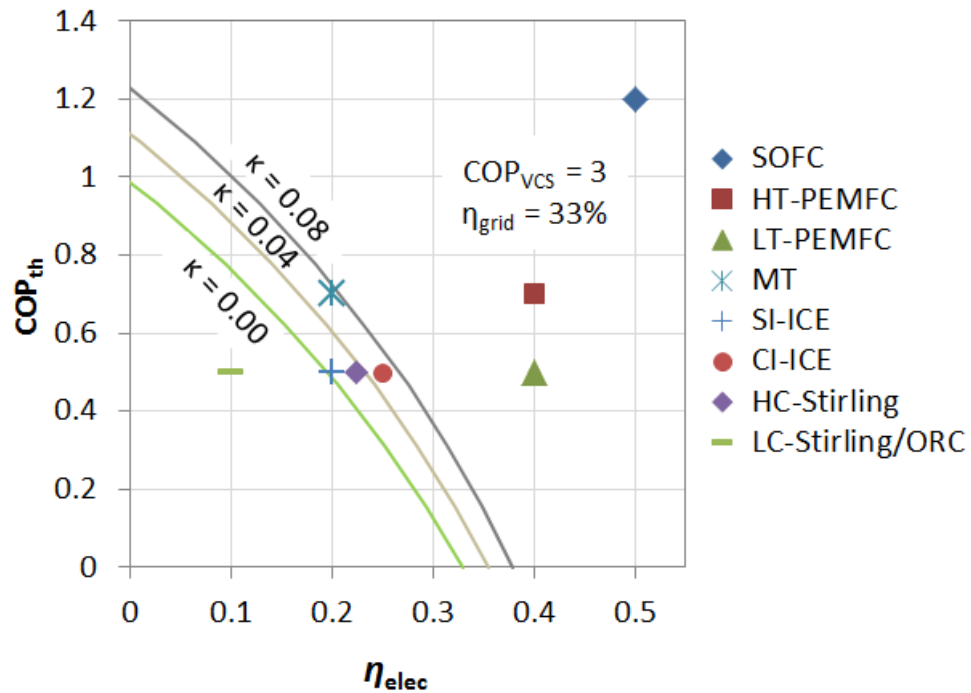


Figure 28: Effect of parasitic electrical loads of thermally driven equipment on energetic suitability of trigeneration

Figure 29 is the same as Figure 25, but introduces the non-idealities that $\lambda=0.1$ and $\kappa=0.02$. It also superimposes the matched systems to get an idea what is $f_{clg,inh}$ for each micro trigeneration system.

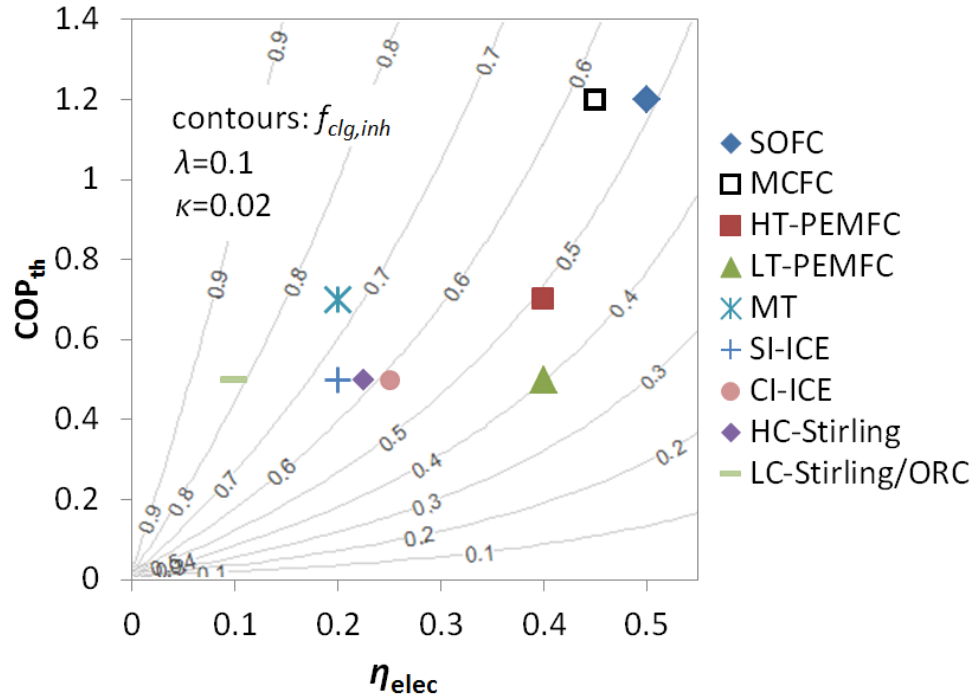


Figure 29: Inherent cooling load fraction as function of prime mover electrical efficiency and chiller COP, for $\lambda=0.1$ and $\kappa=0.02$

Both λ and κ are varied together in Figure 30 with COP_{VCS} fixed at 3. This results in a wide range of suitability depending on the heat losses and parasitic power consumption. Also, even with pessimistic assumption about heat losses and parasitic power, the fuel cell-based trigeneration systems can save energy.

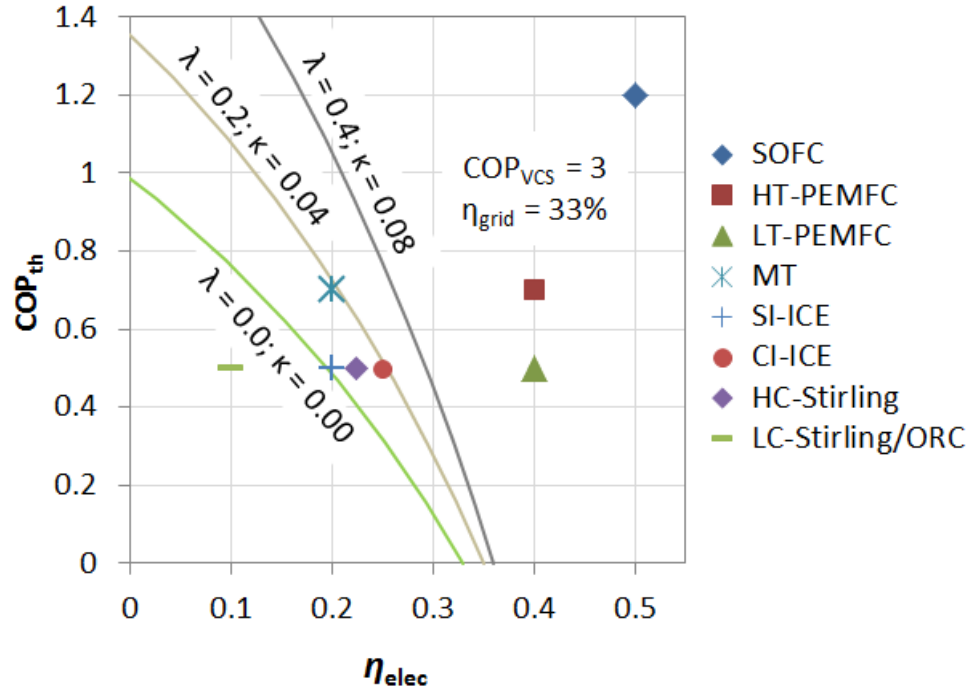


Figure 30: Effect of both parasitic loads and heat losses

Finally, to show the broad range of system performance possible based on varying assumption within reasonable values, Figure 31 shows two extreme cases. One case makes only optimistic assumption for COP_{VCS} , η_{grid} , λ and κ ; and the other makes pessimistic assumption for all these parameters. The resulting enclosed area is huge, encompassing nearly all possible trigeneration systems. If the pessimistic case's grid efficiency assumption is extended to 60% (the marginal grid efficiency of a new combined cycle power plant), even the SOFC-based system no longer saves energy. This demonstrates that it is possible to argue that almost any trigeneration system uses more or less energy than conventional cooling, simply by changing the assumptions made in the argument.

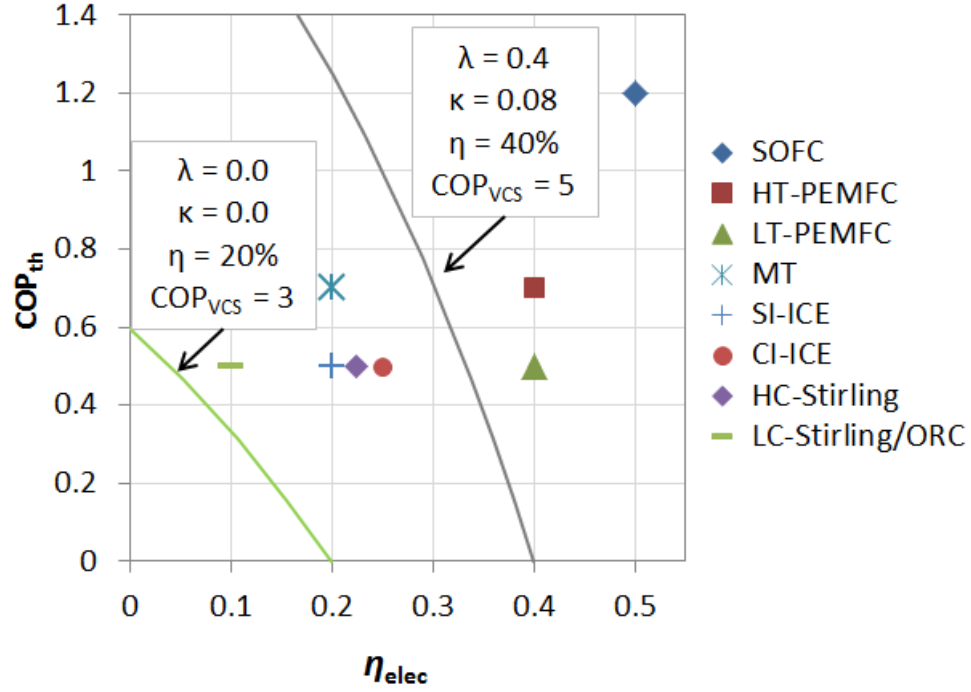


Figure 31: Full range of suitability possible based on optimistic assumptions (green) and pessimistic assumptions (gray)

For reference, Table 8 to Table 10 summarize the expressions that have been developed. Table 8 shows the inherent cooling fractions. The equations for $f_{clg,inh}$ of trigeneration systems have a very tractable meaning by inspection. The numerator is the amount of cooling per unit fuel, and the denominator is the sum of electrical and cooling outputs per unit fuel.

Table 8: Inherent cooling fractions for various ideal and non-ideal systems

	Inherent f_{clg} , ideal case	Inherent f_{clg} , non-ideal case
Grid-VCS	Any value from 0 to 1	
AB-HACD	1	
PM-HACD (w/ or w/out VCS and w/ or w/out AB)	$f_{clg,inh} = \frac{COP_{th}(1-\eta_{PM})}{\eta_{PM} + COP_{th}(1-\eta_{PM})}$	$f_{clg,inh} = \frac{COP_{th}(1-\eta_{PM}-\lambda)}{\eta_{PM} + COP_{th}(1-\eta_{PM}-\lambda)(1-\kappa)}$

Table 9 shows expressions for PER of systems operating at their inherent cooling load fraction. Note the inclusion here of a burner-driven HACD (B-HACD).

Table 9: Summary of expressions for PER of systems operating at their inherent cooling load fractions

	Ideal case	Non-ideal case
Grid-VCS	$PER^{-1} = \frac{1}{\eta_{elec} COP_{VCS}}$	
B-HACD	$PER^{-1} = \frac{1}{COP_{th}}$	$PER^{-1} = \frac{1}{\eta_B COP_{th}} + \frac{\kappa}{\eta_{elec}}$
PM-HACD	$PER^{-1} = \frac{1}{\eta_{PM} + COP_{th} (1 - \eta_{PM})}$	$PER^{-1} = \frac{1 + \kappa COP_{th} \left(1 - \frac{1 - \lambda}{\eta_{PM}}\right)}{\frac{\eta_{PM}}{1 - \kappa} + COP_{th} (1 - \eta_{PM} - \lambda)}$
PM-HACD-VCS*		

*since the system is operating at $f_{clg,inh}$, the VCS is inactive

2.4.5 System comparisons for variable cooling load fraction

Table 10 shows expressions for PER of realistic systems at variable cooling load fraction. Each system has two equations, for the cases of f_{clg} being greater than or less than $f_{clg,inh}$.

Table 10: Summary of expressions for fuel consumption as a function of cooling load fraction (f_{clg}) for six cooling systems

	Case 1: $f_{clg} < f_{clg,inh}$ (excess cooling available)	Case 2: $f_{clg} > f_{clg,inh}$	
	PER	PER	exported or excess electricity
Grid-VCS		$PER^{-1} = \frac{f_{clg} (COP_{VCS}^{-1} - 1) + 1}{\eta_{grid}} \quad (10)$	0
PM-VCS		$PER^{-1} = \frac{f_{clg} (COP_{VCS}^{-1} - 1) + 1}{\eta_{PM}} \quad (11)$	0
PM-HACD (without AB option)		$PER = \frac{COP_{th} (1 - \eta_{PM} - \lambda)}{f_{clg}}$ (16) [also (18) for export]	see Equation (17)
PM-HACD (with AB option)	$PER^{-1} = \frac{1 - f_{clg} (1 - \kappa)}{\eta_{PM}}$	see Equation (20)	0
PM-HACD-VCS (without AB option)	(15) (VCS and AB are not in use)	see Equation (21)	0
PM-HACD-VCS (with AB option)		see Equation (25)	0

An observation that can be drawn from Table 10 is that the terms λ , COP_{th} , COP_{VCS} , and η_{AB} are all missing from the $f_{clg} < f_{clg,inh}$ column. This makes sense, since the system is effectively running in electrical-load-following mode when $f_{clg} < f_{clg,inh}$. Thus any term dealing with the efficiency of the thermally-driven equipment is not important to PER. Of course, all of the missing terms (except η_{AB}) do play a role in determining $f_{clg,inh}$ – see Equation (14).

It can also be observed that the term for electrical parasitics, κ , is missing from the $f_{clg} > f_{clg,inh}$ column for systems without auxiliary burners, and present for systems with

AB. This also makes sense, since, without an AB backup, a system must produce excess electricity. In the presence of excess electricity, parasitic electric loads are not important. With an AB backup, excess electricity need not be produced and κ is again important. The amount of parasitic loads will affect the value of $f_{clg,inh}$, however – see Equation (14). Also, if excess electricity is exported and thus offsets electrical production elsewhere, then κ reappears in the expression – see Equation (18).

Figure 32 shows an evaluation of the previously developed expressions for HTPeMFC prime mover technology. One system is left out, the PM-HACD-VCS with AB, since its treatment requires an optimization with respect to the variable f_{VCS} . Inverse PER is shown to highlight the linearity of the expressions – non-inverse PER would have all curved lines. Inverse PER can be thought of as fuel consumption per unit loads, where a unit of load is characterized by a normalized sum of cooling and electrical loads.

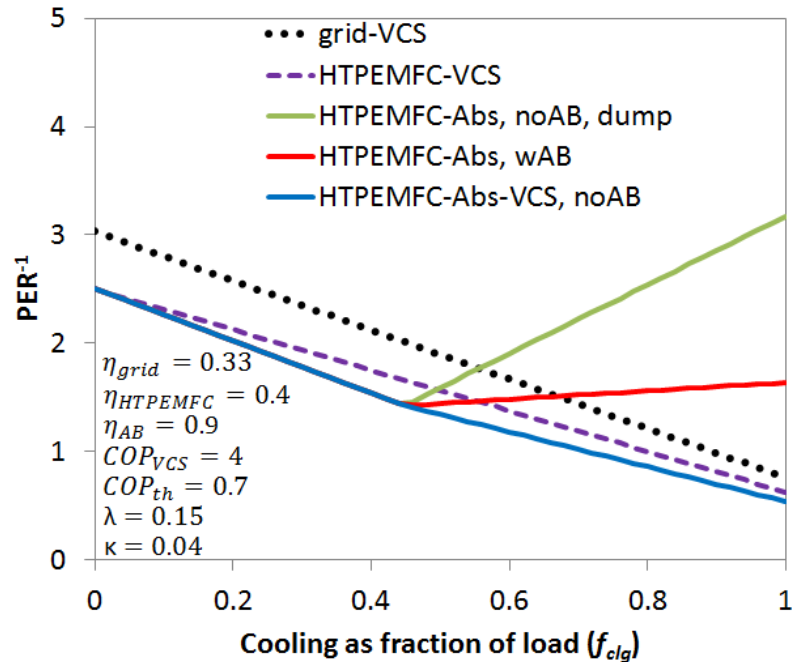


Figure 32: Comparison of grid-VCS and HTPeMFC-based systems

After a brief discussion of the features of Figure 32 , it will not be necessary for the reader to look at the legend for successive plots to identify the system corresponding to each curve. The following points are relevant to this understanding.

- Observe that the grid-VCS line stands alone with a left-y-axis-intercept equal to η_{grid}^{-1} . In contrast, all four PM-based systems share a left-y-intercept. This y-intercept corresponds to simple production of electricity without any cooling, and is thus simply equal to η_{PM}^{-1} .
- The right y-axis-intercepts for the grid-VCS and PM-VCS system correspond, respectively, to $\eta_{grid}^{-1}COP_{VCS}^{-1}$ and $\eta_{PM}^{-1}COP_{VCS}^{-1}$. Both of these systems involve separate generation, thus their left- and right-y-axis intercepts are connected by a straight line.
- Observe that the PM-VCS system uses more fuel than PM-HACD-based systems when $f_{clg} < f_{clg,inh}$. This is the region in which excess cooling is being produced; a PM-VCS system would be wasting this heat, while a PM-HACD system is producing “free” cooling with only a small penalty for parasitic HACD loads. In other words, the advantage of HACD-based trigeneration is conditional on ECOP being greater than COP_{VCS} . This can be demonstrated by setting equal the PER expressions for the two systems, Equation (11) and (15). Solving yields $COP_{VCS}^{-1} = \kappa$. Substituting the definition that $\kappa \equiv ECOP^{-1}$ yields the condition $ECOP > COP_{VCS}$ for trigeneration to save energy over separate generation from a given PM at $f_{clg} < f_{clg,inh}$.
- The three HACD-based systems diverge above $f_{clg,inh}$. Dumping excess electricity has the worst performance (although exporting could mitigate or reverse this problem), using an auxiliary burner (AB) improves performance considerably, and having a backup VCS results in the best performance.

In fact the VCS backup has a lower right-y-intercept than any system, and thus dominates the entire selection of systems when $\eta_{PM} < \eta_{grid}$. The PM-HACD-VCS system is able to take advantage of the benefits of trigeneration at low cooling fractions, while taking advantage of the VCS and still deriving benefit from waste heat utilization at high cooling fractions.

To facilitate rapid visual comparison, Figure 33 shows simplified versions of Figure 32 for various prime mover technologies. All plots have f_{clg} from 0 to 1 in the x-axis, and share the same y-axis limits on PER^{-1} except for the LC-Stirling plot.

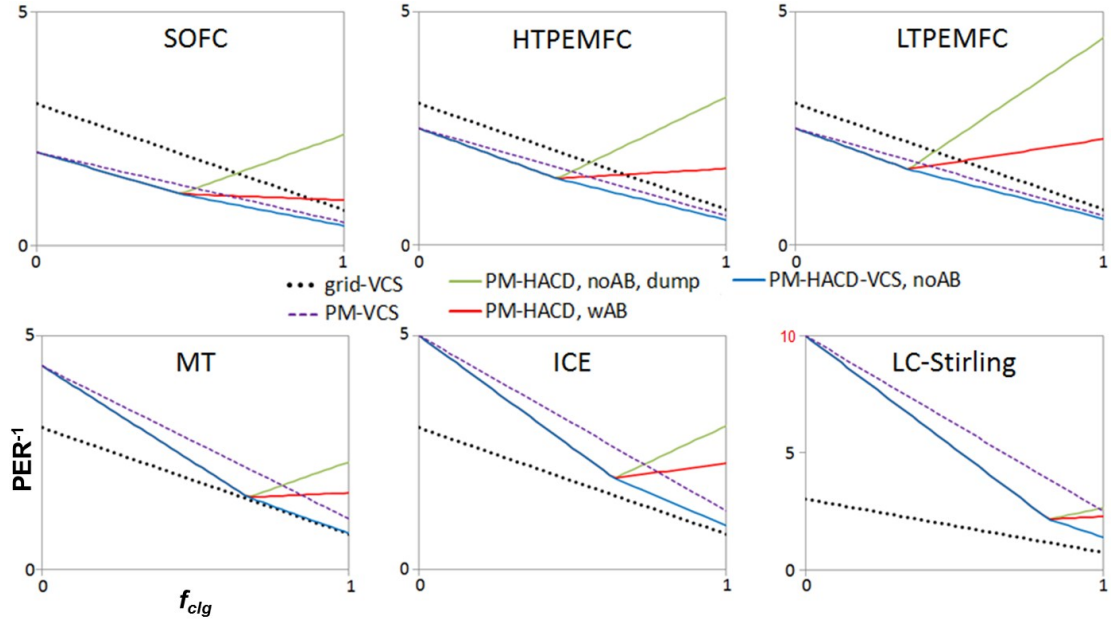


Figure 33: PER^{-1} vs. f_{clg} for various PM-based systems and grid-VCS

From this analysis it is clear that a grid-connected trigeneration system requires a high-electrical efficiency prime mover. The micro systems that can save energy in a grid-connected context are the fuel cells, especially the high temperature fuel cells which also benefit from a higher COP_{th} (SOFC, MCFC and HTPEMFC).

2.4.6 Sensitivity analysis

Utilizing partial derivatives of the analytical expressions, the sensitivity of PER for each system with respect to each variable can be determined. Results of such an exercise are presented numerically in this section.

Figure 34 is based on Equations (15) and (16), for a SI-ICE-based trigeneration system without a backup boiler (denoted “noAB”). The figure shows the sensitivity of PER to changes in the five variables in Equations (15) and (16), all as a function of f_{clg} .

At $f_{clg} < f_{clg,inh}$, it can be seen that increasing the cooling load fraction or prime mover efficiency results in the largest increases in PER, while the effects of other variables are negligible. At $f_{clg} > f_{clg,inh}$, increases in COP_{th} help the PER proportionally, while a small detriment to PER is experienced with increases in λ or η_{PM} . At the assumed value of $\kappa=0.04$, changes in κ are not very important, but the sensitivity to κ increases dramatically once κ reaches higher values (not shown).

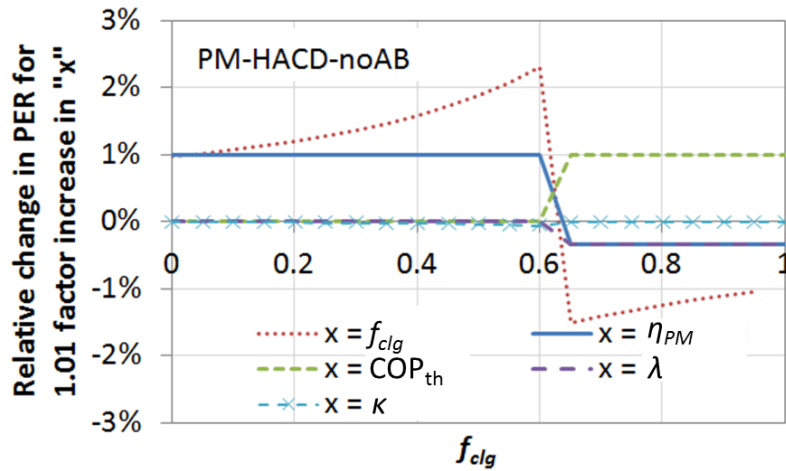


Figure 34: Sensitivity of PER to each variable affecting a SI-ICE-based trigeneration system without auxiliary burner

Figure 35, based on Equations (15) and (20), shows the same type of data for a SI-ICE-based trigeneration system, this time *with* an auxiliary burner (AB).

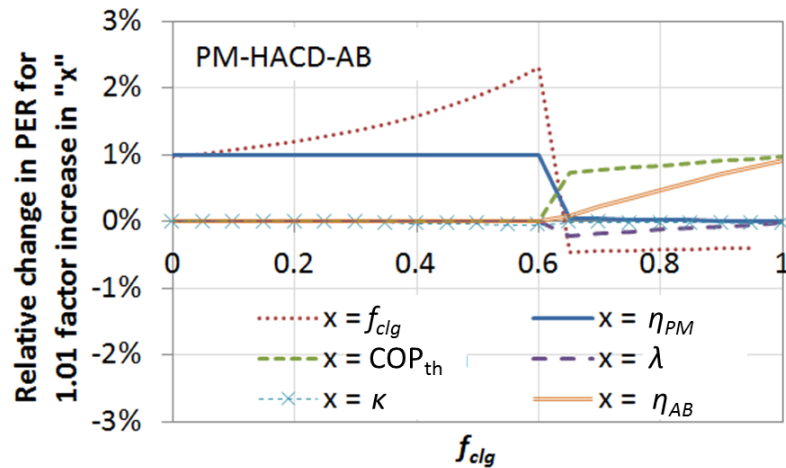


Figure 35: Sensitivity of PER to each variable affecting a SI-ICE-based trigeneration system with an auxiliary burner

In Figure 35, the variable η_{AB} has been introduced for a total of six variables. The auxiliary burner, by allowing the trigeneration system to only produce as much electricity as needed at high values of f_{clg} , removes the penalty associated with higher values of η_{PM} at high values of f_{clg} which was seen in the system without AB. It also slightly reduces the importance of COP_{th} at moderately high values of f_{clg} . At very high values of f_{clg} , the η_{AB} is very important.

2.5 Conclusions based on first-order comparisons

Several useful conclusions can be drawn based on the preceding analytical approach.

Fuel cells hold the most promise as prime movers for high efficiency trigeneration. This is due to their high electrical efficiency. Prime movers that can combine high electrical efficiency with high temperature waste heat, such as SOFC, MCFC, and HT-PEMFC, have the most potential of all.

For off-grid applications, nearly all prime movers have potential to save fuel over separate generation. This is generally because the electrical efficiency of off-grid generation is already low, so that all prime movers are at least as electrically efficient as the conventional alternative.

Note that a similar analytical analysis for on-grid CHP would show that all prime movers (even Stirling engines with 10% electrical efficiency) always save fuel compared with the conventional furnace heating. The barrier to saving energy with CCHP is higher than with CHP. This is basically because heating is conventionally primarily done with exergetically inefficient combustion, while cooling is conventionally done with heat

pumps. If the analysis for heating is carried out with heat pumps as the conventional technology, then CHP systems as well as CCHP systems rely on relative high electrical efficiency prime mover technologies in order to show energy savings.

To summarize for on-grid applications: if the prime mover has yearly-averaged electrical efficiency greater than the grid efficiency, then it is guaranteed to save energy. For CHP systems, when the prime mover electrical efficiency is less than the grid, CHP savings come from boiler/furnace replacement but not necessarily from heat pump replacement. For CCHP systems, when the prime mover electrical efficiency is less than the grid, CCHP savings are difficult to achieve.

To summarize for off-grid applications: both CHP and CCHP nearly always save energy over off-grid separate generation.

An additional observation from this chapter is the lack of an advantage of Carnot trigeneration over Carnot separate generation, with the trigeneration advantage growing as all systems move farther from the Carnot ideal. This represents a long term challenge for trigeneration since the potential benefits of trigeneration are reduced as power generation and vapor compression systems become more efficient.

Chapter 3: Separate Sensible and Latent Cooling Strategies for Trigereneration

Many heat-activated technologies suffer from limitations on the temperature lift they can achieve. When the ambient temperature is too high, the machine can no longer provide cooling. In adsorption systems, sorbent properties that allow high COP at low activation temperature (a steeply “S”-shaped isotherm) result in this limitation. In water/LiBr absorption machines, crystallization of the salt solution is the mechanism behind the limitation. In both cases, the problem can be resolved by lowering the heat rejection temperature or raising the evaporator temperature.

In practice, most water/LiBr commercial systems today rely on expensive and high-maintenance wet cooling towers to keep the heat rejection temperature low. Commercial adsorption chillers generally use a very high regeneration temperature. For very small scale systems, air cooling is required, and thus some way of raising the evaporator temperature, without sacrificing dehumidification capacity, is needed.

The SSLC approach developed in this work (see Gluesenkamp et al. (2011e)) is one way to address this limitation.

3.1 Past approaches to the crystallization limit

The crystallization limit (equivalently, the solubility limit) of aqueous LiBr can be plotted from Boryta’s (1970) experimental data on a Dühring chart, as shown in Figure 36. For air-cooled machines, the primary challenge is that the crystallization limit will be reached, since high absorber temperatures require the solution entering the absorber to become very salty in order to maintain a sufficiently low vapor pressure.

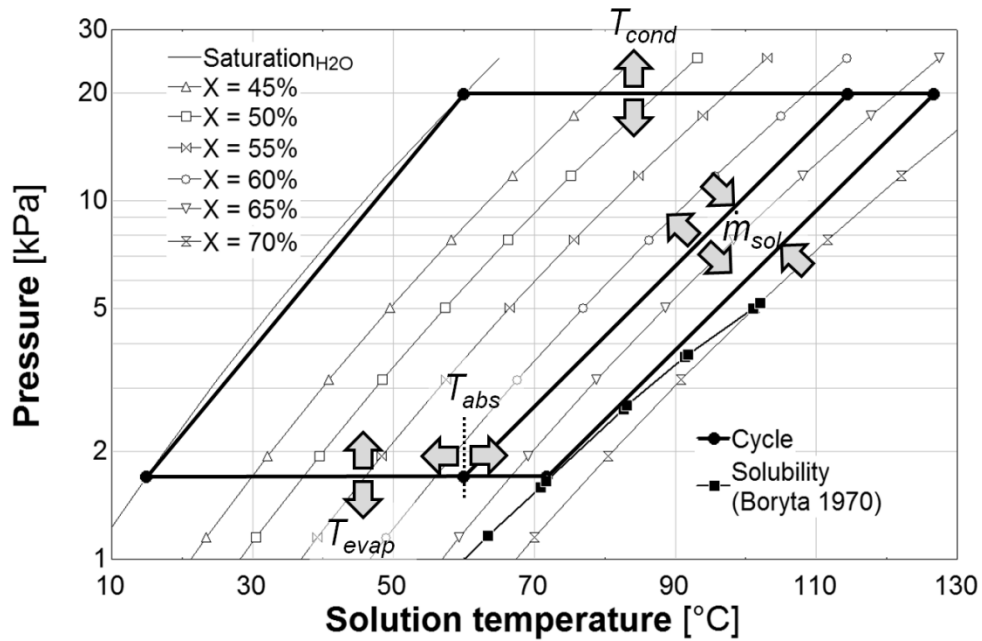


Figure 36: Effect of changing independent operating variables on the shape of the Dühring plot

Since the solution entering the absorber is the critical state point most prone to crystallization, the crystallization margin of an operating machine can be characterized by how closely the solution state at that critical point approaches the crystallization line. This can be expressed as the temperature change (at fixed concentration) that would result in crystallization (T_{margin}), or as the concentration change (at fixed temperature) that would result in crystallization (X_{margin}).

Several strategies for avoiding crystallization can also be inferred from Figure 36. For example, increasing T_{evap} and/or decreasing T_{abs} move the lowest-right state point away from the crystallization line. T_{cond} can be seen to not have a direct effect on the crystallization, so that cooling the absorber and condenser in series may help avoid crystallization by decreasing T_{abs} at the expense of increasing T_{cond} . Increasing the solution pump flow rate (and therefore flow ratio) brings the saltier solution closer to the concentration of the less salty solution. However, it also decreases the heat transfer effectiveness of the absorber, resulting in slightly higher absorber temperatures. In

practice increasing solution pump flow rate does typically move the critical state point further from the crystallization line, although generally at the expense of a lower COP.

Not shown in Figure 36 is the impact of anti-crystallization additives. Since these are different solution compositions, they shift both the solubility curve and the isosteres of the Dühring plot.

Various strategies for avoiding crystallization were considered, including working fluid additives, cycle modifications (absorber pressurization), and air-conditioning system-level changes (SSLC and cascade VCS-AS cycle).

3.1.1 Working fluid modifications

Working fluid modifications are discussed in Gluesenkamp et al. (2011a). They are not discussed further here.

3.1.2 Absorption pressurization

One method to avoid crystallization (which has been discussed by Zogg et al. (2005) and Zogg and Westphalen (2006)) is to separate the evaporator and absorber, and place a compressor between them to raise the absorber pressure. Figure 37 shows the effect that this would have on the cycle.

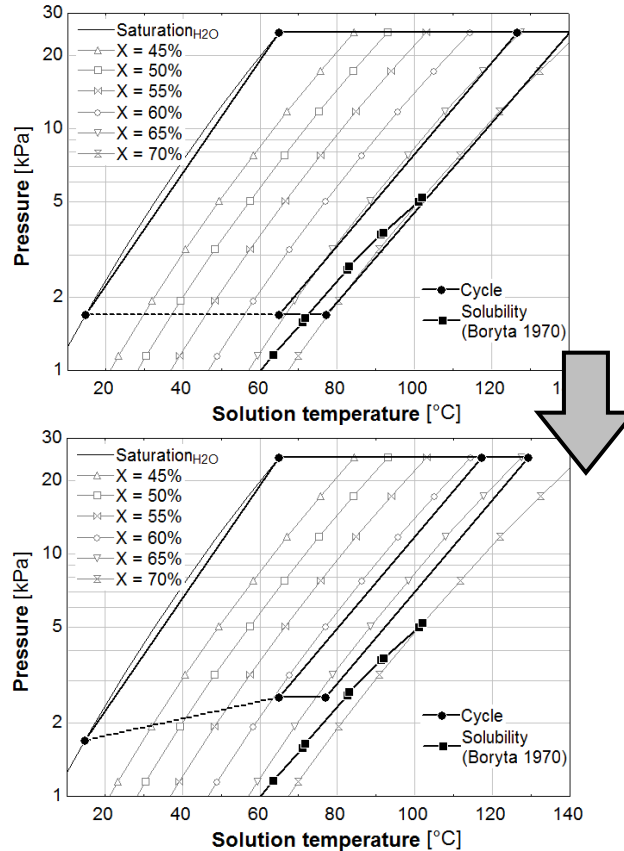


Figure 37: Dühring plots of the absorption cycle showing the effect of the pressurized absorber

It can be seen in Figure 37 that the absorber is lifted out of the crystallization range in the bottom right portion of the cycle. It was found that a pressure ratio of 2.3 (corresponding to a power consumption of 250 W with an isentropic efficiency of 75%) would be sufficient to prevent the crystallization of the LiBr solution, if a suitable compressor could be found and the difficulty in separating the evaporator and absorber could be solved. However, an appropriate compressor would need to be oil-free and able to handle a very high volume of very low density refrigerant. Centrifugal compressors, oil free lobe and screw type compressors and axial fans were investigated, but they either did not meet the desired pressure ratio or were impractically bulky.

3.1.3 Cascaded absorption/VCS system

Another way to boost the absorption cycle evaporator temperature is to cascade a VCS with the absorption cycle. If the absorption cycle evaporator cools the space directly, its absorber (and possibly also condenser) can be cooled by the VCS, with the VCS condenser dumping heat to the ambient. In this “AS to VCS” configuration, the VCS would have to run continuously, unless a bypass valve were installed which allowed the absorber to dump heat directly to ambient (with the VCS off) when conditions permit, and to dump heat to the VCS evaporator when crystallization is a possibility. In contrast to the SSLC supplemental VCS, the cascade VCS would have to handle the full cooling load of the space; however its COP would remain high due to the small temperature lift (e.g. 35°C evaporation and 60°C condensing temperatures, for a temperature lift of only 25 K).

If a “VCS to AS” cascade were chosen, the VCS would work across an even smaller temperature lift (e.g. 7°C evaporating and 20°C condensing temperatures, for a temperature lift of only 13 K). However, it would have to run all the time, regardless of ambient condition, unless two evaporators were provided to the space (one for the VCS and one for the AS).

Initial modeling of the cascade configurations indicated that the SSLC system was more promising in terms of minimizing fuel consumption at the design condition, and thus the SSLC system was selected as the final design.

3.2 SSLC approach

Even though one goal of utilizing an absorption system is to avoid electrically-powered VCS systems, a small VCS can be used to address the crystallization issue while still maintaining acceptably low electrical requirements. As shown in Figure 38, a large air stream (points 4-5-6) consisting of the return and exhaust air is sensibly cooled (not dehumidified at all), while a small air stream (1-2-3) consisting of the outdoor ventilation air is over-cooled and dehumidified to 9°C. When the streams mix to form the supply air, the appropriate supply air condition is achieved. This allows the absorption evaporator to operate at a higher temperature (only cooling points 2 and 6 to 24°C).

An unusual feature of Figure 38 is the split nature of the AS evaporator. The two air streams (1-2 and 5-6) do not mix with each other, and each stream is cooled to about the same temperature (at points 2 and 6). For an air-to-refrigerant evaporator/absorber, this could be accomplished with parallel air channels. For a water-to-refrigerant evaporator/absorber, this could be done with parallel air channels (ducted separately across the fan coil unit) or two parallel fan coil units.

In addition, the power requirement of the VCS is kept low by utilizing return and exhaust air to cool the VCS condenser (points 4-5), at the expense of increasing the load on the absorption cycle. If the VCS condenser were to dump its heat outdoors, the condensing temperature would likely be about 59°C, and the COP of a typical R134a system would be 1.2 (requiring 1.07 kW to provide the necessary 1.3 kW of cooling between state points 2 and 3). By cooling the VCS condenser with a larger flow rate of air – 0.28 kg/s (525 CFM) instead of perhaps 0.044 kg/s (90 CFM) – at lower temperature (32°C instead of 49°C), the condenser achieves a better approach temperature and a much

lower high side pressure. Thus, the VCS COP in the proposed configuration is 2.91 and the VCS only consumes 446 W to provide the same capacity. Although adding the VCS condenser's heat to the return air stream increases the load on the absorption cycle, the dramatic reduction in electricity allows a smaller engine to be used. The resulting temperature and humidity ratio at point 7 are 22°C and 14.4 g/kg, appropriate for a SHF of 0.9. Psychrometric state points corresponding to Figure 38 are shown in Figure 39.

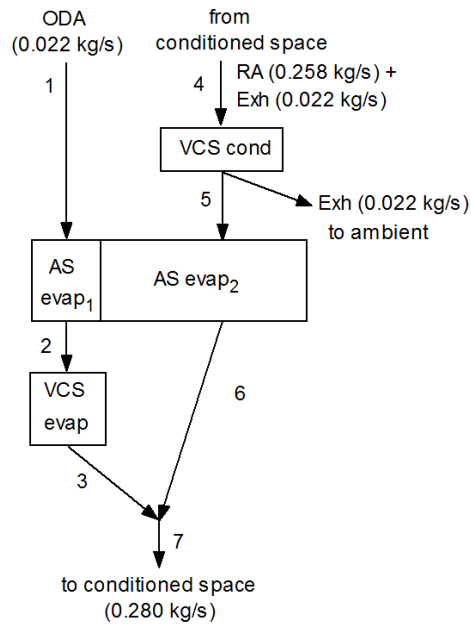


Figure 38: Air flow schematic of the separate sensible and latent cooling (SSLC) system

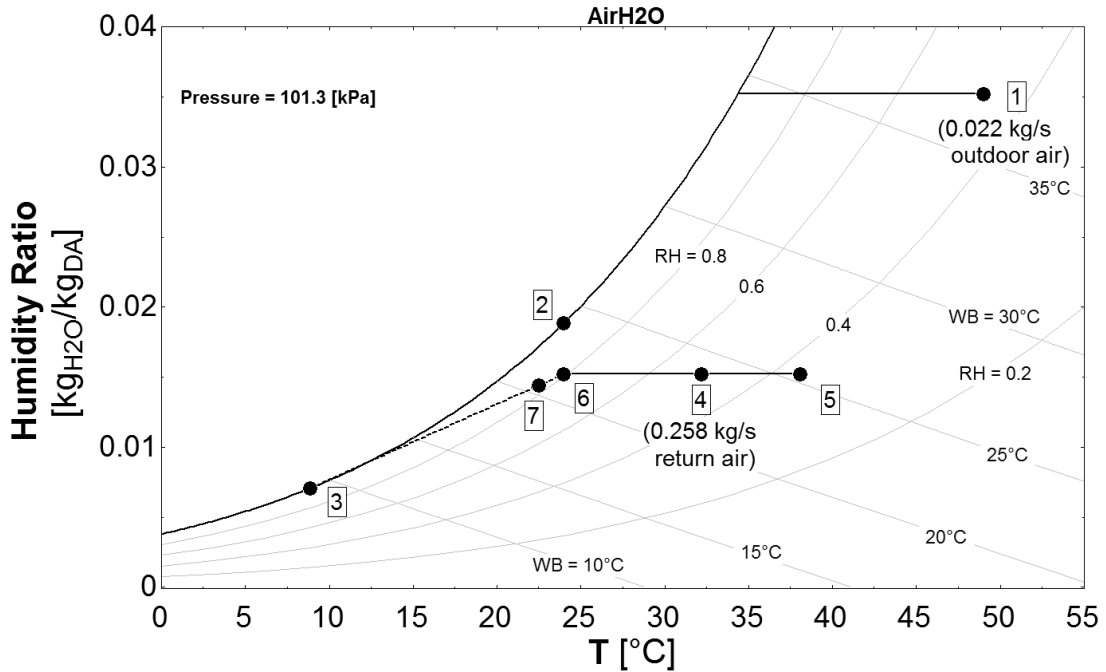


Figure 39: Psychrometric chart of SSLC system at design point

3.2.1 Description of SSLC and conventional system models

Two systems were modeled in detail in this study: the conventional system in Figure 40, and the absorption system-based SSLC configuration with a small VCS in Figure 41. The conventional system's genset powers the VCS and 3 kW of non-cooling loads, while the proposed system's genset powers the supplemental VCS and 3 kW of non-cooling loads, with engine exhaust and a duct burner powering a water/LiBr absorption system. Table 1 shows the engine and cooling capacities for each system.

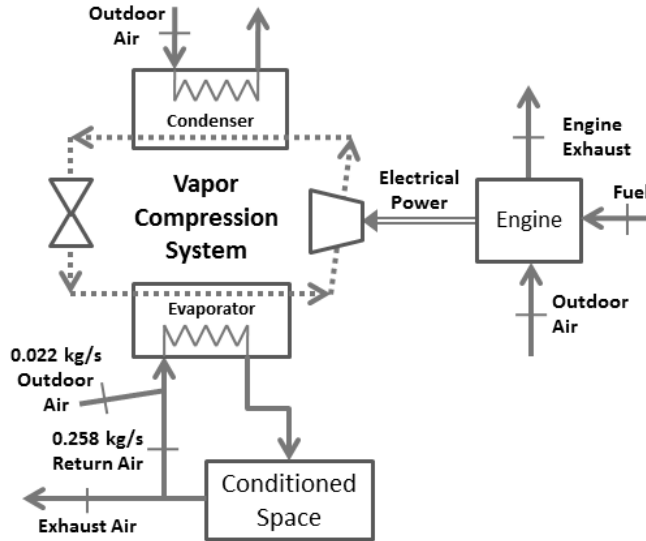


Figure 40: Schematic of conventional system with VCS for cooling

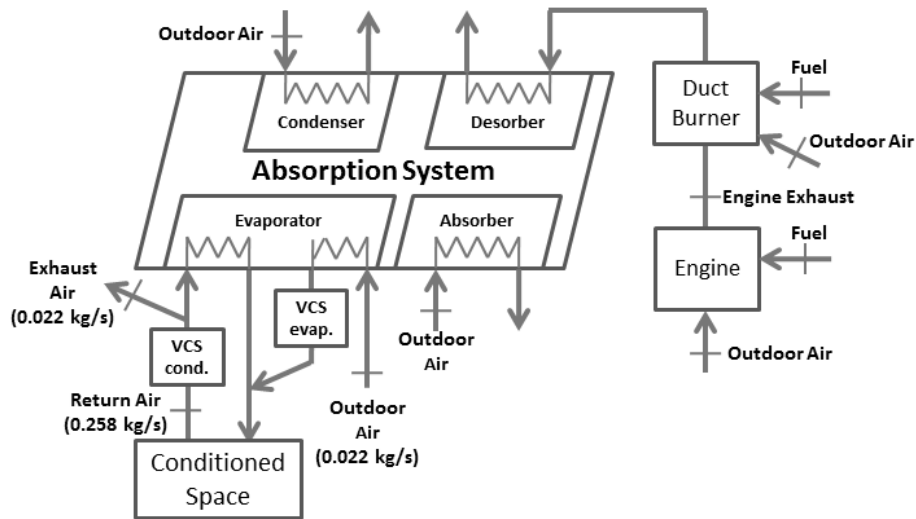


Figure 41: Schematic of SSLC system model with LiBr absorption system and supplemental VCS

The VCS in each system utilizes R134a as the working fluid. Fan power was neglected for the absorption and both the VCS systems.

Table 11: VCS specifications and requirements for cooling

System configuration	AS cooling capacity [kW]	VCS cooling capacity [kW]	VCS COP [-]	VCS compressor power [kW]	Engine size [kW]
Conventional	N/A	5.3	1.8	3.0	6.0
Absorption with SSLC	5.6	1.3	2.9	0.45	3.5

3.2.2 Available heat from engine

The primary source of heat for the absorption system is the engine exhaust (engine coolant is not used). When this is insufficient, a duct burner supplies additional heat. Experimental performance data for a 3.0 kW diesel engine in the field was obtained as shown in Table 12. This data was used as a basis for the engine models in each of the systems, with fuel consumption and exhaust flow rate scaled up proportionally for sizes larger than 3.0 kW.

Also shown in Table 12 is the calculated usable exhaust heat. For a practical system, the engine exhaust temperature must stay above the acid dewpoint (about 115°C) at all off-design conditions. The fixed UA value of the desorber was set so that the exhaust is not cooled below 130°C in the desorber at minimum load. Because of this, at full load it is only cooled to 278°C.

Table 12: Performance data for 3.0 kW engine

Electrical load [kW]	Fuel consumption (measured) [L/hr]	Exhaust temp. (measured) [°C]	Usable exhaust heat (calculated) [kW]
0.75	0.680	329	1.35
1.5	0.847	385	1.77
2.25	1.062	413	1.97
3.0	1.334	454	2.26

3.2.3 Duct burner

The duct burner requirements were determined from the UA-based thermodynamic absorption system model; to provide 5.56 kW of cooling with a COP of 0.66, the desorber requires a heat input of 8.37 kW. Utilizing the engine exhaust heat leaves about 6.1 kW to be provided by the duct burner. To ensure that the acid dewpoint is not reached at low part load, the exhaust leaving the desorber at full load is still very hot. Thus the duct burner needs to burn up to 7.6 kW of fuel.

For the best efficiency, the duct burner should be mounted in-line with the engine exhaust stream. Since the engine is diesel, there is normally excess oxygen in the exhaust available for combustion in the duct burner. However, fresh air does need to be introduced to the duct burner under high engine and AS loads, and in situations where the duct burner outlet temperature would exceed the temperature limits of the desorber and duct burner materials.

3.2.4 Modeling assumptions

The absorption system model follows the UA-based heat exchanger method outlined in Herold et al. (1996), who also provide effectiveness definitions for absorption cycle heat exchangers. The UA and effectiveness values at the design point are shown in Table 13. The condenser and absorber heat exchangers were air cooled in parallel, each with a 0.3 kg/s air mass flow rate. The desorber UA value was tuned to avoid the acid dewpoint at low part load. The solution pump flow rate was set at 0.03 kg/s. Table 14 shows key VCS modeling assumptions.

Table 13: Absorption system heat exchanger data

Heat exchanger	Type	UA value [kW/K]	Effectiveness @ design pt
Absorber	solution-to-air	1.080	0.890
Desorber	exhaust gas-to-solution	0.0115	0.788
Condenser	refrigerant-to-air	0.720	0.893
Evaporator	air-to-refrigerant	0.840	0.890
Solution HX	solution-to-solution	0.093	0.64

Table 14: Key VCS modeling assumptions

	Conventional VCS system	Supplemental VCS for SSLC
Evaporator approach temperature	7 K	7 K
Condenser approach temperature	12 K	5 K
Superheat	7 K	7 K
Subcooling	5 K	3 K
Compressor isentropic efficiency	0.70	0.74
Compressor motor efficiency	0.85	0.85
Evaporator air inlet	49°C	24°C
Evaporator air outlet (T, RH)	19°C, 100%	9°C, 100%
Condenser air inlet	49°C	32°C
Pressure drop in evaporator (refrigerant)	50 kPa	50 kPa
Pressure drop in condenser (refrigerant)	100 kPa	100 kPa
Refrigerant	R134a	R134a

3.2.5 Results

The results in Table 15 show that the most fuel is consumed by an oversized engine powering a vapor compression system. The most efficient option is using waste heat and a duct burner to power an absorption system. There is also some fuel savings for an absorption system that does not utilize waste heat. The results are for the design condition and full electrical load on each of the engines. However, at lower ambient conditions and electricity requirements, the fuel savings will become even more pronounced. This is partly because the oversized engine will not perform as efficiently at lower part loads when compared to the smaller sized system. Additionally, the small VCS system can simply be shut off when crystallization is not a threat.

Table 15: Fuel consumption at the design conditions of 49°C and 35 g/kg humidity ratio.

System configuration	Engine size [kW]	Cooling system	Additional components	Engine fuel cons. [g/s]	DB fuel cons. [g/s]	total fuel cons. [g/s]
Conventional VCS	6.0	VCS	N/A	0.607	0	0.607
Absorption w/ waste heat	3.5	Absorption w/ SSLC	Duct Burner	0.360	0.177	0.537
Absorption w/out waste heat	3.5	Absorption w/ SSLC	Duct Burner	0.360	0.230	0.590

Table 16 shows the absorption system’s heat exchanger heat loads at the design point. The duct burner heat combined with the exhaust heat provides about 1.5 kW more than is required by the desorber, as required to avoid the acid dewpoint at low part load with a fixed desorber UA value.

Table 16: Heat loads of absorption system heat exchangers

Configuration	Q_e [kW]	COP	Q_d [kW]	Q_{exh} [kW]	Q_{db} [kW]
Absorber w/ waste heat	5.562	0.664	8.375	2.26	7.617
Absorber w/ fuel only	5.562	0.664	8.375	0	9.875

The SSLC system prevents crystallization with a T_{margin} of 12.5 K and an X_{margin} of 1.3%. If it were determined that less of a margin would be appropriate, then an even smaller supplementary VCS (or lower absorption evaporator temperature) could be used.

However, it is important to note the sensitivity of the results to the “inter-evaporator temperature” (the temperature of state points 2 and 6 in Figure 38 and Figure 39). As the inter-evaporator temperature increases, the VCS evaporator load increases at the same air flow rate; and above an inter-evaporator temperature of 25°C frost formation at the VCS evaporator becomes an issue. The ODA ventilation flow rate should not be increased to solve this, since it would increase the total cooling load. For an inter-evaporator temperature below 23°C, crystallization of the absorption cycle occurs. Thus an inter-evaporator temperature of 23 to 25°C is required.

The narrow range of acceptable compromise between these issues can be expanded by allowing the total supply air flow rate to vary or by introducing a defrost cycle. For a practical system, a robust control strategy would need to be identified.

3.2.5 Conclusions

An air-cooled, off-grid absorption system using VCS-assisted SSLC can save fuel compared to an engine-drive VCS. Fuel is saved even at high ambient conditions while incurring parasitic loads to successfully address the issue of crystallization. The fuel savings are 11.5% at the outdoor condition of 49°C and 35.2 g/kg using engine exhaust heat and a duct burner, and the savings are 2.8% if no engine waste heat is utilized. The savings are expected to be even greater at lower electrical loads and less extreme weather conditions, when less cooling (or none at all) would be required from the supplemental VCS to avoid crystallization.

Control of the system may be a challenge, and a suitable control strategy needs to be identified.

Chapter 4: Development of Dynamic CCHP Test Facility

4.1 Integration of CHP engine with simulated loads

4.1.1 Test facility

The test facility includes the prime mover (currently a reciprocating internal combustion spark ignition engine) with integrated heat recovery components, an 800 L water storage thermal buffer tank, an outdoor radiator heat-dump, and water connections with the tap and drain. Constant speed pumps circulate water between components. The heat flows between components are regulated by electronically actuated mixing/diverting valves that control the amount of water recirculation. Thermocouples and turbine flow meters throughout the system measure the hydronic heat transfer between components, as shown in Figure 42.

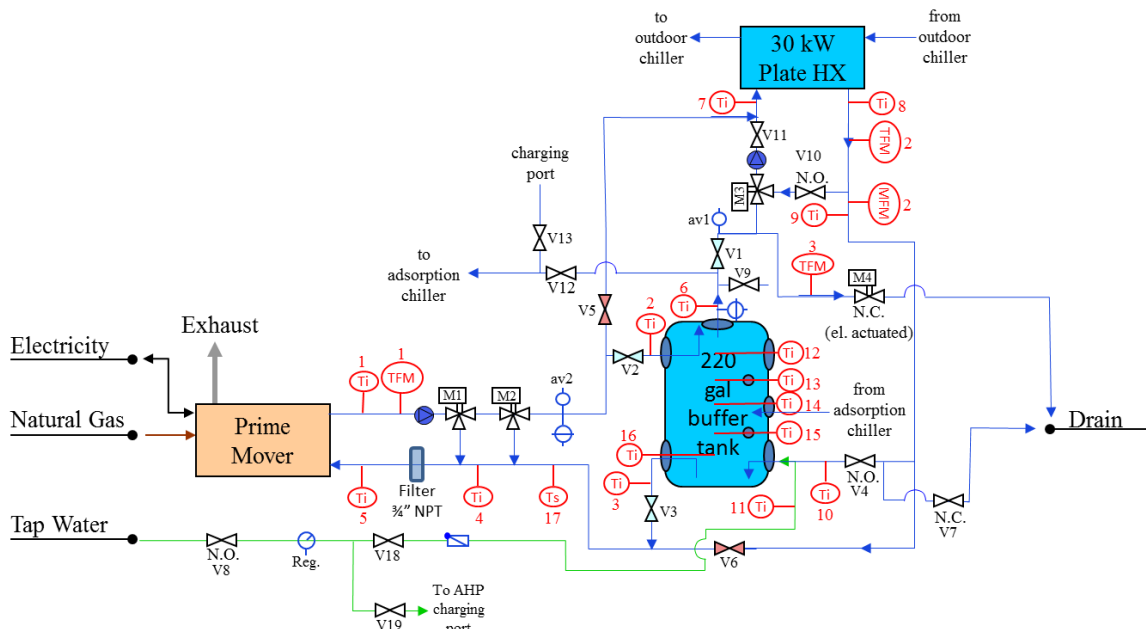


Figure 42: Schematic of test facility hydronics and hydronic instrumentation

Figure 42 shows the numbering scheme for measurement devices that was kept consistent throughout all tests (not shown are the tank’s surface thermocouples). It was used in combination with the scheme shown in Table 17 to quickly implement the manual valve changes necessary to switch from one operation mode to another.

Table 17: Valve settings for the two operating modes and the draining/charging and de-aerating modes (O=open; X=closed)

Code	Description	Transient	Steady State	De-aerating	Draining
V1	Tank Top Center	O	X	X	(either)
V2	Tank Upper	O	X	X	X
V3	Tank Lower Left	O	X	O	O
V4	Tank Lower Right	O	X	O	X
V5	Tank Bypass	X	O	O	O
V6	Pump Bypass	X	O	X	X
V7	Drain Bypass	X	X	X	O
V8	Fill Valve	O	X	O	X
V9	Air Vent	X	X	X	O
V10	M3 Bypass Shutoff	O	X	X	X
V11	Pump Throttle Valve	~half	X	~half	X
M1	Ecopower	ECO-PID	OFF	(any)	AB-A
M2	Tank to Eco	OFF	PID	(any)	AB-A
M3	Tank to Plate HX	PID (SH)	OFF	(any)	(any)
M4	Drain	PID (DHW)	X	X	X

The tank is fitted with five in-stream and eight surface thermocouples. These 13 measurements were vertically spaced as shown in Figure 43. A perfectly even vertical spacing could not be implemented due to the available openings in the tank.

Thermocouple placement

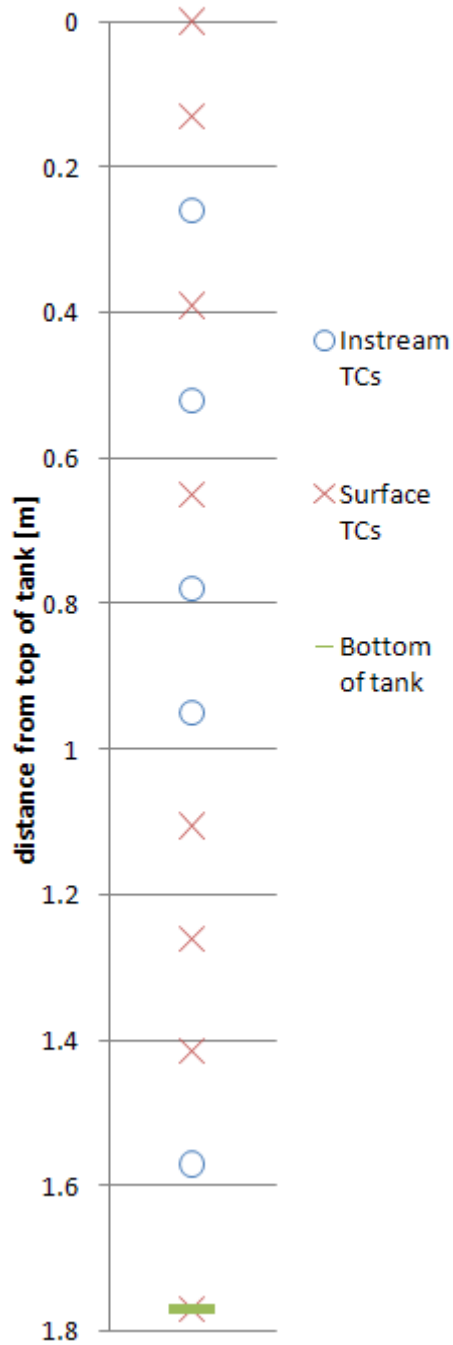


Figure 43: Vertical locations of in-stream and external thermocouples on tank

The outdoor radiator contains a water-glycol solution, and exchanges heat with the indoor water loop through a plate heat exchanger. It can be used to simulate hot water

used in a fan coil for space heating. The drain and tap connections to the water tank allow hot water to be replaced directly with cold tap water, simulating domestic hot water use. The capacity of the heat load being dumped is regulated by varying the effective water pumping rates through use of mixing valves. For steady state testing, the buffer tank can be bypassed and the primary loop flow rate fixed.

Within the prime mover cabinet, the heat recovery loop operates in the sequence shown in Figure 44, with engine coolant used as the heat recovery medium. After dumping heat in the plate heat exchanger, the coolant first services the generator, then oil cooler, then exhaust gas, then cooling jackets. This arrangement keeps the generator coolest for better electrical efficiency. Although a higher supply temperature could be obtained by servicing the cooling jackets and then exhaust, the reverse is done. Since the engine is designed for the heating season, a higher supply temperature is not advantageous, and this arrangement minimized exhaust losses, the most significant type of loss from the system. Thermocouples are installed as shown in Figure 44. The flow rate is inferred from an energy balance on the plate heat exchanger, since the flow rate on the other side is measured directly.

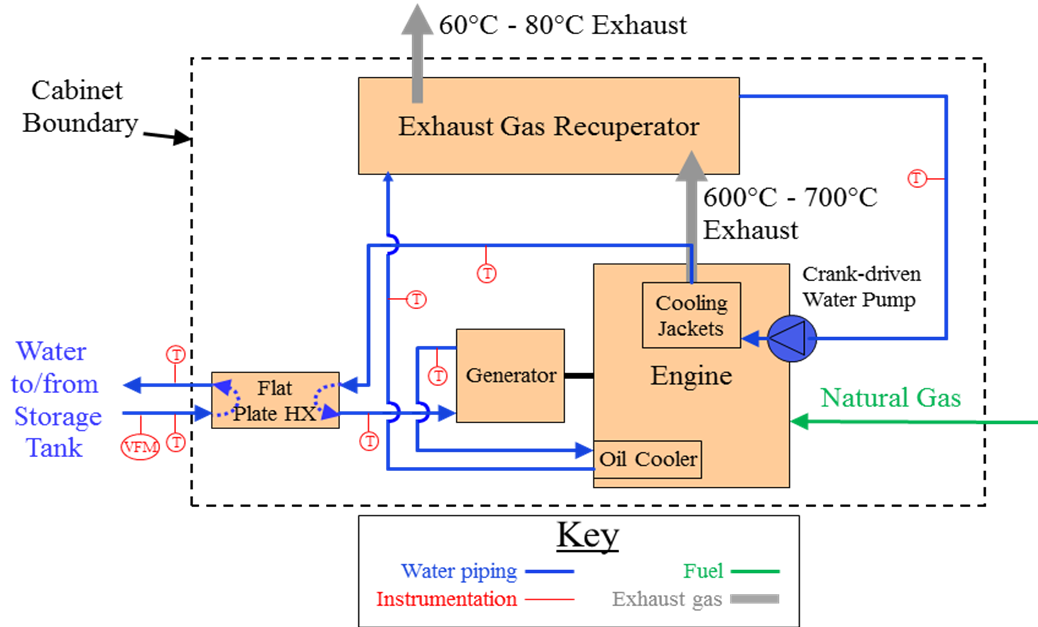


Figure 44: Schematic of heat recovery loop within prime mover cabinet

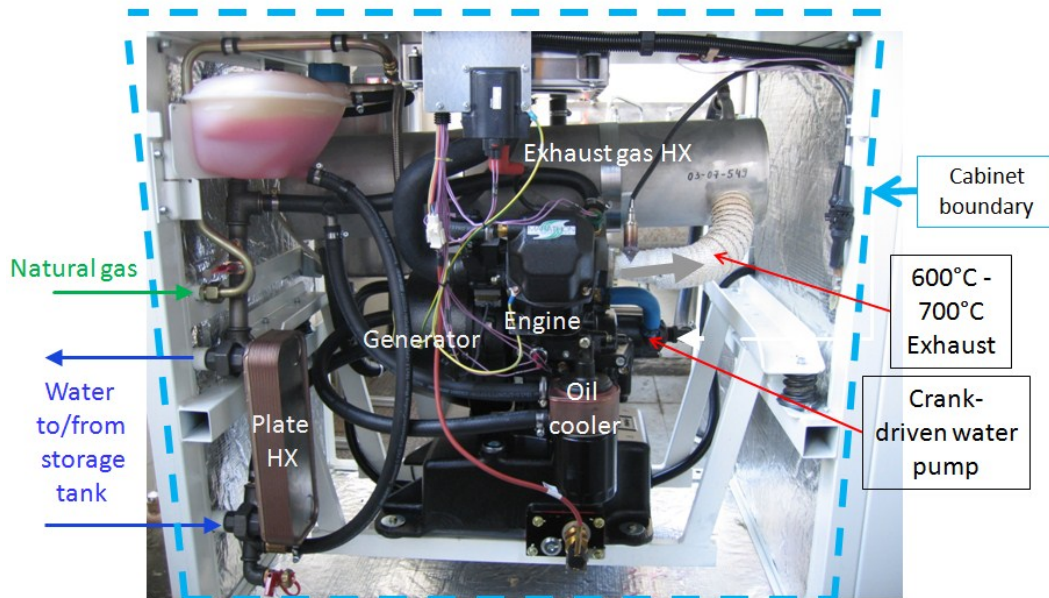


Figure 45: Photo of Ecopower cabinet interior with labeled heat recovery components

With this arrangement, the cooling jackets are the last heat recovery point. This sets a practical upper limit on the heat recovery temperature due to engine material reliability concerns (and the potential for surface autoignition in SI engines (Heywood 1988)). For typical internal combustion engines, this limit is about 77-85°C (170-185°F).

The systematic uncertainties of all system instrumentation are depicted in Table 18. The uncertainty in the data acquisition (DAQ) module is considered negligible due to its relatively small magnitude in comparison with the measurement instruments. For analog inputs, the DAQ module has 16 bit resolution, over the range of 4-20mA (effective resolution: 15 mA) or 0-10 VDC (effective resolution: 190mV), depending on the type of input.

Table 18: Systematic uncertainties of all instrumentation

Instrument	Absolute error	Relative error	Units
AL-425 gas meter (by volume)	-	0.025	L/s
CMF025 Coriolis gas meter (by mass)	-	0.025	g/s
Ohio Semitronics voltage transducers	-	0.005	V
Ohio Semitronics watt transducers	-	0.01	kW
RTD sensors	0.2	-	°C
Sponsler turbine flow meters	-	0.01	kg/s
T-Type thermocouples	0.5	-	°C
Vaisala RH sensors	1%RH*	-	RH

* uncertainty ranges from 1%RH to 2%RH depending on RH value

Table 19: Systematic uncertainties of selected values that were not measured directly

Calculated values	Absolute error	Relative error	Units
Natural gas density	-	0.01 [†]	kg/m ³
HHV of natural gas	-	0.03 [†]	kJ/kg
Q _{radiation}	-	0.4	kW
Q _{convection}	-	0.6	kW

[†] indicates uncertainty values that are based on statistical analysis of measurements made at NIST's facility

4.2 Adsorption chiller: design, construction and CCHP integration

This section describes the design and implementation of the experimental adsorption chiller. It includes the development of an equilibrium thermodynamic cycle model used for component sizing and performance estimation.

First the basics of the adsorption cycle are briefly outlined for context and for the reader unfamiliar with adsorption chillers. Next the experimentally implemented process

and instrumentation schematic is introduced to give perspective to the following sections, which describe the sizing of heat exchange components, chiller fabrication and integration with the CCHP system.

The temperature nomenclature used throughout this section is illustrated in Figure 46.

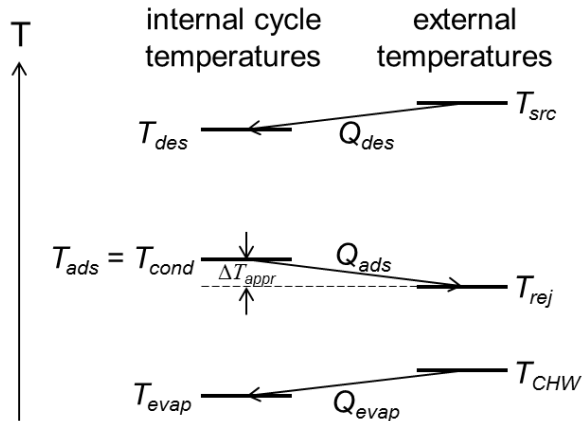


Figure 46: Adsorption heat pump temperature nomenclature

4.2.1 Adsorption cycle: working principle and operational phases

In a common basic adsorption heat pump configuration, illustrated in Figure 47, two adsorbent-coated heat exchangers (or adsorbent beds) are placed in separate sealed chambers. The only vapor phase species in the chambers is the chosen refrigerant. Each coated heat exchanger has internal piping to allow heating or cooling fluid (heat transfer fluid or HTF) to flow within. By heating one of the heat exchangers (the desorber), refrigerant will desorb from its surfaces, pressurizing its chamber. Eventually the pressure in the desorber chamber will exceed the pressure in the condenser chamber, and the upper valve will open, allowing refrigerant vapor to pass to and condense in the condenser (which is cooled by ambient-temperature water). The condensed refrigerant flows by gravity to an expansion device and adiabatically cools upon expansion. The

expansion process generates two-phase refrigerant, with the liquid refrigerant evaporating from the surfaces of the evaporator to cool the chilled water within. Low pressure is maintained in the evaporator despite refrigerant evaporation by cooling the second coated heat exchanger (the adsorber) with ambient-temperature HTF, thus causing refrigerant vapor to adsorb onto its coated surface. This arrangement can be maintained until the desorber approaches a “dry” state and the adsorber approaches a saturated state. The adsorber/desorber roles of the two coated heat exchangers are then reversed, allowing evaporation and condensation to continue. Note that the switching period is initiated by changing the temperature of HTF entering the adsorber HXs, which would typically be implemented with HTF valves. It is thus possible to have entirely passive vapor valves. If active vapor valves are used, they need to be activated according to the differential pressure between chambers.

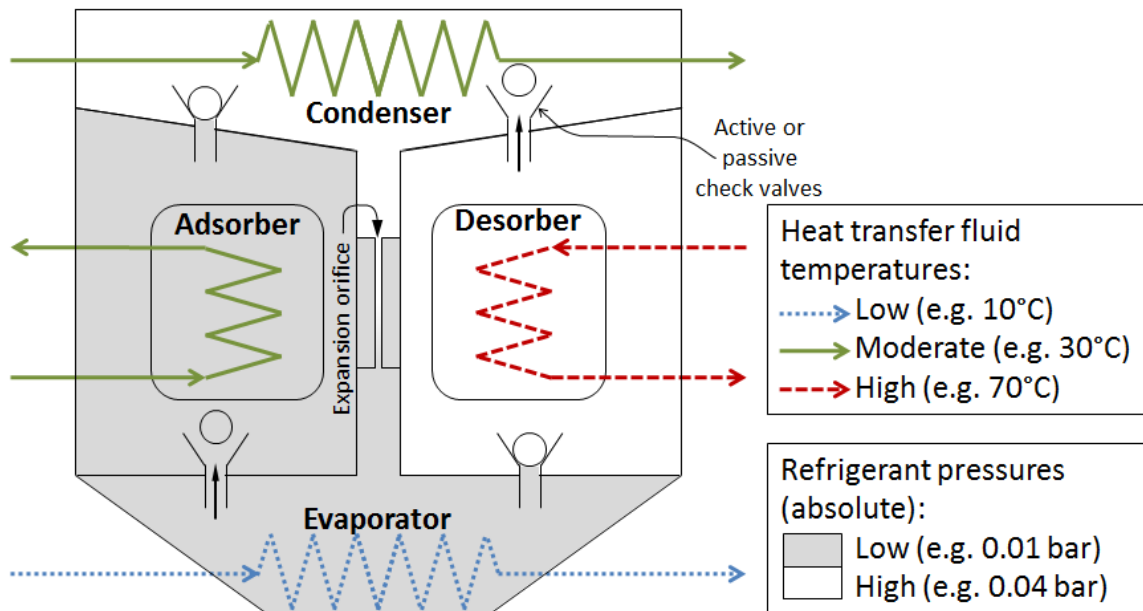


Figure 47: Illustration of a simple adsorption chiller

The necessity of periodically heating and cooling the adsorber heat exchangers and associated piping accounts for the generally lower thermal COP of adsorption

systems compared with absorption systems, since heating this “dead mass” consumes driving heat (which is then rejected to the ambient in the next adsorption phase) without contributing additional cooling capacity. However, since no solution pump is required for an adsorption heat pump, the potential exists for improving the ECOP compared with absorption systems. Also, the wide variety of adsorbents available and in development, particularly a diversity of zeolites, hold much promise for enabling adsorption heat pumps to efficiently operate under a wide range of conditions, including utilizing much lower heat source temperatures than required by absorption systems.

In addition to the basic adsorption/desorption phase just described, heat recovery (HR) and pressure recovery (PR) phases can also be implemented in adsorption chillers.

The HR phase occurs at the end of ad/desorption, and involves transferring the HTF between adsorbers to pre-heat the cool adsorber and reduce the heat that must be added in the subsequent desorption phase. Generally HR improves COP while decreasing capacity, but very short durations of HR can improve capacity as long as the HR heat transfer [kW] in the new desorber exceeds the heat transfer that would take place at the beginning of normal desorption – this means having a higher HTF flow rate in HR than in normal desorption. HR requires provisions for the HTF to pass through the adsorbers directly, and possibly a dedicated HTF pump. In the beginning of HR, the process is isosteric with the evaporator and condenser isolated. If HR is effective enough to either (a) lower the new adsorber chamber pressure below the evaporator pressure and/or (b) raise the new desorber chamber pressure above the condenser pressure, then HR can proceed isobarically in either ad/desorber.

The PR phase occurs after the ad/desorption phase and before HR. It involves directly connecting the adsorber and desorber chambers to allow vapor to travel from the desorber to the adsorber. This effectively “pre-unloads” the desorber to accept more refrigerant in the next adsorption phase. The evaporator and condenser are isolated during PR. PR requires an actively actuated vapor valve that directly connects the adsorber chambers. It can have a very short duration (~2 seconds) to only allow the mass transfer of refrigerant already present as vapor in the chambers, or it can have a longer duration with continued heating and cooling of the de/adsorbers to approach an isobaric process. PR has the potential to increase capacity as long as the PR refrigerant mass transfer rate [kg/s] remains greater than the mass transfer rate that had been taking place at the end of normal desorption. It would normally be expected to increase COP if the HTF mass flow is zero during PR, but the effectiveness of PR is limited, especially when normal desorption is already relatively complete. Typically, due to faster kinetics at higher temperatures, adsorption machines are more adsorption-limited than desorption-limited, which means that PR typically has a small or negligible effect. But PR may have benefits under conditions where the cycle is desorption-limited.

4.2.2 Piping and instrumentation of prototype

Two process and instrumentation diagrams (P&ID) are shown Figure 48 and Figure 49. Figure 48 focuses on (and is very accurate about) the experimentally implemented HTF plumbing schematic, but does not show vapor lines or all instrumentation. It is also roughly correct in regard to the physical layout of the plumbing between the adsorber chambers. Figure 49 shows all instrumentation and vapor lines but does not have sufficient room to accurately or completely reflect the complete HTF

plumbing. It has no correspondence at all to physical layout. The evaporator chilled water (CHW) plumbing is an independent loop and is shown later.

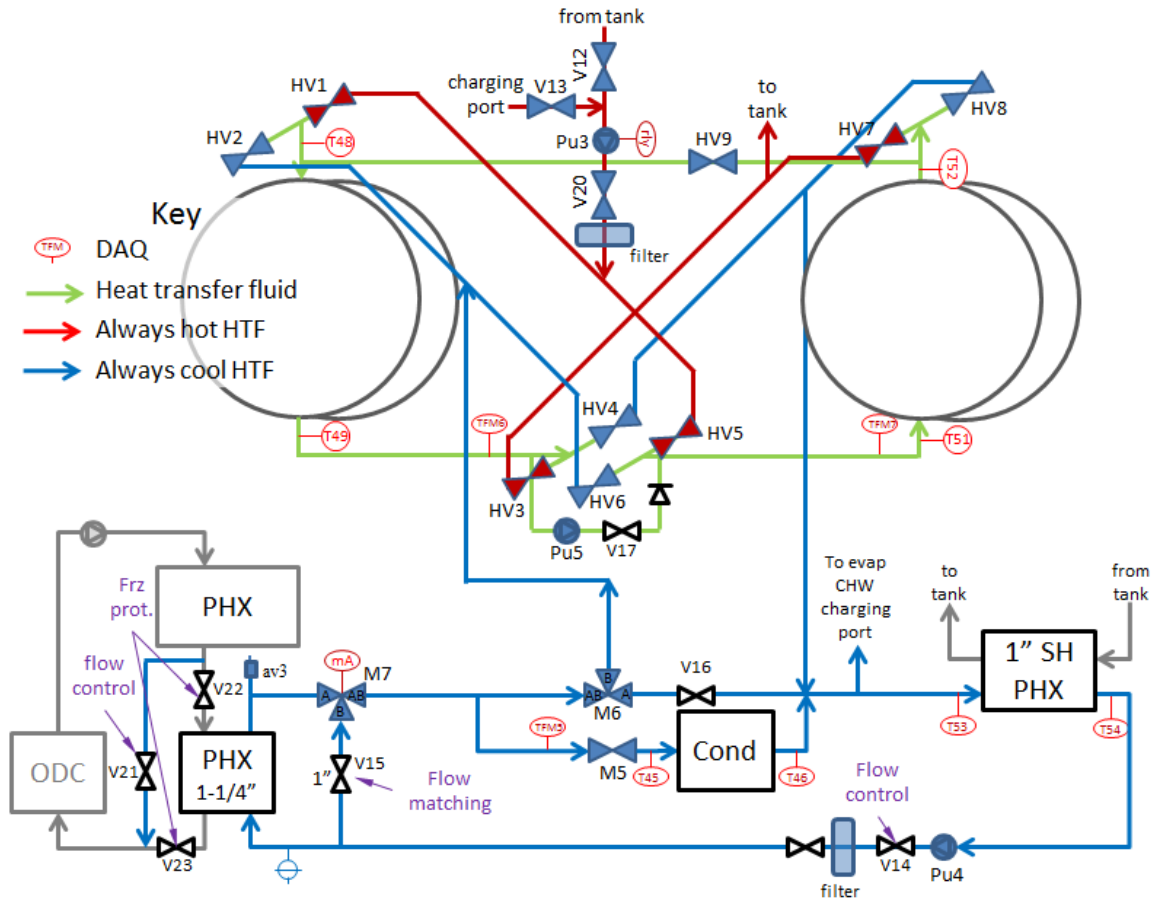


Figure 48: Process and instrumentation diagram focusing on HTF plumbing

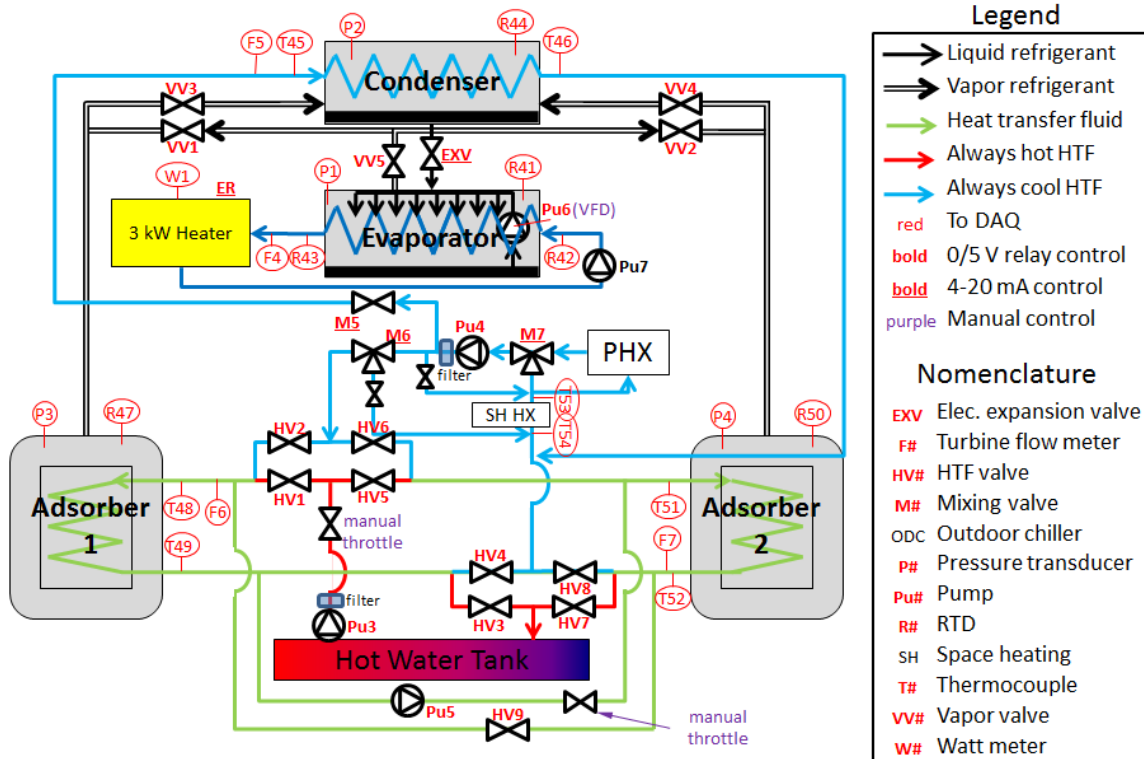


Figure 49: Process and instrumentation diagram focusing on instrumentation and vapor plumbing

The layout shown in Figure 48 and Figure 49 allows for temperature and flow control through all of the components, as described presently. Cooling water is provided to the condenser and adsorber via an outdoor chiller (ODC). Since the ODC loop using glycol, a plate heat exchanger (PHX) transfers heat from the adsorption system to the ODC. Cooling water temperature is PID-controlled via mixer “M7” (the condenser and adsorber are in parallel so their inlet temperatures are the same in this configuration). The condenser HTF flow rate is PID-controlled via 2-way mixer “M5”. The adsorber HTF flow rate is PID-controlled via the 3-way mixer “M6.” During periods with zero cooling HTF flow through either adsorber (such as the HR phase when HV2 and HV6 are closed), M6 remains fixed in its last location and M5 will generally close down slightly to maintain the same condenser HTF flow rate. The HR flow rate is manually controlled by

throttling valve “V17.” The hot HTF flow rate is manually controlled by throttling valve “V20.” All HTF valves (HV), vapor valves (VV) and pumps are relay actuated.

The evaporator CHW schematic is shown in Figure 50, and a schematic of the evaporator recirculated refrigerant (falling film) is shown in Figure 51.

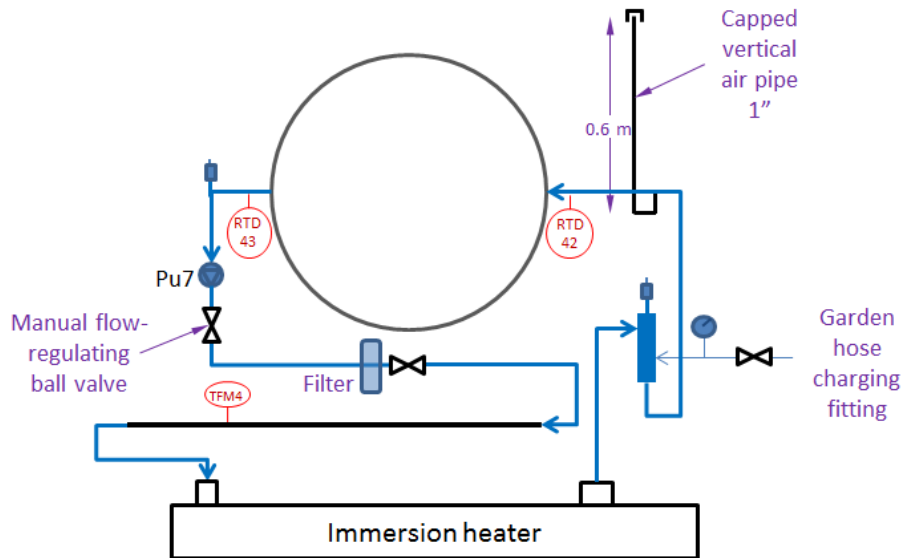


Figure 50: Chilled water schematic

In Figure 50 the flow rate of relay-actuated pump “Pu7” is regulated by a manual throttling valve. Temperature control of the CHW supply temperature (RTD 43) is achieved by three relay-actuated electrical heating elements inside the immersion heater. Water pressure is maintained on the CHW loop via a pressure regulator. Also included are an air separation chamber, two air vents, an expansion volume, and a particulate filter.

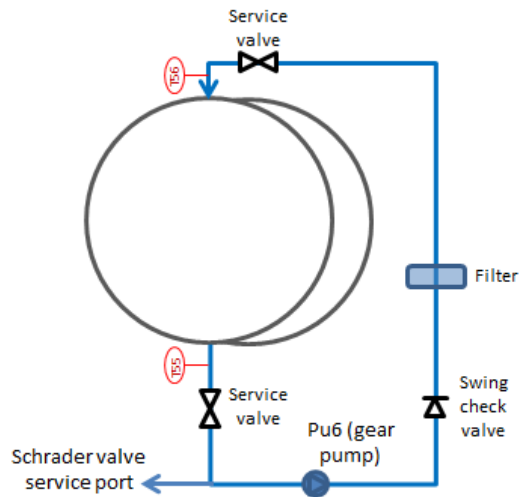


Figure 51: Recirculated refrigerant loop schematic

Challenges associated with the recirculated refrigerant loop are discussed in the section on chiller fabrication.

In conjunction with Figure 48 and Figure 42, Table 20 shows the valve setting for various service procedures and normal operation of the adsorption chiller.

Table 20: Valve settings for conducting various procedures on AHP

Code	Description	Normal operation	De-aerate PM loop	De-aerating tank	Draining tank	Deaerating AHP
Pump(s)			Tap	Tap	Pu1 on	Tap
V1	Tank Top Center	O	X	X	(either)	X
V2	Tank Upper	O	X	X	X	X
V3	Tank Lower Left	O	O	O	O	(any)
V4	Tank Lower Right	O	X	O	X	(any)
V5	Tank Bypass	X	O	O	O	(any)
V6	Pump Bypass	X	X	X	X	(any)
V7	Drain Bypass	X	O	X	O	X
V8	Fill Valve	O	O	O	X	O
V9	Air Vent	X	X	X/O with hose	O (air)	O (w/hose)
V11	Pump Throttle Valve	~half	X	~half	X	(any)
V12	AHP-tank isolation	(any)	X	(any)	(any)	X
V13	AHP charging port	(any)	Any	(any)	(any)	O (charging)
V14	Clg water flow ctrl	(any)	Any	(any)	(any)	O
V15	Flow matching (M7)	(any)	Any	(any)	(any)	X/O both
V16	Flow matching (M6)	(any)	Any	(any)	(any)	X/O both
V17	HR flow control	(any)	Any	(any)	(any)	X/O both
V18	Tap to tank or AHP	(any)	Manual	(any)	(any)	X
V19	Tap to CHW loop	(any)	Any	(any)	(any)	O
M1	Ecopower	ECO-PID	AB-A	(any)	AB-A	(any)
M2	Tank to Eco	OFF	AB-A	(any)	AB-A	(any)
M3	Tank to Plate HX	PID (SH)	AB-A	(any)	(any)	(any)
M4	Drain	PID (DHW)	X	X	X	X
M5	Cond. flow control	(any)	(any)	(any)	(any)	O
M6	Ads. flow control	(any)	(any)	(any)	(any)	Middle
M7	Heat rej. temp. cont.	(any)	(any)	(any)	(any)	Middle
Open HV	HTF valves to open	(any)	(any)	(any)	(any)	service setting
Close HV	HTF valves to close	(any)	(any)	(any)	(any)	service setting
av1, 2	Air vents	1-op, 2-cl	1-op, 2-op	1-op, 2-op	1-op, 2-cl	(any)

4.2.3 Sizing of adsorption chiller components – equilibrium thermodynamic model

The initial design process for the chiller was published in Gluesenkamp (2011c) in a way that could be adopted by others. The design process included the use of an equilibrium adsorption model (described in Chapter 6) to size the heat exchangers and determine the required vapor transfer tube diameter. The overall cost of the system was sensitive to this diameter since large electronically actuated ball valves scale dramatically with size.

Based on the COP and SCP predicted by the model, the required capacity [kW] of each heat exchanger was known.

The evaporator and condenser were designed based on heat transfer correlations. An adsorption system condenser needs to reject about the same heat as the evaporator absorbs. A general rule of thumb would be to design the condenser to maintain less than a 5°C temperature difference between the condensation temperature of refrigerant and the ambient temperature. This temperature difference is composed of three individual differences, as shown in Figure 52. Thus, the difference between tube surface and refrigerant saturation temperature should be around 2°C. Equation (29), a correlation for condensation on horizontal tubes was used (Incropera, 2007) to plot this difference as a function of tube length and diameter, as shown in Figure 53.

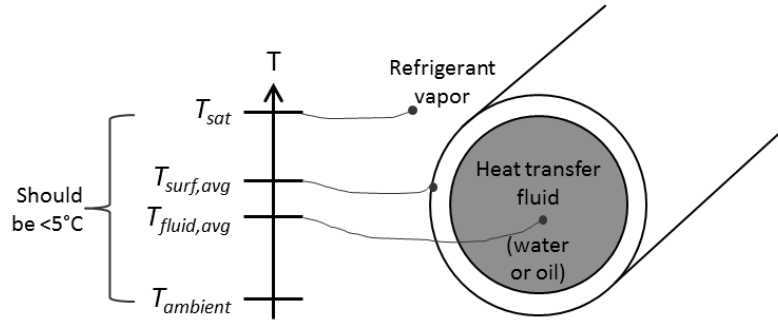


Figure 52: Illustration of temperatures associated with condenser

$$\bar{h}_D = C \left[\frac{g \rho_l (\rho_l - \rho_v) k_l^3 h'_{fg}}{\mu (T_{sat} - T_{surf}) D} \right]^{1/4} \quad (29)$$

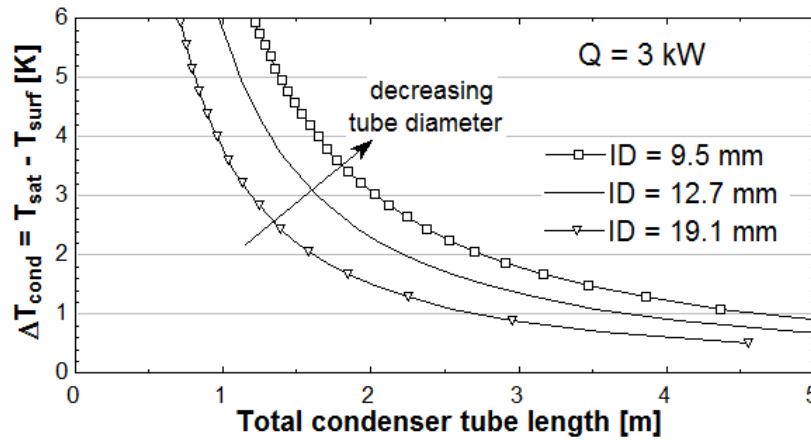


Figure 53: Relationship among condenser tube diameter, tube length, and ΔT_{cond}

The falling film evaporator design followed a similar procedure: select a geometry and use heat transfer correlations to calculate the required tubing length for a desired approach temperature. According to the system specifications, the evaporator should handle 3 kW. Falling film evaporation correlations were found in (Thome, 2009).

Thome (2009) defines Equation (30) as a general form for falling film heat transfer coefficient (HTC).

$$\alpha_{ff} = K_{ff} \alpha_{npb} \quad (30)$$

where α_{ff} is the falling film HTC, α_{npb} is the HTC for non-falling film nucleate pool boiling, and K_{ff} is a correction factor. K_{ff} , in turn, is given by Roques and Thome (2007) as an empirical function (derived from R134a data). It is dependent on vertical tube pitch (L_{vp}) compared with a reference value ($L_{vp,ref}$) and the heat flux (q) compared with the heat flux at onset of dryout for nucleate boiling (q_{DNB}), as shown in Equation (31).

$$K_{ff} = \left(1 + b_1 \frac{L_{vp}}{L_{vp,ref}} \right) \left[b_2 + \left(b_3 \frac{q}{q_{DNB}} \right) + b_4 \left(\frac{q}{q_{DNB}} \right)^2 \right] \quad (31)$$

Thus evaluation of α_{ff} requires using correlations for α_{npb} and q_{DNB} , in addition to an empirical correlation for K_{ff} . All three of these correlations may have dependence on fluid and reduced pressure.

Data specific to water at very low reduced pressures is very scarce. Thus a number of combinations were evaluated and some empirical guidelines from Power Partners Inc. were taken into consideration. The only correlation for K_{ff} found is the one shown in Equation (31). A correlation from Kutateladze (1948), shown in Equation (32), was used for q_{DNB} .

$$q_{DNB} = 0.131 \rho^{1/2} h_{fg} \left[g (\rho_l - \rho_g) \sigma \right]^{1/4} \quad (32)$$

Several correlations for α_{npb} were used, as shown in Table 21.

Table 21: Correlations for nucleate pool boiling heat transfer

Author	Year	Working fluid(s)	Water-specific coefficients?	Evaporator condition within correlation limits?	See Eqn #
Mostinski	1963	all	no	no	(33)
Cooper	1984	all	no	no	(34)
Gorenflo	1993	various	no	no	(35)
Gorenflo	1993	water	yes	no	(36)

$$\alpha_{npb} = 0.00417q^{0.7}P_{crit}^{0.69} \left(1.8P_r^{0.17} + 4P_r^{1.2} + 10P_r^{10}\right) \quad (33)$$

For Equation (33), α_{npb} is in [$\text{Wm}^{-2}\text{K}^{-1}$], q is in [W/m^2] and P_{crit} is in [kPa].

$$\alpha_{npb} = 55P_r^{0.12-0.4343\ln(R_p)} \left(-0.4343\ln(P_r)\right)^{-0.55} M^{-0.5} q^{0.67} \quad (34)$$

For Equation (34), α_{npb} is in [$\text{Wm}^{-2}\text{K}^{-1}$], q is in [W/m^2], M is the molecular weight of the fluid, R_p is the surface roughness in [μm]. The range of applicability is for reduced pressures from 0.001 to 0.9.

$$\alpha_{npb} = \alpha_0 \left(1.2P_r^{0.27} + 2.5P_r + \frac{P_r}{1-P_r}\right) \left(\frac{q}{q_0}\right)^{0.9-0.3P_r^{0.3}} \left(\frac{R_p}{R_{p0}}\right)^{0.133} \quad (35)$$

For Equation (35), α_{npb} is in [$\text{Wm}^{-2}\text{K}^{-1}$], $\alpha_0 = 5600$ [W/m^2] for water, q is in [W/m^2], $q_0 = 20,000$ [W/m^2], R_p is the surface roughness in μm , and $R_{p0} = 0.4$ [μm].

$$\alpha_{npb} = \alpha_0 \left(1.73P_r^{0.27} + \left(6.1 + \frac{0.68}{1-P_r}\right)P_r^2\right) \left(\frac{q}{q_0}\right)^{0.9-0.3P_r^{0.15}} \left(\frac{R_p}{R_{p0}}\right)^{0.133} \quad (36)$$

Equation (36) is a form of Equation (35) which has been modified specifically for water. It is applicable to the reduced pressure range of 5×10^{-4} to 0.95. The reduced pressure in the evaporator is about an order of magnitude lower than this minimum, about 5×10^{-5} .

Figure 54 shows four calculations for falling film HTC (α_{ff}). All make use of Thome's Equation (30) for the general form, Roques and Thome's Equation (31) for K_{ff} , and Kutateladze's Equation (32) for q_{DNB} . The four calculations differ in the correlation used for α_{npb} . None of the four correlations for α_{npb} was explicitly valid at the very low reduced pressure (P_r) of the evaporator (with $P_r \approx 5 \times 10^{-5}$). Gorenflo's water-specific correlation (blue line in Figure 54) was the most specific, the closest to being valid at the

evaporator conditions, and the most highly recommended. However, it was also the least conservative. Therefore, the evaporator tube area was designed based on the more conservative calculations. Since the falling film flow rate turned out to be smaller than hoped for, this conservative approach turned out well.

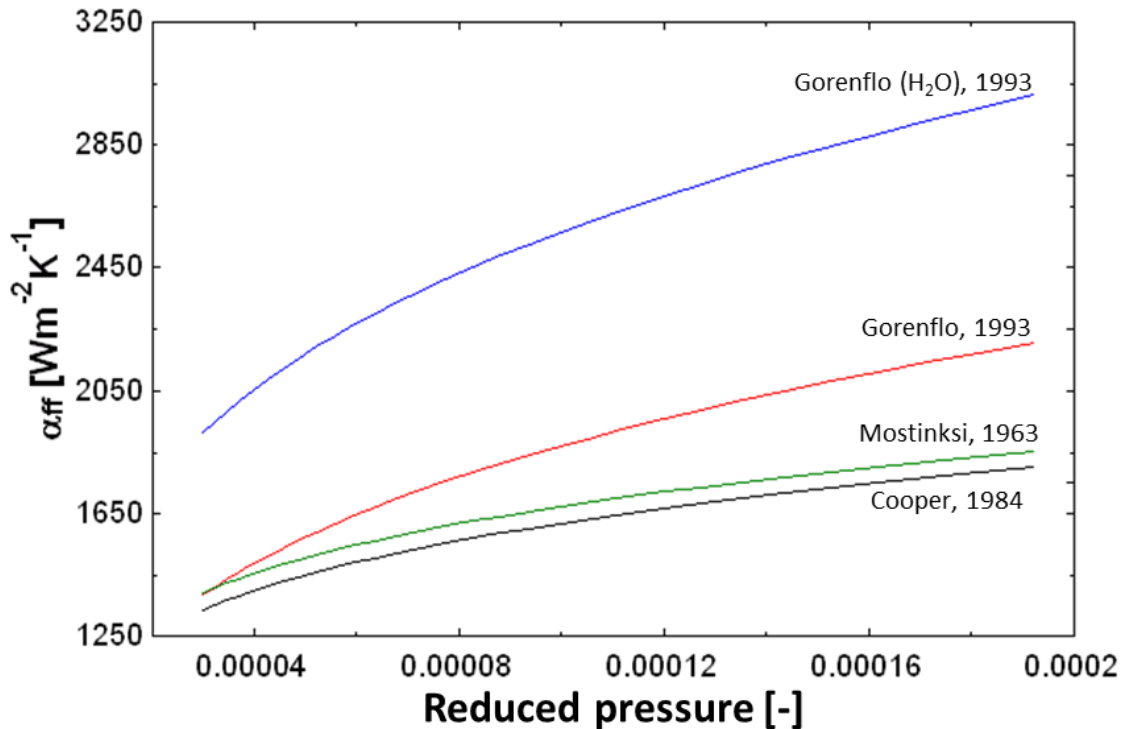


Figure 54: Correlations for falling film heat transfer coefficient

For any water-refrigerant-based system, vapor transfer plays an important role due to the extremely low density of water vapor at typical evaporator and condenser temperatures, and the resulting sensitivity of the saturation temperature to small pressure drops, even on the order of millimeters of water column. This issue has been successfully addressed in water/LiBr absorption chillers by integrated packaging of the components between which vapor must travel (absorber/evaporator and desorber/condenser). However, packaging components in a common vacuum vessel is not possible for

adsorption machines due to the necessity of switching: the vapor must pass through some type of valve from the evaporator to adsorber and from the desorber to condenser.

Some adsorption designs utilize large passive one-way valves. However, in the interest of operational flexibility for research purposes, electronically actuated valves are desirable. Furthermore, given packaging and tube fitting considerations there will be some length of tubing between the valve and the components (reservoirs) on either side. Thus a study was conducted on the vapor line pressure drop as a function of valve diameter, tube diameter, and tube length. Strictly speaking, the loss coefficients are based on the assumption of fully developed flow, so will be less accurate in this case (since the flow is not fully developed everywhere). However, this analysis should still yield order-of-magnitude results sufficient for tubing and valve selection. Figure 55 shows the sources of pressure drop in a vapor transfer line, and Figure 56 and Figure 57 show the resulting pressure drop as a function of valve and tube diameter. Tube length is not varied since, within a reasonable range, it was found to have a much smaller effect than valve and tube diameters.

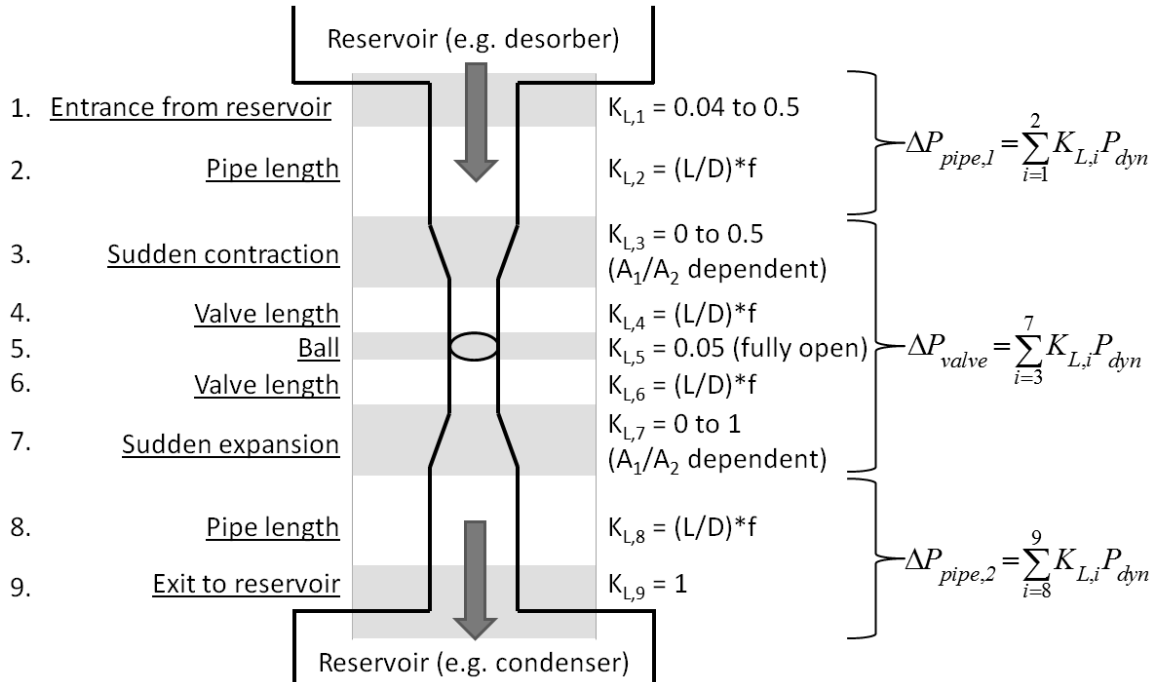


Figure 55: Illustration of 9 components of pressure drop between two reservoirs, grouped into ΔP_{pipe} and ΔP_{valve}

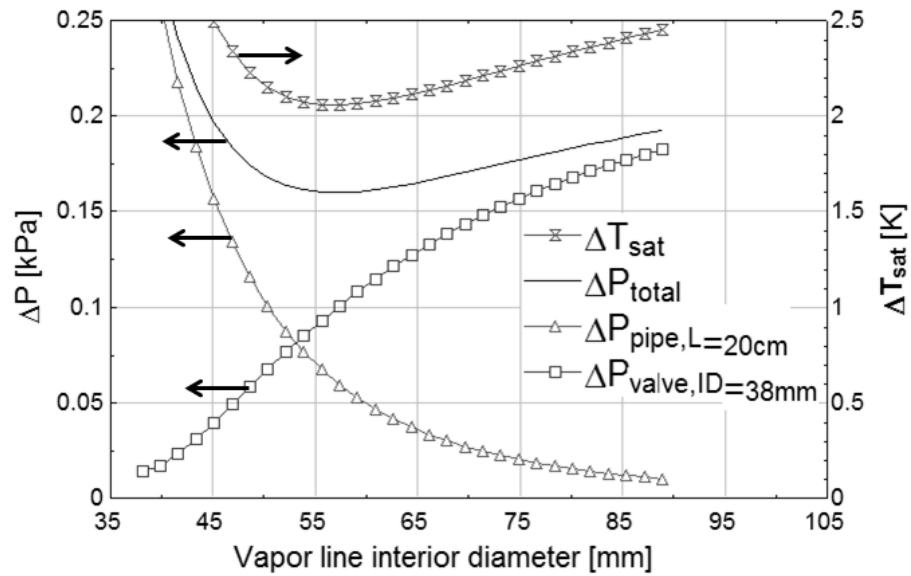


Figure 56: Effect of pipe diameter on ΔP and ΔT_{sat} (38 mm valve ID)

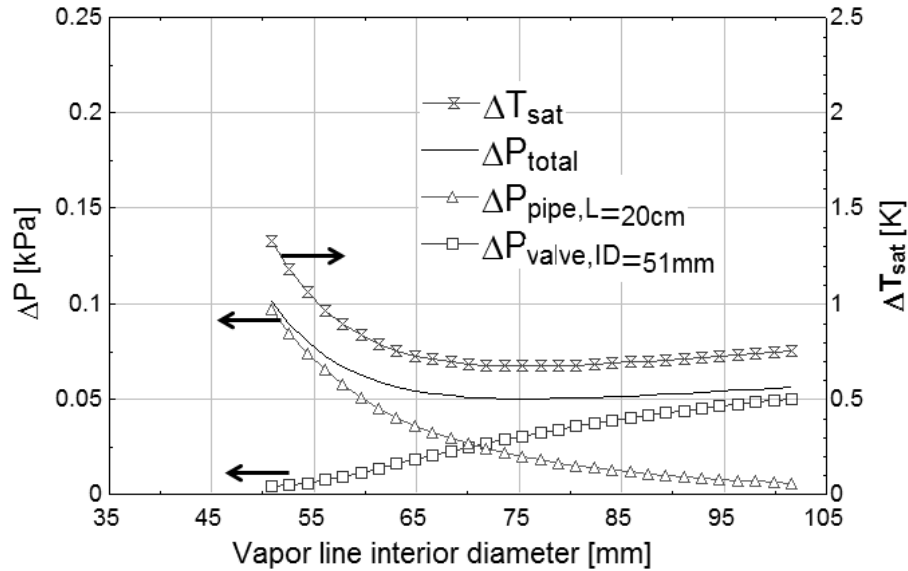


Figure 57: Effect of pipe diameter on ΔP and ΔT_{sat} (51 mm valve ID)

From Figure 56 and Figure 57, for a given valve diameter, there is an optimal tube diameter. Above this optimum, the pressure drops associated with sudden contraction and expansion around the valve outweigh the lower pressure drop associated with the tube.

The equilibrium model will be discussed in more detail in Chapter 6. For now, the results for pressure drop are shown in Figure 58, in which the sensitivity of system-level performance to pressure drop in the vapor lines was explored for fixed T_{src} and T_{CHW} . The effects of vapor pressure drop are to reduce COP and to reduce the feasible operating conditions. By inspection of Figure 58, an example of the latter effect is that, with a 0.2 kPa pressure drop, the maximum feasible heat rejection temperature is about 32.5°C; whereas for a 0.5 kPa pressure drop, the maximum feasible is only about 27.5°C. In other words, minimizing pressure drop will allow the system to operate up to higher ambient conditions. Minimizing pressure drop also allows lower evaporator and heat source temperatures to be achieved, although these results are not shown here.

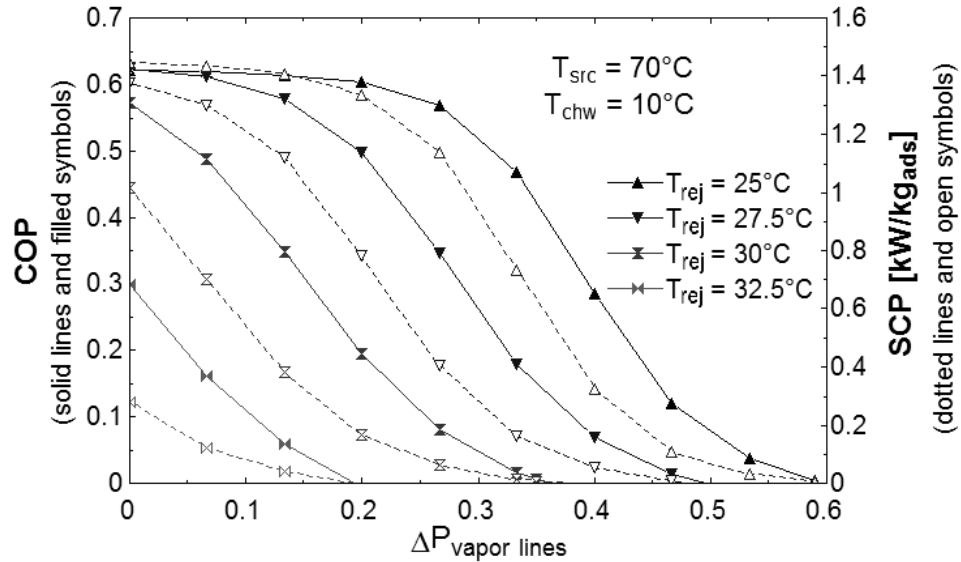


Figure 58: Effect of ΔP on COP (solid lines) and SCP (dotted lines) at various heat rejection temperatures

A vapor pressure drop of less than 0.1 kPa was set as a design target, and the necessary valve size was determined to be 51 mm ID for a system of 3 kW cooling capacity.

4.2.4 Fabrication of adsorption chiller

A photograph of the prototype chiller is shown in Figure 59, where the four vacuum chambers can be seen, each with a Lexan front cover. The condenser is in the top-most chamber, and the evaporator in the lowest. The other two chambers house the adsorber heat exchangers. The chambers are connected by 5.1 cm (2 inch) diameter electronically actuated ball valves and insulated 6.4 cm (2.5 inch) diameter copper tube. Later, not shown in Figure 59, insulation was added to the adsorber chambers and to the flanges and front of the condenser and evaporator.



Figure 59: Prototype adsorption chiller near final configuration

Additional basic specifications of the adsorption chiller are listed in Table 22.

Table 22: Specifications of adsorption chiller

Nominal cooling capacity	2 kW
Number of adsorber HXs	2
Working pair (refrigerant/adsorbent)	water/zeolite
Adsorber HX finned-volume dimensions (excludes headers and u-tubes)	600 x 264 x 102 mm
Calculated adsorbent mass (per HX)	2.82 kg
Adsorbent substrate area (per HX)	16.7 m ²
Charge of HTF (per HX, excl. headers)	2.47 L
Nominal driving temperature	70°C
Heat transfer fluid (HTF) type	water
Refrigerant falling film flow rate	60 – 70 g/s
Refrigerant flow rate through EXV	0.2 – 1.0 g/s
CHW flow rate	60 – 100 g/s
HTF flow rate – condenser	90 – 180 g/s
HTF flow rate – adsorber cooling	180 g/s
HTF flow rate – adsorber heating	90 – 180 g/s
HTF flow rate – heat recovery	240 – 260 g/s
HTF flow channels and feedthroughs	20.0 mm ID steel/copper/PEX
HTF ball valves	19.1 mm ID stainless steel
CHW lines	19.1 mm ID PVC
Refrigerant vapor feedthroughs	63.5 mm ID steel
Refrigerant vapor flow channels	50.8 mm ID steel/copper
Refrigerant vapor ball valves	50.8 mm ID brass
Vacuum chamber interior volume (empty)	52 – 61 L (various lengths)
Condenser tube surface area	0.0016 m ²
Evaporator tube surface area	0.0023 m ²

The adsorber heat exchangers (Figure 60 and Figure 61) were obtained through a donation from Mitsubishi Plastic. They are copper tube and aluminum plain fin type with 12 parallel four-pass circuits and a 0.25 mm thickness coating of Z01 zeolite on all fin and tube surfaces. Headers are 25.4 mm in outer diameter. Additional data are provided in Table 22, Figure 167, Figure 169 and surrounding text.



Figure 60: Adsorber heat exchanger used in prototype chiller

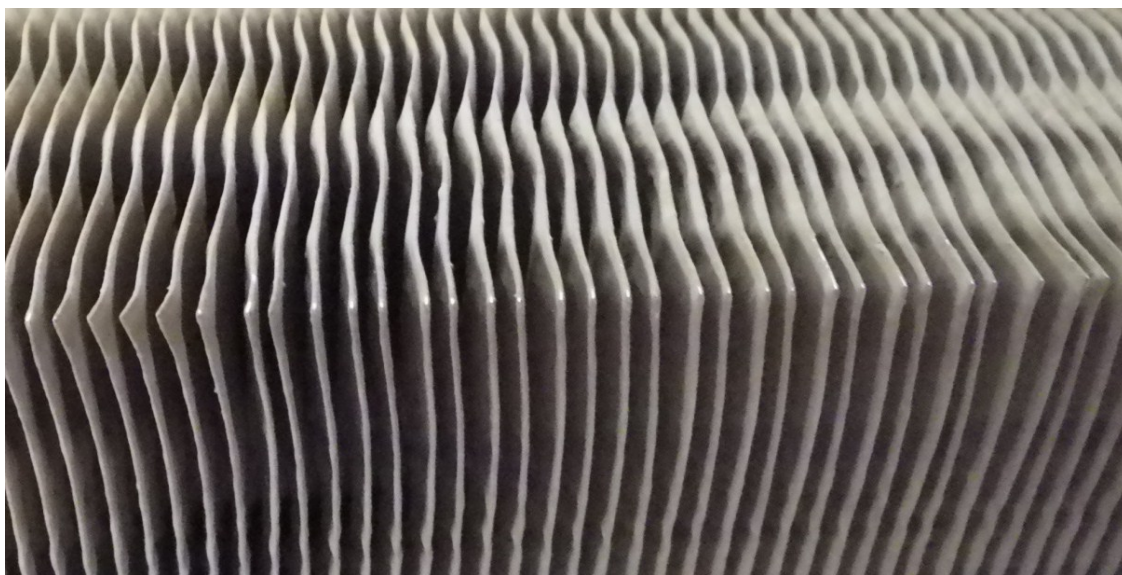


Figure 61: Close-up of adsorber heat exchanger coated fins
1.8 mm fin spacing, 0.115 mm fin thickness, 0.25 mm zeolite coating thickness

Each of the adsorbers, condenser and evaporator were housed in its own carbon steel cylindrical vacuum chamber. A steel flange on one side of each chamber supported

a 1 inch thick plate of Lexan to enable viewing of the heat exchangers during chiller operation.

The vacuum chambers were designed around the manufacturing abilities and limitations of Power Partners, Inc (PPI) in Georgia, USA, a manufacturer of large water/silica gel adsorption chillers. A CAD drawing (Figure 62) was developed and PPI carried out the welding and fabrication of the chambers with feedthroughs and painting of the chamber exteriors (see Figure 63).

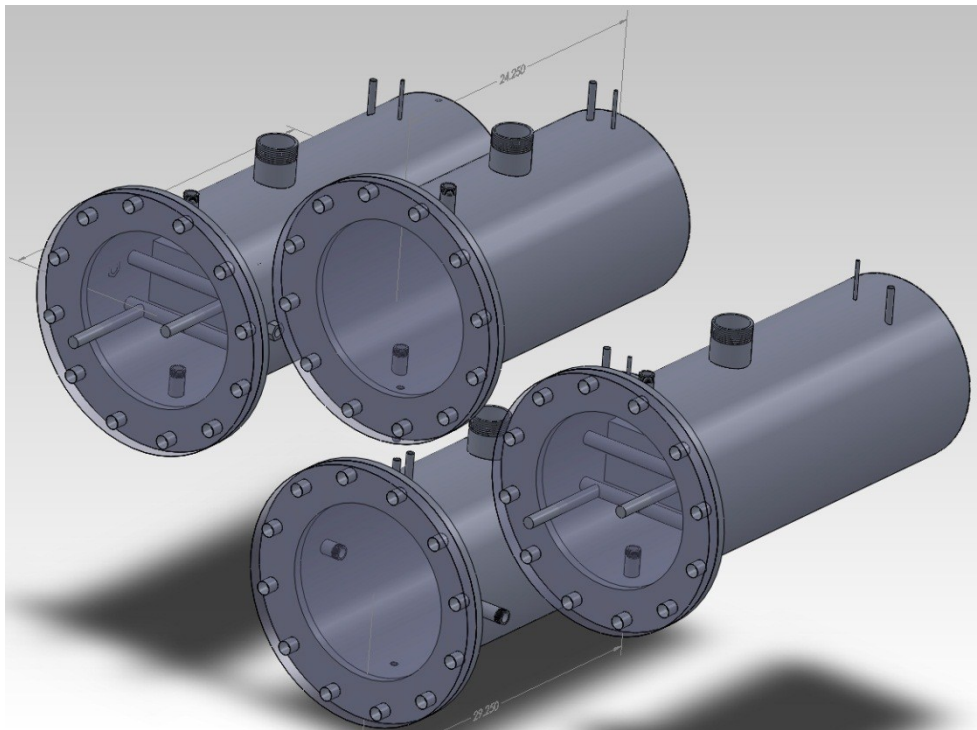


Figure 62: CAD drawing of vacuum chambers with flanges and locations of feedthroughs



Figure 63: Two vacuum chambers as received from PPI

An aluminum frame was constructed (Figure 64) and the chambers were mounted into the frame for plumbing (Figure 65) according to the P&ID design.



Figure 64: Chiller aluminum frame with one chamber and adsorber



Figure 65: Vacuum chambers ready for heat exchanger installation, plumbing and instrumentation

The condenser was soldered together with 22.23 mm OD copper pipe and fittings. The tubes were placed horizontally so that refrigerant dripping off would fall directly to the chamber bottom. Figure 66 shows the 22.23 mm OD plumbing that connects an adsorber and a condenser to their chamber feedthroughs before installation of the Lexan cover.

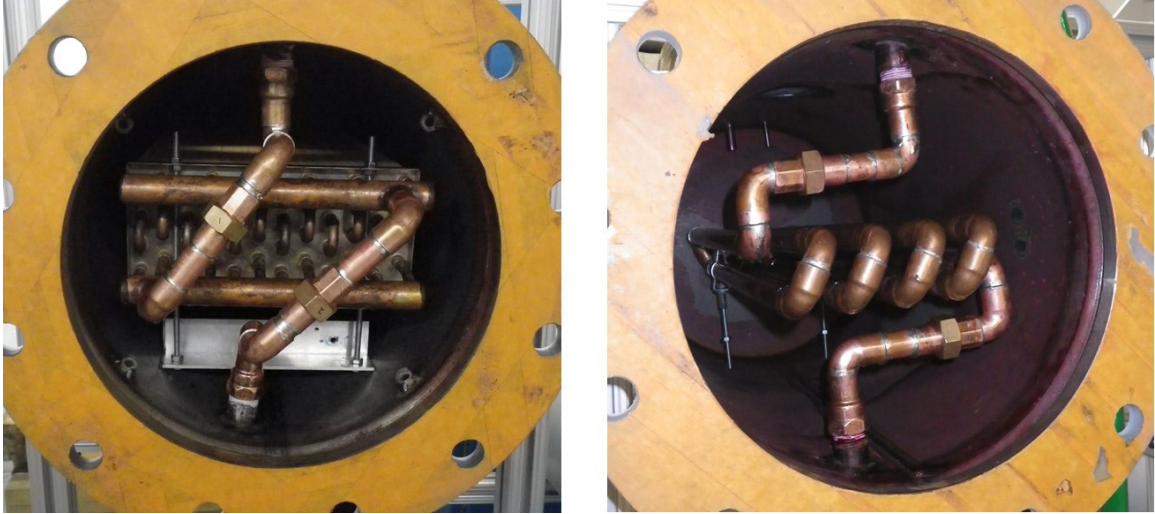


Figure 66: Adsorber heat exchanger (left) and condenser (right) plumbed to chamber feedthroughs

The evaporator, shown in Figure 67, was also soldered together with 22.23 mm OD copper pipe and fittings. The horizontal tubes were stacked vertically in two columns and carefully leveled so that the refrigerant falling film would fall from one tube onto the next. The CHW flowed on the inside and refrigerant flowed around the outside.



Figure 67: Falling film evaporator plumbed to chamber feedthroughs

The falling film distributor (shown schematically previously in Figure 51) is shown in operation in Figure 68 and Figure 69. Distribution of the falling film was implemented with a combination of an orifice tube (the copper tube with many small orifices shown in the top of Figure 68) to ensure even longitudinal distribution, and vee-shaped aluminum distributor trays that ensured the orifice jets landed on the middle of the first tube in the evaporator.



Figure 68: Falling film distributor in operation, close up



Figure 69: Falling film distributor in operation, zoomed out

An unexpected result for the falling film evaporator was that the wettability of the copper tubes increased over time, apparently as iron oxide corrosion built up on the copper tube surfaces. Initially, despite attempts to carefully sand the copper surfaces and

then clean them with acetone, the surface was highly hydrophobic, with refrigerant forming beads. The initial COP and capacity figures during this time were roughly one-fifth of their eventual values. As corrosion built up on the tubes, the wetted surface fraction increased dramatically, and the system COP and capacity increased. Compare the initial wettability (Figure 70) to the later wettability (Figure 68).



Figure 70: Initial wettability of sanded and solvent-cleaned copper tubes

The recirculated refrigerant loop (Figure 51) was a challenge due to pump net positive suction head (NPSH) requirements, and the need for a vacuum-tight hermetic pump. The available NPSH was about 0.6 m (2 feet) of water column, since the liquid refrigerant pool in the evaporator was near saturation and the pump was located 0.6 m below the liquid surface. No pump was found that was manufacturer-rated for required NPSH under such low absolute pressure conditions. A magnetically-coupled, inverter-driven gear pump was chosen due to its known hermetic design and its pre-existing availability in the lab. A much less expensive alternative would need to be sourced to manufacture a cost effective adsorption chiller.

Due to the extremely low available NPSH, the particulate filter had to be placed on the discharge side of the pump. A check valve was added to avoid backwashing of trapped particulates during pump shutoff. Due to the carbon steel vacuum chamber construction and inevitable air contamination of the chamber during periods of system shutdown, iron oxide particulates formed readily in the chamber. These particulates continually clogged the filter. The evolution of filters used is shown in Figure 71. The initial filter was a 60 micron sintered type. This clogged within less than an hour of operation, and fibers deposited by paper towels used to clean the chamber are visible. Next a 90 micron sintered filter was tried, but this only lasted for a few hours before the maximum pump head was exceeded. The 3rd and 4th filters shown are clogged and new 140 micron screens, respectively. These would last for a few tens of hours. Eventually a 230 micron screen was used, which enabled extended testing, with as-yet undetermined effects on the gear teeth of the pump.

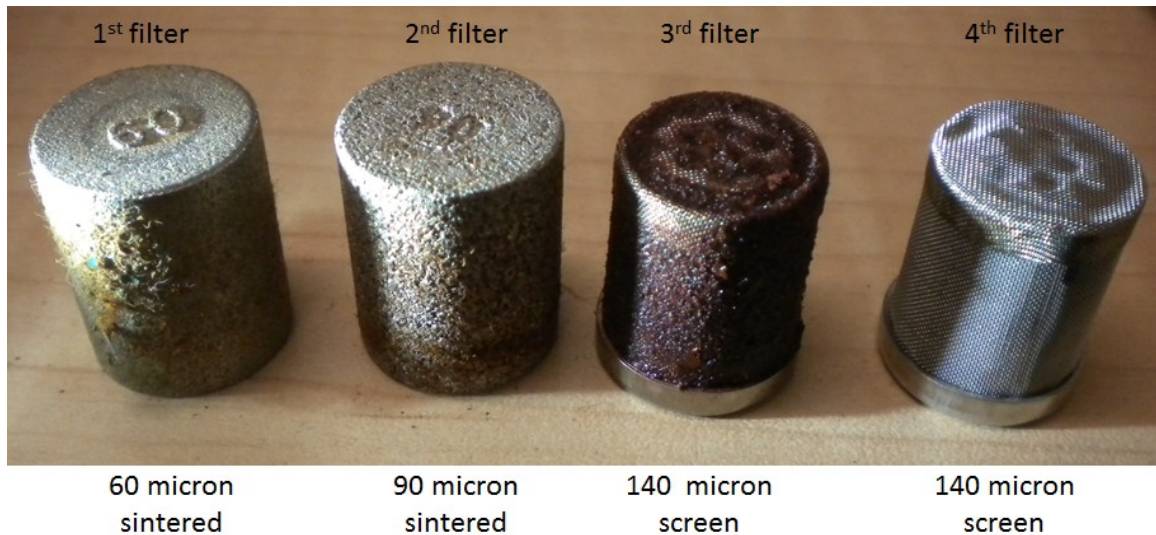


Figure 71: Filters used in refrigerant recirculation line

A 230 micron screen was also added to the inlet (not shown in Figure 51), along with a strong magnet to capture ferrous particles, as shown in Figure 72. However, proper

operation of this screen required that it be fully submerged in liquid. The screen also reduced the available NPSH and was eventually removed.



Figure 72: Inlet screen (230 micron) and magnet for refrigerant recirculation line

4.2.5 Integration of adsorption chiller into CCHP test facility

With regard to mass flows, the chiller is basically self-contained, except for connections for hot water supply/return and cooling water supply/return.

The chiller gets hot HTF from the top of the stratified buffer tank and returns it to the middle of the tank, as can be seen from Figure 42 (see arrows labeled “to adsorption chiller” and “from adsorption chiller”). A dedicated pump (see pump labeled “Pu3” in Figure 48) delivers this hot HTF to the chiller.

In general, it would be possible to either supply hot HTF directly from the prime mover, or via the tank. In this case, a tank-supplied HTF method was chosen. This allowed the chiller to run independently of the engine, simplified trigeneration system control strategy, and simplified flow and temperature controls. It was made possible by

using a stratified buffer tank – a fully mixed tank would not work in this configuration since the return temperature to the prime mover would become too high.

The cooling water is supplied via a plate heat exchanger, and eventually is dumped to the outdoor chiller (see Figure 48).

4.3 Residential load profiles

For the dynamic test facility, thermal load profiles were identified. The thermal load profile consists of domestic hot water (DHW) and space heating (SH) or cooling. This section discusses the DHW and SH loads used for CHP testing (without cooling). The cooling load profiles will be discussed later, in Section 5.5.

Two realistic residential profiles were used to get accurate data for model validation. A synthetic commercial load profile was invented to gauge the performance under more extreme duty cycle. Three additional load profiles were devised in order to interrogate the control strategy of the unit. These six load profiles are detailed in Table 23.

Table 23: Load profiles summary

	Profile name	DHW source	DHW timestep [min]	SH source	SH timestep [min]	Profile duration [hrs]/[days]
1	Residential shoulder season	Annex 42 300 L/day	1	Mueller, 2009	10	168 / 7
2	Residential summer season (no cooling)	Annex 42 300 L/day	1	Mueller, 2009	10	168 / 7
3	Synthetic commercial	max rate until depletion, for 6-10am and 4-8pm	1	15 kW until depletion, for 6-10am and 4-8pm	10	336 / 14
4	Synthetic ramp down	(N/A)	(N/A)	13 - 0 kW (linear ramp)	10	78 / 3.25
5	Synthetic ramp up	(N/A)	(N/A)	0 - 15 kW (linear ramp)	10	90 / 3.75
6	No loads	(N/A)	(N/A)	(N/A)	(N/A)	168 / 7
7	Residential summer season (with chiller)	Annex 42 300 L/day	1	(See section 5.5 for description of cooling load profile)		120 / 5

The first three of these load profiles had space heating and domestic hot water loads. The profiles are shown in Figure 73 to Figure 76. The origin of the space heating and domestic hot water profiles is described in the sections below.

A week of residential winter season was not tested due to the lack of a backup boiler in the experimental facility.

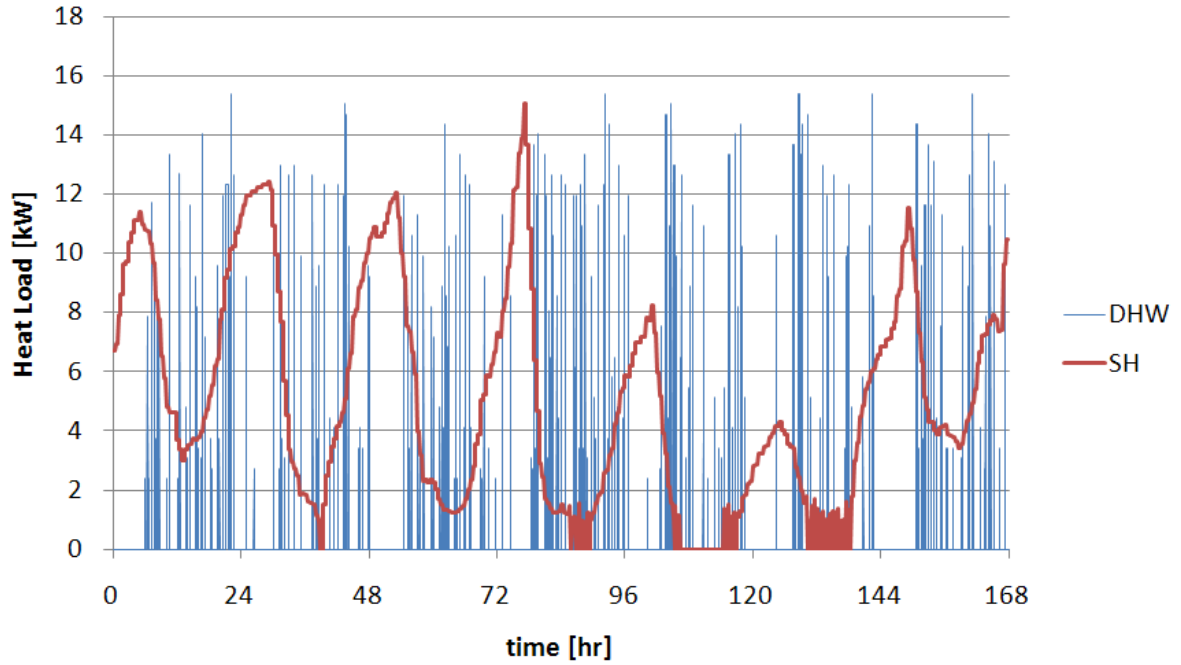


Figure 73: Residential shoulder season load profile

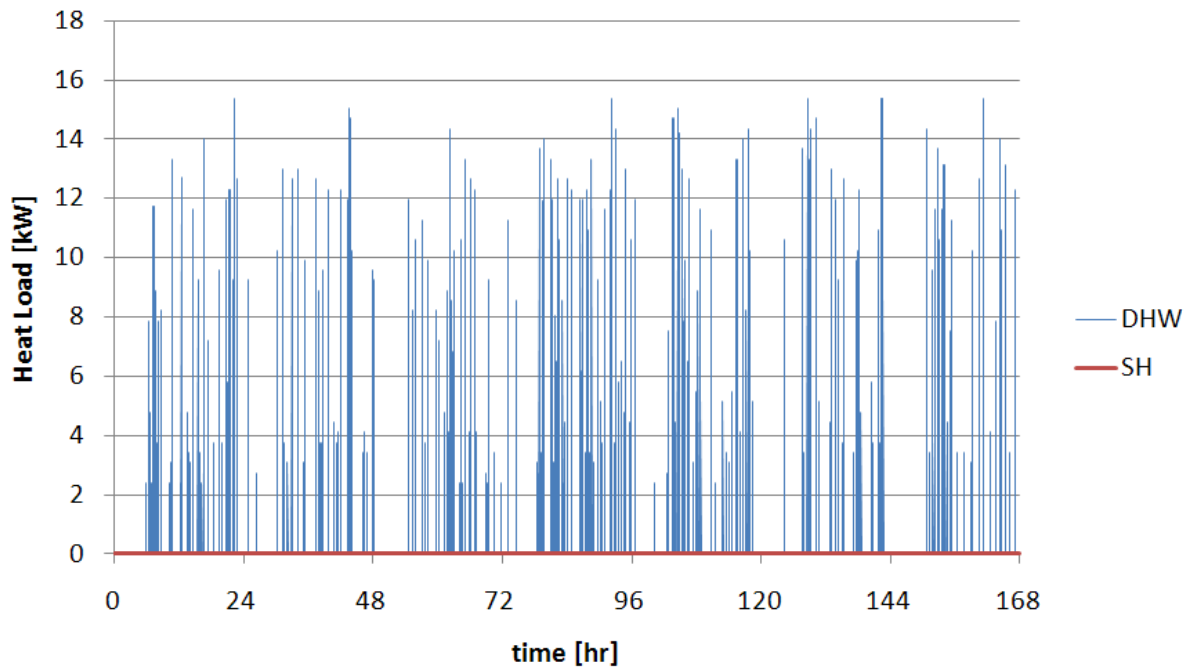


Figure 74: Residential summer season (DHW-only) load profile

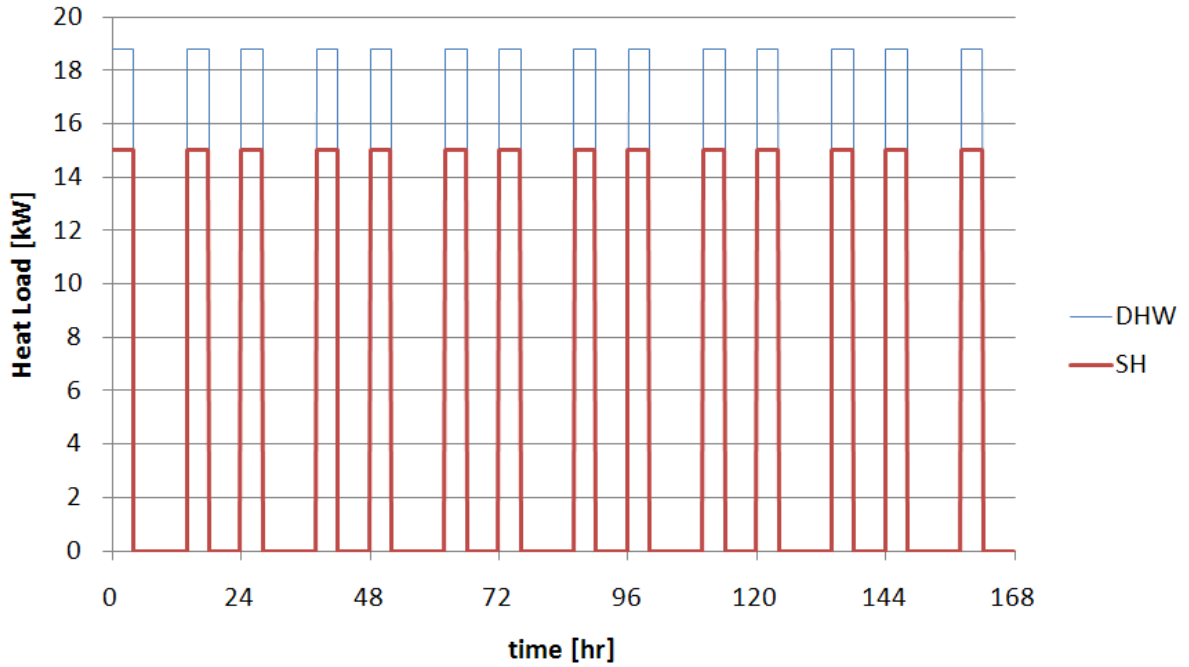


Figure 75: Synthetic commercial load profile

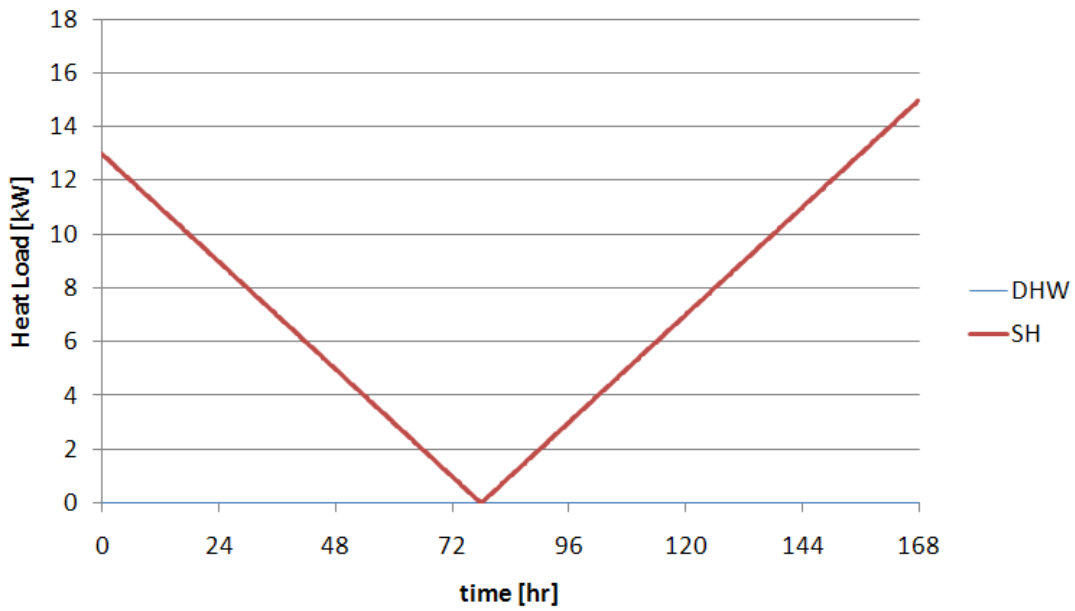


Figure 76: Synthetic ramp-down and ramp-up profiles

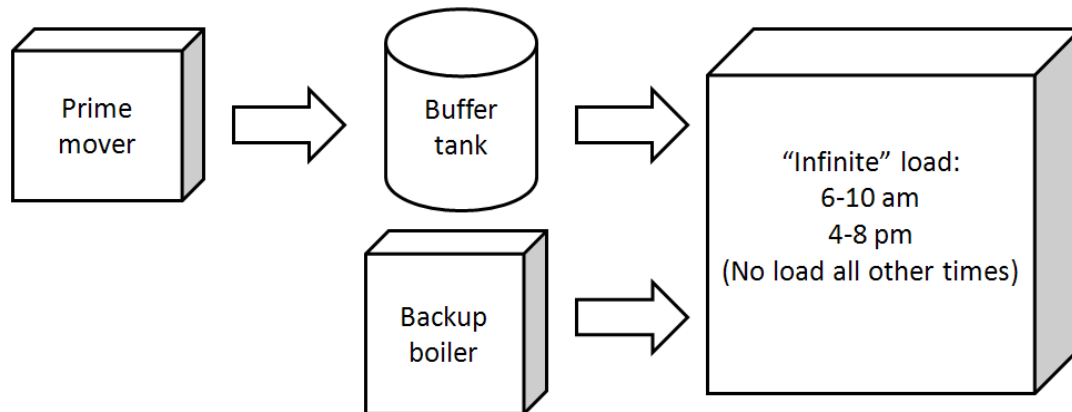


Figure 77: System assumed for developing commercial load profile

As shown in Figure 77, the commercial load profile was developed by assuming that the prime mover were installed as supplementary heat input for some process that required more heating capacity than the prime mover can deliver during two 4-hour blocks of time each day. Any load not met by the prime mover and buffer tank would be handled by a backup system. Once the tank output temperature drops below some critical value ($\sim 60^{\circ}\text{C}$), the tank output is stopped and the tank is allowed to be recharged by the prime mover until some critical state of charge ($\sim 30\%$ recharge) is reached. The tank is then drawn off again, and this continues until the end of the 4-hour block, when all loads cease.

4.3.1 Space heating

The space heating profile for the residential shoulder season was generated using the building model developed in TRNBuild by Mueller, 2009. The modeled building was a “typical US home:” a two-story residence of approximately 230 m^2 (2,500 square feet). The values used for insulation and building envelope were based on construction methods typical for the US in the 1990s. The weather profile imposed on the building was from

the TMY2 database (National Solar Radiation Database, 2010) for Sterling, VA (near Washington, DC).

The space heating load was calculated from the building model by assuming an “infinitely variable capacity” HVAC system, so that cycling of the HVAC system did not occur. One-minute timesteps were used in the simulation, although the weather input to the building model had hourly timesteps. The minutely data generated by the model was reduced to 10-minute timesteps for the experimental profiles.

From the full year of simulated space heating load made available by the model, a qualitatively “typical” week from the spring season was selected as the basis of the shoulder season experimental profile. (A “typical” week from the summer season had space cooling load and no space heating load). This week-long load profile was stored as a vector with 1680 values (one for the space heating load for each six minute interval in the week). Every six minutes the PID controller in LabVIEW adjusted the experimental space heating flow to match the setpoint value specified in the space heating load profile. A relatively smooth profile, along with 10-second timesteps in LabVIEW (for both PID updating and data recording) insured good fit of the PID process variable to the control value.

4.3.2 Domestic hot water

The load profile provided by IEA Annex 42 is given in timesteps of 1 minute. It is derived from a probabilistic method developed by the IEA Solar Heating and Cooling Task 26 (Jordan and Vajen, 2001) for a household consuming an average of 300 L/day at 45°C, in order to realistically represent the minutely DHW consumption of a single-family household. The profile specifies minutely volumetric flow rates of hot water based

on a 45°C delivery temperature (T_p), from which mass flow rate can be easily calculated. Since the experimental storage tank does not generally supply water at 45°C, the profile flow rate has to be adjusted based on the actual outlet temperature of the tank (T_h). Additionally, since the temperature of tap water (T_c) also varies (and is replacing the drawn-off hot water as well as providing the cold stream for mixing), the effect of its variation must be included in adjusting the profile flow rates.

For a stream of fluid produced by the complete mixing of two streams at different temperatures, Equation (37) can be developed from an energy balance by assuming constant specific heat and constant density. Since water is of interest, for simplicity it can be written in terms of C_p with all C_p terms cancelling each other out.

$$\dot{m} \cdot T_p = \dot{m}_h \cdot T_h + \dot{m}_c \cdot T_c \quad (37)$$

In the present case, the load profile stream can be taken as the mixed one, and the hot (tank) and cold (tap) streams as the other two, giving:

$$\dot{m} \cdot T_p = \dot{m}_h \cdot T_h + \dot{m}_c \cdot T_c \quad (38)$$

Where \dot{m} is the flow rate specified in the load profile, \dot{m}_h is the flow rate of water from the hot storage tank, and \dot{m}_c is the flow rate of tap water being mixed with the hot stream. Furthermore, the total flow rate given by the profile is equal to the sum of the two streams:

$$\dot{m} = \dot{m}_h + \dot{m}_c \quad (39)$$

Combining the above two equations gives an expression for the actual tank flow rate that corresponds to the profile flow rate.

$$\dot{V} = \frac{(\dot{V}_h - \dot{V}_c)}{\rho} \quad (40)$$

The profile temperature is a constant 45°C and the profile mass flow rate is specified at every timestep, so this is a function of the tank outlet and tap inlet temperatures. In general, since the tank outlet temperature is much higher than 45°C, the drawdown rate from the tank will be significantly lower than the flow rate specified by the load profile.

Due to limitations imposed by the flow metering equipment, there is a minimum and maximum measureable flow rate. Since the load profile (after adjustment for tank and tap temperatures) has many timesteps above and below the range of the flow meter, the load profile had to be modified. Total flow per hour was kept the same, but flows below the minimum were aggregated, and flows above the maximum were spread over a longer time period.

4.4 Engine instrumentation energy balance with uncertainty

A comprehensive energy balance was conducted for the engine. There was no “other losses” category as is typically the case for energy balances done on engines used only for shaft power. Along with propagation of all uncertainties involved in measuring the energy balance, this allowed objective evaluation and verification of the instrumentation. Thus estimates were made of convection and radiation losses from the insulated cabinet walls, and the exhaust flow rate and enthalpy were measured.

In conventional engine/genset testing, the shaft/electrical output and fuel consumption are the most important variables. In this context, "energy balance" can be used to mean an accounting for how much fuel energy goes to indicated power, net

power, and shaft power, with estimates being made of frictional and heat transfer losses in the conversion from one type of power to the next. Coolant and exhaust loads are generally not measured.

In CHP engine testing, coolant and exhaust loads are also important. Here, the term "energy balance" is often used to mean an accounting of the distribution of fuel energy to shaft/electrical power, coolant heat, and exhaust heat. Usually, no attempt is made to estimate other allocations, which are lumped into the "other" category.

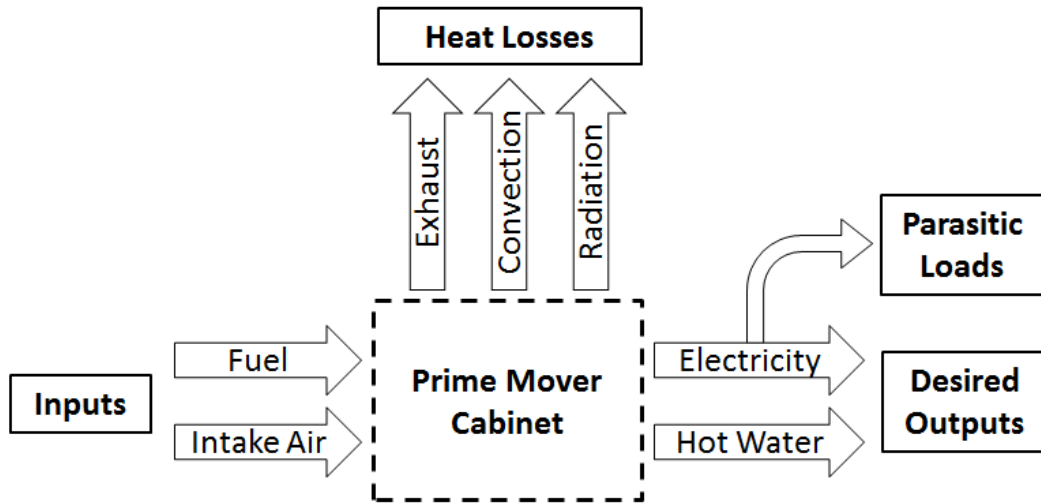


Figure 78: Basic control volume view of prime mover cabinet

Another meaning of the term "energy balance" is when a quantity is measured in two independent ways, and the two measurements are compared as a gauge of their measurement accuracy. It is this most comprehensive type of energy balance that was carried out in this work. This required measuring the energy flow of fuel and intake air (the energy into the system) by one set of instruments, and the energy out of the system by other sets of instruments. A control volume was drawn as in Figure 78. Using this control volume, the forms of energy flow out of the system were, in order of magnitude:

- heat recovery water loop (this includes heat recovered from coolant and exhaust)

- electricity
- exhaust losses (the exhaust heat not captured by the heat recovery circuit)
- buoyancy-driven convection from cabinet surfaces
- buoyancy-driven convection from cabinet vents (passive electronics cooling)
- radiation from cabinet surfaces
- chemical species enthalpy in exhaust (incomplete combustion products)

Measurements or estimates were made for each of these flows, including an uncertainty estimate for each quantity. This allowed the uncertainties to be propagated through the energy balance calculation to provide an objective estimate of how close the energy balance should be to zero.

Thus, the energy balance performed on the CHP engine provided both (1) a detailed accounting of fuel energy allocation and (2) an objective verification of instrumentation and measurement accuracy.

The prime mover enclosure or “cabinet” can be treated as a control volume. Figure 78 shows that a residential CHP prime mover cabinet has one energy input (fuel), two desired outputs (electricity and hot water), three types of undesired heat losses (unrecovered exhaust heat plus convection and radiation from cabinet exterior surfaces), and parasitic loss of electrical output (e.g. to run water pumps). The measurement of each of these seven energy flows is addressed in its own section below. In all cases, for purposes of the energy balance, heat transfer calculations between the system and surroundings were carried out relative to the ambient room temperature which surrounded the system, including the fuel input energy (i.e., the fuel’s HHV was adjusted

for ambient conditions). This is in contrast to the values for efficiency, which are based on standard condition HHV. The energy balance was defined as:

$$EBal = \frac{\dot{Q}_i}{\dot{Q}_f} \quad (41)$$

where

$$\dot{Q}_i = \dot{Q}_{water} + \dot{Q}_{exhaust} + \dot{Q}_{convection} + \dot{Q}_{radiation} \quad (42)$$

and

$$\dot{Q}_f = \dot{Q}_{water} + \dot{Q}_{exhaust} + \dot{Q}_{convection} + \dot{Q}_{radiation} \quad (43)$$

From the perspective of the cabinet control volume, the engine and integrated electrical generator are “black boxes.” For example, inefficiencies in the conversion of mechanical to electrical work in the generator simply convert mechanical energy into thermal energy. This will raise the temperature inside the cabinet, and in turn increase the outputs of hot water, exhaust, and/or convective heat. For the Ecopower unit on a HHV basis, the radiative losses accounted for about 1-2% of total fuel energy input, the convective losses were about twice as large (2-4%), and the exhaust losses comprised 11-14% of the fuel energy input.

4.4.1 Fuel input

The natural gas fuel input was measured volumetrically by a diaphragm-type American DTM-200A meter with an integrated electronic signal generator (a “pulser” unit). The pulser sent an analog voltage signal to the DAQ system each time the meter indicator physically passed a fixed point in its rotation, which occurred every 1.5 to 4 seconds, depending on engine speed. Using a high sample rate (around 60 Hz) in

FieldPoint and LabVIEW, the time between pulses from the meter was measured. A moving average of the previous 8 pulses was used to obtain a smoothed fuel consumption rate.

Logic routines were devised and manually coded into LabVIEW to interpret those pulses. This logic is shown as a decision tree in Figure 79, and a sample output (of the time interval between pulses) from the interpreted analog signal is shown in Figure 80. As an example of something this logic does: when no pulse is received for greater than 1.8 times the interval between the last two pulses, the system assumes that a single pulse event has been missed (this can occur due to a temporary lag in the sample rate as the computer consolidates memory or performs some other task unrelated to DAQ sampling). However, if no pulses continue to be measured for 4 times the previous interval, then the gas flow is inferred to have stopped completely.

This logic routine was validated by taking manual readings from the meter face over several hours during which the engine ran at various speeds and experienced shutdown/restart events. The consumption value recorded by the DAQ system for the time interval was in good agreement with the manually observed readings: there was ~0.2% difference in methods, compared with the 1% uncertainty assigned to the overall meter volumetric reading.

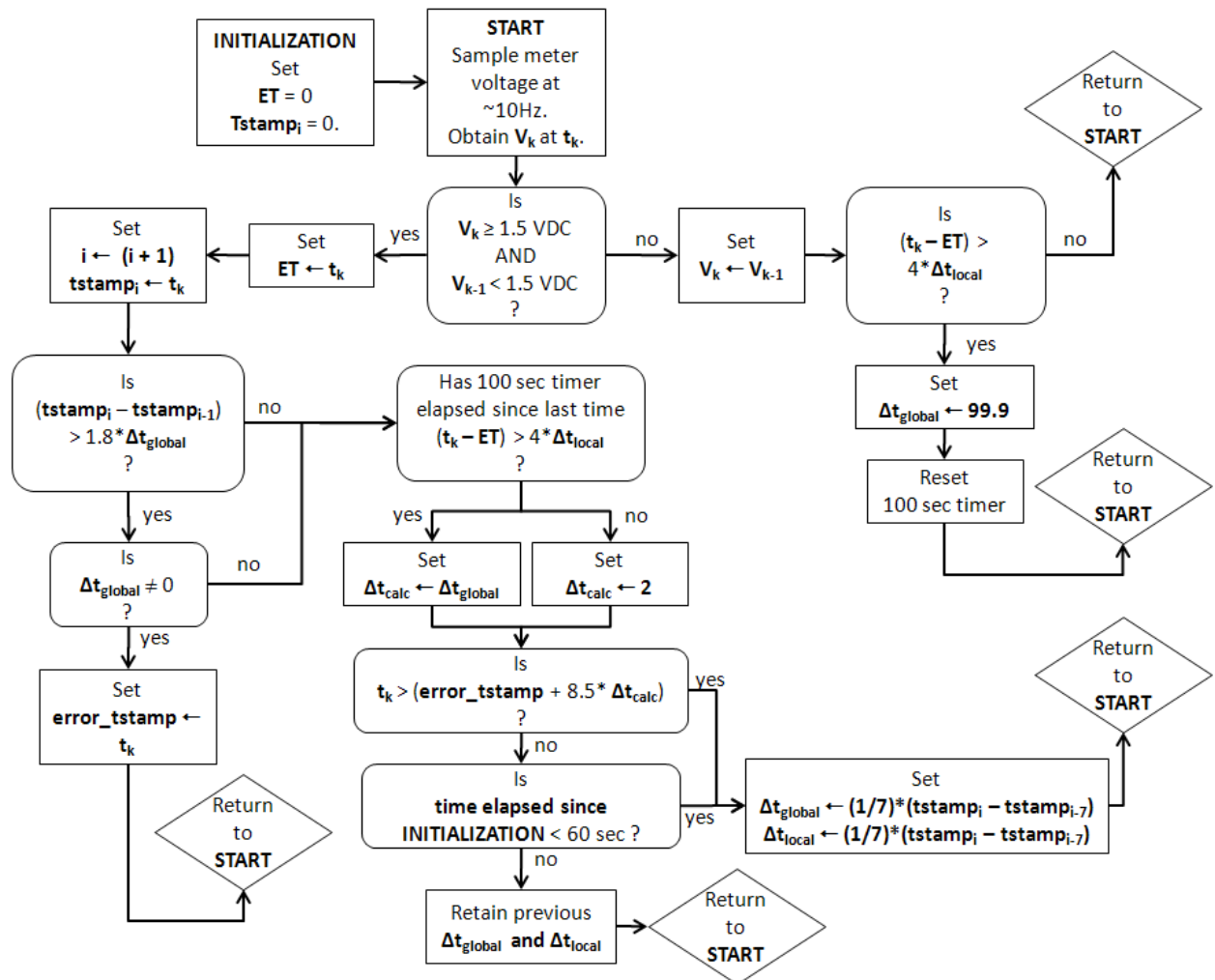


Figure 79: Decision tree depiction of logic programmed into LabVIEW to interpret the 0-5 V analog signals from the gas meter pulser

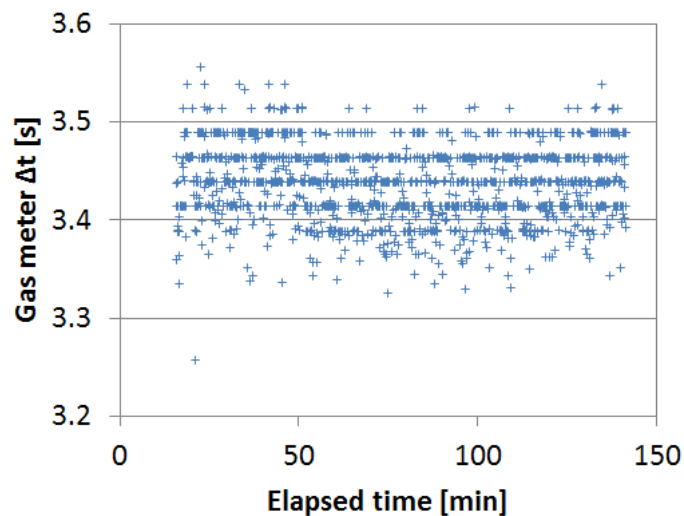


Figure 80: Sample output from gas meter logic routine

The meter does not incorporate temperature or pressure compensation. Thus, using the ideal gas law, the volumetric heating value was adjusted for temperature changes. Atmospheric pressure, with a correction for elevation of 21 m (69 ft) above sea level and a correction for line pressure (about 1.5 kPa, or 6 in w.c.) were applied. Line pressure variations were less than 0.25 kPa (1 in w.c.), and were neglected. Barometric pressure variations were also neglected.

Table 24: Natural gas composition data

k (component species)		X _k (Mole fraction)	Y _k (Mass fraction)	prod:reac molar ratio (perfect combustion)	HHV	HHV	Molar mass	Density at 60°F (15.56°C) and 14.696psi (101.325 kPa)
chemical formula	name	mol _k /mol _{tot}	kg _k /kg _{tot}	mol _{prod} /mol _{reac}	Btu/lb	kJ/kg	kg/kmol	kg/m ³
CH ₄	Methane	94.90%	90.17%	1.0000	23,875	55,533	16.0428	0.6772
C ₂ H ₆	Ethane	2.50%	4.45%	1.0283	22,323	51,923	30.0696	1.2693
C ₃ H ₈	Propane	0.20%	0.52%	1.0403	21,669	50,402	44.0965	1.8614
C ₄ H ₁₀	n-Butane	0.03%	0.10%	1.0470	21,321	49,593	58.1234	2.4536
C ₄ H ₁₀	Isobutane	0.00%	0.00%	1.0470	21,271	49,476	58.1234	2.4536
C ₄ H ₈	n-Butene	0.00%	0.00%	1.0338	20,854	48,506	56.1075	2.3685
C ₄ H ₈	Isobutene	0.03%	0.10%	1.0338	20,737	48,234	56.1075	2.3685
C ₅ H ₁₂	n-Pentane	0.01%	0.04%	1.0512	21,095	49,067	72.1503	3.0457
C ₅ H ₁₂	Isopentane	0.01%	0.04%	1.0512	21,047	48,955	72.1503	3.0457
C ₅ H ₁₀	n-Pentene	0.00%	0.00%	1.0409	20,720	48,195	70.1344	2.9606
C ₆ H ₁₄	n-Hexane	0.01%	0.05%	1.0541	20,966	48,767	86.1772	3.6378
N ₂	Nitrogen	1.60%	2.65%	1.0000	0	0	28.0134	1.1825
CO ₂	Car. Dioxide	0.70%	1.82%	1.0000	0	0	44.0098	1.8578
O ₂	Oxygen	0.02%	0.04%	1.0000	0	0	31.9988	1.3508
H ₂	Hydrogen	0.00%	0.00%	0.6667	61,095	142,107	2.0159	0.0851
Totals		100.01% *	98.98%	1.0009	22,706	52,815	16.8845	0.7127

* Totals depicted in table do not sum to 100% due to rounding. More significant digits were used in calculations.

To convert the volumetric fuel consumption to an energy basis, the fuel's HHV was used. The fuel's HHV was obtained by analyzing two weeks (August 25 to September 16, 2008) of minute-by-minute data recorded by a calorimeter located at the Gaithersburg campus of the National Institute of Standards and Technology (NIST)

campus, which is serviced by the same gas utility (Washington Gas) as the University of Maryland. The dataset is shown in Figure 81. Over the two weeks of recorded data, the average HHV was 1024.6 Btu/scf (29.014 Btu/L, or 30.612 kJ/L). The maximum deviations from this average were + 2.92%, and – 2.87%. The standard deviation from the average was 0.84%. Given the difference in location between the NIST campus and the lab in Maryland, the systematic uncertainty in HHV was assumed to be 3%. The NIST calorimeter dataset also included the temperature and line pressure of the gas at each recorded minute. The values recorded by NIST were adjusted for elevation (508 ft above sea level in Gaithersburg, versus 69 ft above sea level in College Park).

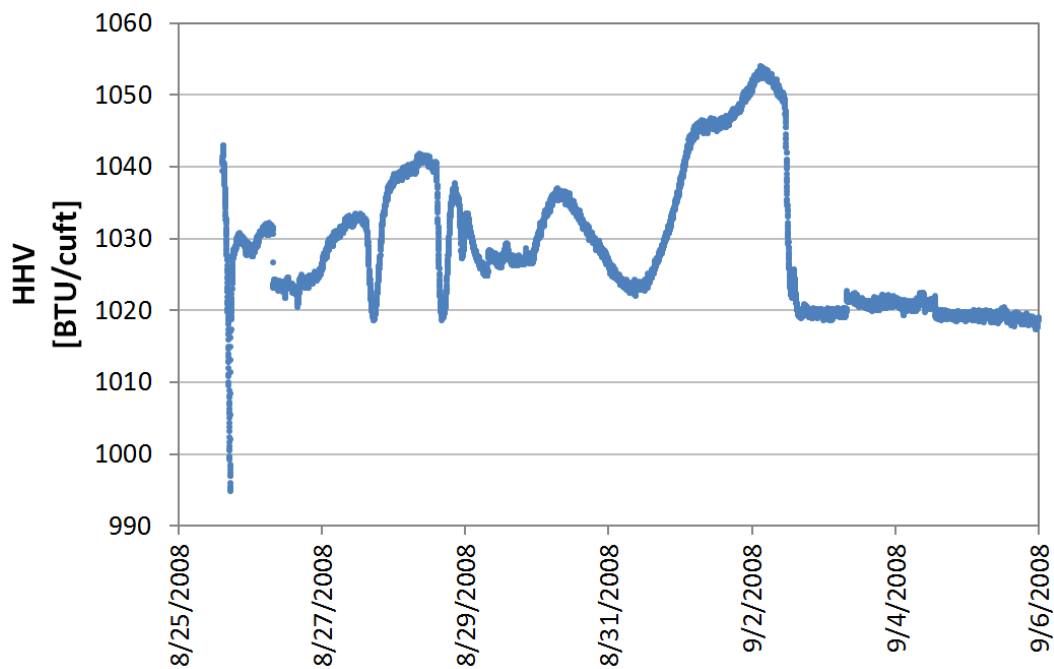


Figure 81: Raw calorimeter data taken at NIST

A comparison of the measured calorific value of the fuel was made to two other sources, as shown in Figure 82.

For The Washington Gas composition data, the given values were used to compute the average HHV. The error bars were computed by manipulating the range of

values for each component, first to minimize and then to maximize the volumetric heating value of the fuel. The “Field Samples” represent the minimum, maximum, and average values of five samples taken throughout the country and presented on page 42 of Petchers (2003).

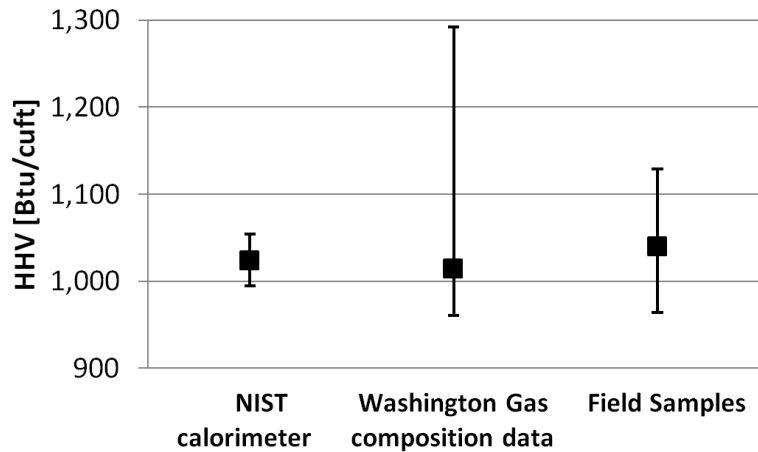


Figure 82: Comparison of three sources of HHV data
 Note: 1024.6 Btu/cuft is equal to 38.173 MJ/m³

The values measured by NIST are corroborated by other sources, are clearly within the range of possible gas constituency as specified by Washington Gas, and appear to be the most accurate estimate available.

4.4.2 Electricity output

The electrical output was measured by an Ohio Semitronics watt transducer. The transducer was placed on the grid-side of the isolation transformer. In order to obtain the pre-transformer output (in accordance with using the cabinet as a control volume boundary), the measured value was adjusted for losses in the transformer. Also, two parasitic loads draw electric power directly from the cabinet and dissipate it outside the cabinet: the water pump and mixing valve. Their electrical consumption was added back

in to the electrical output value. This was done both for the reported electrical output values as well as the energy balance calculation.

The water pump was packaged with the Ecopower, and has three speeds which draw power (at actual system backpressure) as depicted in Table 25. The mixing valve draws about 5 Watts while operating, less than 1 Watt while idle, and only operates a small percentage of the time. Its consumption was neglected. The Cutler-Hammer transformer was also packaged with the unit, and according to manufacturer data has efficiency (as a function of part load ratio) and losses as depicted in Figure 83 and Figure 84.

Table 25: Grundfos water pump power consumption

Pump setting	Power [W]
high	60
medium	31
low	18

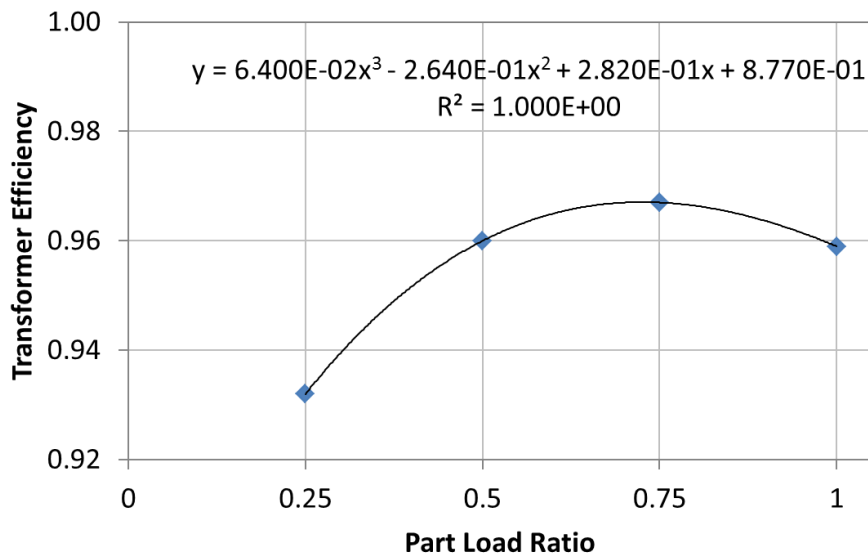


Figure 83: Transformer efficiency as a function of its part load ratio
Transformer is rated at 7.5 kVA. Diamonds are manufacturer data, and the line is curve fit to that data.

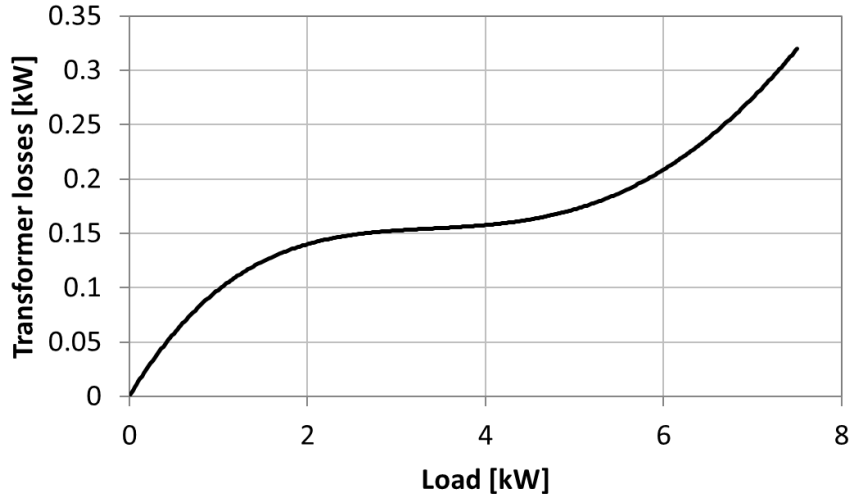


Figure 84: Transformer losses as a function of transformer load
Curve is based on efficiency curve fit in Figure 83.

All other parasitics (e.g. ignition system, gas mixer stepper motor, etc.) are located inside the cabinet, and were treated as part of the cabinet “black box.” Thus the same electricity output was used for the energy balance calculation as was reported in the final results.

4.4.3 Hot water output

Following Equation (44), the hot water output was measured by two in-stream RTDs and a Sponsler turbine flow meter. The volumetric flow rate of the flow meter was converted to a mass flow rate by real-time calculations of density based on temperature.

$$\dot{Q} = \frac{\dot{V}}{\rho_{water}} (\rho_{supply} h_{supply} - \rho_{return} h_{return}) \quad (44)$$

Water density and enthalpies were calculated in real time in LabView as functions of temperature. The average of h_{supply} and h_{return} was used for the density calculation. All property calls were carried out in real time using CEEE XProps™ software (XProps™, 2012), which is based on NIST’s RefProps database.

It is typical in heat flow measurements for the uncertainty in temperature measurement to dominate the overall uncertainty in the heat flow. If it is assumed that the flowrate and specific heat are known perfectly, the relative uncertainty in the heat flow can be obtained as a function of the temperature difference and the uncertainty in those temperature measurements, as shown in Equation (45).

$$\sigma_Q = \frac{\sqrt{2}\omega_T}{\Delta T} \quad (45)$$

This result has been plotted as a contour plot in Figure 85. This plot places a lower bound on the relative uncertainty in a heat flow measurement for a given temperature sensor uncertainty and ΔT . In practice, for single phase water flow, since flow meters with uncertainties better than 1% are common and the specific heat is well known, the total uncertainty will generally be very close to the minimum set by considering only the ΔT and the temperature uncertainty.

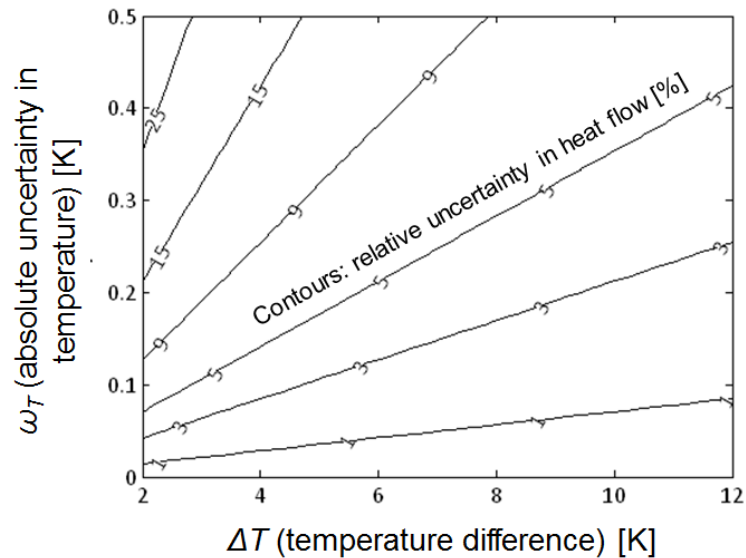


Figure 85: Relative uncertainty [%] in a heat flow based on ΔT and the absolute uncertainty in temperature measurement

The RTDs used to measure the supply and return temperatures of the prime mover had an uncertainty of 0.15°C for all tests. The delta T between them ranged from about 5°C (at minimum part load and maximum water flow rate) to 12°C (at full load and minimum water flow rate). This variation in horizontal location of Figure 85 accounts for the difference in relative uncertainties in heat output at different operating conditions.

4.4.4 Exhaust heat losses

Measuring the heat lost through the exhaust was the most complex of the six energy transfer calculations. The overall governing equation for this heat loss was:

$$\dot{Q}_{\text{exhaust}} = \dot{m}_{\text{exhaust}} (h_{\text{exhaust}} - h_{\text{ref}}) \quad (46)$$

Each term in Equation (46) is addressed in detail in its own section below. An overview of the measurements and calculations involved is provided in Figure 86.

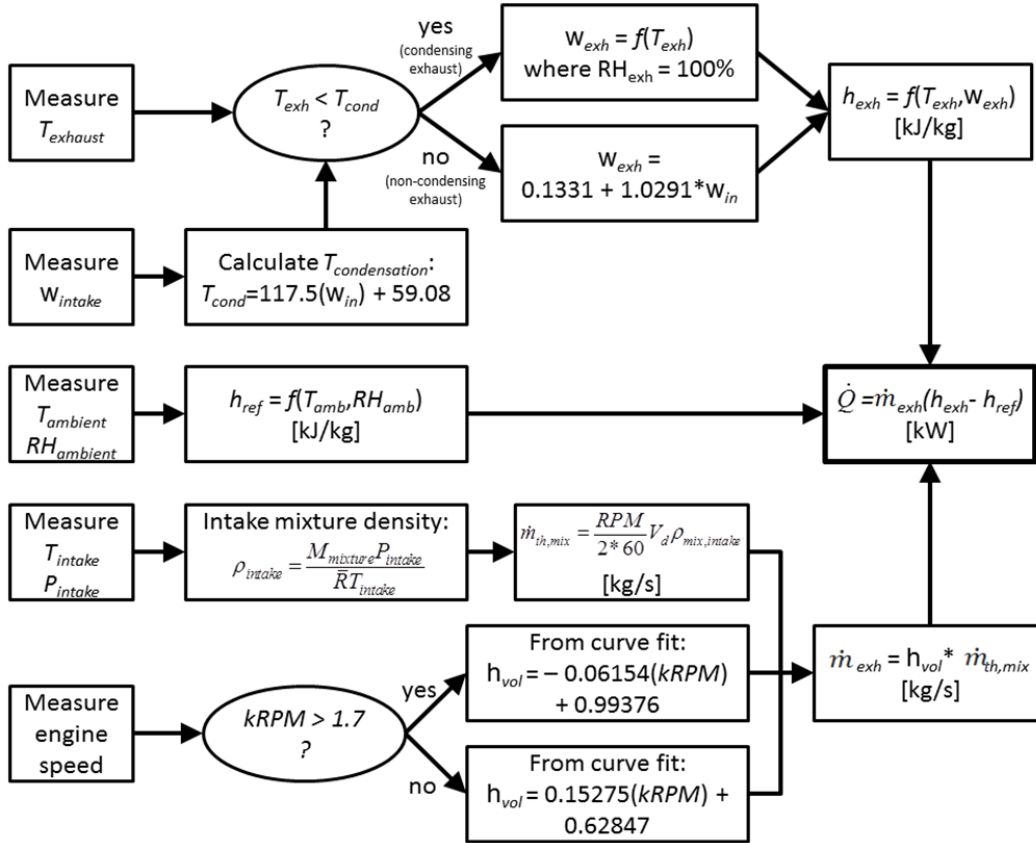


Figure 86: Flowchart of measurements and calculation involved in determining the exhaust mass flow rate (see text)

4.4.1.1 Reference enthalpy

For purposes of the energy balance, the reference enthalpy was taken as the psychrometric enthalpy of air at the temperature and humidity entering the cabinet intake port. These conditions are distinct from the condition of the air entering the engine intake port (which was used as a reference in the volumetric efficiency correlation).

4.4.1.2 Exhaust enthalpy

The exhaust stream enthalpy was calculated using an ASHRAE moist air enthalpy correlation (ASHRAE, 2005).

$$h = 1.005T + \omega(2500.9 + 1.805T) \quad (47)$$

Where ω is the humidity ratio of the exhaust, and T is the exhaust dry bulb temperature measured by an in-stream thermocouple at the point where the exhaust leaves the cabinet boundary. The enthalpy is per unit mass of dry air.

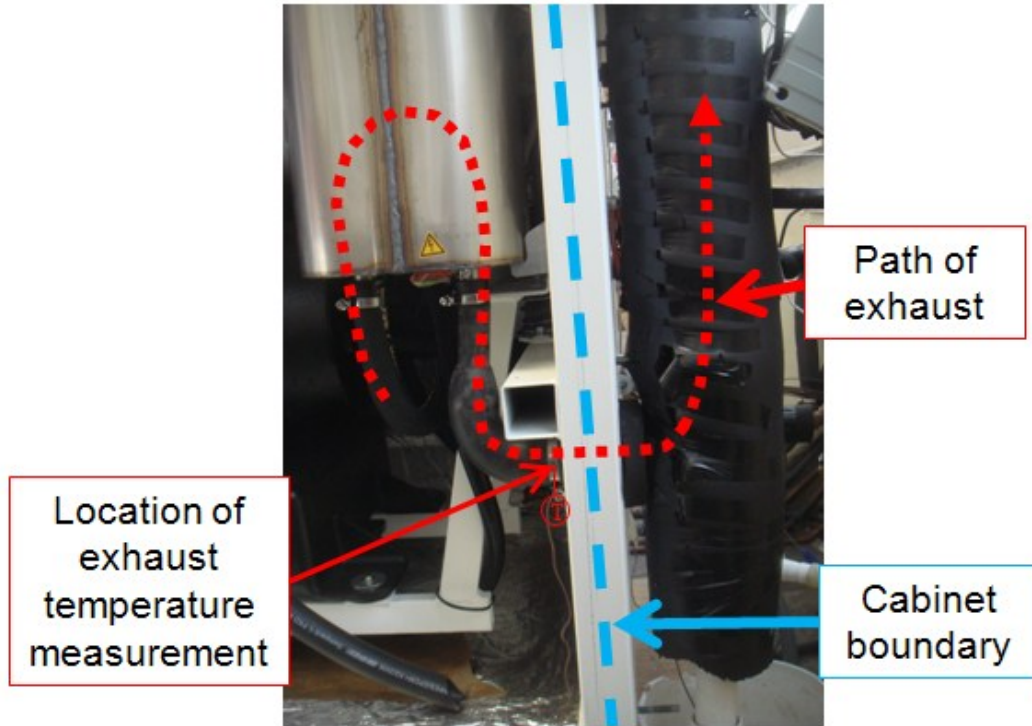


Figure 87: Location of exhaust temperature measurement

The ASHRAE correlation has the following physical meaning:

$$h = C_{P,DA}T + \omega(h_{fg} + C_{P,water\ vapor}T) \quad (48)$$

where the specific heats and the enthalpy of vaporization are assumed constant.

An in-stream, 4-thermocouple grid was used to measure the exhaust temperature. It was placed inside the exhaust pipe where the pipe crosses the cabinet boundary in such a way that condensation could not drip onto it, ensuring that the measurement was truly a dry bulb temperature.

The ASHRAE correlation, Equation (48), was developed for air of standard atmospheric composition. The exhaust gas has considerably more CO₂ than standard

atmosphere, and no O₂. However, the correlation remains accurate for the exhaust gas. This is because, at atmospheric pressure and the temperature range of interest, all components behave ideally and the change in enthalpy for the exhaust gas components is the same as the change for standard atmospheric components. The difference was confirmed to be negligible across more than the range of temperatures and humidities encountered in the exhaust stream using EES, as shown in Table 26. The “AirH2O” fluid properties were used in EES, which account for the changes in specific heat with changes in temperature.

Table 26: Comparison of exhaust enthalpies calculated from ASHRAE moist air correlation and EES

T [°C]	RH [%]	h _{EES} [kJ/kg]	h _{ASHRAE} [kJ/kg]	Absolute difference [kJ/kg]	Relative difference [%]
40	0.05	46.12	46.05	-0.06926	-0.15%
40	0.5	100.8	100.7	-0.119	-0.12%
40	0.95	159.4	159.2	-0.1722	-0.11%
70	0.05	96.07	95.9	-0.1689	-0.18%
70	0.5	368.3	367.7	-0.6234	-0.17%
70	0.95	747.2	745.9	-1.256	-0.17%
105	0.05	212.1	211.6	-0.5265	-0.25%
105	0.5	2581	2575	-6.819	-0.26%
105	0.75	14266	14228	-37.85	-0.27%

4.4.1.3 Exhaust mass flow rate and volumetric efficiency

Since the engine is equipped with lambda control (to maintain stoichiometric combustion) and a 3-way catalytic converter, combustion was assumed to be perfect (i.e. stoichiometric and complete). Thus, the exhaust humidity ratio ω was calculated based on perfect combustion of natural gas with moist atmospheric air. The only variable involved is the atmospheric humidity. The fuel gas composition used for this calculation is given in Table 27. Intake air moisture content was measured in real time, and the exhaust humidity ratio was calculated dynamically in LabVIEW as a function of that moisture

content (using the curve fit to analytical results shown in Figure 88). Additionally, the cooled exhaust outlet pressure was assumed to be atmospheric. This assumption is valid because the flow only passes through 2.0 m of laminar flow through an unobstructed PVC pipe (ID = 6.2 cm) with two 90° bends before being vented to the atmosphere.

Table 27: Average composition of natural gas
(data provided by Washington Gas, utility provider of natural gas to the lab)

Gas Component	Mole Fraction
Methane	94.9%
Ethane	2.5%
Propane	0.2%
n-Butane	0.03%
Isobutene	0.03%
n-Pentane	0.01%
Isopentane	0.01%
Hexane	0.01%
N ₂	1.6%
CO ₂	0.7%
O ₂	0.02%
H ₂	0.00%

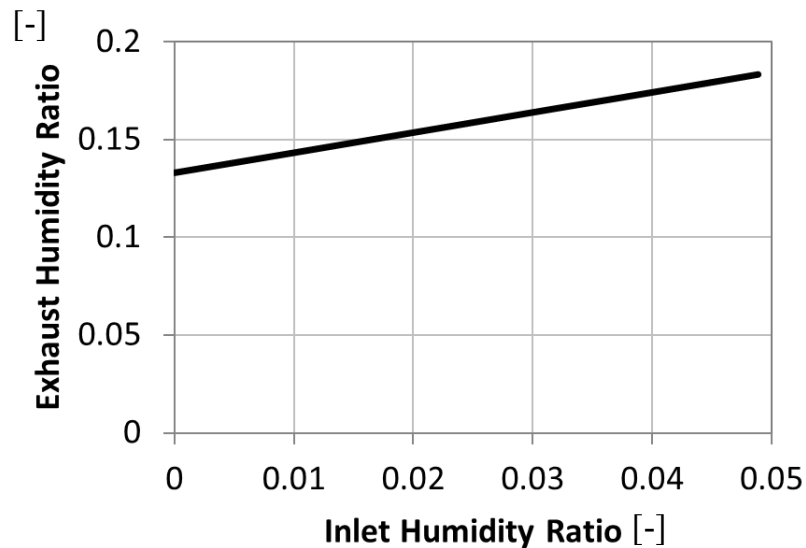


Figure 88: Exhaust humidity ratio as a function of inlet humidity ratio for non-condensing exhaust

The mass flow of the exhaust was found by mapping the engine’s volumetric efficiency as a function of RPM. The volumetric efficiency of an engine describes how fully the cylinder is filled with fresh air/fuel gases on each intake stroke. For a naturally

aspirated four stroke that is not directly injected, the rate at which volume is displaced by the piston can be called the theoretical volumetric flow of mixture:

$$\dot{V} = (\text{volume displaced by piston}) \times \left(\frac{\text{intake strokes}}{\text{unit time}} \right) \quad (49)$$

Since there are 60 seconds per minute and 2 revolutions per intake stroke, and multiplying volume by density, the theoretical mass flow of fuel/air mixture is:

$$\dot{m} = \frac{\pi D^3}{6} \frac{V_d}{60} \rho_{mix, intake} \quad (50)$$

The density here is of the mixture just before it enters the engine intake port. This differs slightly from the traditional definition (Heywood, 1988), which would consider only the air portion of the mixture, and thus the term here has been denoted as \dot{V} instead of simply \dot{V} . This mixture-basis convention has been adopted since the whole purpose of calculating volumetric efficiency is to determine the exhaust mass flow rate (equal to overall mixture mass flow rate) for the energy balance calculation.

For multiple cylinder engines, the density in Equation (50) is defined in the intake manifold, i.e. after fuel injection and before the intake port. For the single-cylinder Ecopower engine, it was not possible to non-destructively place an in-stream thermocouple between the injector and the intake port, due to the arrangement of throttle plate, throttle plate stepper motor, injector, and their close proximity to the head. However, an acceptable location was found 1cm before the throttle plate, 2cm before the injector and 10cm before the exhaust port. This location is adequate because the intake air and natural gas are both independently heated to the high cabinet temperature by traveling extensively through the hot cabinet interior in their respective hoses.

Additionally, since natural gas is a gaseous fuel, it does not draw heat from the intake air to vaporize. Thus, the measured intake air temperature was adequately close to the mixture temperature actually reaching the intake port. Any discrepancy is surely negligible given the relatively large uncertainties involved in the volumetric efficiency calculation, and the leeway that results from defining volumetric efficiency based on density in the “intake manifold,” which could be directly after injection or directly before the intake port.

The intake air density was calculated based on the ideal gas law, as shown in Equation (51). For this calculation, intake pressure was ambient pressure (a constant 101.325 kPa) corrected for the intake vacuum (see Figure 89), molar mass was of a stoichiometric air/fuel mixture, and temperature was the measured intake air temperature.

$$\rho_{mix,intake} = \frac{M_{mix} (P_{atm} - \Delta P_{intake})}{\bar{R}T_{intake}} \quad (51)$$

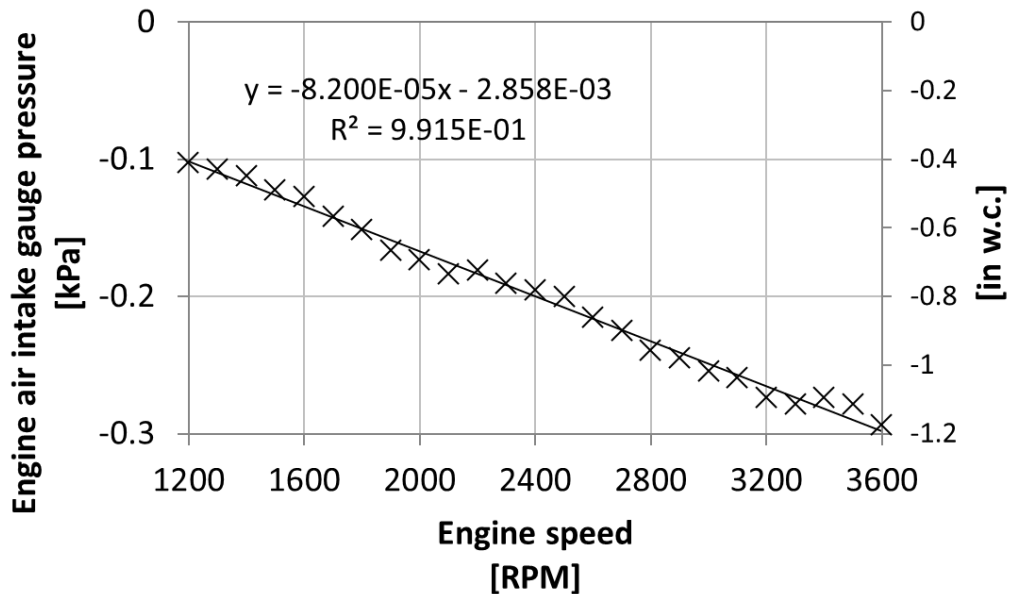


Figure 89: Engine air intake vacuum as a function of engine speed

A micro CHP engine is optimized to minimize heat losses, which usually involves insulating the prime mover cabinet and drawing the cabinet air into the engine in order to minimize radiative and convective losses from engine surfaces, leading to a much higher intake temperature. Thus, when compared to an engine optimized for mechanical power production alone, a CHP engine will have lower intake density and less mass flow into the cylinder for the same volumetric efficiency.

The volumetric efficiency is defined as the actual mass flow of air into the cylinder divided by the theoretical mass flow at intake density. The factor of two is introduced for four-stroke engines, since an intake stroke occurs only every other revolution:

$$\eta_{vol} = \frac{\dot{m}}{\dot{m}_{theoretical}} = \frac{\dot{m}}{V_d \rho_{air,inlet} RPM \frac{60}{2}} \quad (52)$$

However, since the primary value of interest for the purpose of developing an energy balance is the exhaust mass flow rate, a modified definition of volumetric efficiency was used, based on the mixture mass flow rate (which is equal to the exhaust flow rate), as shown in Equation (53).

$$\eta_{vol,m} = \frac{\dot{m}}{\dot{m}_{theoretical}} = \frac{\dot{m}}{V_d \rho_{inlet} RPM \frac{60}{2}} \quad (53)$$

Measurements were conducted across the RPM range of the unit in order to determine its volumetric efficiency. These measurements were conducted using an electric resistance heating element; with one thermocouple grid upstream and one downstream (after a mixing section) of the heater. By calculating the heat capacity of the exhaust and estimating the heat loss from the pipe in the region between the two

thermocouple grids, the exhaust mass flow rate can be calculated with governing Equation (54). The methods used to measure each of the five terms in the r.h.s. of this equation are described below.

$$\dot{m} = \frac{\dot{Q}}{C_{P, exhaust} (T_{post-heater} - T_{pre-heater})} \quad (54)$$

First term (\dot{Q}):

The heat into the electric resistance heater was measured with a watt transducer.

Second and third terms ($T_{pre-heater}$ and $T_{post-heater}$):

The two temperatures were measured with in-stream thermocouple grids. The pre-heater temperature was measured with a 5-thermocouple grid, placed 2 pipe diameters upstream of the heater. The Reynolds number in the exhaust pipe ranged from 750 to 1500, depending on engine speed. Thus, multiple measures were taken to ensure uniform temperature distribution in the flow after the heater. Nine thermocouples were used for the second thermocouple grid, and it was placed 12 pipe diameters after the heater. There were two 90° elbows between the heater and second thermocouple grid, and two counter-rotating turbulators were also placed between the elbows. The last thermocouple grid was placed 2 pipe diameters from the outlet of the pipe, and a flow straightener was included 1 pipe diameter from the end to ensure that no mixing with ambient air could affect the temperature measurement.

Fourth term ($C_{P, exhaust}$):

The heat capacity of the exhaust is a function of exhaust gas composition (particularly water content) and exhaust gas temperature. Since combustion is

stoichiometric and complete, the exhaust water content depends on intake humidity and whether condensation is taking place in the exhaust. Figure 90 below demonstrates the dependence of exhaust gas heat capacity on inlet humidity ratio and exhaust gas temperature. Among the components of the exhaust gas, water has the highest heat capacity. Thus, at condensing temperatures, as the temperature gets lower, water condenses out of the gas, and this change in gas composition drives a large decrease in the heat capacity of the mixture. On the graph, the condensing temperature for a given inlet humidity corresponds to the point where the line undergoes a discontinuous change in slope. This condensing temperature gets lower for drier intake air. When the exhaust is above the condensing temperature, its composition does not vary with temperature, and the heat capacity has approximately a linearly proportional dependence on temperature.

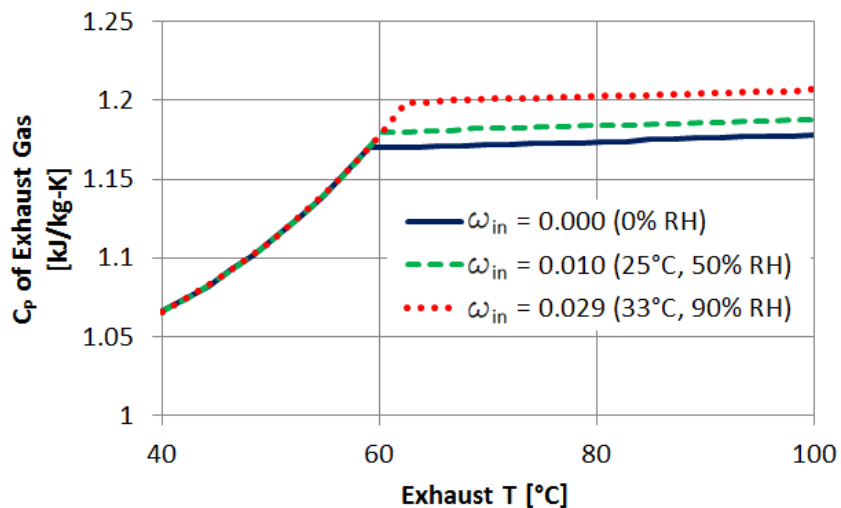


Figure 90: Heat capacity of exhaust gas as a function of temperature, for three inlet humidities

Fifth term (ζ):

To minimize heat losses from the pipe, a layer several inches thick of Armacell insulation was wrapped around the pipe exterior. The basic 1-D planar heat conduction

equation, Equation (55), was adapted for radial coordinates and applied to the exhaust pipe insulation to estimate the heat losses from the pipe.

$$\dot{Q} = \frac{k A (T_{interior} - T_{surface})}{L} \quad (55)$$

Equation (55) can be written in terms of an R-value:

$$\dot{Q} = \frac{A (T_{interior} - T_{surface})}{R} \quad (56)$$

where, for planar geometries, $R = 1/k$. For radial geometries,

$$R = \frac{\ln\left(\frac{OD}{ID}\right)}{k} \quad (57)$$

The insulation ID and OD, along with thermal conductivity data provided by the manufacturer, were used to determine the radial-equivalent R-value of the insulation. Along with the interior and surface temperatures of the insulation, Equations (56) and (57) were used to estimate the heat loss from the pipe.

Tests were then run on the engine at a range of RPMs in order to determine the volumetric efficiency, as defined in Equation (53), as a function of RPM. The results are shown in Figure 91. The general shape of the curve of volumetric efficiency as a function of engine speed is well established empirically and theoretically, for example by Heywood (1988). At high RPM, flow velocities are very fast and large pressure drops exist in the intake system, especially through the intake valve(s). At very low RPM, velocities are not high enough to take advantage of the dynamic effects for which the engine was designed. These dynamic effects include resonance in the intake and exhaust systems, early intake-boosting due to intake/exhaust valve timing overlap, and delayed

inlet valve closing, all of which depend on the engine operating at some minimum speed in order for the air to contain enough momentum. Thus, an engine will have its peak volumetric efficiency in the lower RPM range, once dynamic effects have come into play, but before large pressure drops develop due to high flow velocities and turbulence-inducing flow separation as the air enters the cylinder through the intake valve. Thus, for the data measured for the Ecopower, two linear curve fits were chosen to allow a maximum volumetric efficiency value in the lower RPM range.

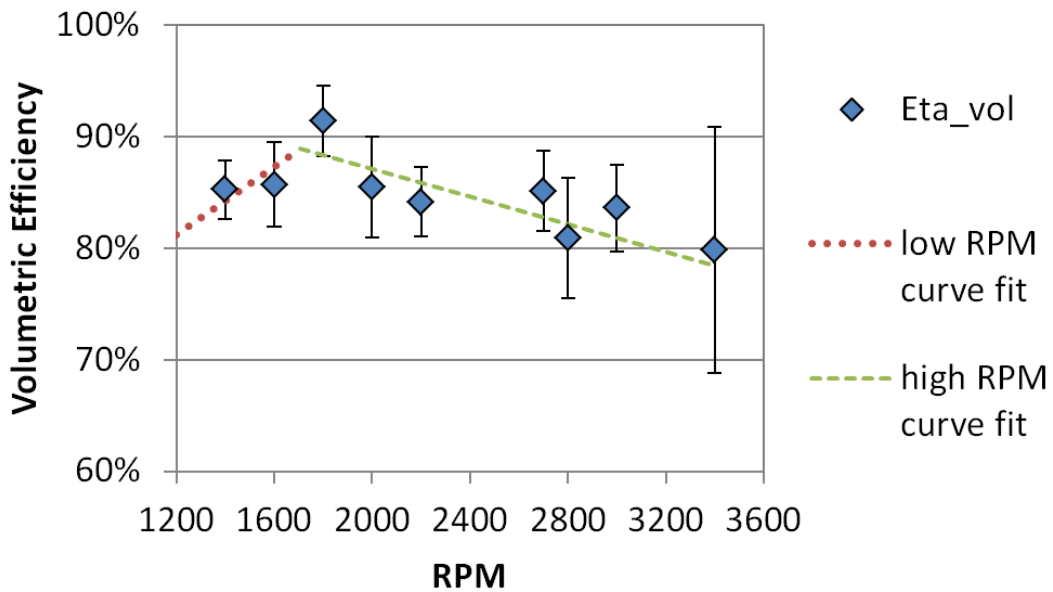


Figure 91: Measured volumetric efficiency of the engine with error bars and linear curve fits

Finally, the equation used in LabVIEW to determine the real-time exhaust flow rate was:

$$\dot{V} = \eta_{vol} * \dot{V} \tag{58}$$

where η_{vol} was a curve fit function of engine speed, and \dot{V} was calculated directly from the engine speed and engine air intake temperature – see Equation (53).

4.4.5 Convective losses from cabinet walls

The convective losses were estimated using empirical correlations for external natural convection from Incropera and Dewitt (2002). For each of the six cabinet surfaces (four vertical, one upward-facing horizontal, and one downward-facing horizontal), an average surface temperature was obtained by pointing an IR temperature sensor at a grid of 25 evenly distributed points. The IR sensor accuracy was confirmed to be within +/- 1°C at several selected location by thermocouple measurements.

4.4.6 Radiative losses from cabinet walls

To approximate the radiative heat losses, the cabinet surface temperature distribution was measured by a survey of surface temperatures taken with an IR temperature sensor and confirmed by thermocouple measurements, similar to the method used in estimating the convective heat loss.

Since radiation is proportional to the fourth power of temperature, the radiative losses were estimated using a bin method. The surfaces of the cabinet were divided into a grid, with each grid facet representing a bin and being treated independently of the other facets. The grid resolution was adaptively refined based on the observed temperature gradients along the cabinet surfaces. Each grid facet was made small enough that the range of most temperature readings within it spanned less than 4°C. An example grid (for the cabinet's left side panel) is shown in Figure 92. Such a grid was created for all cabinet surfaces.

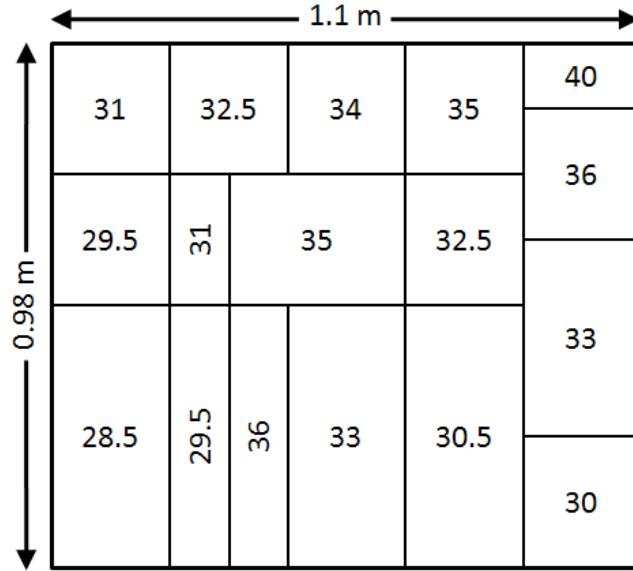


Figure 92: Example surface temperature grid (one out of six used) for purpose of radiative loss calculation
All numbers represent degrees Celsius.

For each bin (i.e. grid facet), the radiative heat loss is:

$$\dot{Q} = A \varepsilon \sigma (T_{bin}^4 - T_{ambient}^4) \quad (59)$$

Where A is the bin surface area, σ is Boltzmann's constant and ε is the total hemispherical emissivity of the surface. An ε value of 0.85, typical of white paint in the infrared band, was used.

To estimate the effective ambient temperature, the IR temperature sensor was pointed radially outward from the cabinet in 22 random directions, and the average of all those readings was used. These 22 measurements had an average of 25.0°C and a standard deviation of 1.7°C, and were within a few degrees of the air temperature in the room.

Several repeat measurements were taken after the system reached steady state at the lowest and highest engine RPM, and negligible differences in surface temperature were found. Thus it was assumed that the surface temperature distribution is constant for

all operating conditions. To get an idea of the uncertainty associated with the radiation estimate, a parametric study across various ambient temperatures was conducted, as shown in Figure 93. Of course, as the ambient temperature increases, the cabinet surface temperature will increase also, meaning that the extreme values of Q_{rad} depicted in Figure 93 are limits that would not actually be reached. Based on this, a constant value of 293 Watts for Q_{rad} was used in the energy balance calculation, and a systematic uncertainty in the calculated value of Q_{rad} was assumed to be 30%.

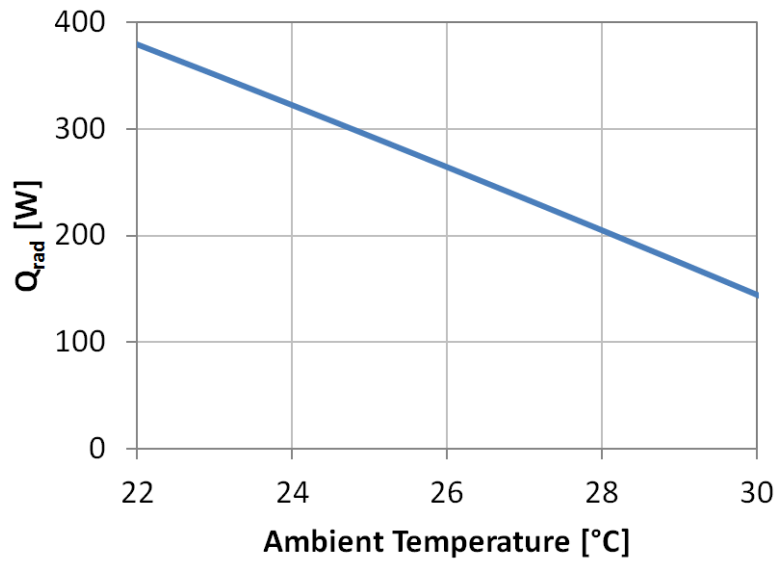


Figure 93: Maximum possible variation in radiation heat losses for different ambient temperatures
Surface temperature distribution is assumed constant.

The cabinet has some small protruding extended surfaces which experience non-zero view factors of other cabinet surfaces. However, the protruding surfaces with non-zero view-factors of the main cabinet walls account for less than 2% of the total cabinet surface area. Thus, the internal view factor was assumed to be zero for all surfaces.

4.4.7 Parasitic losses

Based on the control volumes shown in Figure 94, the parasitic loads (“parasitics”) involved in the operation of the CHP system can be classified into four types based on where they dissipate work into heat (a particular parasitic load might also dissipate heat into more than one category, such as the circulation pump between PM and tank). The relevance of this classification scheme is explained in the following paragraphs, and the classification of parasitics specific to the Ecopower unit is shown in Table 28.

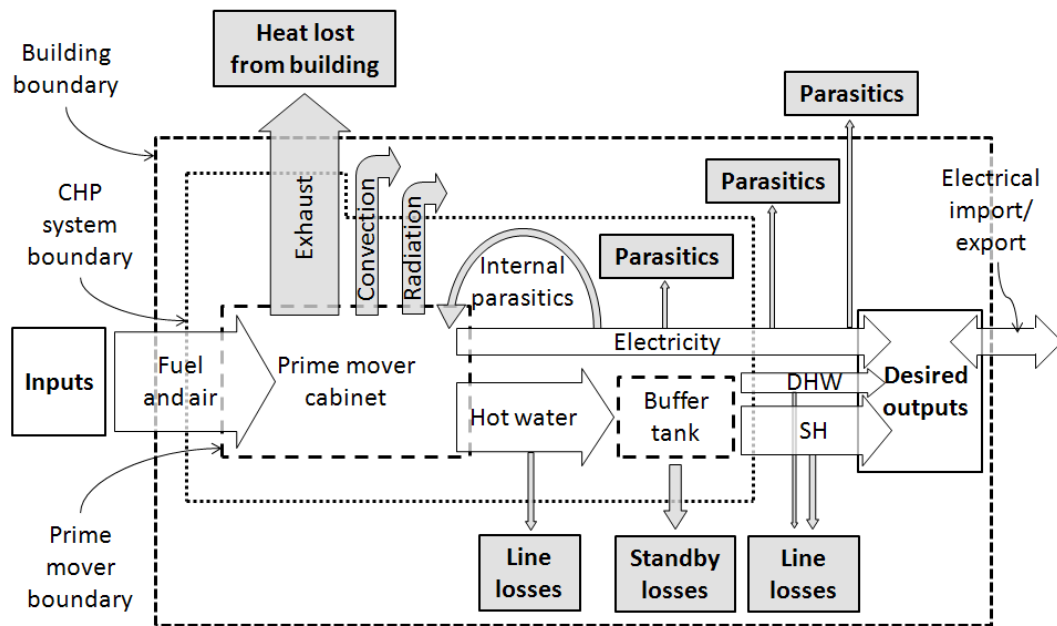


Figure 94: Detailed CHP view showing four control volumes (dotted lines)
 Solid squares with bold text: energy sources and sinks. Arrows: energy flows. Gray boxes and arrows: losses of energy or exergy.

Table 28: List of parasitic loads for laboratory Ecopower unit

Ecopower parasitic loads		Power dissipated [W]	Internal to PM cabinet	Internal to CHP system	Internal to building
Mechanical	Engine coolant pump	(not measured)	yes	yes	yes
Electrical	3-phase rectifier	(not measured)	yes	yes	yes
	2-phase inverter	(not measured)	yes	yes	yes
	Power conditioning electronics	(not measured)	yes	yes	yes
	Control circuitry and relays	(not measured)	yes	yes	yes
	PM-tank water pump	18 (low) to 60 (high)	no	partially	yes
	PM-tank diverter valve	5	no	partially	yes
	Isolation transformer	110 - 160	no	no	yes

All parasitics in the Ecopower system are internal to the building; however it is conceivable that a CHP installation could have the isolation transformer outside the building.

The heat created by electrical and mechanical loads dissipated (i.e. used) inside the prime mover cabinet boundary may be partially captured as useful heat. This capture can be direct (as in the case of an alternator generating heat which is captured by water-cooling the alternator) or indirect (as in the case of power conversion electronics heating the cabinet, thereby decreasing heat loss from the engine surface to the cabinet air – while also increasing heat losses through the cabinet walls). Electrical internal parasitics can be measured by subtracting the electrical power produced at the alternator/generator from the 220 VAC power exiting the cabinet. Mechanical internal parasitics are of a more theoretical nature, as they can only be estimated (for example, by externally motoring the engine without auxiliaries attached, or using estimates of alternator and water pump

efficiency). In the present work, parasitics internal to the prime mover were not measured or estimated since a system-approach was taken.

Parasitic loads dissipated outside the prime mover boundary are usually partially within the CHP system, dissipating some energy to the system and some to the building (e.g. the PM-tank water circulation pump, which adds some of its energy to the water travelling through it and some to the building air surrounding it).

Parasitic loads dissipated inside the building are not complete losses of energy during the heating season: they are conversion of mechanical/electrical energy to heat energy. However, during the cooling season only the parasitics internal to the prime mover have this benign characteristic; parasitics dissipated outside the prime mover and inside the building are worse than complete losses because they convert useful mechanical/electrical energy into heat that must then be removed from the space by an HVAC system.

Thus, for installations in heating-dominated climates, parasitic losses internal to the building are relatively unimportant. For installations that will operate a large number of hours during the cooling season, minimizing these building-internal parasitic losses is much more important. For cooling-dominated installations, it may be prudent to locate the isolation transformer, and maybe even the whole CHP system, outside of the building to be cooled.

4.5 Heat pump energy balance

Two energy balances were calculated in real time for all tests on the heat pump. An overall energy balance was based on a control volume that encompasses all four vacuum chambers, and an additional energy balance on the chilled water loop compared

the energy added by the pump and electric heater to that removed in the evaporator coils. Descriptions of each with experimental results are presented below.

4.5.1 Overall energy balance

The energy into the evaporator and desorber should equal the heat removed from the condenser and adsorber. The only complicating factors for this energy balance are the heat gains to the evaporator, and heat losses from the ad/desorber and condenser chambers. The ad/desorber chambers were insulated with ½” thick Armacell insulation around all metal surfaces, while the condenser and evaporator had 1” thick Armacell around the entire surface including flange and Lexan cover. The recirculated refrigerant lines also had insulation with 1” or greater wall thickness.

The overall energy balance for all tests is shown as a function of rejection temperature in Figure 95. These results have not been corrected for estimated heat losses. Except for a few outliers (which occurred before insulation was finished), the results lie within 5%. Furthermore they are consistently positive. This is consistent with the expectation that the heat lost from the three chambers above ambient temperature (which require additional heat input to the system) will be greater than the heat gained to the one chamber below ambient temperature.

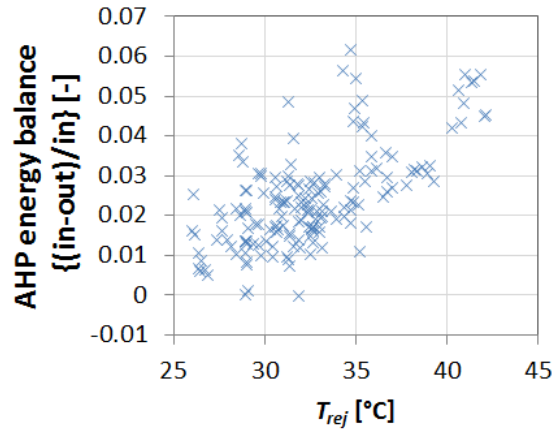


Figure 95: Overall chiller energy balance for steady state tests

The overall energy balance is shown for about 45 minutes of a steady state test in Figure 96. A moving average of one half cycle duration was applied. Note that an upward or downward spike in the energy balance occurs with each adsorption/desorption switch. This is due to an asymmetry in the plumbing of the adsorber HXs which will be explained shortly (see discussion before Figure 98).

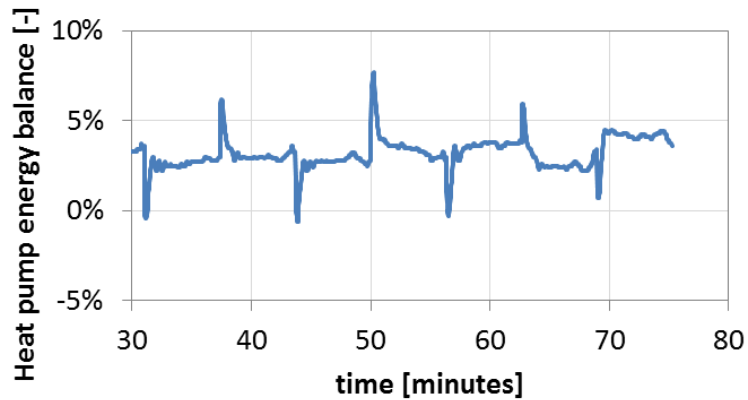


Figure 96: Overall chiller energy balance during a steady state test

The overall energy balance is shown for the load following test with a 10-minute moving average applied in Figure 97. The average value over the full 120 hours was +1.2%.

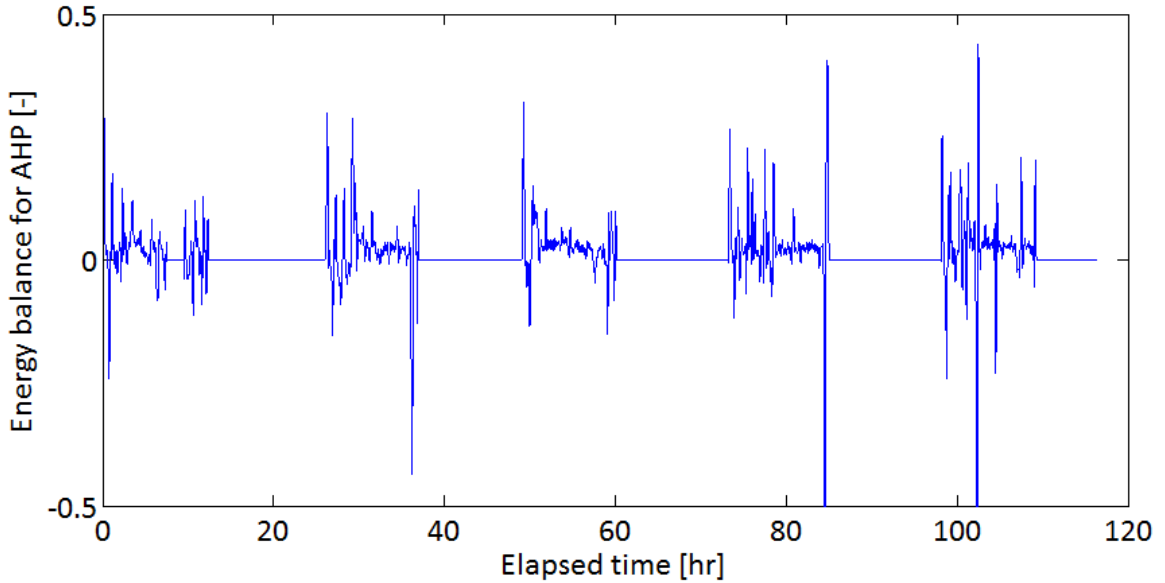


Figure 97: Overall chiller energy balance for 5-day load-profile test

Regarding the asymmetry in heat recovery: during the heat recovery phase, one of the adsorber HXs receives fluid that has passed through extra plumbing and the relatively bulky cast iron centrifugal pump that pumps the HTF during heat recovery (see Pu5 and associated lines in Figure 48, and note that the physically implemented distance to Pu5 is much longer than shown in the schematic). This pathway has considerably more thermal mass (especially including the HTF charge of the line itself) than the other half of the HR HTF pathway. Due to thermal energy asymmetrically stored in this way, a deficit of heat is measured into one heat exchanger each time it is heated during heat recovery, followed by a corresponding excess into that heat exchanger during cooling in the next heat recovery phase. The effects of this asymmetrical thermal mass are clearly visible in Figure 98. This figure shows measured data from two complementary periods of heat recovery, each lasting about 45 seconds. For clarity, the plot skips several minutes of normal ad/desorption that occurred between the two heat recovery phases. In the first half of the figure, the right adsorber is being preheated by heat recovery. The inlet temperature to the right adsorber slowly rises to a peak after about 27 seconds of heat

recovery. In contrast, in the second half of the figure, the left adsorber is being preheated. Within 2 seconds of the onset of heat recovery, its inlet temperature rises to about 85% of its peak temperature change.

Another way to see this is to observe that the right outlet is almost identical in temperature to the left inlet, whereas there is a large lag between the left outlet and right inlet.

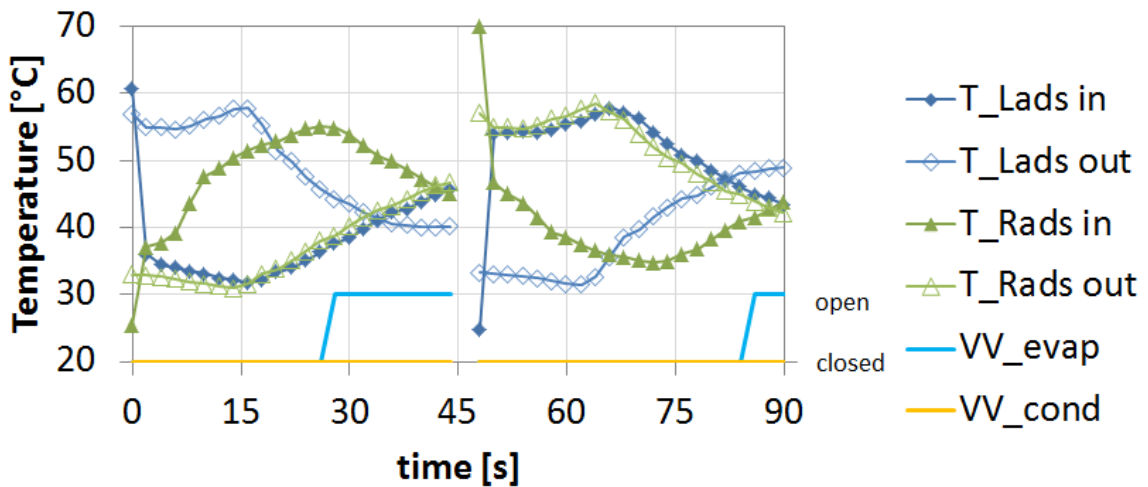


Figure 98: Temperature profile of two heat recovery events

Incidentally, another effect clearly visible in Figure 98 is the residence time of the heat exchangers at the heat recovery flow rate of 0.250 kg/s. There is clearly a 15 second delay before a step change in inlet temperature results in any change in the outlet temperature.

Another effect visible in Figure 98 is the opportunity for isobaric heat recovery. The vapor valve between evaporator and adsorber (VV_{evap}) opens around 25 seconds into heat recovery for the left adsorber (about 35 seconds for the right adsorber). The opening is triggered by an equalization of pressures in the adsorber and evaporator. It happens much sooner in the left adsorber which does not have the heat recovery HTF thermal mass penalty.

4.5.1 Chilled water energy balance

An energy balance on the chilled water line was also carried out. In this case, the chilled water capacity (Q_{CHW}) should be equal to the electrical resistance heat added to the chilled water plus the pump energy added to the CHW. Note that, since all surfaces of the pump are below ambient temperature, all electrical energy into the pump (65 W) goes to the chilled water. This pump energy has been included with the electrical resistance heat in the values shown here. The values shown here have not been corrected for estimated heat gains through the surfaces of the evaporator and refrigerant recirculation lines. The evaporator energy balance was generally better than 5% except for the low capacity cases, as shown in Figure 99.

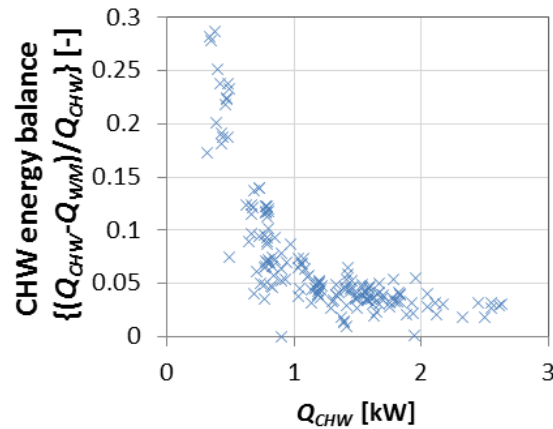


Figure 99: CHW energy balance for steady state tests

The poor energy balance at low capacity can be explained by the heat gains to the chilled water getting large. The heat gains [kW] can be seen to be a fairly linear function of chilled water temperature in the left of Figure 100, as would be expected for heat gains from the ambient. The heat gains are also seen to be fairly independent of Q_{CHW} in the right of Figure 100, with a possible slight trend towards higher gains at lower capacities only due to the correlation between low T_{CHW} and low capacity. The poor energy balance

at low capacities is thus a valid result of low capacity operation, and no attempt was made to correct for it.

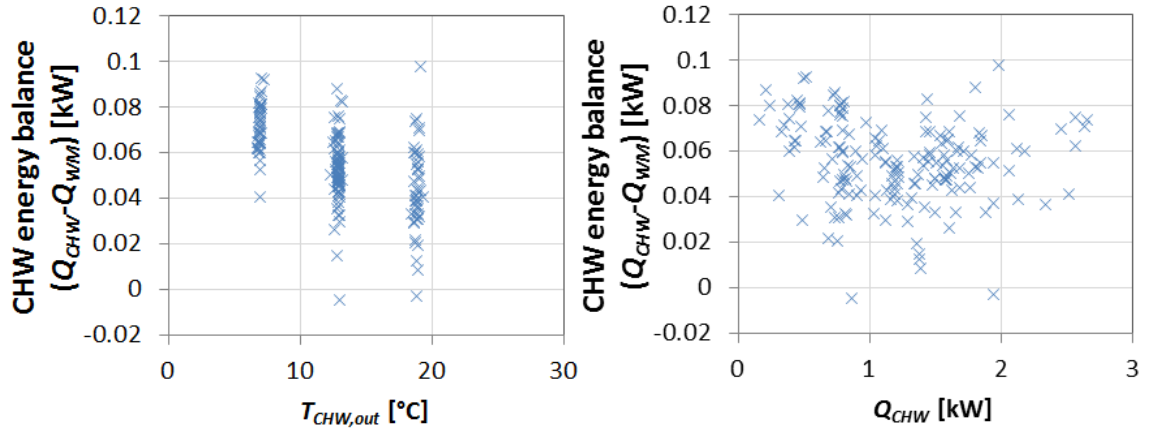


Figure 100: CHW dimensional energy balance vs. T_{CHW} and Q_{CHW}

4.6 Buffer tank energy balance

The water storage buffer tank has one mode of heat gain, three modes of heat loss, and also has heat storage, as shown in Equation (60). The prime mover is the only source of heat gains, while heat losses occur to the space heating loop, domestic hot water loop, and by losses through the insulated walls.

$$EBal_{tank} = E_{in} - E_{out} - E_{store} = Q_{PM} - Q_{SH} - Q_{DHW} - Q_{loss} - E_{store} \quad (60)$$

This energy balance has units of energy and would equal zero for perfect measurements. It is valid both for steady state and transient modes of tank operation, and was applied both instantaneously and over time-averaged periods.

Each term in Equation (60) was measured as follows. Heat exchanges with the prime mover (Q_{PM}), space heating loop (Q_{SH}), and domestic hot water loop (Q_{DHW}) were directly measured using flow meters and differential temperature measurements. To estimate the heat loss through the tank walls (Q_{loss}), an empirical correlation was

developed as a function of average tank temperature (see Figure 101). The energy storage term (E_{store}) was measured with 13 thermocouples distributed vertically in the tank, as will be described following the Q_{loss} description.

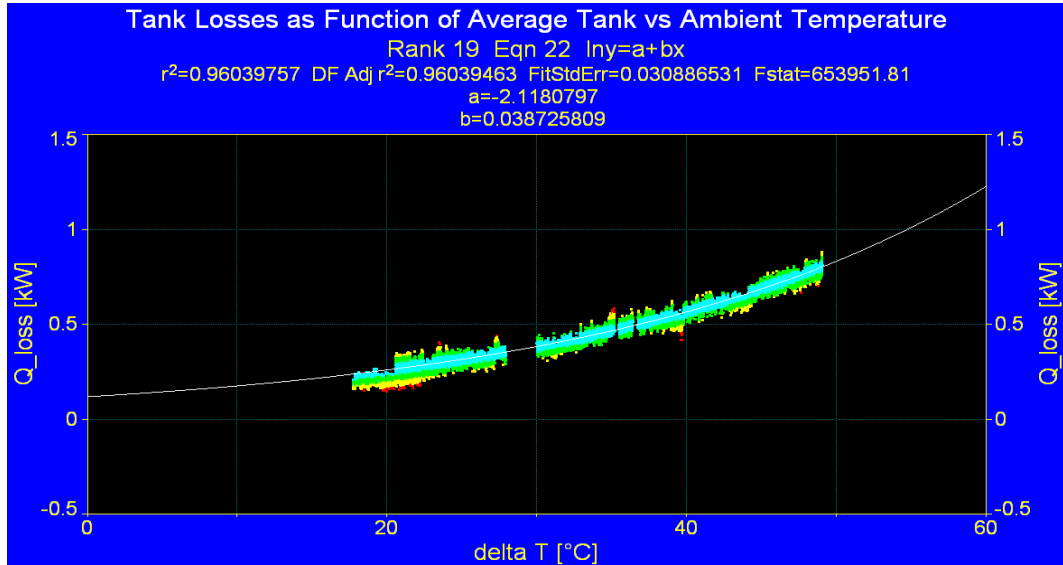


Figure 101: Tank heat losses as function of difference in temperature between average tank temperature and surrounding air temperature

The exponential correlation for tank losses was determined by first fully heating the tank to $\sim 70^\circ\text{C}$, then ceasing all water flows into and out of the tank, so that natural convective losses from the insulated tank surfaces was the only heat transfer mode affecting the tank. Under this condition, then tank was allowed to cool over the course of ~ 2 days, and the temperature at all 13 vertical tank locations was recorded every 10 seconds over that time interval. The average tank temperature at each measurement interval could then be calculated based on a modified version of Equation (64). The ambient air temperature surrounding the tank was subtracted from this average tank temperature to obtain the ΔT relevant to natural convection from the tank surface to the air. Additionally, by using finite differences in the value of energy stored from one timestep to the next, the heat lost from the tank could be calculated. In practice this had to

be averaged over ~15 minutes in order to make the data less noisy. The gap seen in Figure 101 in the region of $\Delta T \approx 24^\circ\text{C}$ was due to an open window which affected the ambient temperature measurement, making the ΔT calculation extremely noisy. This region was therefore eliminated from the curve-fitting calculation.

The exponential correlation has a standard deviation of only 31W, or roughly 4% to 12% relative error, depending on the magnitude of the ΔT .

The amount of thermal energy stored in the tank at any given time was estimated based on the 13 temperature measurements taken throughout the tank, which were located as shown previously in Figure 43.

The four in-stream temperature measurements were used directly, whereas a correction was applied to the 9 surface temperature measurements to make them directly comparable to the in-stream values. This was done by placing two additional and redundant surface thermocouples (for a total of 15) at the same vertical location as two of the in-stream thermocouples, to establish the temperature difference between in-stream and surface measurements, normalized by the difference between surface and ambient temperatures. This normalized difference was defined as β :

$$\beta = \frac{T_{surf,meas} - T_{is,meas}}{T_\infty - T_{surf,meas}} \quad (61)$$

This factor was then applied to all 9 independent surface measurements as shown in Equation (62) to obtain their equivalent in-stream values.

$$T_{is,equiv} = T_{surf} + \beta(T_\infty - T_{surf}) \quad (62)$$

Tank temperature measurements were taken at 13 distinct vertical locations, including one at the top-most surface of the tank, and one at the bottom-most surface of

the tank. The average temperature of each adjacent pair of measurements defines a node temperature; thus there are 12 nodes. The temperature of each node is defined as a simple average:

$$T_n = \frac{T_i + T_{i+1}}{2} \text{ for } i = n = 1 \text{ to } 12 \quad (63)$$

The energy stored in the tank is the sum of the energy stored in all 12 nodes:

$$E_{sto} = \sum_{n=1}^{12} (T_n - T_{ref}) C_{P,n} V_n \quad (64)$$

where n is the node number, $C_{P,n}$ is the volumetric heat capacity of water at the temperature of the n^{th} node, and V_n is the volume of node n .

4.6 Other energy balances

Due to the often very low water flow rate out of the tank to the space heating loop, problems were encountered trying to achieve accurate flow measurements. Thus the rate of heat removal from the tank (low mass flow rate; high ΔT) was compared to the heat rejected on the other side of the mixing valve into the plate heat exchanger (high mass flow rate; low ΔT) to verify the space heating heat flow. This energy balance was monitored in real-time and recorded in the data acquisition files.

Chapter 5: Experimental Results and Control Strategies

Steady state and load-following experiments were conducted on both the CHP and CCHP systems. In addition, a control strategy for the adsorption heat pump was developed. In this chapter, first the engine performance map is presented, followed by load-following tests for the engine in a combined heat and power configuration. Then the performance map of the adsorption chiller and its control strategy are discussed. Lastly, the combined cooling, heating and power load profile test is presented.

5.1 Steady state experimental results for engine

To provide calibration data for the CCHP simulations, the engine was tested in steady state mode to develop a performance map. The map characterizes the relevant metrics of the engine as a function of all relevant variables. Testing revealed that performance could be very well described as a function of two variables: the part load ratio and the heat recovery temperature.

5.1.1 Performance metrics

For the engine performance, First Law efficiencies are used for electric, heat recovery, and overall fuel utilization rate, as in Equations (65) – (67) below. Note that “heat recovery” for the prime mover is completely unrelated to “heat recovery” for the adsorption chiller.

$$\eta_{electric} = \frac{\dot{V}}{\dot{Q}} \quad (65)$$

$$\eta_{HR} = \frac{\dot{Q}_{out} - \dot{Q}_{in} + \dot{Q}_{return}}{\dot{Q}_{in}} \quad (66)$$

$$\eta_{overall} = \frac{\dot{W}_{net}}{\dot{Q}_{in}} \quad (67)$$

5.1.2 Performance maps

Following screening tests that identified the most important variables to test, the steady state test matrix shown in Table 29 was run on the engine.

Table 29: Test matrix for steady state prime mover performance mapping

Test #	kRPM	Supply T [°C]	Return T [°C]	Pump speed	Test # cont'd	kRPM	Supply T [°C]	Return T [°C]	Pump speed
1	3.4	(float)	65	high	41	3.4	75	(float)	low
2			60		42		70		
3			55		43		65		
4			50		44		60		
5	2.7		50		45	60			
6			55		46	65			
7			60		47	70			
8			65		48	75			
9	2.1		65		49	75			
10			60		50	70			
11			55		51	65			
12			50		52	60			
13	1.6		50	53	60				
14			55	54	65				
15			60	55	70				
16			65	56	75				
17	1.2		65	57	75				
18			60	58	70				
19			55	59	65				
20			50	60	60				
21	1.2	50	61	60					
22		55	62	65					
23		60	63	70					
24		65	64	75					
25	1.6	65	65	75					
26		60	66	70					
27		55	67	65					
28		50	68	60					
29	2.1	50	69	60					
30		55	70	65					
31		60	71	70					
32		65	72	75					
33	2.7	65	73	75					
34		60	74	70					
35		55	75	65					
36		50	76	60					
37	3.4	50	77	60					
38		55	78	65					
39		60	79	70					
40		65	80	75					

The lowest RPM tests (representing 16 experiments) in this matrix were not run due to the instability of the engine at that speed. Thus, 64 tests were run from the test

matrix. In addition to these, another 28 tests were run at intermediate engine speeds (1400, 1800, 1900, 2000, 2300, 2400, 3000, and 3200 RPM). Thus the total number of tests conducted was 92.

It should also be pointed out that some repeat tests are effectively built into the original 64 tests in the matrix. For example, at certain RPMs and flowrates, the temperature rise through the prime mover is almost exactly 10°C. Since the temperature interval in the matrix is in multiples of five, some tests are effectively identical, for example, test numbers 33 and 48. This leads to the test matrix having 58 distinct test conditions rather than 64.

The results of the steady state test matrix were used to develop empirical curve fits. All possible dependent variables were plotted as functions of various numbers of independent variables. Many functional forms were tried, although in most cases, simple polynomial functions gave the best fit. The best fits for each dependent variable are presented in the following sections. The main criterion for evaluating fit was the root mean square error (RMSE).

The dependent variables investigated were:

1. Electricity production
2. Thermal production (i.e. heat recovery capacity)
3. Fuel consumption
4. Electrical efficiency (the quotient of 1 and 3 above)
5. Thermal efficiency (the quotient of 2 and 3 above)
6. Combined efficiency (the sum of 4 and 5 above)

The potential independent variables investigated for each dependent variable

were:

1. Engine RPM (explicit in test matrix)
2. Supply temperature (explicit in test matrix)
3. Return temperature (explicit in test matrix)
4. Water flow rate (explicit in test matrix)
5. Ambient temperature (a nuisance variable)
6. Cabinet interior temperature (dependent on 1-5 above)
7. Engine air intake temperature (dependent on 1-5 above)

Table 30: Variables and functional forms resulting in best fits for each dependent variable

Dependent variable	x	y	Functional form of best fit function	RMSE	R^2
E_{elec}	RPM	T_{supply}	$E_{elec} = p_{00} + p_{10}x + p_{01}y + p_{20}x^2$	0.0479	0.9968
Q_{HR}	RPM	T_{supply}	$Q_{HR} = p_{00} + p_{10}x + p_{01}y + p_{20}x^2$	0.136	0.9969
$Q_{HHV,1}$	RPM	T_{supply}	$Q_{HHV} = p_{00} + p_{10}x + p_{01}y + p_{20}x^2$	0.191	0.9976
$Q_{HHV,2}$	RPM	$T_{inlet\ air}$	$Q_{HHV} = p_{00} + p_{10}x + p_{01}y + p_{20}x^2$	0.190	0.9976
η_{elec}	RPM	T_{return}	$\eta_{elec} = p_{00} + p_{10}x + p_{01}y + p_{20}x^2$	0.467	0.851
η_{HR}	RPM	T_{supply}	$\eta_{HR} = p_{00} + p_{10}x + p_{20}x^2 + n_{01}y^{-1}$	1.14	0.36
$\eta_{comb,1}$	RPM	$T_{ambient}$	$\eta_{comb} = p_{00} + p_{10}x + p_{01}y + p_{20}x^2 + p_{11}xy + p_{02}y^2$	1.38	0.67
$\eta_{comb,2}$	RPM	T_{supply}	$\eta_{comb} = p_{00} + p_{10}x + p_{01}y + p_{20}x^2 + p_{02}y^2$	1.44	0.64

Table 31: Coefficient values for Table 30

	E_{elec}	Q_{HR}	$Q_{HHV,1}$	$Q_{HHV,2}$	η_{elec}	η_{HR}	$\eta_{comb,1}$	$\eta_{comb,2}$
p_{00}	-1.078	1.930	3.050	3.662	3.032	48.05	12.12	89.52
p_{10}	0.002035	0.003172	0.005089	0.005478	0.01096	0.004275	0.0193	0.01543
p_{01}	-0.388e-3	-0.02305	-0.02663	-0.04310	0.005365	0	2.707	-0.9346
p_{20}	-1.319e-7	1.640e-7	2.679e-7	2.128e-7	-1.879e-6	-5.969e-7	-2.943e-6	-2.524e-6
p_{11}	0	0	0	0	0	0	-6.408e-5	0
p_{02}	0	0	0	0	0	0	-0.04313	0.006435
n_{01}	0	0	0	0	0	322	0	0

Electrical efficiency is primarily a function of RPM, with some dependence on the supply and return temperatures. The goodness of fit indicators for electrical efficiency are significantly weaker than for either electricity production or fuel consumption. The best fit is obtained by plotting electrical efficiency as a second-order function of RPM, and introducing a linear term as a function of supply temperature makes a small improvement.

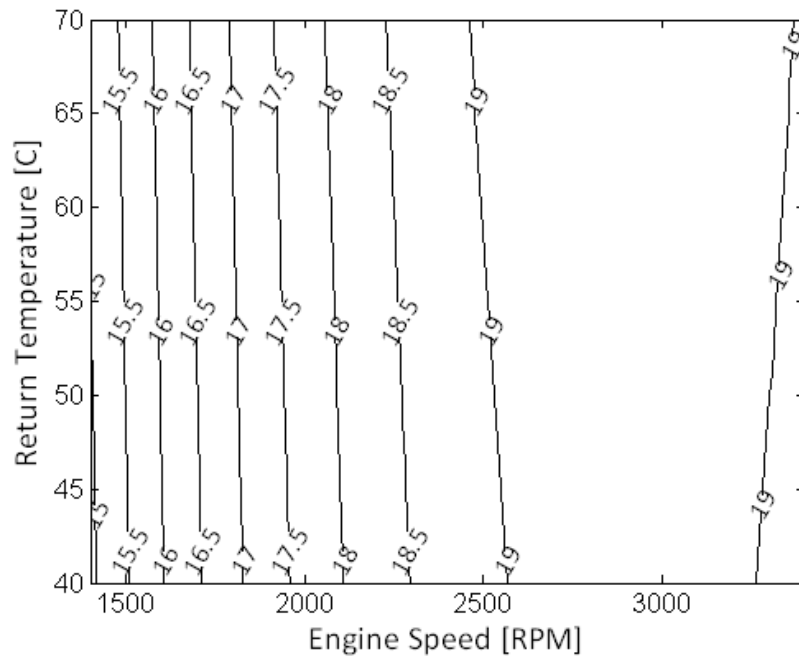


Figure 102: Contours of electrical efficiency [%HHV] as a function of engine speed and return water temperature

The best curve fit for heat recovery efficiency is second order in engine speed and first order in inverse supply or inverse return temperature. However, even this four coefficient model has an RMSE of more than one percentage point, with maximum residuals of about 3 percentage points.

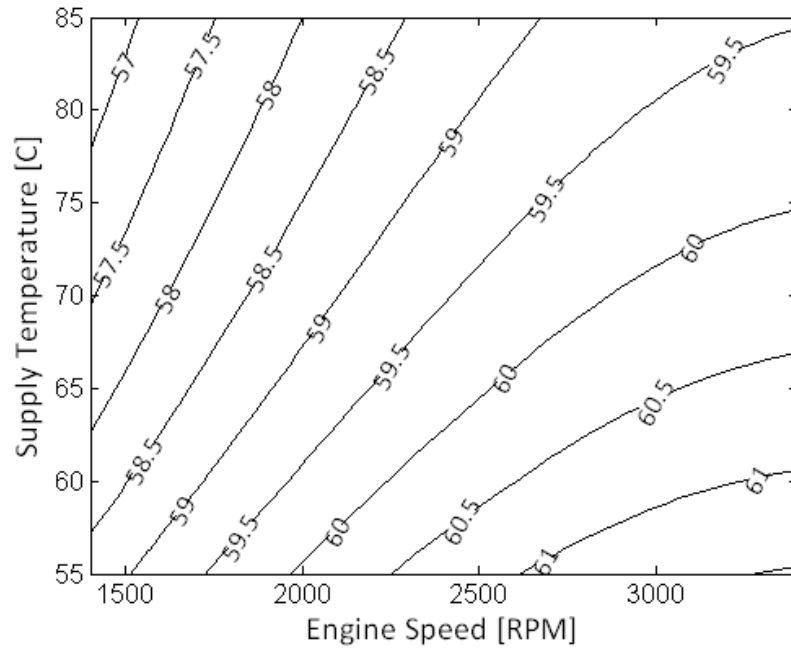


Figure 103: Contours of heat recovery efficiency [%HHV] as a function of engine speed and supply temperature

The combined efficiency curve fit reveals the tradeoff between electrical and heat recovery efficiency for different supply temperatures. As described above, electrical efficiency increases with supply/return temperatures, while heat recovery efficiency declines.

5.1.3 Allocation of measured outputs

The allocation of measured outputs were distributed according to Figure 104. For part load operation, losses become proportionally larger compared to the fuel input. Since the heat recovery fluid stays at about the same temperature (along with the engine and

cabinet surface temperatures), the absolute magnitude of convection and radiation losses is roughly constant for all engine speeds.

Another effect apparent at low part load operation is that the bulk of the heat recovery comes from the engine coolant instead of the exhaust gas recuperator. This is to be expected, as lower RPM operation corresponds to lower exhaust gas temperature and less available heat in the exhaust; and slower piston speed means longer residence time of the hot gases in the cylinder.

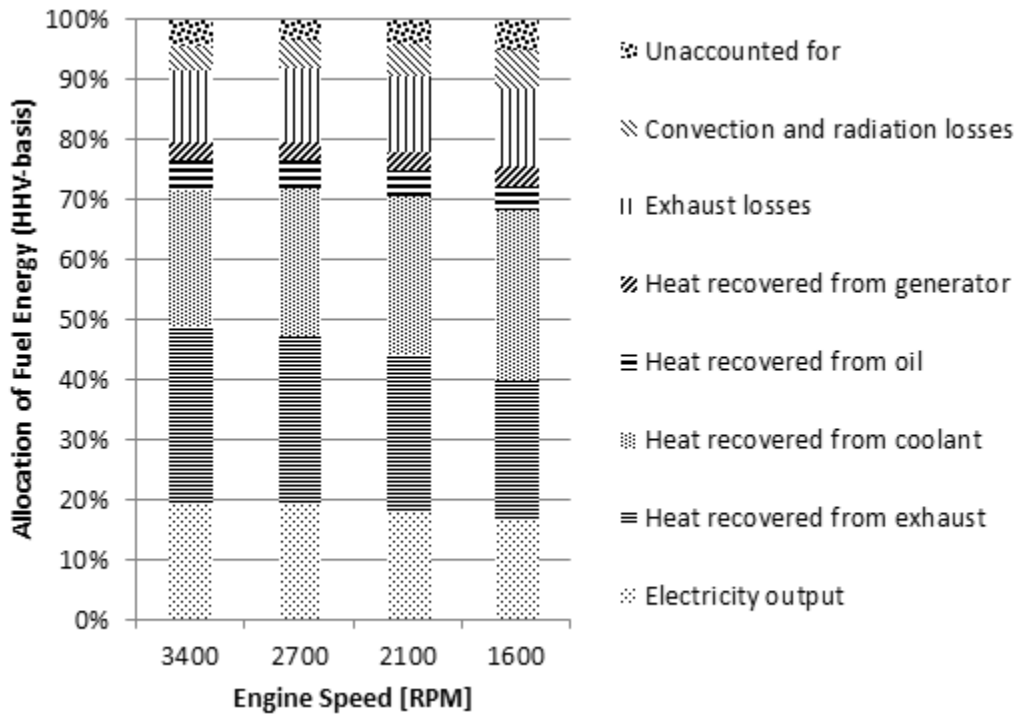


Figure 104: Allocation of fuel input (HHV) for various speeds

5.1.4 Engine instrumentation energy balance

The energy balance (defined in Equation (41)) had a typical systematic error of 5.1 percentage points. This uncertainty value ranged from 4.3 to 6.3 percentage points, depending on operating conditions. Additionally, the random error in the energy balance throughout the course of a typical test was about 1 percentage point. The energy balance

results, with associated total absolute uncertainty bars, are presented in Figure 105. The energy balance had no correlation with ambient temperature, suggesting that the dependence of energy losses on ambient temperature were well captured. Looking at the plot of energy balance vs. engine speed, it is apparent that certain engine speeds had much less variation than others. This may be due to variability in how the engine runs at different RPMs. In particular, it was noted that the engine RPM fluctuated significantly around its set point during 1600 RPM operation, while being steadiest at the 2100 and 3400 RPM settings.

The energy balance for 81% of the tests lies within its error band of the zero line. For the remaining 19% of the tests, the error band on the energy balance does not encompass zero.

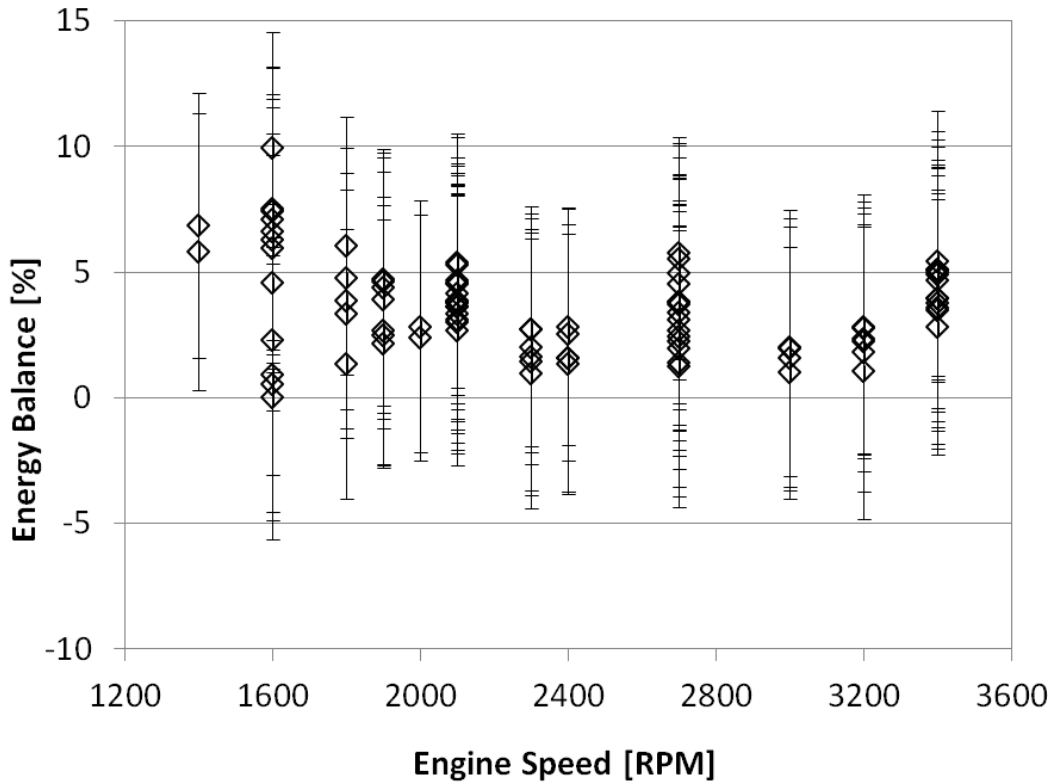


Figure 105: Energy balance plotted against engine speed for all 92 steady state tests

There are three possible explanations for why the energy balance is consistently too high: (1) the fuel input could have been overestimated (2) the outputs could be underestimated or (3) there could be un- or under-accounted for losses.

Any of these three explanations could be caused by a systematic measurement error. If the systematic uncertainty associated with that measurement is too small, then the error bars will not reach the zero line.

For example, if the systematic uncertainty in the RTDs measuring supply and return water temperature are taken as $\pm 0.5^{\circ}\text{C}$ instead of $\pm 0.2^{\circ}\text{C}$, then the average uncertainty in energy balance would increase from 5.1 to 6.7 percentage points. Under this scenario, 97% of the data would have error bars which encompass the zero line, consistent with the 95% confidence interval associated with the error bars. Of course this would not correct the distribution of the data, but it would mean that the data is consistent with the stated measurement accuracy.

5.1.5 Comparison with others' data

The Ecopower unit was also tested by Bernd Thomas (Thomas, 2008) at Reutlingen University in Germany. In this work, data was taken based on a LHV basis. Efficiencies were reported at full load and 50% load, and also plotted as functions of supply temperature (while holding return temperature fixed at 55°C). The reported LHV-basis values have been adjusted to HHV-basis assuming a HHV:LHV ratio of 1.11. This value was calculated based on the gas composition reported as average by Washington Gas.

A graphical comparison is made between the two experimental setup results in Figure 106 and the data is also tabulated below.

Table 32: Full load comparison of results between CEEE and B. Thomas

	B. Thomas (LHV)	B. Thomas (HHV)	Ecopower (LHV)	Ecopower (HHV)	CEEE (HHV)
η_{elec} full load	24.7%	22.2%	~25%	~ 22.5%	18.8%
η_{HR} full load	64.2%	57.8%	~65%	~ 58.6%	59.9%
η_{comb} full load	88.9%	80.1%	~90%	~ 81.0%	78.7%

Table 33: Part load comparison of results between CEEE and B. Thomas

	B. Thomas (LHV, 50% load)	B. Thomas (HHV, 50% load)	CEEE (HHV, 58% load)
η_{elec} part load	24.0%	21.6%	17.9%
η_{HR} part load	60.5%	54.5%	58.7%
η_{comb} part load	84.5%	76.1%	76.6%

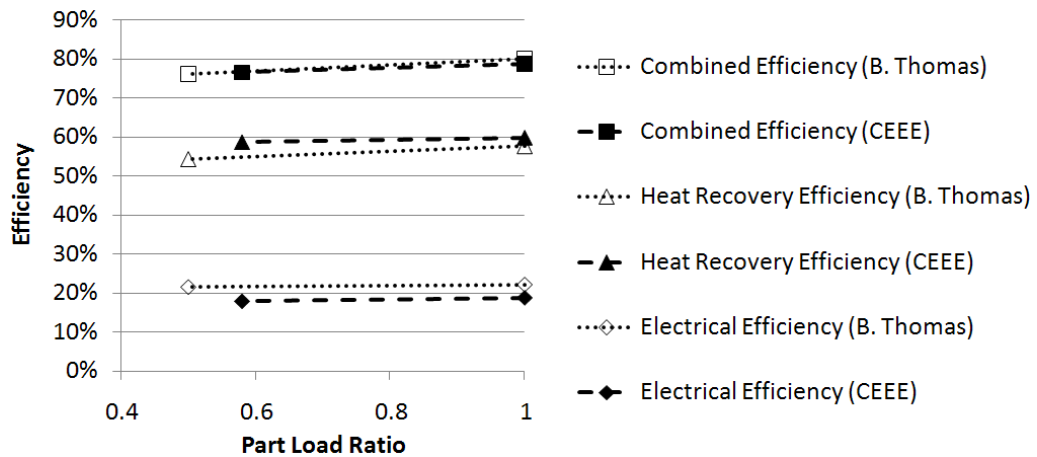


Figure 106: Comparison of CEEE results with B. Thomas' results for two part load ratios

In terms of the combined efficiency, the experiments are in very good agreement with each other. However, the individual efficiencies are different. The thermal efficiency discrepancy is just within that value's uncertainty, while the electrical efficiency discrepancy is greater than its uncertainty.

One possibility for the discrepancy between the electric efficiency values is the use of 208 VAC power in the CEEE lab. The unit was untested by the manufacturer at this voltage, and may suffer an efficiency penalty as a result. Different generator control

strategies and power conversion/conditioning electronics might also be used in the US version compared with the EU version tested in Germany.

Another possible contributor to the discrepancy between the efficiency values is that the temperature conditions are not specified under which B. Thomas' "full load" measurement were taken. The highest recorded electrical efficiency in the CEEE lab was 19.3%.

One last possible source of discrepancy is inconsistency in the data reported by B. Thomas: tabulated data lists full load electrical efficiency as 24.7% and half load as 24.0%. However, the data versus supply temperature graph shows a peak value of about 23.7% electrical efficiency.

Figure 107 compares the data that B. Thomas presented as functions of supply temperature with the results from the CEEE lab. These data are not directly comparable, because B. Thomas held the return temperature fixed at 30°C for all of these tests, whereas the return temperature varied from 45 to 55°C for the CEEE results shown.

The lowest supply temperatures (below 55°C) were not explored in the test matrix because they were considered as impractically low. However, perhaps a wider range of temperatures in the test matrix would help bring out the temperature-dependent trends for the purpose of curve fitting.

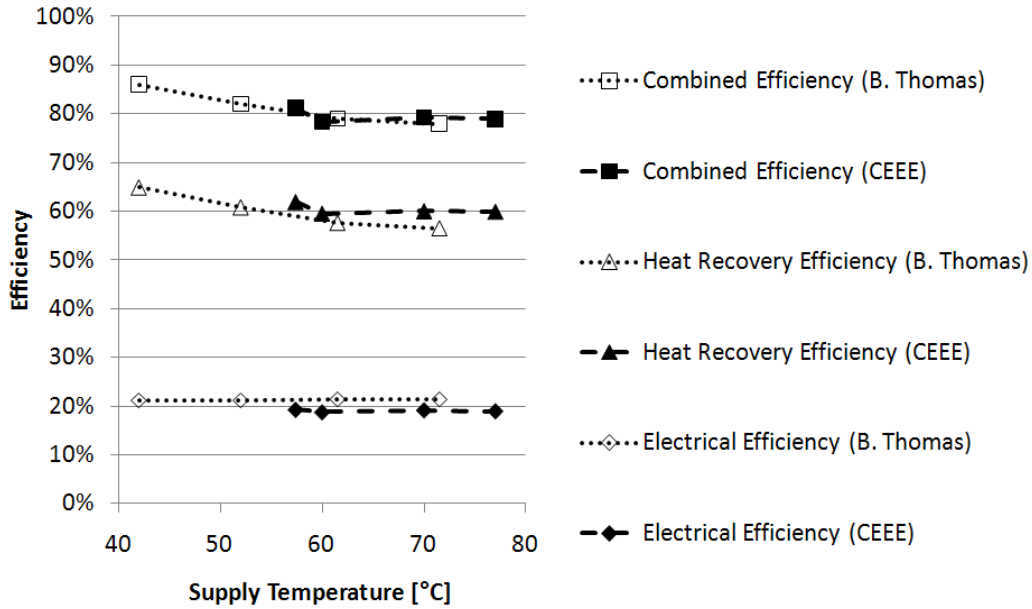


Figure 107: Comparison of CEEE results with B. Thomas' results for supply temperature

5.1.6 Proposed improvements to heat recovery

Two modifications to the heat recovery in the engine are proposed. The first would increase heat recovery efficiency while keeping the supply water temperature constant. The second would increase both the heat recovery efficiency and the supply water temperature (but would involve more complexity than the first modification).

The combined efficiency of the Ecopower unit, about 85-90% (LHV) or 75-80% (HHV), is lower than for condensing furnaces. This can be attributed to two factors: the exterior dimensions of the prime mover engine and cabinet are each much larger than a furnace cabinet (implying larger surface convective and radiative losses to ambient), and the exhaust outlet temperature from the cabinet is not low enough to condense out water. The cabinet is quite well insulated, evidenced by the fact that most of the heat losses are in the exhaust (see Figure 104). Aside from more insulation, there is little that can be done to reduce the convective and radiative losses from the cabinet, especially since the coolant temperature (which strongly influences the engine surface temperature and

therefore cabinet wall temperature) cannot be lowered without adversely affecting the electrical efficiency and reliability and operational life of the engine. On the other hand, additional heat could be captured from the exhaust.

At first glance, since the engine coolant temperature is about 70°C and the dewpoint of the exhaust is about 60°C, it would seem that little can be done to condense water out of the exhaust. However, modifications to the heat recovery plumbing and control may allow exhaust heat to be condensed.

Figure 108 shows the current heat recovery scheme. By inspection, it can be seen that the lowest achievable exhaust outlet temperature in the most ideal case (0 K approach temperature and zero heat from the generator and oil cooler) would be 60°C, not low enough to condense significant amounts of water. The coolant flows through the exhaust gas HX before the cooling jackets in order to achieve a lower exhaust gas outlet temperature, since the temperature of coolant in the cooling jackets is fixed by engine reliability requirements.

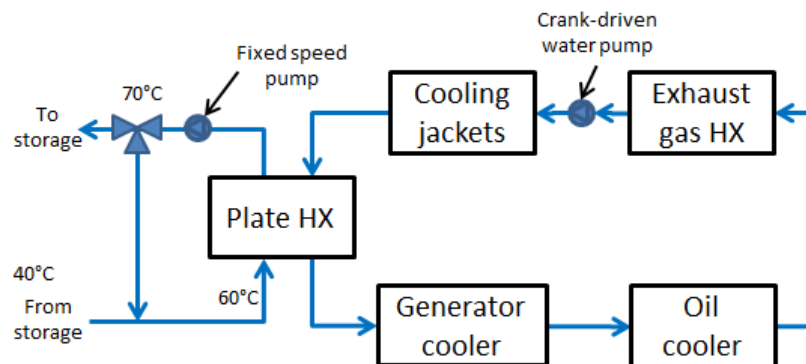


Figure 108: Current heat recovery scheme for Ecopower

Figure 109 shows the first proposed method of heat recovery. By lowering the mass flow rate of the exterior loop (to/from storage), a larger temperature change is possible on the external side (for example, from 45 to 70°C instead of 60 to 70°C). By separating the exhaust heat recovery loop from the coolant/oil/generator loop, and

lowering the mass flow rate of fluid in the exhaust loop, it is theoretically possible to achieve much lower exhaust outlet temperatures. The cost of this approach is an additional pump and an additional heat exchanger (two 6 kW in place of a single 12 kW HX). However, based on a psychrometric calculation, and assuming that exhaust gas enters HX at 650°C, lowering the exhaust outlet condition at full load from 70°C dry bulb and 60°C dewpoint to 50°C dry bulb and 100% RH would increase the capacity of exhaust heat recovery by about 25% (e.g. from 5 to 6.25 kW) and the total heat recovery capacity by about 10% (e.g. from 12 to 13.2 kW). This would raise the engine fuel utilization factor from about 85% (LHV) to about 92% (LHV).

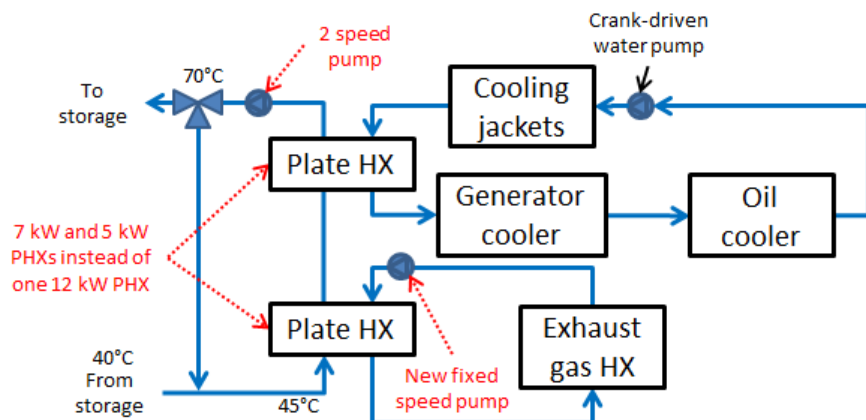


Figure 109: First proposed modification to Ecopower heat recovery

This system reduces the exergy-destroying process that previously existed of mixing cold (e.g. 30°C) water from the bottom of the tank with hot (70°C) supply water in order to obtain the desired return temperature to the engine of 60°C. Since the new desired return temperature is much lower (e.g. 45°C), the cold water that must be mixed with hot water is much reduced. The benefit of preserving this exergy shows up in the ability to extract more heat from the exhaust gases.

It must be noted that, at times, the bottom of the tank may reach temperatures in excess of 45°C. In these rare cases, either (a) the engine would be ramped down or shut

down or (b) the mass flow rate of the external fluid would need to increase in order to maintain the required capacity, effectively returning the system to the old type of heat recovery (this is the reason for specifying a two-speed pump in Figure 109). However, the normally sharp stratification present in the tank, and the fact that the tank return temperatures from DHW and SH loads are generally below 45°C, would tend to minimize the frequency of this occurrence.

Figure 110 shows the second proposed modification. This could be pursued in order to raise the supply temperature of the engine, while also improving heat recovery efficiency over the original configuration. This approach requires the same additional pump and split plate heat exchangers as the first proposed modification, plus splitting the exhaust gas HX into two sections. By separating the exhaust gas HX into low and high temperature sections, the same benefits of lower exhaust outlet temperature can be achieved from lowering the external fluid flow rate, while the high temperature exhaust gas HX can now be placed after the cooling jackets (in contrast to the original order of components) to boost the supply temperature of the engine. The limiting factor here is preventing the cooling jacket temperature from rising. If the crank-driven water pump flow rate is kept constant, then the supply temperature would increase from 70 to 75°C while maintaining the exact same temperatures and flow rate in the cooling jackets. If that flow rate could be cut in half while holding constant the cooling jacket outlet temperature, then the supply temperature would increase to 80°C.

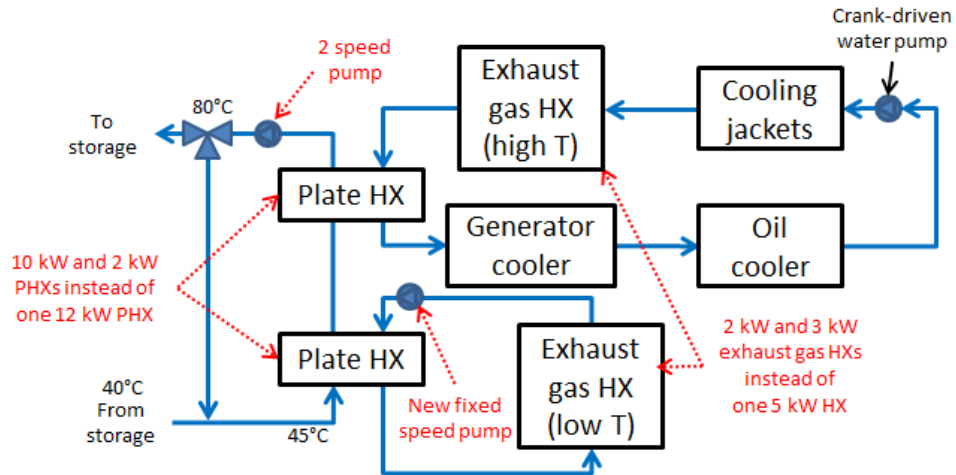


Figure 110: Second proposed modification to Ecopower heat recovery

Depending on the importance of oil temperature and generator temperature, those components could also be placed after the cooling jackets for a further boost of supply temperature, perhaps to 85°C. This higher temperature would accommodate a wider range of thermally-driven options, as well as potentially increasing the maximum temperature lift for a Z01-based adsorption chiller.

Figure 111 shows these three configurations in semi-quantitative T-Q diagrams, with an x-axis normalized to the current configuration. The return and supply temperatures are labeled on the y-axis.

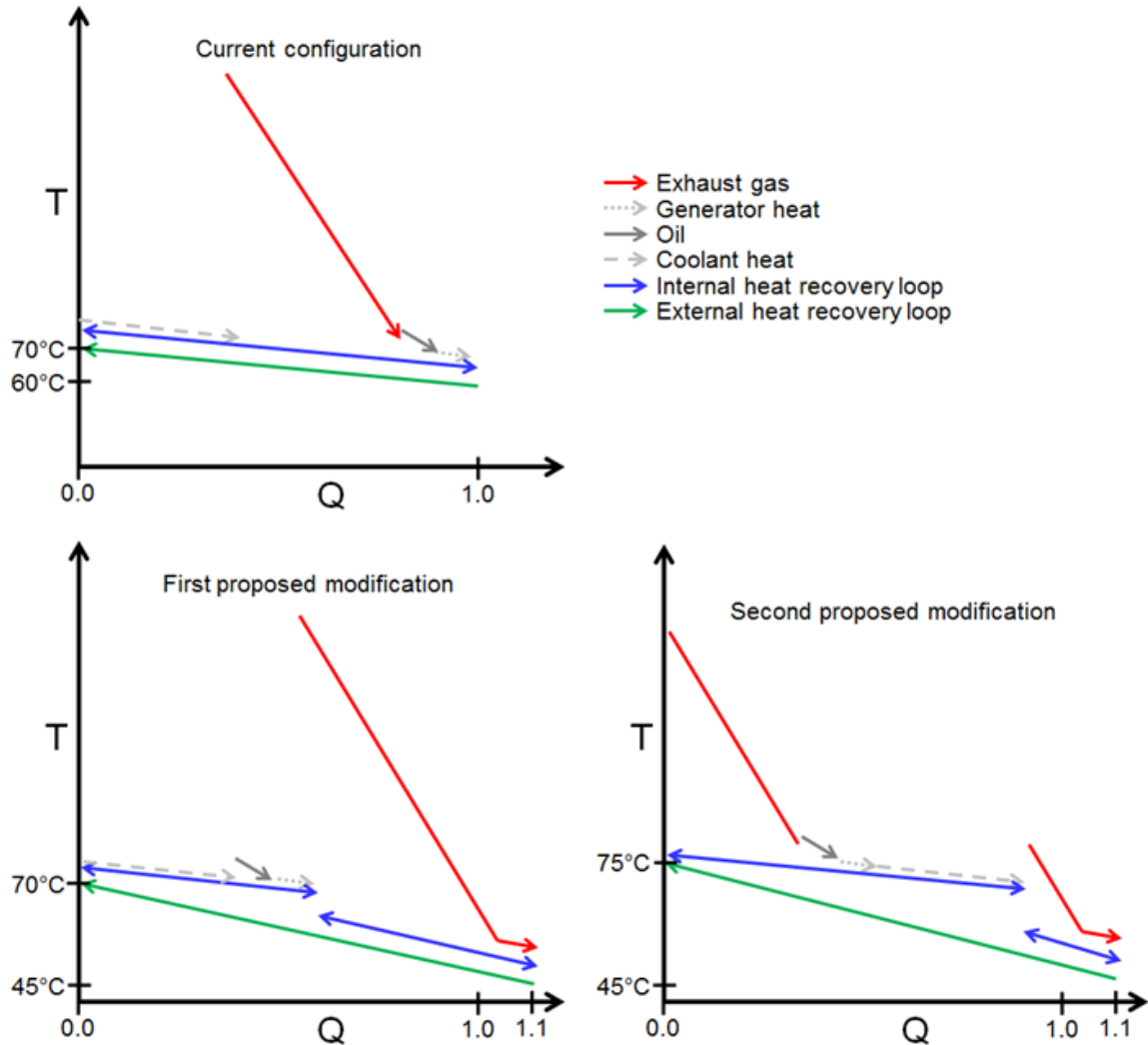


Figure 111: T-Q diagrams for current and two proposed heat recovery configurations

From Figure 111 it can be seen that, among these three options, the engine coolant is maintained at constant inlet and outlet temperatures and mass flow rates. The coolant heat results in the primary pinch point (it does so indirectly via the internal heat recovery fluid in the second proposed modification). It can also be seen that the first proposed modification increases total heat recovery by 10% by taking advantage of a larger temperature change on the external loop to recover some heat of condensation from the exhaust stream. The second proposed modification accomplishes the same increase in

heat recovery while also increasing the external fluid exit temperature to create more thermodynamically valuable waste heat.

Another possible configuration (to maximize supply temperature) is shown in Figure 112. This is a flexible configuration which would allow even higher supply temperatures at the expense of a decrease in heat recovery efficiency ($Q' < 1$), with the pinch point again occurring with the engine coolant. The maximum possible supply temperature (denoted T_H in Figure 112) will depend directly on the return temperature (denoted T_L), and rely on modulation of a variable speed pump to dynamically adjust to engine load and variations in T_L . Despite the lower heat recovery efficiency, this configuration may allow a higher overall efficiency for a dedicated combined cooling and power application by allowing a higher thermal COP device to be used. However, achieving high supply temperatures depends on the return temperature staying low. This could be made possible, for example, by a true trigeneration system which also has low return temperatures from DHW usage. Another possibility is rejecting recovered heat to ambient when high supply temperatures are required. This may prove advantageous on a yearly basis if dumping is only required a few hours per year. In the full load limit of conventional $\sim 60^\circ\text{C}$ return temperature, the supply temperature from this configuration would drop to the $\sim 75^\circ\text{C}$ of the second proposed modification in Figure 111.

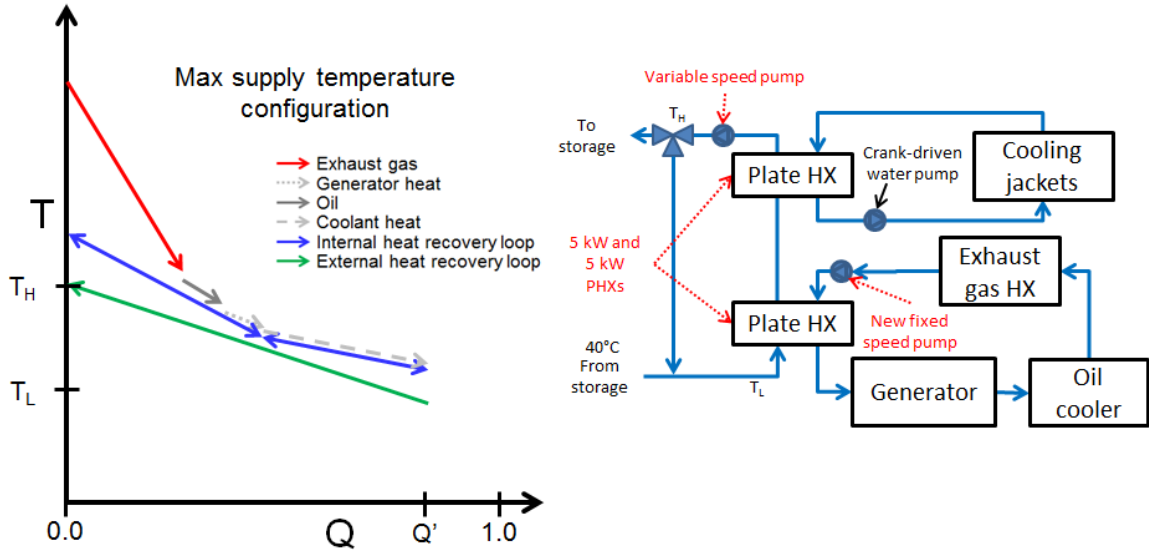


Figure 112: Maximum supply temperature configuration for ICE heat recovery

The show the maximum practical potential, one last possible configuration is shown in Figure 113. This configuration has greater complexity than all the preceding, requiring three independent internal loops.

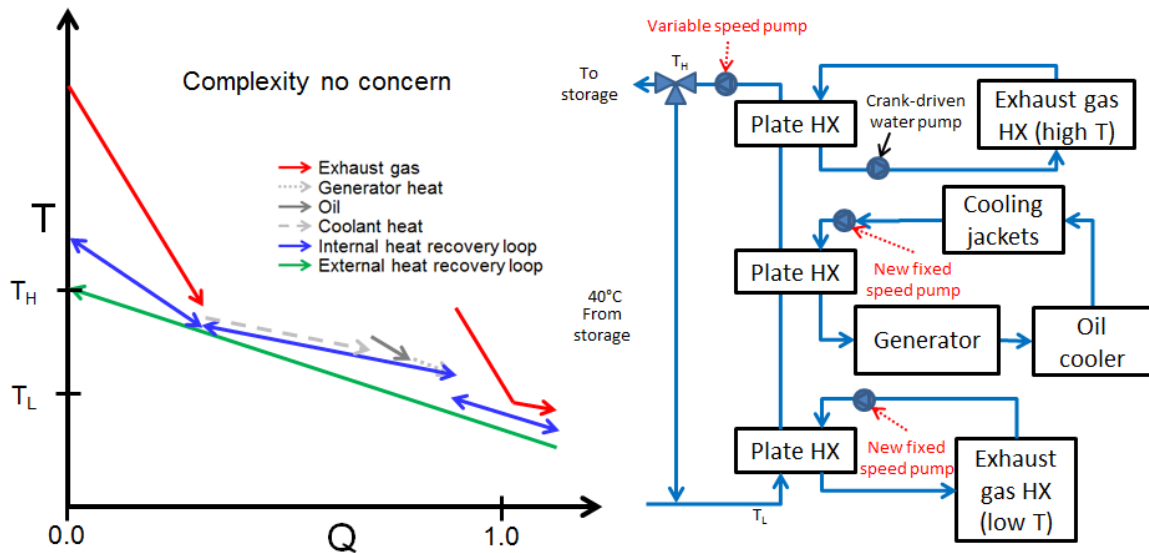


Figure 113: "Complexity no concern" configuration for ICE heat recovery

Finally, Figure 114 shows a comparison of all the preceding configurations in a max-max Pareto plot. Each configuration has two points, representing the dependency on prime mover return temperatures from 45°C to 60°C. The amount of heat recovered (per

unit fuel input) is normalized to be one for the current configuration with 60°C return temperature. The plot is fairly qualitative (it was not created from detailed quantitative calculations) and is meant to show the proper trends and relative positions.

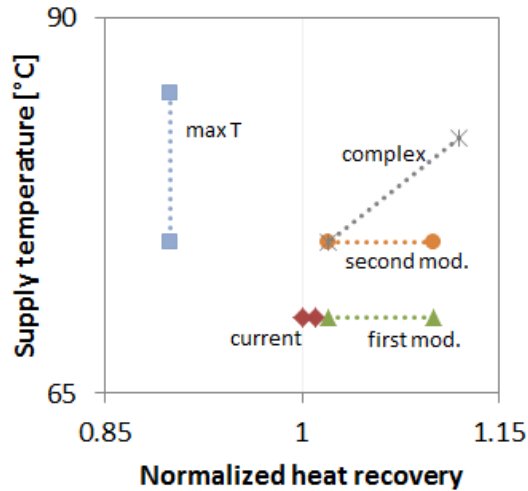


Figure 114: Comparison of relative merits of heat recovery configurations

With the exception of the “max T” configuration, the point on the right for each configuration represents the lower 45°C return temperature. In the case of “max T,” the internal fluid loop on the left side of the T-Q diagram is “floating.” This is in contrast to the others, in which internal fluid loop on the left side is fixed to the coolant heat recovery. Thus, when return temperature increases, the LMTD in the coolant plate HX increases but the LMTD in the exhaust plate HX decreases. To a first-order approximation, this has a neutral effect on heat recovery. If the “max T” configuration used a variable speed pump on the exhaust internal loop, it would actually be able to improve heat recovery at higher return temperatures.

Figure 114 does not capture the complexity or cost of each approach, but the order of complexity mirrors the ranking in the Pareto diagram as follows (simplest to most complex): current, first modification, “max T,” second modification, and “complex.”

5.2 CHP: dynamic load-following results

The performance of the CHP system under one load profile (the residential shoulder season) is shown as representative results in Figure 115 through Figure 118. Then the performance under all load profiles is summarized.

Figure 115 shows the heat flows into the storage tank (positive values) and out of the tank (negative values).

5.2.1 Representative detailed results

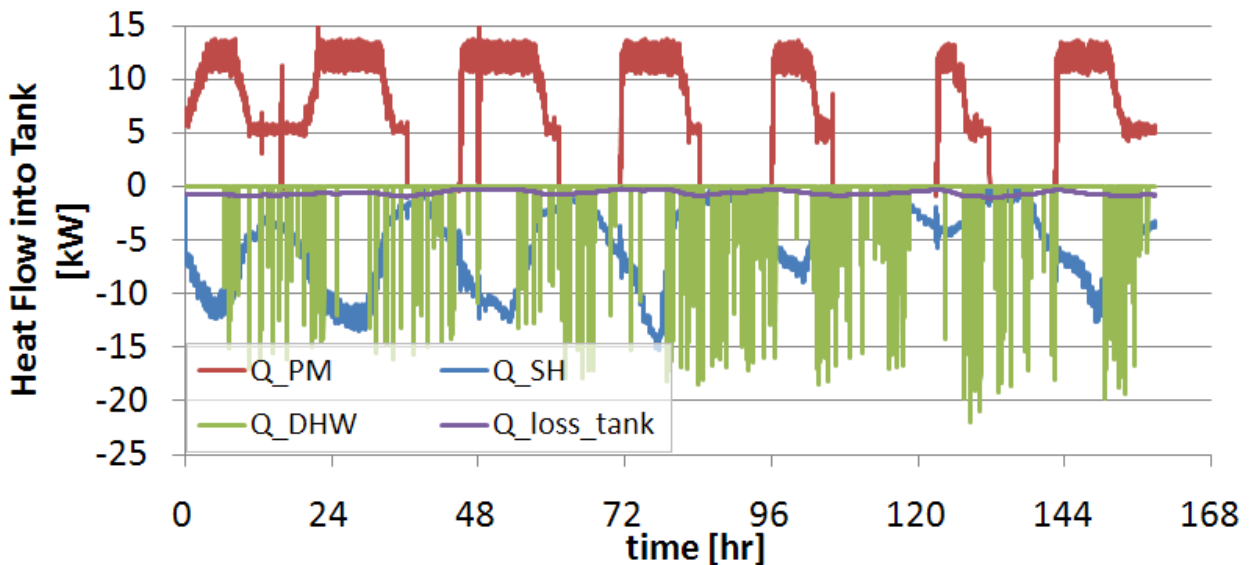


Figure 115: Energy flows into and out of the tank for the residential shoulder season test

Figure 116 shows the temperatures at 13 vertical levels in the tank throughout the week-long test. A legend is not included, but note that vertical stratification is consistently present.

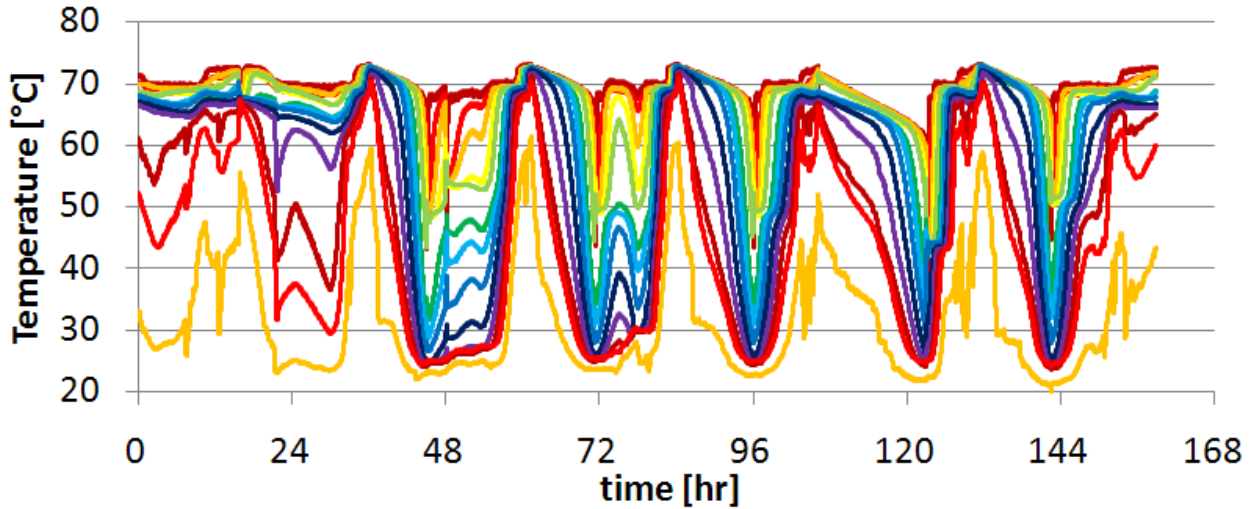


Figure 116: Tank temperatures for residential shoulder season test

Figure 117 shows an energy balance on the prime mover over the test duration.

The energy balance is defined as relative difference between the energy measured entering the prime mover cabinet control volume and the energy measured leaving that control volume.

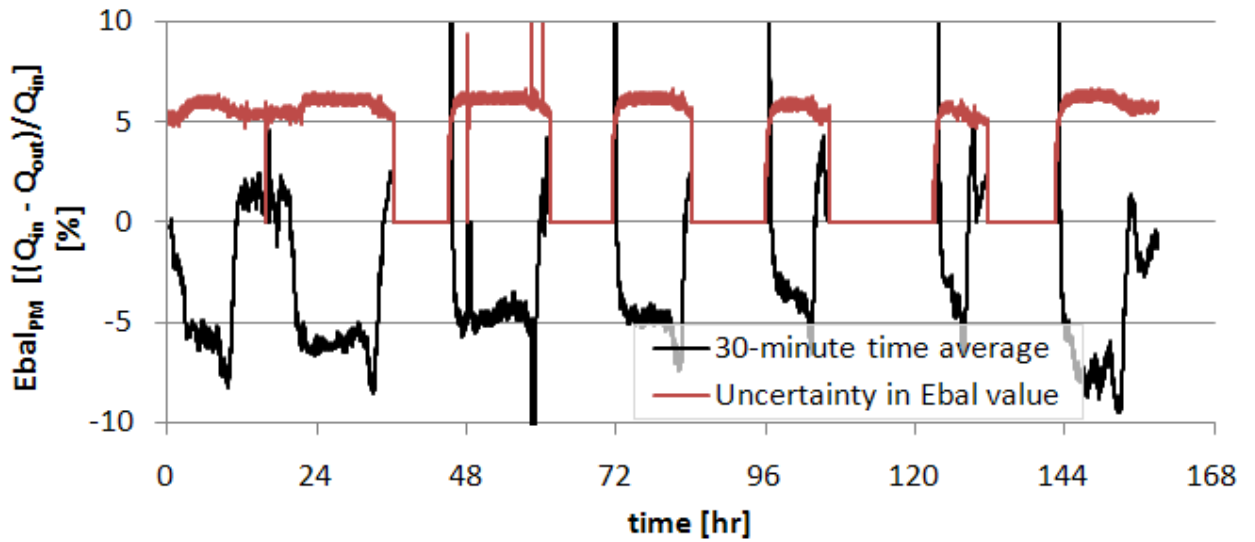


Figure 117: Prime mover energy balance for residential shoulder season test

Figure 118 shows an energy balance on the storage tank over the test duration.

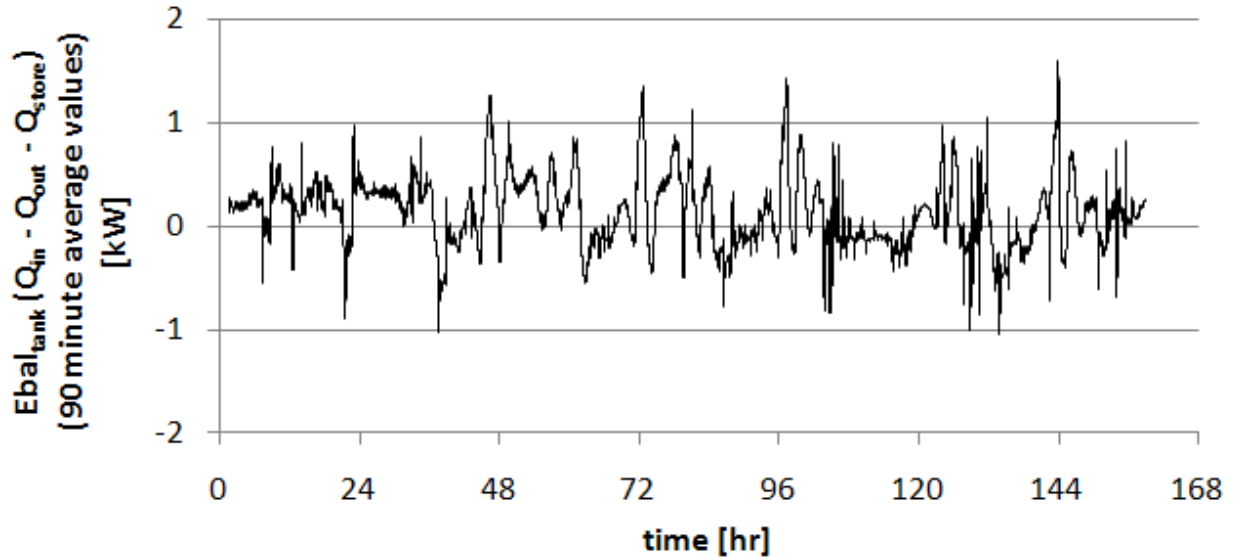


Figure 118: Tank energy balance for residential shoulder season test

5.2.1 Comparison of load profiles

Comparing the aggregated energy allocations for each type of load profile reveals the conditions under which the CHP system performs best. Figure 119 and Figure 120 use three approaches to accounting for the fate of all the fuel energy that entered the prime mover over the course of each profile test: cumulative energy flows, average energy flows, and the proportional distribution of energy flows, respectively. In Figure 119 and Figure 120, all terms are defined based on the “CHP System” control volume defined in Figure 94.

The $Q_{tank,loss}$ term represents the energy lost by convection from the surface of the storage tank, and “other losses” refers to all other losses from the system control volume (including losses through the exhaust, convection and radiation from the prime mover cabinet, line losses from all hydronic piping, etc.) The ΔE_{tank} term represents the difference between the energy charged to the storage tank at the end of the test compared

with the beginning. It is positive when the end with more energy than it started with, and negative for the opposite scenario.

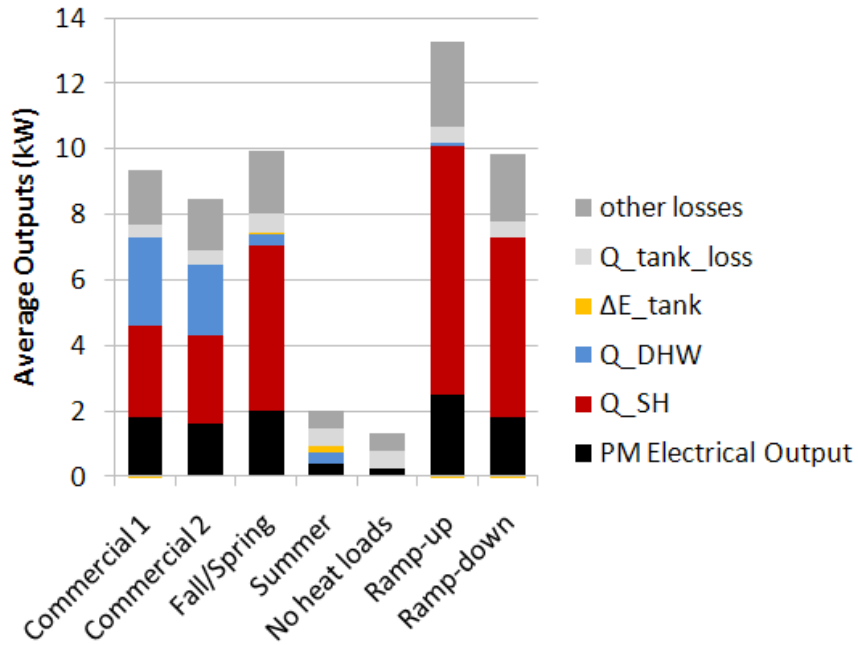


Figure 119: Average outputs for all CHP profiles

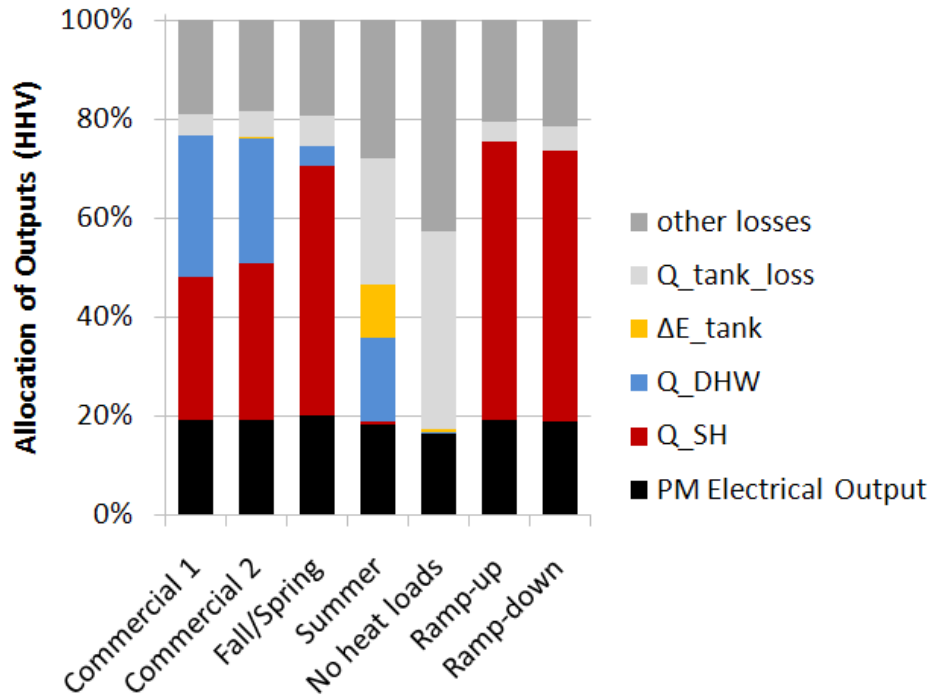


Figure 120: Allocation of outputs for all CHP profiles

Figure 121 compares the results using either the PM control volume or system control volume described in Figure 94. The difference is due primarily to heat losses from the tank and lines.

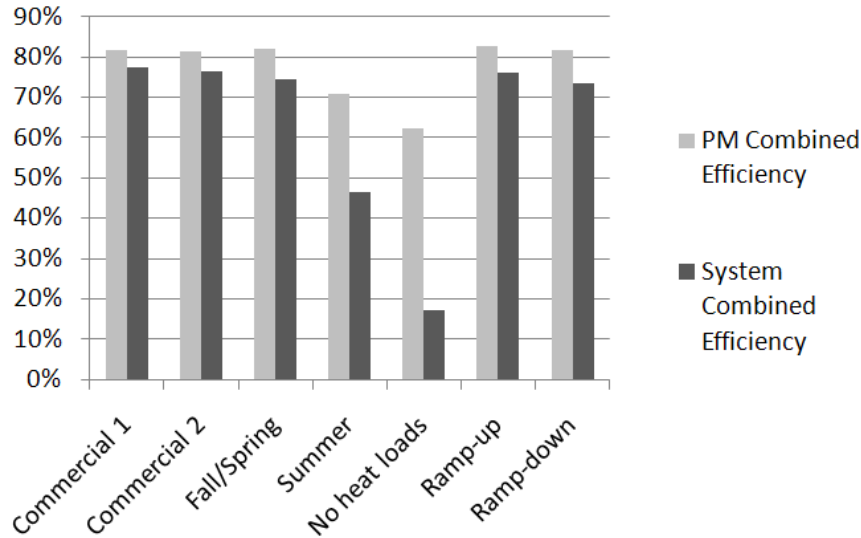


Figure 121: Comparison of PM to system control volume approach

5.3 Adsorption heat pump: cyclic steady state results

In this section, performance metrics are discussed, an overview of the steady state tests is given, and experimental results are presented.

For temperature nomenclature, refer to Figure 46 in the adsorption heat pump design section. Figure 122 shows the nomenclature used to describe heat pump operation. The heat pump will have a certain repeatable response (i.e. performance) at a given set of inputs (i.e. operating point). An operating point is defined by an internal state and an external state. This is a set of external and internal conditions or variables. Evaporator temperature is considered an external condition since the required evaporator temperature is a function of the desired dehumidification capacity. Capacity is a special variable, since it can be considered an external condition (denoted $Q_{desired}$) in the context of

deciding how to run the heat pump; and can be considered a response variable (denoted Q , Q_{evap} or Q_{CHW}) when evaluating the performance at a given operating point. The control strategy is the way in which the internal state is determined based on the external state. The control strategy will be discussed in the next section.

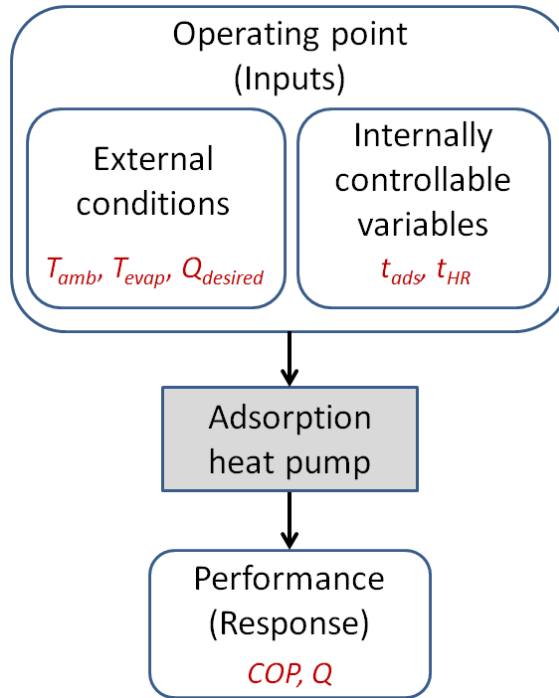


Figure 122: Nomenclature for heat pump operation and control

The performance metrics used with the adsorption chiller are primarily the thermal COP (COP_{th}), chilled water capacity (Q_{evap} or Q_{CHW}), and electrical COP (ECOP). The Q_{CHW} can easily be converted to specific cooling power (SCP) using the adsorbent mass of 2.82 kg per adsorber (i.e. 5.64 kg in the whole system).

The thermal coefficient of performance (COP_{th} or COP) is defined as the useful cooling produced divided by the high-temperature thermal energy consumed by the heat pump. Parasitic electrical loads, such as for pumps, are not normally included in the COP_{th} .

The electrical COP (ECOP) is the useful cooling divided by the electrical loads required to run the heat pump. In this prototype, the ECOP is very high (parasitic loads are low). Since pumps for the evaporator, condenser, adsorber and desorber were not optimized in the way that a commercial system's pumps would be, the ECOP for the prototype was calculated based on the HX-only ideal pumping power (ΔP times volumetric flow rate) multiplied by a factor of 3 to account for additional piping, divided by a generic 20% pump efficiency. The pumping power calculated this way still came to less than 20 W, and was thus neglected. Parasitic power incurred through heat rejection was handled by applying the assumption that 1 unit of electricity is required for every 100 units of heat rejection (i.e. $\varepsilon_{rej} = 100$). With an energy balance around the chiller and the definitions of COP_{th} and κ , a relationship can be established between minimum κ (maximum ECOP) which considers only heat rejection parasitics and COP_{th} , as in Equation (68). This gives values for κ_{min} from 0.06 (for $COP_{th} = 0.2$) to 0.027 (for $COP_{th} = 0.6$), or ECOP from 37.5 to 17.

$$\kappa_{min} = \left(1 + \frac{1}{COP_{th}} \right) / \varepsilon_{rej} \quad (68)$$

The chilled water schematic, Figure 50, shows the location of temperature measurements for the determination of capacity, Q_{CHW} (RTDs 42 and 43).

Figure 123 shows an overview of steady state tests of the adsorption chiller.

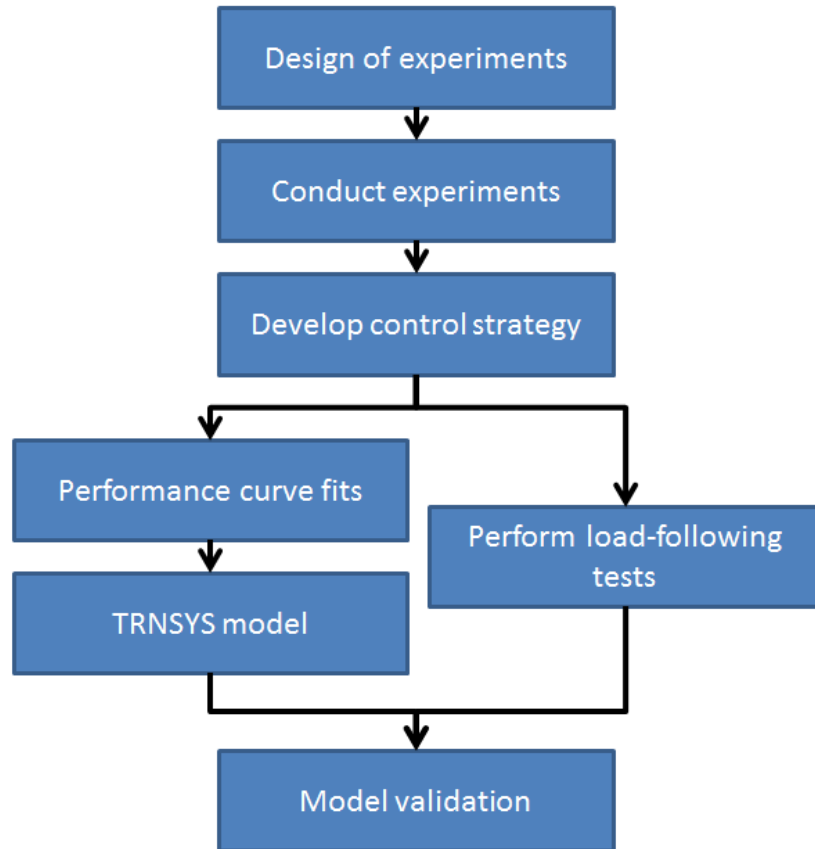


Figure 123: Overview of adsorption chiller test methodology

To give an overall sense of the tests conducted and their results, Figure 124 to Figure 126 show all 145 experimental tests in performance-space, external condition-space, and internal condition-space, respectively.

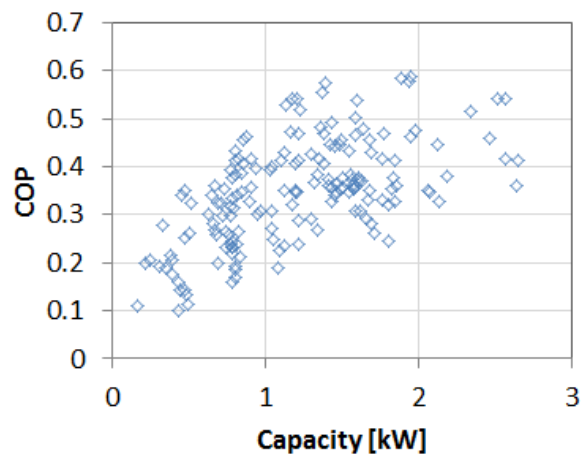


Figure 124: All experimental tests in performance-space

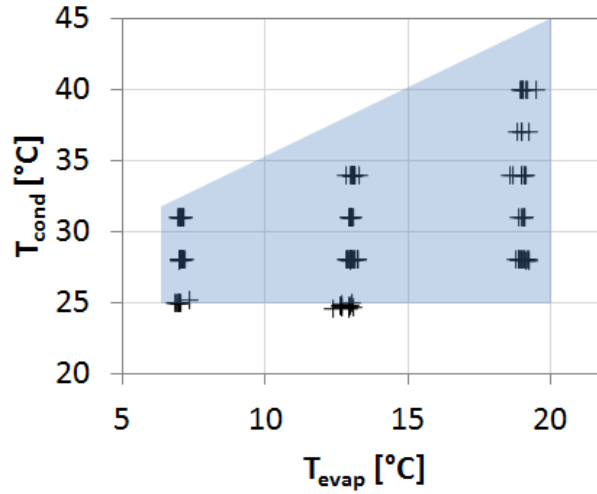


Figure 125: All experimental tests in external condition-space

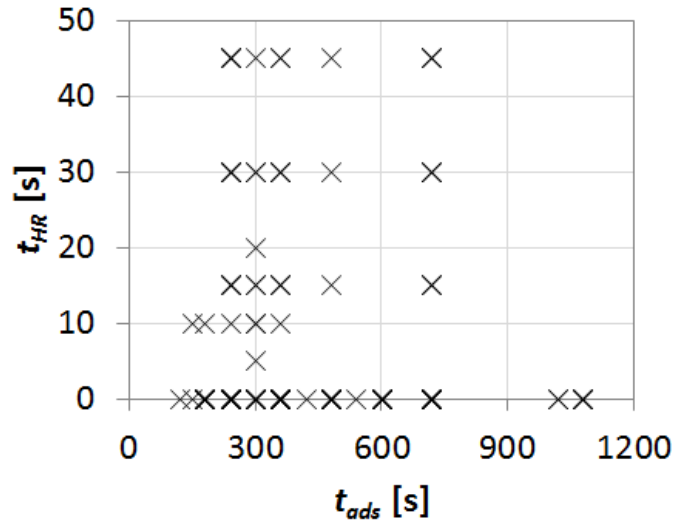


Figure 126: All experiments in internal condition-space

Figure 127 shows the fraction of Carnot COP achieved by all 145 tests. Note that the Carnot COP can be defined based on external temperatures or internal temperatures, according to the illustration in Figure 46.

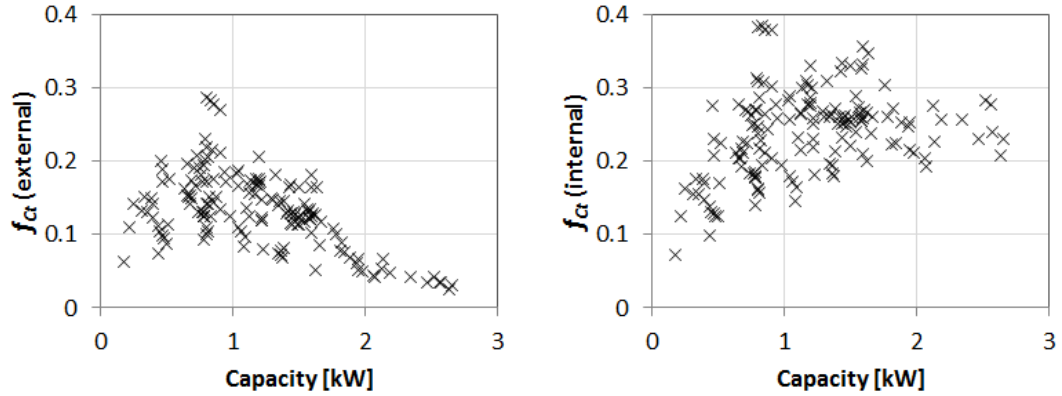


Figure 127: Fraction of Carnot performance achieved by all 145 experiments

Figure 128 shows the differential loading (ΔY) achieved by all the experimental tests, as well as the equilibrium differential loading that would have been achieved if the zeolite had reached equilibrium at the final ad/desorber HTF outlet temperature, and the saturation pressure corresponding to the outlet temperature of the CHW or condenser HTF.

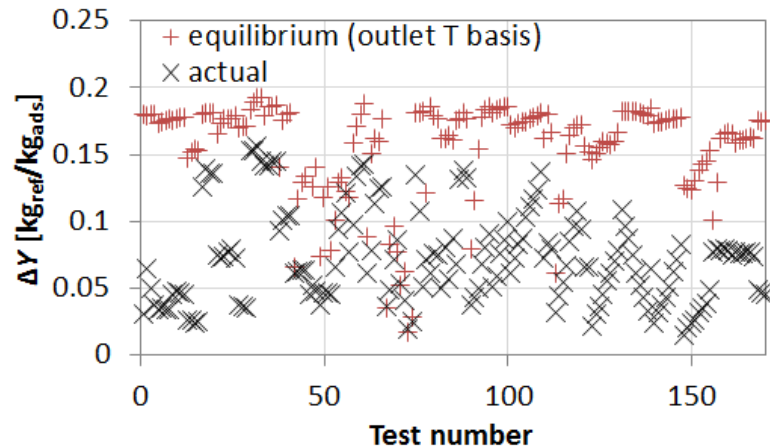


Figure 128: Differential loading (equilibrium and actual) of all experimental tests

Design of experiments

Various methods were used to determine the tests to be run, including a Plackett-Burman factor screening test matrix, parametric runs, and intuitive space filling methods.

The first step was a factor screening test matrix. The objective was to eliminate from consideration as many variables as possible from a list of 10 potentially important

variables. The Plackett-Burman factor screening experimental design was chosen. This design of experiments method is useful since the number of experiments scales as $N+1$, where N is the number of variables to be tested. It is an economical method for detecting large main effects (NIST/SEMATECH 2011).

Later, due to the ease with which parametric sweeps could be conducted while running the facility in automatic mode overnight, many parametric test matrices were conducted rather than following an established DOE design. The reason for this was pragmatic: a rigorous DOE design would only allow for 2-4 experiments to be run each day, whereas parametric runs could accomplish 6-8 experiments per day, since parametric runs did not require a technician to be present (24 hour testing was possible) and because they could reach steady state quickly (making only a single small change in operating conditions for each successive test). Thus the theoretical gains in efficient sampling of a DOE method would have been outweighed by the decreased experimental output.

Parametric results

Another advantage of the parametric tests is that they reveal clear trends as one variable is varied at a time. Figure 129 and Figure 130 show 55 parametric tests (a subset of the 145 total experimental tests). All 55 were with $t_{HR}=0$. These parametric studies serve almost as contour plots, showing the separate effects of adsorption time, evaporator temperature and condenser temperature on COP and capacity.

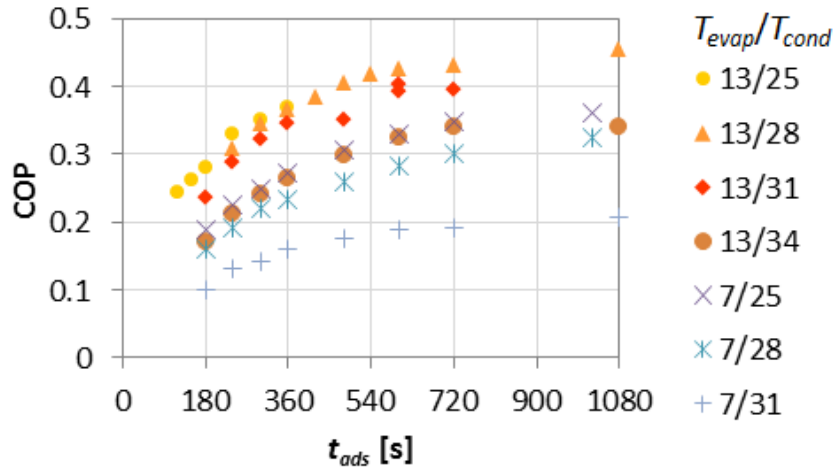


Figure 129: Experimental COP results for parametric study of t_{ads} , T_{evap} , and T_{cond}

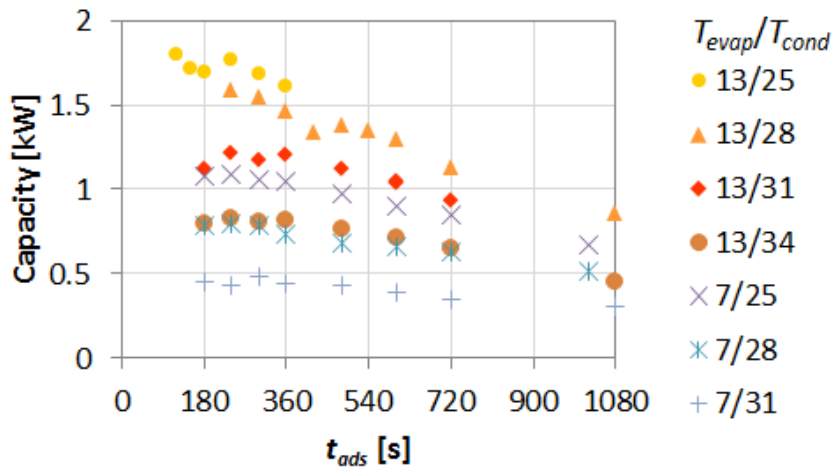


Figure 130: Experimental capacity results for parametric study of t_{ads} , T_{evap} , and T_{cond}

Standard tests

The chiller was tested according to European standard for small thermally driven chillers, EN12309. This test requires a chilled water outlet temperature of 7°C at a 30°C inlet temperature to the condenser and adsorber. At this condition, according to the chiller control strategy derived later in this work, the minimum and maximum capacities are 0.46 and 0.57 kW. The system was run at Q_{min} which has $t_{ads} = 528$ and $t_{HR} = 17.7$ [s] (however, at the time the test was run, an earlier control strategy curve fit gave 555 and

17.4 s, which were actually used for the test). At this condition the chiller had a COP of 0.33 and a measured Q_{CHW} of 0.37 kW.

The development of a control strategy (and an empirical performance map based on that control strategy) for the chiller is described in the next section.

5.4 Adsorption heat pump: control strategy and empirical model

The experimental heat pump results were used to develop a control strategy for the heat pump. Since the development of an empirical cycle model was intimately tied up with the control strategy development, the developments of both are discussed in parallel in this chapter. The results of the control strategy are also discussed here; while the results of the empirical model are discussed in Chapter 6.

The function of the control strategy is to select an internal state (cycle time t_{ads} and heat recovery time t_{HR}) that maximizes efficiency given an external state (T_{cond} and T_{evap}) and desired capacity ($Q_{desired}$). The control strategy establishes a relationship between internal and external conditions as a function of capacity. A schematic of the control strategy is depicted in Figure 131.

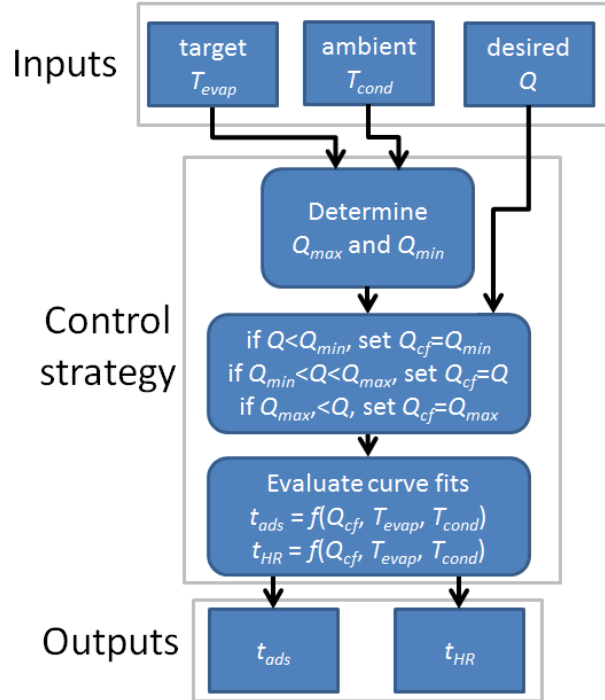


Figure 131: Schematic of control strategy evaluation

Figure 132 shows an overview of how the curve fits for t_{ads} and t_{HR} were obtained from experimental results. This procedure was developed for this thesis and could be applied to control strategy development for other systems. For this reason, the following generic nomenclature is used:

- N = number of discretizations in each state variable
- \tilde{x} = internal state variables
- \tilde{y} = external state variables
- \tilde{z} = performance (or response) variables
- c = capacity
- p = # of variables in \tilde{z}
- q = # of variables in \tilde{y}

In the present work, these had the following values:

- $N = 10$
- $\tilde{z} = t_{ads}, t_{HR}$
- $\underline{y} = T_{cond}, T_{evap}$
- $\tilde{z} = COP, Q_{CHW}, f_{Cl}$
- $p = 2$
- $q = 2$

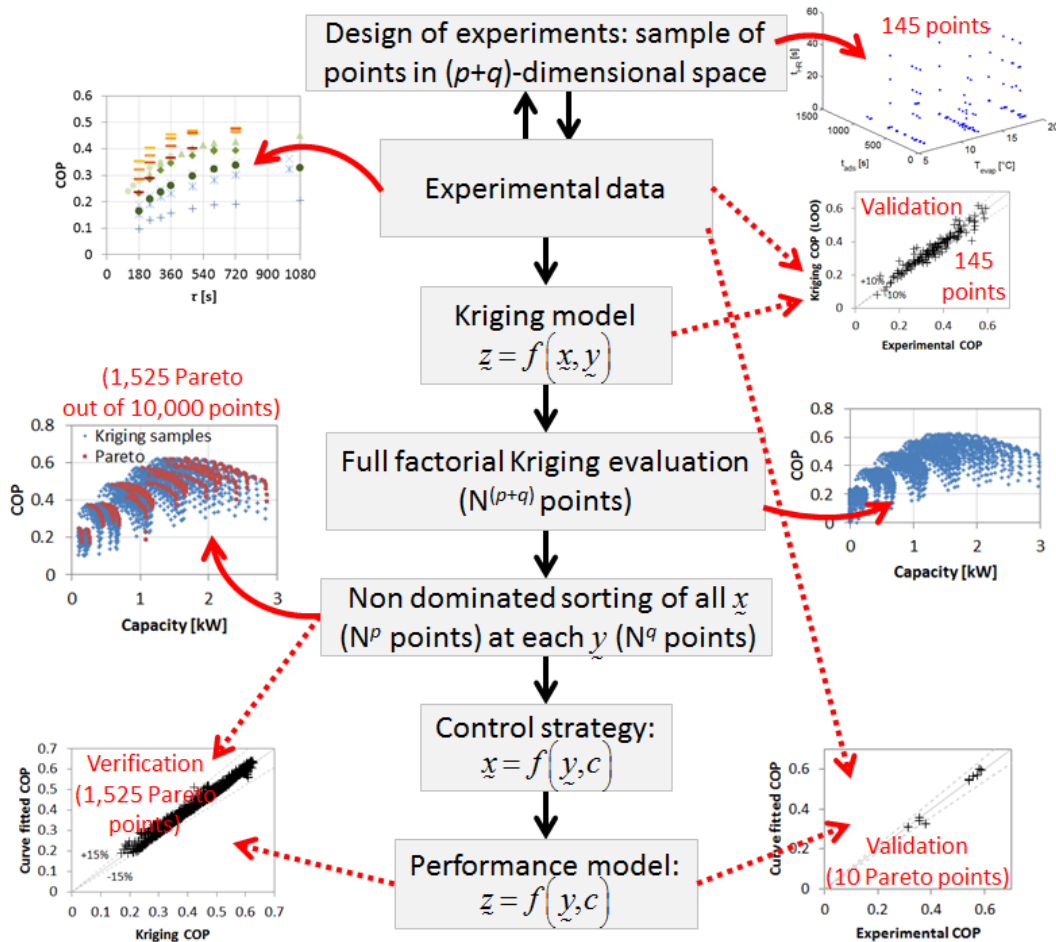


Figure 132: Overview of control strategy and empirical model development

First, a Kriging model was created based on the 145 steady state experimental results. The Kriging model outputs performance as a function of four variables: two describing the internal state plus two for the external state. The experimental tests were conducted to determine the performance of the heat pump at a sample of all possible

operating states. The Kriging model is a highly accurate way of interpolating between those samples. The Kriging model was a critical intermediate step since it allowed a full factorial evaluation over a sample of 100 internal variables (10 t_{ads} values by 10 t_{HR} values) and a sample of 100 external conditions (10 condenser by 10 evaporator temperatures) for a total of 10,000 Kriging evaluations. This full factorial evaluation in turn allowed non-dominated sorting to establish a well-populated Pareto front at each external state.

The Kriging model was validated using the leave-one-out (LOO) method (Li et al 2010). For M experimental data points, the Kriging model is constructed using M-1 points, then the single point that was left out is predicted. The error in the prediction for this point is denoted ϵ_{LOO} . A value of ϵ_{LOO} can be calculated for each of M points by constructing M separate Kriging models, resulting in M values of ϵ_{LOO} . Figure 133 shows the predicted values using the LOO method versus all 145 experimental values of COP, after applying a filter of COP>0.1. The Kriging predictions generally fall within +/-10% of the experimental value, especially at moderate and higher COPs.

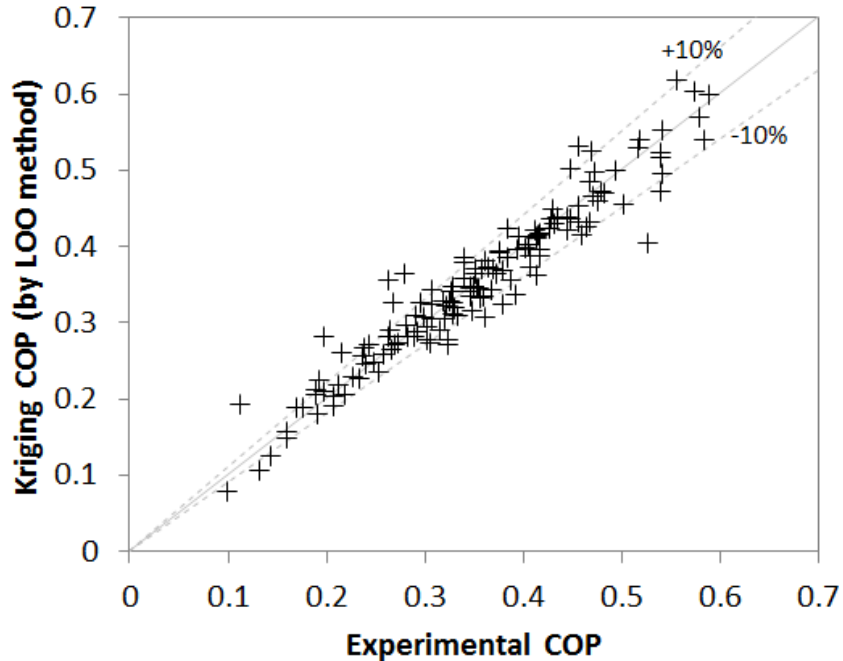


Figure 133: Kriging predictions vs. 145 experimental points using LOO method

Figure 134 demonstrates the non-dominated sorting. It shows a sample of only 2,500 points (100 internal states over 25 external conditions), since 2,500 points are much easier to visualize than the 10,000 actually used in calculations (100 internal states over 100 external conditions). The results are plotted in response-space (COP vs. capacity). For a given capacity, the heat pump should always operate at the maximum achievable COP. Thus the 2,500 points are reduced to 25 sets of non-dominated points (one set for each of the 25 external conditions). These sets are called Pareto sets, and their individual points are shown in red. The blue dominated points are undesirable operating points, since they unnecessarily involve a lower COP than is possible at a given capacity. Note that, for clarity, not all points are shown: a filter has been applied based on thresholds of $COP > 0.1$ and $Capacity > 0.1$ kW (as a result there are only 22 Pareto sets shown in Figure 134).

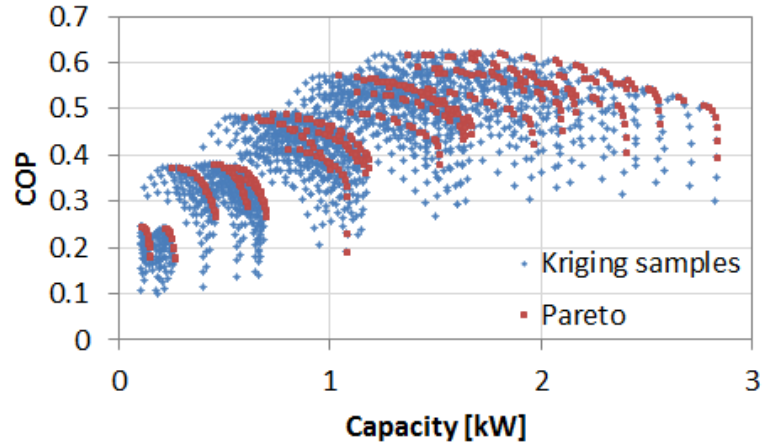


Figure 134: Pareto sets in response-space for operation at 25 external conditions

Out of the 10,000 points sampled by Kriging model evaluation, 1,525 met threshold criteria and were non-dominated (i.e. Pareto). These were distributed among 86 of the 100 external conditions – 14 external conditions had no internal conditions capable of meeting the threshold requirements of $COP > 0.1$ and $Capacity > 0.1$ kW. Figure 135 shows the 86 external conditions having performance meeting the threshold criteria. It can be seen that a limit on temperature lift of about 25°C was observed in experimental tests. This is clear from the figure since an imaginary line along the border between feasible and infeasible has a slope of about 1, and $T_{cond} - T_{evap} \approx 25^{\circ}\text{C}$ along that imaginary line.

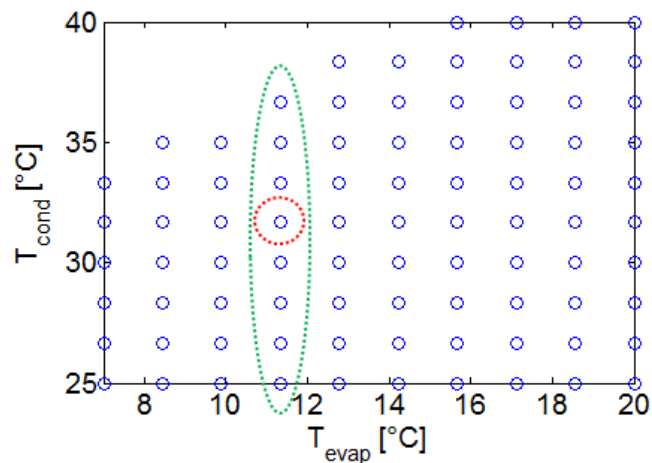


Figure 135: External conditions with $COP > 0.1$ and capacity > 0.1 kW

To further illustrate the method, Pareto points at 11.3°C evaporator temperature, circled in green in Figure 135, are expanded in response-space in Figure 136 to show their performance.

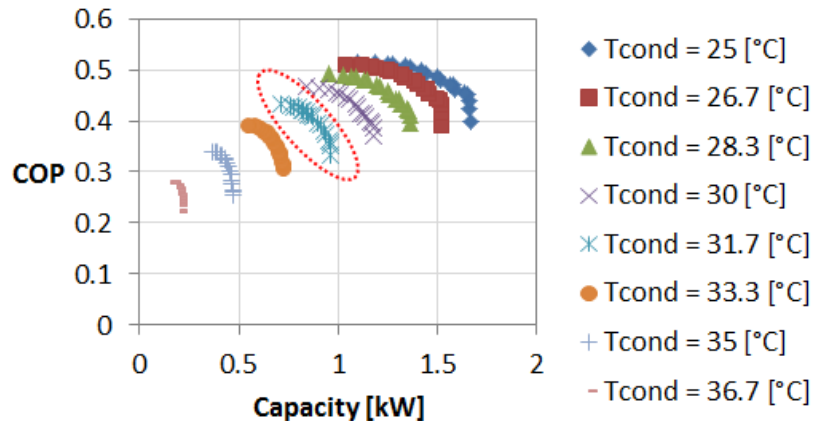


Figure 136: Solutions circled in green from previous figure in performance-space

When seen in performance-space, it is clear that capacity is consistently dropping off as heat rejection temperature rises, until the heat pump is no longer able to meet the capacity threshold above 37°C condenser temperature.

Next, the single external condition circled in red in Figure 135 and Figure 136 is expanded to show the effects of internal cycle variables on performance at a single external condition. This is shown in Figure 137. Note that only 18 of the original 100 combinations of internal operating variables turned out to be Pareto points. These 18 Pareto points make up Figure 137, are all shown in the red circled region in Figure 136, and collapse to a single (red-circled) point in Figure 135.

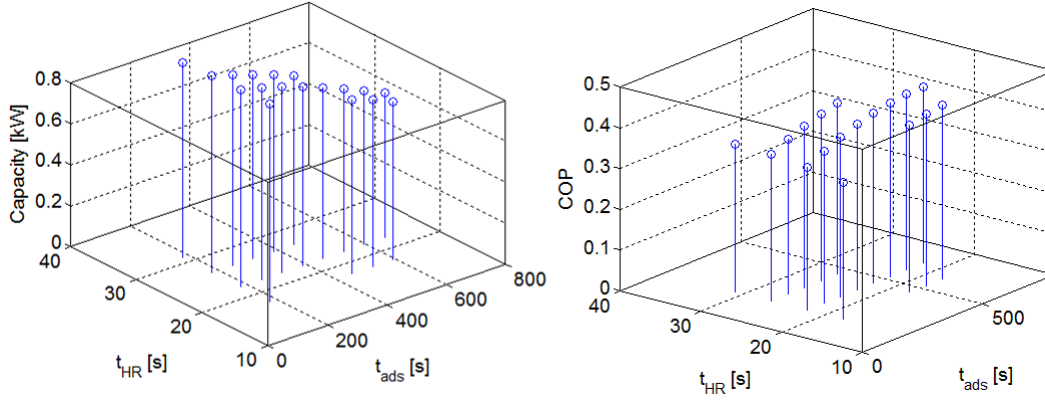


Figure 137: Performance as a function of cycle times for condition circled in red in previous two figures

By examination of Figure 137, the tradeoff between COP and capacity with respect to adsorption time can be seen: within the range of about 180 to 660 seconds, longer adsorption times result in higher COP but lower capacity. Adsorption times below or above this range are not present in the Pareto set: both COP and capacity suffer outside this Pareto range.

The same general trends also hold for heat recovery times, although the effect is not discernible from visual inspection of Figure 137. A heat recovery duration less than 15 seconds always resulted in a dominated solution for this set of external conditions. This is not true for every external condition, however, since at some external conditions $t_{HR}=0$ is included in the Pareto set.

Next, several 6-coefficient or 10-coefficient second-order polynomial curve fits were created based on the Pareto sets. Each of the following was curve fitted:

- $COP = f(T_{evap}, T_{cond}, Q_{desired})$
- $Q_{min} = f(T_{evap}, T_{cond})$
- $Q_{max} = f(T_{evap}, T_{cond})$
- $t_{ads} = f(T_{evap}, T_{cond}, Q_{desired})$
- $t_{HR} = f(T_{evap}, T_{cond}, Q_{desired})$

Each curve fit was verified by comparison with the Kriging prediction across the set of 1,525 Pareto samples. An example result, for COP, is shown in Figure 138.

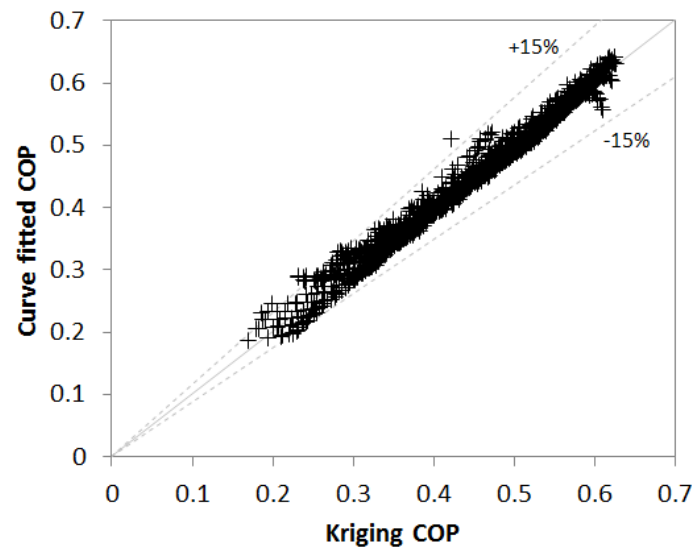


Figure 138: Comparison of curve fitted and Kriging-predicted COP for 1,525 Pareto points

Then each curve fit was validated against experimental data. However, only experimental points evaluated at (or within a threshold distance from) the Pareto internal operating conditions could be used for validation. Out of the 145 experimental data points, only 10 met the following threshold criteria:

- within 20% of the Pareto value of t_{ads} for the particular external condition evaluated
- within 15 s of the Pareto value of t_{HR} for the particular external condition evaluated

The location of the 10 validation points in external condition-space are shown in Figure 139. The region of interest is blue.

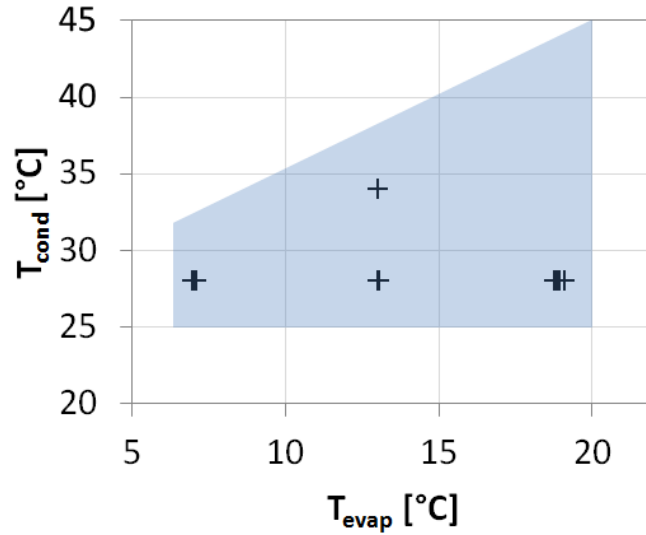


Figure 139: External conditions of 10 validation points

The 10 validation points are compared with the curve fitted COP in Figure 140.

Nine out of the ten points are within 5% agreement.

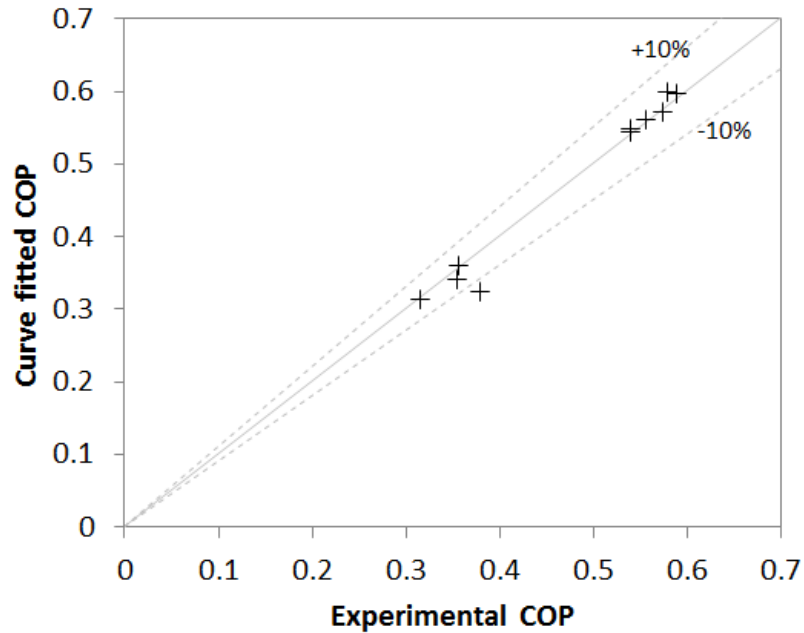


Figure 140: Curve-fitted vs. experimental COP for 10 experimental validation points

Note that the main reason so few points meet the threshold criteria is that the majority of experimental tests involving non-zero heat recovery were conducted at $T_{\text{cond}} = 28^{\circ}\text{C}$. Thus additional steady state validation tests were run in order to better sample the external condition- and internal condition-spaces. The condition spaces were sampled

with new tests as shown in Figure 141 through Figure 143, and the validation results for all validation tests are shown in Figure 144. The original validation tests are shown as black crosses, with additional validation shown as red circles.

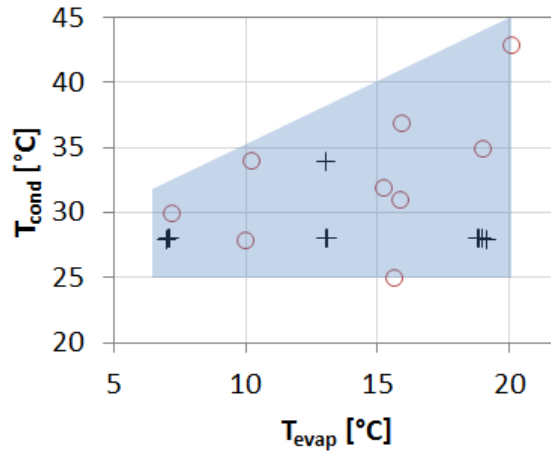


Figure 141: Validation experiments in external condition-space

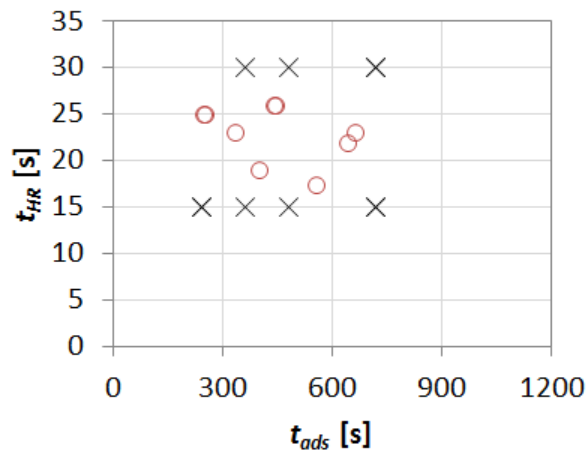


Figure 142: Validation experiments in internal condition-space

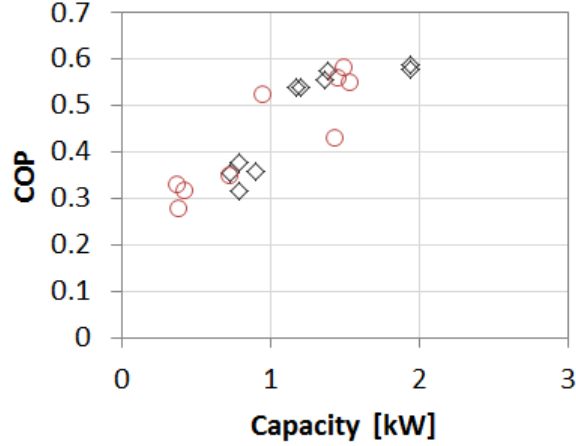


Figure 143: Validation experiments in response-space

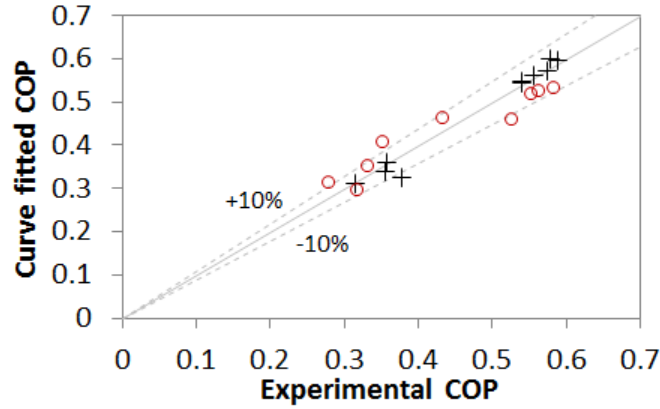


Figure 144: Curve fit vs. experimental COP for validation experiments

The 6-coefficient curve fits for Q_{min} and Q_{max} are second-order polynomial functions of two variables, T_{evap} and T_{cond} . They can be evaluated using Equation (69) and Table 34.

The 10-coefficient curve fits for COP, t_{ads} and t_{HR} are also second-order polynomials, but are functions of three variables (T_{cond} , T_{evap} , and Q_{evap}). They can be evaluated using Equation (70) and Table 35.

$$Q_{min}, Q_{max} = \sum_{i=1}^6 k_i T_{evap}^{m_i} T_{cond}^{n_i} \quad (69)$$

Table 34: Coefficients for curve fits for Q_{min} and Q_{max}

i	$k_i (Q_{min})$	$k_i (Q_{max})$	m_i	n_i
1	-6.385E-04	3.829E-04	2	0
2	1.986E-03	1.567E-03	1	1
3	4.181E-02	8.703E-02	1	0
4	-3.900E-03	-4.211E-03	0	2
5	1.351E-01	1.183E-01	0	1
6	-7.593E-01	-1.503E-01	0	0

$$COP, t_{ads}, t_{HR} = \sum_{i=1}^{10} k_i T_{evap}^{m_i} T_{cond}^{n_i} Q^{p_i} \quad (70)$$

Table 35: Coefficients for curve fits for COP, t_{ads} and t_{HR}

i	$k_i (COP)$	$k_i (t_{ads})$	$k_i (t_{HR})$	m_i	n_i	p_i
1	-4.899E-03	-8.733E+00	-2.233E-01	2	0	0
2	8.621E-03	1.585E+01	3.054E-01	1	1	0
3	5.122E-02	8.389E+01	3.524E+00	1	0	1
4	-1.385E-01	-2.074E+02	-7.345E+00	1	0	0
5	-4.996E-03	-1.035E+01	-7.731E-02	0	2	0
6	-4.202E-02	-5.869E+01	-2.669E+00	0	1	1
7	1.994E-01	3.715E+02	3.845E+00	0	1	0
8	-1.655E-01	1.986E+00	-1.874E+01	0	0	2
9	7.471E-01	-5.460E+02	8.290E+01	0	0	1
10	-1.675E+00	-1.958E+03	-3.857E+01	0	0	0

Together, the curve fits for COP, Q_{min} and Q_{max} form an empirical model that can be used for heat pump simulations and performance prediction as shown in Figure 131.

The curve fits for Q_{min} , Q_{max} , t_{ads} and t_{HR} form a control strategy for heat pump operation.

Example evaluations of the control strategy and empirical performance map are shown in section 6.5.

5.5 CCHP: dynamic load-following experimental results

To evaluate the dynamic experimental performance of the trigeneration system, the “simulated residence” laboratory capabilities were used to impose thermal loads typical of a moderate summer week in Maryland for a single-family home. A DHW

profile very similar to that used for the CHP tests was used in the CCHP test, and an air conditioning profile was selected based on the loads from a TRNBLD building model (Mueller, 2009).

It is important to note that the load-following CCHP test suffered from a valve malfunction which was neither diagnosed nor corrected until after the end of the test. This malfunction resulted in the heat recovery flow rate being zero throughout the five day test. This caused a very significant penalty in COP and a small capacity penalty, since heat recovery generally boosted the COP in cyclic steady state tests by 20 to 50% and boosted capacity by 5-15%. Also, not only was the flow rate zero, but the system sat idly for the duration of what was supposed to be heat recovery time, incurring an additional capacity penalty, typically of about 5-10%. Over the 5 day test, the measured time-averaged thermal COP without heat recovery was 0.35. It is expected that, with heat recovery active, the time-averaged thermal COP would have been 30 to 50% higher.

5.5.1 CCHP load profiles and SSLC strategy

Since the performance of the chiller is relatively poor at conventional (7°C) chilled water temperatures, it was operated in an SSLC configuration for the load following test. This allowed the chiller to operate at 14-20°C chilled water temperature to handle sensible loads, while it was assumed for simplicity that the latent loads of the home would be handled, completely independently of the adsorption chiller operation, by a VCS-based dehumidifier with COP of 5. Latent-only cooling with a relatively high COP is possible using the configuration shown in Figure 145, in which the VCS evaporator inlet air is precooled and the condensed refrigerant subcooled by the

dehumidified air. Over the duration of the 5-day test, the VCS dehumidifier would have consumed 6.8 kWh of electricity.

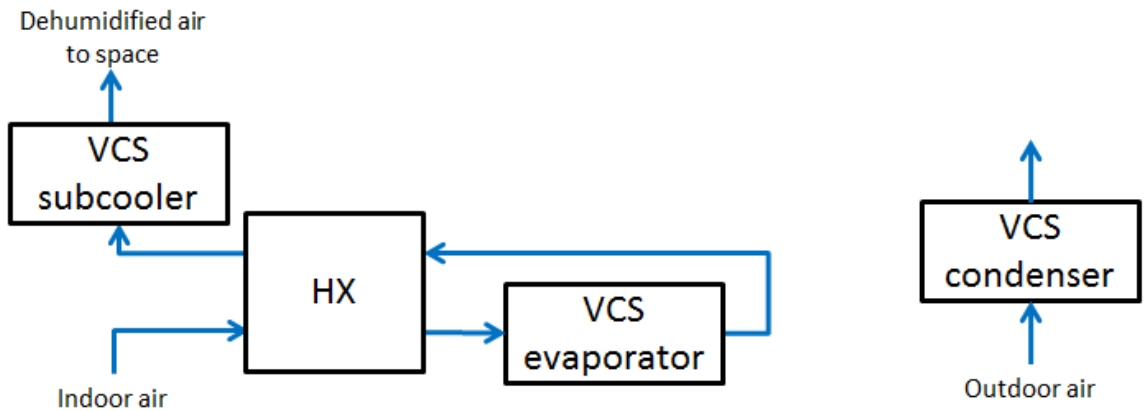


Figure 145: VCS-based dehumidification configuration

The weather profile for Stirling, VA from TMY2 data (National Solar Radiation Database, 2010) is shown in Figure 146. This profile was used to determine the residential loads shown in Figure 147 by Mueller (2009).

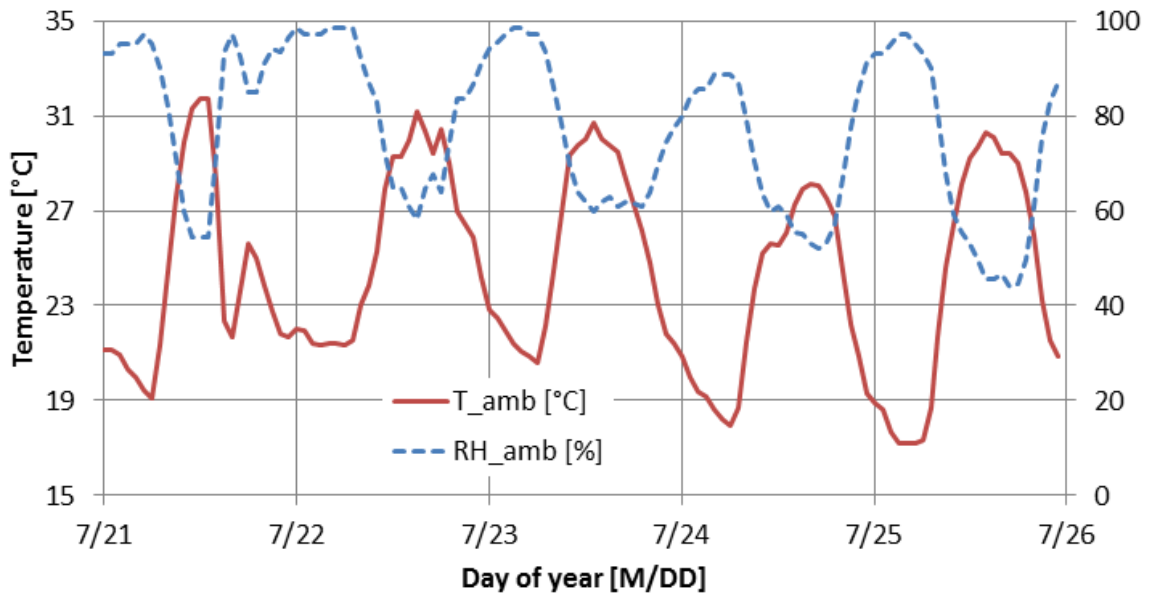


Figure 146: Weather profile for Stirling, VA for late July (TMY data)

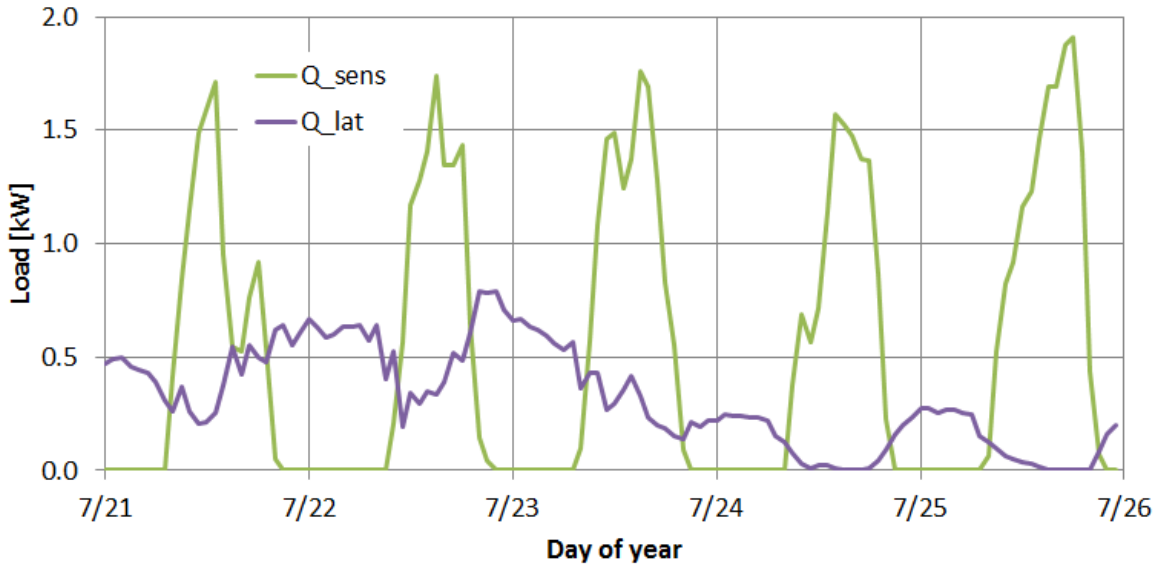


Figure 147: Load profile for building in Stirling, VA

Next, different air flow rates were investigated to see what supply air temperature would be required in order to meet the sensible load, as shown in Figure 148.

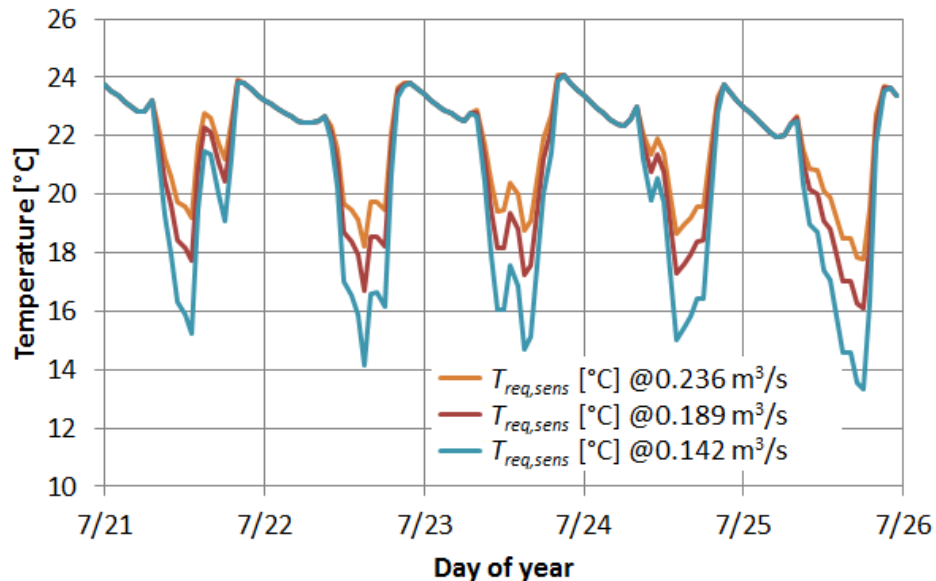


Figure 148: Required supply temperature for sensible cooling for three different air flow rates

Then the empirical model of the chiller was used to determine the minimum and maximum capacity that the chiller could supply given the supply air temperature and outdoor temperature. At $0.142 \text{ m}^3/\text{s}$ (300 cfm), shown in Figure 149, the chiller is not

always able to meet the load, while at $0.236 \text{ m}^3/\text{s}$ (500 cfm), shown in Figure 150, the chiller often has a large over-capacity and would have to be cycled on and off.

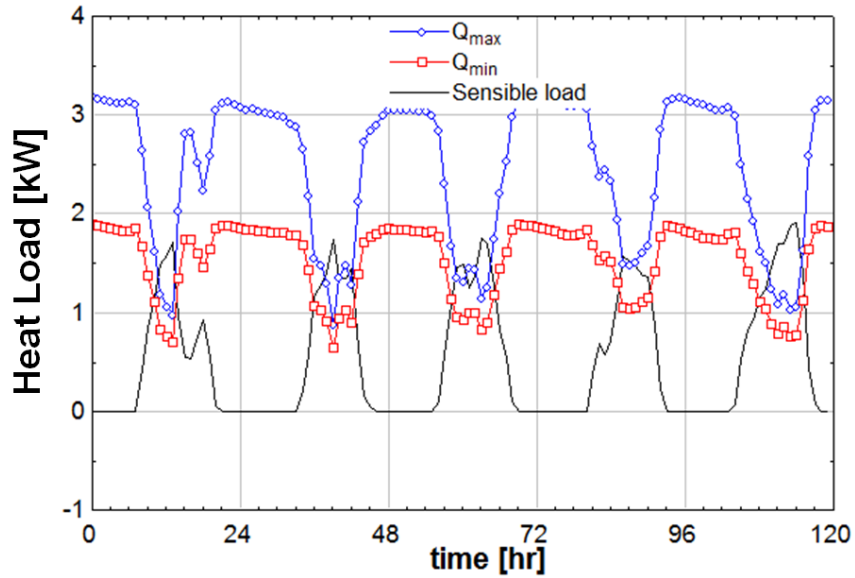


Figure 149: Building sensible load and chiller minimum and maximum capacity for 300 cfm supply air flow rate

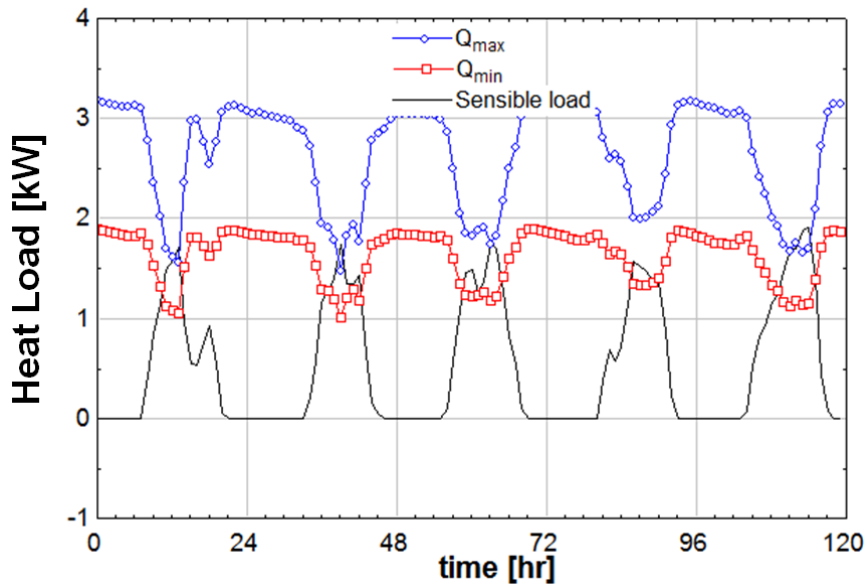


Figure 150: Building sensible load and chiller minimum and maximum capacity for 500 cfm supply air flow rate

In order to minimize cycling of the chiller, a strategy was adopted that the chilled water would run at the $0.142 \text{ m}^3/\text{s}$ (300 cfm) temperature when it has enough capacity, and switch to the $0.236 \text{ m}^3/\text{s}$ (500 cfm) temperature otherwise.

To deal with pulldown at startup (chilling the thermal mass of the evaporator and evaporator liquid refrigerant pool), the chiller was run at full capacity for ten minutes each time that it had been off for longer than 30 minutes. After those 10 minutes of pulldown, it would revert to the capacity of the load profile. The capacity, within bounds of Q_{max} and Q_{min} , was determined by selecting the appropriate t_{ads} and t_{HR} from the chiller control strategy.

The chilled water supply temperature was chosen to be 3°C lower than the required supply air temperature. When required capacity is less than minimum chilled water capacity, the chiller is cycled. The end result is the profile shown in Figure 151.

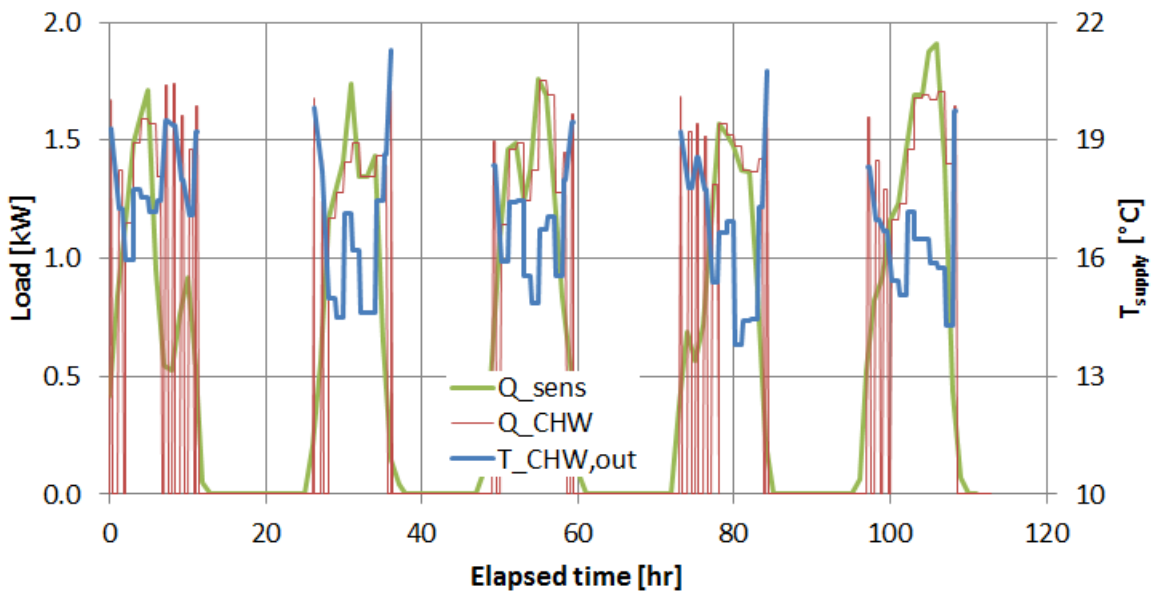


Figure 151: Profile of capacity and chilled water supply temperature for adsorption chiller

5.5.2 CCHP load-following results

The cumulative totals for the trigeneration system were as shown in Table 36 with all energy forms expressed in units of kWh.

Table 36: Cumulative totals for CCHP 5-day profile

Energy type	kWh	fraction of fuel (LHV)	fraction of fuel (HHV)
Fuel consumption (HHV)	517.7	-	-
Fuel consumption (LHV)	466.3	-	-
Electricity production	90.4	19.4%	17.5%
Chilled water production	61.6	13.2%	11.9%
Domestic hot water production	23.8	5.1%	4.6%
Tank ΔE_{stor}	4.38	0.9%	0.8%
Desorber heat input	177.7	38.1%	34.3%

The allocation of fuel energy is also shown for the load following test in Figure 152. Interpreting Figure 152 in the nomenclature of Chapter 2, $\lambda \approx 0.38$ for the laboratory system. This is quite poor and would be readily improved by better insulation to reduce thermal line losses and tank losses. The laboratory tank was not as well insulated as commercial tank options, and due to space restrictions, dozens of meters of high temperature pipe connected the PM, tank and chiller. With much better insulation and reduced piping distance, the value of λ would approach 0.15, the value characteristic of the prime mover itself.

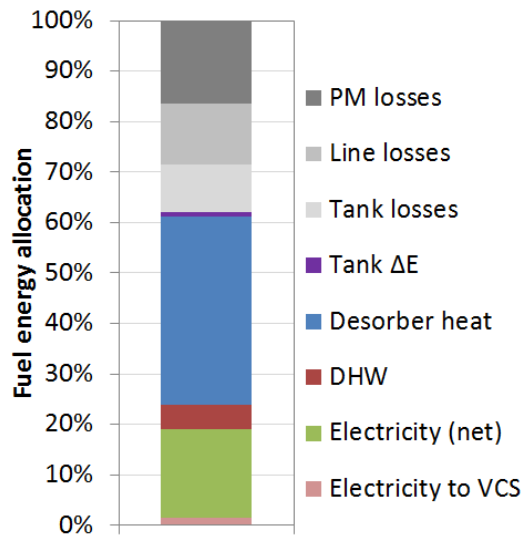


Figure 152: Cumulative fuel energy allocation measured for 5-day experimental trigeneration experiment

Table 37 defines three baseline scenarios and shows the additional energy they would use relative to the experimental trigeneration results, if all baseline scenarios produced the same amount of cooling and net electricity. The grid-VCS system would actually use less energy, while trigen would have significant savings relative to all off-grid alternatives. These results are as expected based on the analytical analysis in Chapter 2. The savings of trigeneration would increase with reduced line and tank losses.

Table 37: Trigenation savings vs. three baseline scenarios

Baseline scenario				Trigen savings
<i>name</i>	<i>electricity from:</i>	<i>DHW from:</i>	<i>cooling from:</i>	
grid-VCS	grid	boiler	VCS	-15.6%
off-grid conventional	generator	boiler	VCS	36.1%
off-grid CHP, VCS	CHP engine	CHP engine	VCS	28.6%

Having discussed the summary of experimental results, the rest of this section details the data which was recorded every 2 seconds over the duration of the 5-day test.

Figure 153 shows the fuel consumption, electricity production, chilled water production, and DHW output of the system over the 5-day profile. The engine would run during the day when cooling loads were present, and when the chiller shut down the DHW loads would be provided from the storage tank.

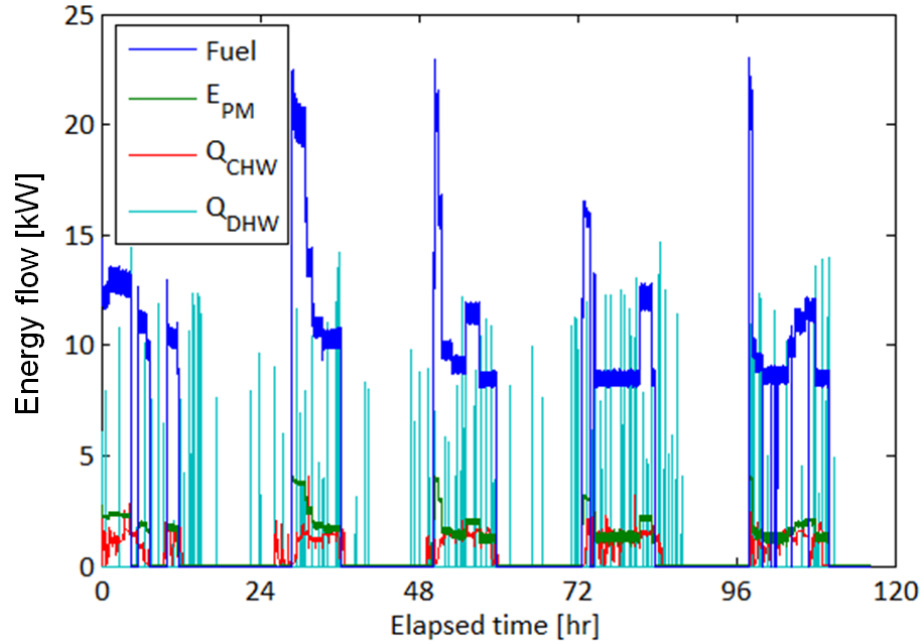


Figure 153: Inputs and outputs of trigeneration system during profile test

Next, Figure 154 shows the energy transfers to/from the storage tank, and the thermal energy stored in the tank with time. The only input to the tank is heat from the prime mover (Q_{PM}), with extractions from the tank in the form of DHW (Q_{DHW}), desorption heat for the chiller (Q_{des}), and convection/radiation losses from the tank walls (Q_{loss}).

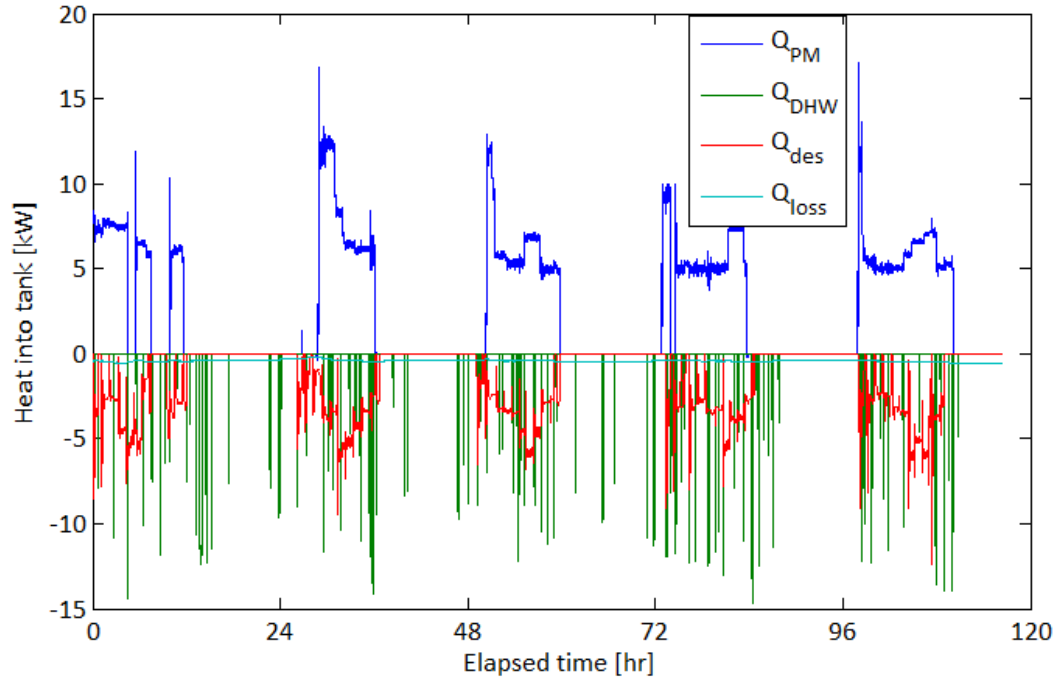


Figure 154: Heat into tank

The thermal energy stored in the tank with time is shown in Figure 155, and the temperature profile in the tank with time is shown in Figure 156.

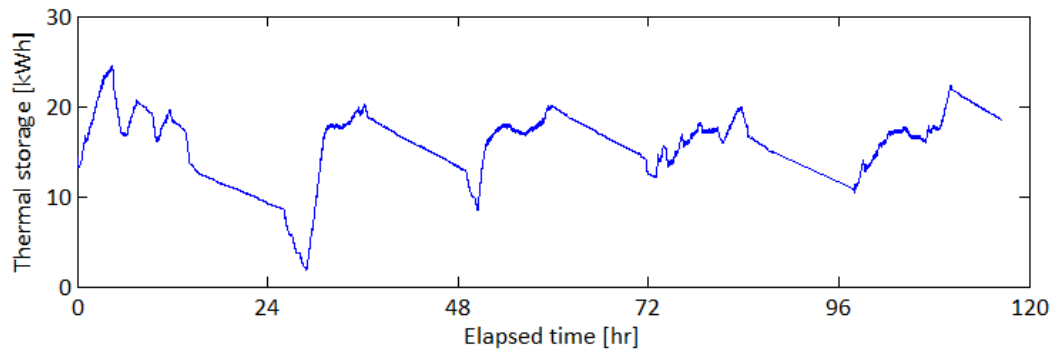


Figure 155: Thermal energy stored in 800 L tank

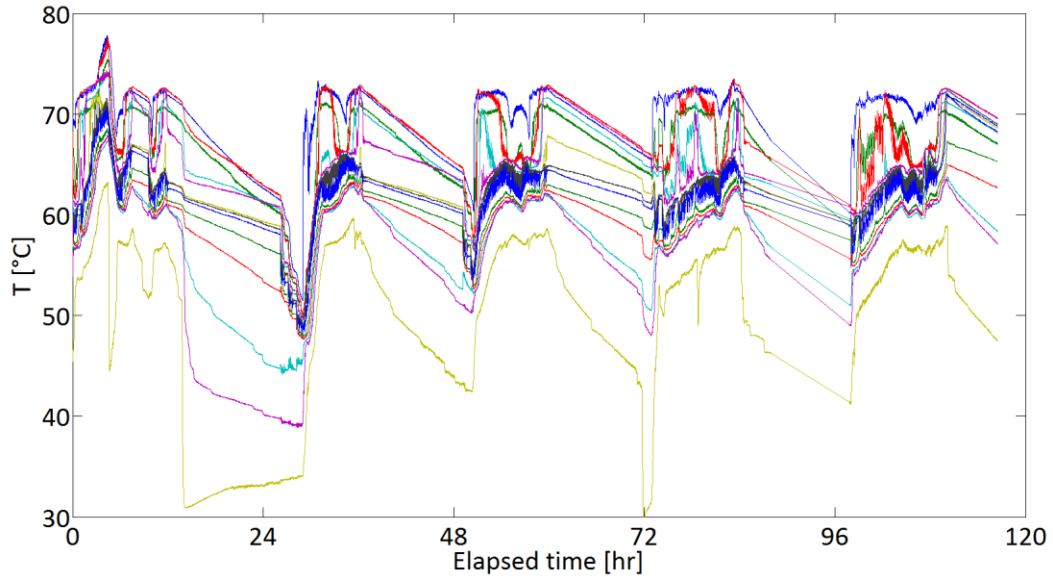


Figure 156: Temperature profile in 800 L tank

Next, more detailed load-following results are shown for the profile itself and the chiller performance.

The profile imposed on the trigeneration system consisted of the following items:

1. ambient temperature (assumed to be 3 K below the condenser inlet temperature)
2. chilled water cooling capacity
3. chilled water supply temperature
4. domestic hot water demand

Each of these is shown below in Figure 157 through Figure 162.

In Figure 157, the experimentally controlled condenser inlet temperature can be seen to closely follow the profile. The apparent scatter of about 10 K is due to short transient spikes in the condenser inlet temperature at the time of adsorption phase switching. This is illustrated better in Figure 158, which zooms in on the time period of 34.4 to 35 hours.

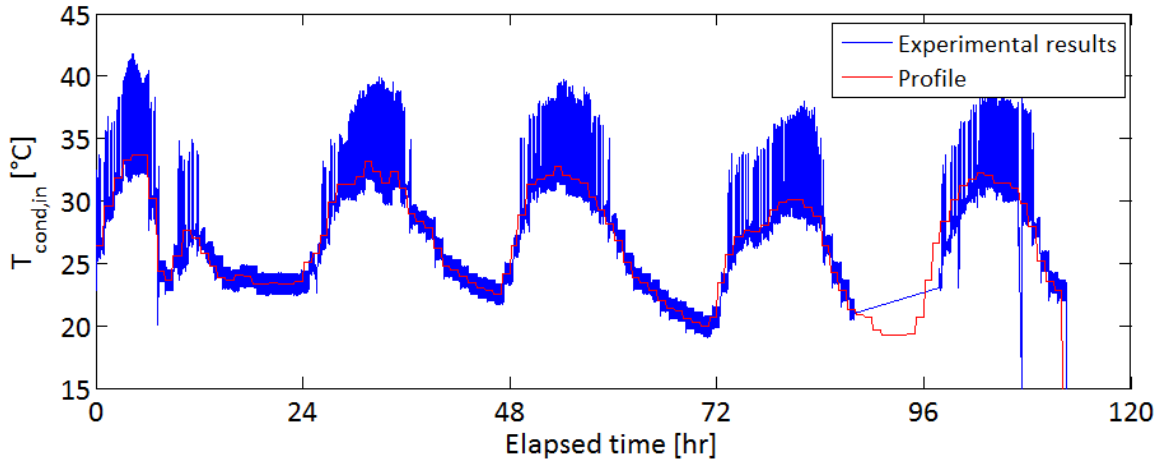


Figure 157: Profile and experimental results for condenser HTF inlet temperature

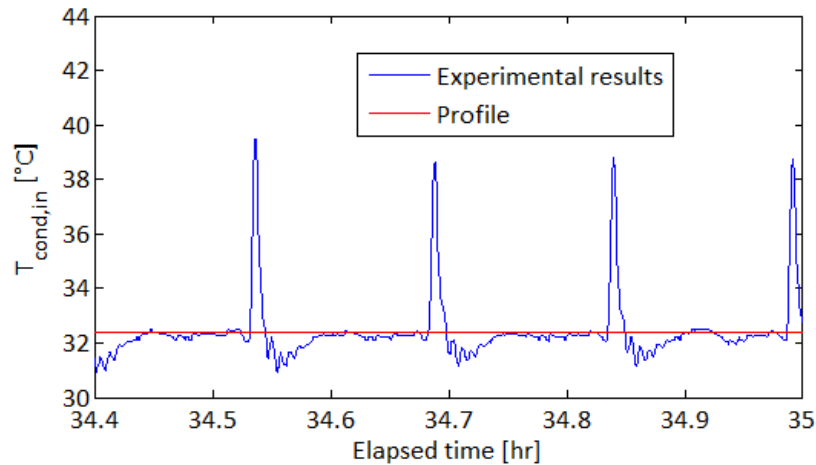


Figure 158: Zoom-in on profile of condenser HTF inlet temperature

Figure 159 shows the chilled water capacity with a 10-minute moving average applied to the experimental results. The profile has some intervals in which it cycles between zero and some higher value. This was done to force the chiller to cycle when its capacity would be greater than the cooling required. There is one period around 8-10 hours where the chiller was accidentally not running, and two periods around 27 and 50 hours where the engine was accidentally not turned on until the tank temperature had dropped to a low level that hurt the chiller capacity. In general the capacity was slightly lower than predicted by the profile since the heat recovery was not operational during the 5-day test.

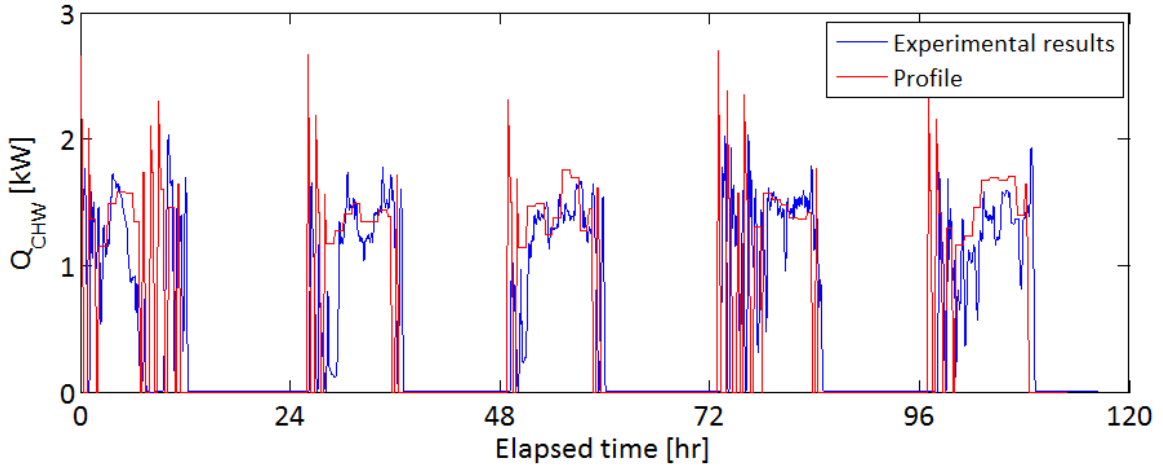


Figure 159: Profile and experimental results for chilled water capacity

Figure 160 shows the chilled water supply temperature. The periods when the heat pump is in operation has profile values of about 15 to 19°C, and the periods when the chiller is off has arbitrary profile values. The measured temperature matches closely during times when the chiller is operating, and the measured value drifts up to ambient temperature over several hours when the chiller is shut off. The short transient spikes that occur during chiller operation are due to an artifact of the moving average calculation, in which the time being averaged changes when the chiller cycle duration changes. The steady offset seen around ET=8 is a period when the chiller was off. Thus the chilled water supply temperature closely matched the profile.

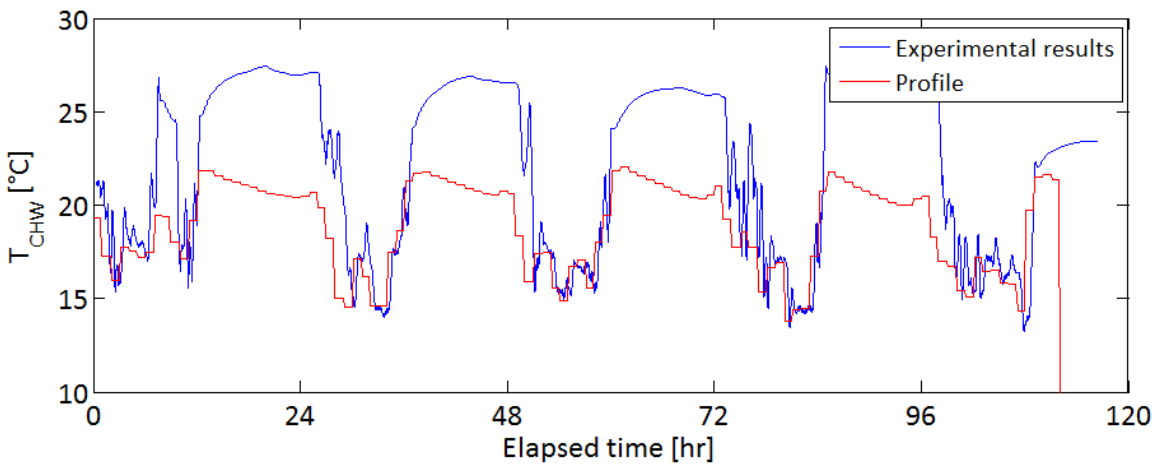


Figure 160: Profile and experimental results for chilled water supply temperature

Figure 161 shows the DHW. On the scale of the plot, it is very hard to see what is happening, so a zoomed-in figure follows this one. At around 96 hours the DHW was accidentally disabled for a few hours.

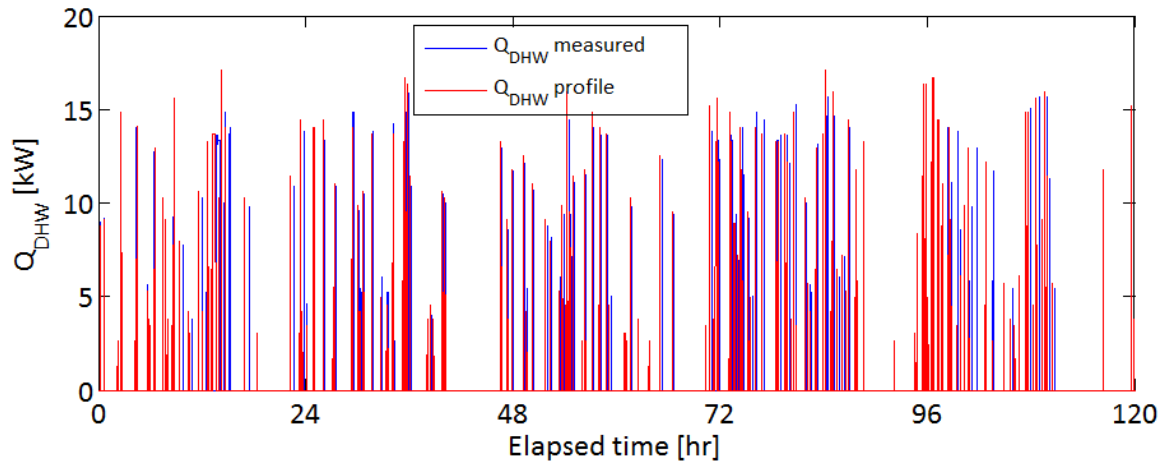


Figure 161: Profile and experimental results for DHW

Figure 162 zooms in on the 4.4 to 4.6 hour region to show an example DHW draw lasting about 15 minutes.

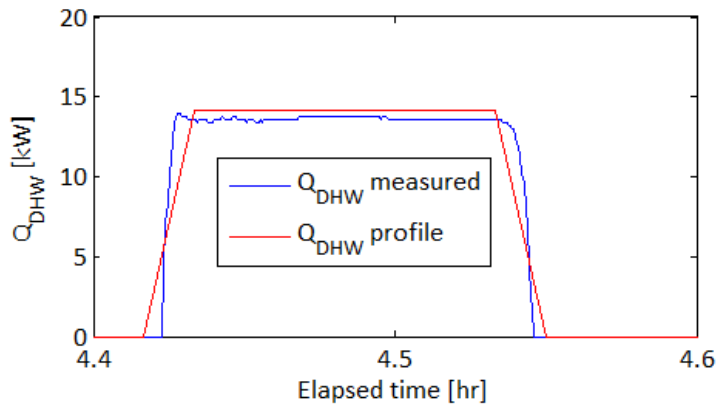


Figure 162: Zoom-in on DHW profile

Chapter 6: Model Development and Validation

In this thesis, models were developed for polygeneration systems at various levels of detail. Some basic analytical and first-order models of polygeneration systems were already discussed in Chapter 2. This chapter describes subsystem models of the adsorption heat pump, SI-RIC engine and storage tank. Then it describes a polygeneration system model comprised of a set of empirical models of each component.

First the models of subsystems are discussed (engine, heat pump, thermally stratified storage tank), and then the overall polygeneration system simulation.

6.1 CHP: dynamic model development and validation

A model of the CHP system was developed in TRNSYS. The first step was to determine the control strategy of the prime mover. The control strategy of the Ecopower unit was derived in an iterative process: a proposed strategy was formulated by observation, then modeling in TRNSYS and modified as required. This process is detailed in Bush (2010). The control strategy can be represented as a decision tree, shown in Table 38, Figure 163, and Figure 164.

Table 38: List of all variables involved in determination of Ecopower part load ratio

Input/Output Variables		
Symbol	Description	
PLR(i)	(output) Part load ratio at each timestep i	
T _b (i)	(input) Bottom tank temperature at each timestep i	
T _m (i)	(input) Middle tank temperature at each timestep i	
Internal Variables		
Symbol	Description	
PLR(i) _{calc}	Temporary PLR used for internal calculations at each timestep i	
Parameters		
Symbol	Value	Description
PLR _{min}	0.39	Minimum PLR at which PM is capable of running
T _{b,LTH,1}	37.5°C	First lower threshold temperature for bottom tank temperature
T _{b,UTH,1}	70°C	First upper threshold temperature for bottom tank temperature
T _{b,LTH,2}	40°C	Second lower threshold temperature for bottom tank temperature
T _{b,UTH,2}	55°C	Second upper threshold temperature for bottom tank temperature
T _{m,TH}	32°C	Threshold temperature for middle tank temperature
PLR _{calc,LTH}	0.2	Lower threshold PLR _{calc} which determines whether unit shuts off or runs at PLR _{min}
PLR _{calc,UTH}	0.6	Upper threshold PLR _{calc} which determines whether to pursue accelerated decrease in PLR
ΔPLR _{calc,Tm}	0.5	Increase in PLR _{calc} used when T _m is below T _{m,TH}
ΔPLR _{calc,decr}	0.01	Accelerated decrease in PLR _{calc} used when PLR is below PLR _{calc,UTH} and decreasing
C _{PLR}	0.025	Coefficient of PLR determination equation

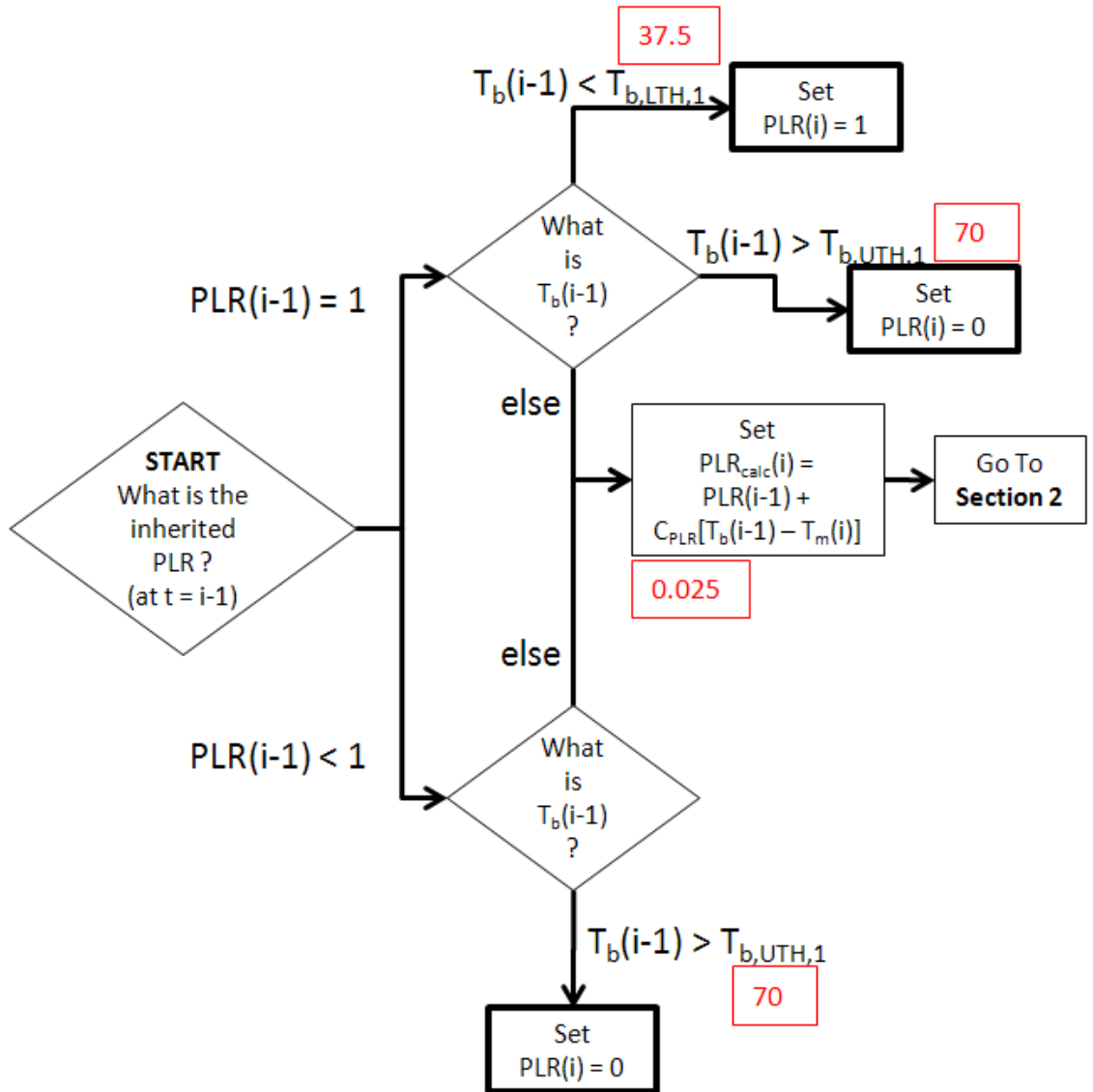


Figure 163: Ecopower control strategy depicted as a decision tree, part 1 of 3

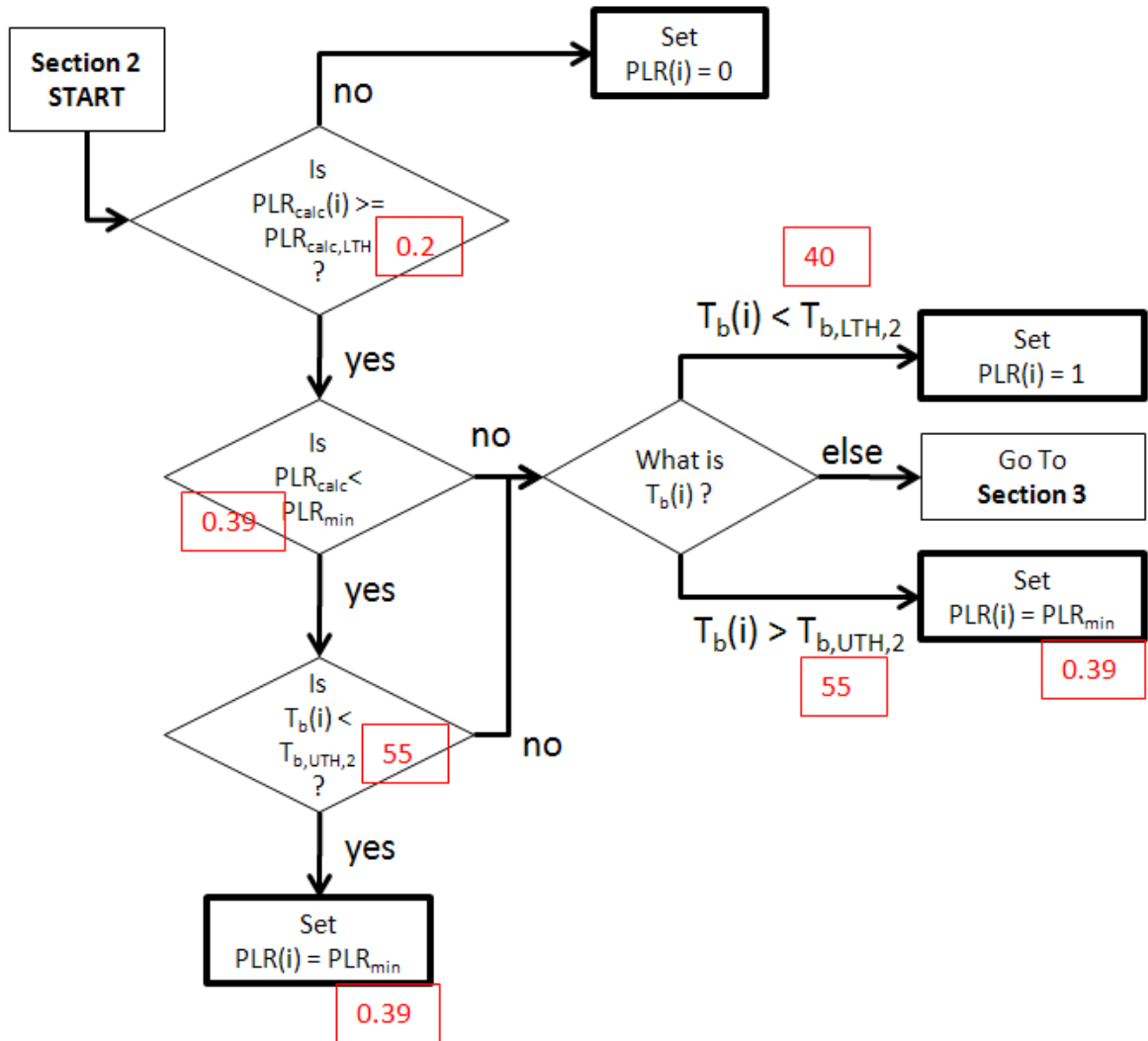


Figure 164: Ecopower control strategy depicted as a decision tree, part 2 of 3

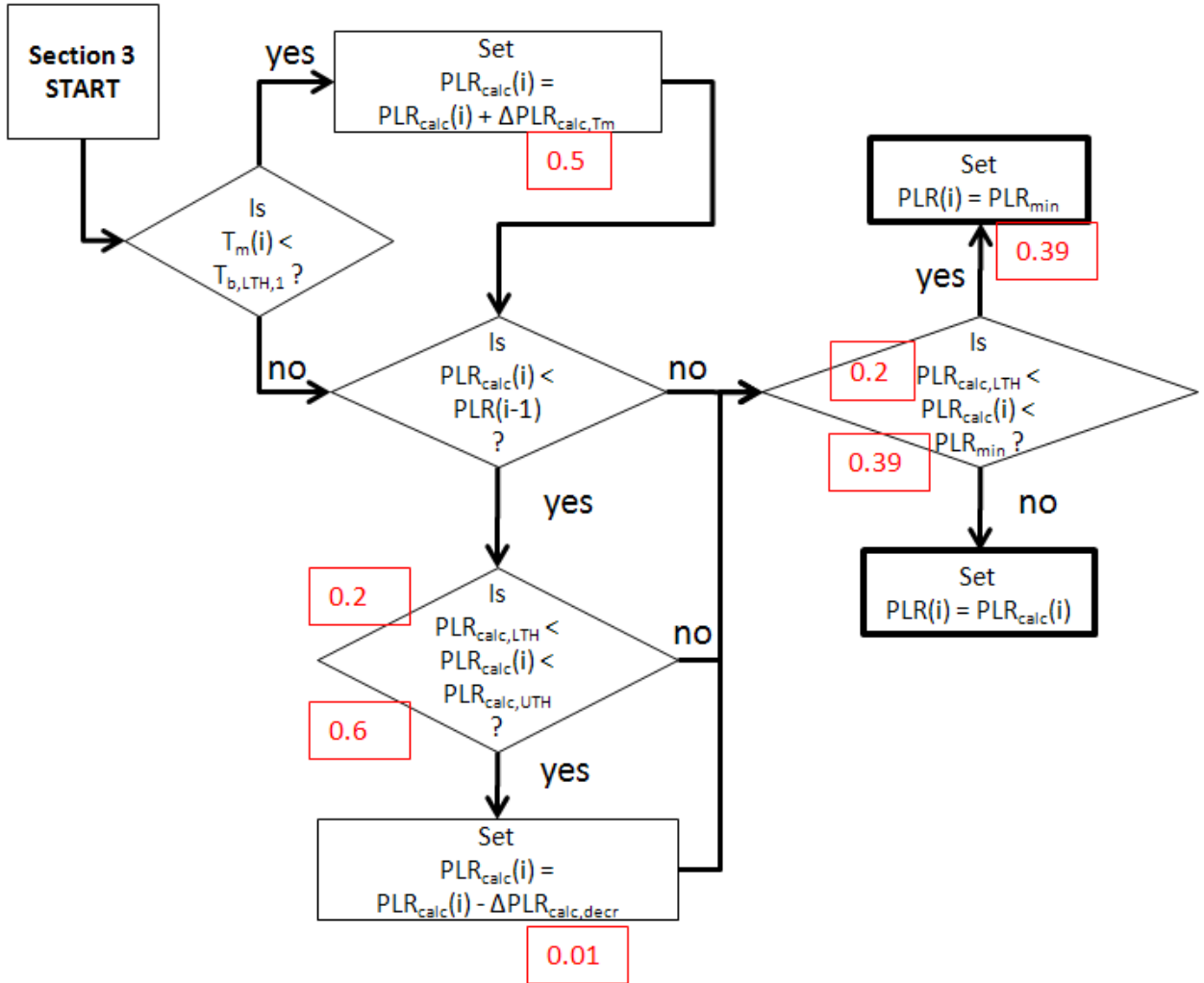


Figure 165: Ecopower control strategy depicted as a decision tree, part 3 of 3

6.2 Adsorption heat pump: analytical models and validation

In this section, analytical models of sorption cycle performance are discussed, starting with the well-known Carnot limit, and ending with the discussion of a novel and more complete expression for the COP of adsorption systems. This novel expression is also developed in parallel for absorption systems, so that these two sorption systems can be compared.

This section culminates in the development of Equations (84) and (90) for the COP of absorption and adsorption systems, and the evaluation of the adsorption expression for the experimental facility.

It is well known that the Carnot efficiency of thermally-driven equipment increases with higher regeneration temperature. Further insight can be gained by restating of the Carnot COP in terms of the temperature lift (ΔT_L) and driving temperature difference (ΔT_D), defined as $\Delta T_L \equiv T_1 - T_0$ and $\Delta T_D \equiv T_2 - T_1$. This allows Equation (2) to be restated as shown in Equation (71).

$$COP_{Ct,clg} = \left(\frac{T_0}{T_2} \right) \frac{\Delta T_D}{\Delta T_L} \quad (71)$$

The quotient of absolute temperatures T_0 and T_2 , which effectively anchors the expression at a specific location within the absolute temperature scale, can equivalently be expressed in terms of a single absolute temperature (T_1) as in Equation (72).

$$COP_{Ct,clg} = \left(\frac{T_1 - \Delta T_L}{T_1 + \Delta T_D} \right) \frac{\Delta T_D}{\Delta T_L} \quad (72)$$

Equations (71) and (72) are identical. Keeping in mind that T_0 , T_1 and T_2 are expressed in units of Kelvin or Rankine, the first quotient in both equations approaches unity¹ with the assumption that $T_0 \approx T_2$, or that $\Delta T_L \ll T_1$ and $\Delta T_D \ll T_1$. Thus an approximate Carnot COP can be expressed as a simple ratio of temperature differences as in Equation (73).

$$COP_{Ct,clg,approx} = \frac{\Delta T_D}{\Delta T_L} \quad (73)$$

¹ In practice the value of this quotient ranges from 0.62 (for refrigeration applications with high regeneration temperature, $T_0=263$ K and $T_2=423$ K) to 0.83 (for air conditioning applications with low

Since the first quotient in Equation (71) and (72) is always less than 1, Equation (73) is always an optimistic approximation. Furthermore, it becomes more accurate for smaller ΔT terms. Thus, for low driving temperature devices in particular, it offers a very compact, reasonably accurate and useful concept. Based only on first principles derived directly from Carnot expressions, it has been shown that low driving temperatures imply low efficiencies and/or limited temperature lifts.

Two observations can follow from this analysis. Although the Carnot efficiency becomes lower for lower driving temperatures, the cyclical sensible heating required in adsorption cycles also becomes less, meaning that the fraction of Carnot (fCt) could be expected to increase slightly for low regeneration temperature systems. Also, if a low-regeneration temperature adsorbent were developed that were capable of larger temperature lifts, it could be expected to have a lower COP.

Note that a similar procedure can be carried out for HAHD with similar conclusions. The $COP_{Ct,htg}$ is rewritten in terms of ΔT s and two or one absolute temperature in Equations (74) and (75), respectively.

$$COP_{Ct,htg} = \left(\frac{T_1}{T_2} \right) \frac{\Delta T_D + \Delta T_L}{\Delta T_L} \quad (74)$$

$$COP_{Ct,htg} = \left(\frac{T_1}{T_1 + \Delta T_D} \right) \frac{\Delta T_D + \Delta T_L}{\Delta T_L} \quad (75)$$

Again, the first quotient is approximately 1 for $T_1 \approx T_2$ or $\Delta T_D \ll T_1$, yielding the always-optimistic approximation shown in Equation (76).

$$COP_{Ct,htg,approx} = \frac{\Delta T_D + \Delta T_L}{\Delta T_L} = COP_{Ct,clg,approx} + 1 \quad (76)$$

The Carnot efficiency sets a limit on the performance of thermally-driven heat pump cycles, but does not address additional limitations imposed by properties of the working pair. For sorption-based systems without heat recuperation, one working fluid limitation that is easy to express is given by Equation (77). At ordinary temperatures, this limit will generally be lower than the Carnot efficiency limit, and is only a function of working pair properties; it is not a function of temperature (with the exception of small variations in fluid properties with temperature). Note that the relative heat of desorption, ψ , is defined as $\psi \equiv L_{des}/L_{evap}$.

$$COP_{th,max} = \frac{Q_{E,max}}{Q_{D,min}} = \frac{L_{evap}}{L_{des}} = \psi^{-1} \quad (77)$$

Equation (77) can be explained easily by looking at the system per unit mass flow of refrigerant. The amount of heat removed by the evaporator (Q_E) is at most proportional to the latent heat of the refrigerant, and the amount of heat consumed by the desorber (Q_D) is at least proportional to the latent heat of desorption of refrigerant from the sorbent.

One simple improvement in the accuracy of Equation (77) can be made by introducing the evaporator inlet liquid fraction² (equal to one minus the inlet vapor quality x), as shown in Equation (78).

$$COP_{th} = \frac{L_{evap} (1 - x_{evap,inlet})}{L_{des}} \quad (78)$$

² Refrigerants such as water with a high ratio of $L_{evap}/C_{p,liq}$, and applications with low temperature lift, have high evaporator inlet liquid fraction, with the quantity $(1 - x_{evap,inlet})$ approaching very near 1. On the other extreme are refrigerants such as CO₂ with very low ratios of latent heat to liquid sensible heat, in applications with high temperature lift, where this quantity may be significantly less than 0.5.

This inlet liquid fraction depends mainly on temperature lift and choice of refrigerant. By assuming constant specific heat and constant latent heat, Equation (79) can be derived, where ΔT_L is the temperature lift ($T_{cond} - T_{evap}$).

$$x_{evap,inlet} = \frac{C_{P,liq}\Delta T_L}{L_{evap}} \quad (79)$$

Substituting Equation (79) into Equation (78), a more explicit form that is easier to calculate from tabulated properties is obtained. This is shown in Equation (80).

$$COP_{th} = \frac{L_{evap} - C_{P,liq}\Delta T_L}{L_{des}} \quad (80)$$

So far, Equation (80) applies equally to absorption and adsorption systems without heat recuperation as an upper limit on performance. It is a slight function of temperature lift, but has no dependence yet on driving temperature difference (ΔT_D). Unlike the Carnot limit, it depends on the choice of working pair and is generally more accurate in the region of ordinary heat pump operation. It also correctly reflects the empirically observed trend for sorption systems to have relatively constant COP across a range of temperatures, which the Carnot expression misses.

Improving the accuracy of Equation (80) further can be divided into treatments for the numerator and the evaporator.

However, the numerator (i.e. the evaporator heat) is already basically correct, since the largest possible refinement would be accounting for superheating in the evaporator. Compared to latent heat transfer, and per unit refrigerant mass flow, the energy content of superheating is proportional to the quantity $\Delta T_{sh}C_{p,vap}/L_{evap}$. In vapor

compression evaporators, the ΔT_{sh} term is significant since vaporized refrigerant in the evaporator is forced to stay in contact with the heat source, even after all liquid has evaporated (and superheat must be designed-in to protect mechanical compressors). However, in the falling film evaporators common to sorption technology, the ΔT_{sh} term is approximately zero since as soon as refrigerant vaporizes it is no longer in contact with any heat transfer surface. In fact, without proper design the ΔT_{sh} can be truly zero (the vapor quality entering the ad/absorber can be less than 1), if splashing results in liquid droplets escaping the evaporator to be ad/absorbed directly as a liquid. In addition, even if non-falling film evaporator is used, common sorption refrigerants such as water, ammonia and methanol have low ratios of $C_{p,vap}/L_{evap}$. Thus for sorption systems, evaporator superheating effects are negligible, and the numerator can be left alone.

An exception is when an internal heat exchanger (IHX) is used. An IHX exchanges heat between the evaporator leaving vapor and condenser leaving liquid, superheating the former to subcool the latter. This improves the liquid fraction entering the evaporator, and in the ideal limit would result in $x_{evap,inlet}=0$.

The denominator of Equation (80), in contrast with the numerator, has potential for considerable refinement, and requires different approaches for absorption and adsorption.

For absorption systems, the primary refinement to the denominator would be accounting for the sensible heating of the solution which passes through the desorber. Evaluation of this requires the “flow ratio,” the ratio of liquid solution mass flow to refrigerant mass flow. The flow ratio can be defined based on the liquid inlet or outlet flow. A good approximation of flow ratio can be obtained by making the assumption that

solution leaves the desorber and absorber in equilibrium. Then the equilibrium refrigerant mass ratio (i.e. “loading”) at the end of desorption ($Y_{min,eq}$) and the end of absorption ($Y_{max,eq}$) can be calculated from a Dühring chart (see note in next paragraph regarding mass fraction vs. loading). The equilibrium differential loading ΔY_{eq} is defined as $\Delta Y_{eq} \equiv Y_{max,eq} - Y_{min,eq}$, and it can be shown by species mass balance that the flow ratio (outlet basis³) is given by $(1+Y_{min})/\Delta Y_{eq}$. Note that Y_{min} corresponds to $w_{abs,max}$.

With this expression for flow ratio, the denominator of Equation (80) (the amount of heat added to the desorber) can be increased by the amount of sensible heat added to the solution, yielding Equation (81). With more detailed knowledge of the kinetics of ab/desorption, a better estimate of Y_{min} and ΔY could be inserted, and the “eq” subscript dropped.

$$COP_{th} = \frac{L_{evap} - C_{p,liq} \Delta T_L}{L_{des} + C_{p,sol'n} \Delta T_D} \frac{1 + Y_{min,eq}}{\Delta Y_{eq}} \quad (81)$$

Note that the conventions for measuring refrigerant sorption are different between the fields of absorption and adsorption. Absorption conventionally uses absorbent mass fraction (mass of absorbent per mass of solution). Here this is denoted w_{ads} and the absorption literature generally uses X . In contrast, adsorption conventionally uses adsorbate loading, a form of mass ratio (mass of refrigerant per mass of “dry” adsorbent). Here this is denoted Y , and the adsorption literature uses Y or q^* . The current chapter adopts the adsorption convention of mass ratio Y throughout. For convenience,

³ The flow ratio can legitimately be defined based on inlet or outlet solution flow rate. For evaluating the sensible heat requirements of the desorber, the inlet-basis flow ratio neglects sensible heating of refrigerant which is subsequently desorbed, but the outlet-basis flow ratio (used by Herold et al., 1996) overestimates the sensible heating of desorbed refrigerant, due to the temperature glide of solution. In either case the inaccuracy is minor. Outlet basis is chosen here so that Y_{min} can be used, and neglected for sorbents with near-zero values of Y_{min} .

conversions between sorbent mass fraction (denoted w_{abs}) or refrigerant (sorbate) mass fraction (denoted w_{ref}) to refrigerant loading (equivalently, refrigerant mass ratio, denoted Y) are given in Equations (82) and (83).

$$Y = \frac{w_{ref}}{1 - w_{ref}} = \frac{1 - w_{abs}}{w_{abs}} \quad (82)$$

$$w_{ref} = \frac{Y}{1 + Y} \quad \text{or} \quad w_{abs} = \frac{1}{1 + Y} \quad (83)$$

While Equation (80) slightly over-predicts COP, Equation (81) actually under-predicts it, yielding a value of 0.60 for water-LiBr chillers⁴ whereas commercial chillers have COP \approx 0.7. This is because it neglects the benefits provided by the solution heat exchanger (SHX). Heat recovery in the SHX can be reasonably approximated by a small modification to this expression. Heat exchanger effectiveness (ε) is defined as the ratio of actual heat transfer to maximum possible heat transfer. Thus, for constant fluid specific heats, and for the side of the flow with minimum heat capacity flow rate (the product $\dot{m}C_p$), ε can be expressed as the ratio of actual temperature change to maximum possible temperature change. The heat capacity flow rates through the two sides of the SHX are nearly identical, allowing Equation (84) to be derived, which gives very realistic values for COP of absorption chillers. For comparison, an example numerical model for single effect absorption chillers in Herold et al. (1996) predicts a COP of 0.720. Solving that model requires iteration by computer, and each iteration requires dozens of property calls for mixture enthalpies, equilibrium mass fractions, and saturation pressures. Under identical conditions, shown in Table 39, Equation (84) predicts a COP of 0.735 and requires only two mass fraction property calls.

⁴ Under typical conditions and $\Delta Y_{eq}=0.15$, equivalent to $\Delta w_{abs} = 0.05$ (for $w_{abs,max}=0.62$, which is $Y_{min}=0.60$).

Note that $L_{des} = L_{evap} + \Delta h_{mix}$, $\Delta T_L = T_{cond} - T_{evap}$, and $\Delta T_D = T_{des} - T_{abs}$.

$$COP_{th} = \frac{L_{evap} - C_{P,liq} \Delta T_L}{L_{des} + C_{p,sol'n} (1 - \varepsilon_{SHX}) \Delta T_D} \frac{1 + Y_{min,eq}}{\Delta Y_{eq}} \quad (84)$$

Table 39: Conditions used in sample evaluation of Equation (84)

Variable		Value
Inputs	T_{evap}	1.5°C
	T_{cond}	32.9°C
	T_{abs}	39.9°C
	T_{des}	89.4°C
	ε_{SHX}	0.64
Properties based on inputs	L_{evap}	2497 kJ/kg
	Δh_{mix}	370 kJ/kg
	$C_{P,liq}$	4.18 kJ/kg-K
	$C_{P,sol'n}$	1.96 kJ/kg-K
	$w_{abs,max}$	0.619 kg _{LiBr} /kg _{sol'n}
	$w_{abs,min}$	0.563 kg _{LiBr} /kg _{sol'n}
Results	Herold et al. (1996) (full simulation)	COP=0.720
	Equation (84)	COP=0.735

Note that the $(1 - \varepsilon_{SHX})$ term accounts for heat recovery in the solution heat exchanger, but the expression lacks a way of accounting for systems with generator-absorber heat exchange (GAX cycles). The GAX cycle actually functions by reducing the L_{des} term, by supplying heat of desorption required by the desorber from the heat of adsorption released in the adsorber. A modification for GAX systems would include a term for the GAX efficiency, which would act on the L_{des} term.

Absorption systems must sensibly heat the solution (absorbent and retained refrigerant) flowing through the desorber. Similarly, adsorption systems experience degradation in performance due to the need to sensibly heat adsorbent and retained refrigerant. In addition, adsorption systems must sensibly heat metal and other “dead”

mass in the adsorber heat exchanger with each cycle. The dead thermal mass ratio (DTMR) is a novel term that captures the effects of these dead masses. The DTMR will be defined in order to facilitate the simple modification to Equation (80) shown in Equation (85).

$$COP_{th} = \frac{L_{evap} - C_{p,liq} \Delta T_L}{L_{des} (1 + DTMR)} \quad (85)$$

To satisfy Equation (85), the DTMR needs to be defined as the ratio of these terms:

- numerator: all sensible heat added to the adsorber heat exchanger per cycle
- denominator: the latent heat added to desorb refrigerant per cycle

In other words, the DTMR is the ratio of sensible heat (dead thermal mass) to latent heat in the desorber. In the present discussion, it is used as an intermediate step in the derivation of a COP expression for adsorption. But in general, because of its strong dependence on heat exchanger geometry and straightforward relation to COP, the DTMR can stand alone as a useful metric by which to compare adsorber heat exchanger designs.

An expression of the DTMR is shown in Equation (86), which includes sensible contributions from heat transfer fluid (HTF), non-adsorbent heat exchanger material, the sensible heat of the adsorbent itself, and sensible heat of “retained refrigerant.” Retained refrigerant is the refrigerant still remaining in the adsorbent at the end of desorption, and has mass of $m_{ads} Y_{min}$. Its C_p is approximately equal to the C_p of liquid refrigerant. It is analogous to the refrigerant still in solution leaving the desorber of an absorption system. Note that Y is the mass loading of the adsorbent, defined as mass of refrigerant adsorbed per unit mass of dry adsorbent. The differential loading is ΔY , defined as the loading at

the end of adsorption minus the loading at the end of desorption. The driving temperature difference, $T_{des} - T_{ads}$, is denoted ΔT_D . Products of density and volume have been written instead of masses to emphasize the dependence on heat exchanger geometry.

$$DTMR = \frac{\Delta T_D \left(\rho_{HTF} V_{HTF} C_{P,HTF} + \rho_{mat} V_{mat} C_{P,mat} + \rho_{ads} V_{ads} (C_{P,ads} + Y_{min} C_{P,ref}) \right)}{\Delta Y (\rho_{ads} V_{ads} L_{des})} \quad (86)$$

Rearranging terms, Equation (86) can be restated as in Equation (87).

$$DTMR = \frac{\Delta T_D}{\Delta Y L_{des}} \left(\frac{\rho_{HTF} V_{HTF} C_{P,HTF} + \rho_{mat} V_{mat} C_{P,mat}}{\rho_{ads} V_{ads}} + C_{P,ads} + Y_{min} C_{P,ref} \right) \quad (87)$$

The terms in Equation (87) can be categorized as follows:

- the ΔT_D term depends on application (see note below)
- the $C_{p,ads}$, ρ_{ads} and L_{des} terms depend on adsorbent/adsorbate working pair
- the ΔY and Y_{min} terms depend on both application and working pair
- the remaining terms depend on heat exchanger materials (ρ and C_p of HTF, material) and geometry (V_{HTF} , V_{mat} , V_{ads})

The terms can also be categorized according to their time dependence:

- L_{des} , ρ , C_p , and V terms are all independent of cycle time
- ΔT_D is a slight function of cycle time (it is very nearly constant for any practical cycle)
- ΔY and Y_{min} are strong functions of cycle time (ΔY_{eq} and $Y_{min,eq}$ are not)

Regarding the ΔT_D term, the application would primarily determine the available driving heat temperature and the ambient heat rejection temperature. However, a feasible working pair must be selected for the application. Also, there is typically some design and operational flexibility in driving temperature. Adsorbent properties typically mean that small driving temperature changes involve tradeoffs between COP and capacity. So,

depending on the accuracy desired, ΔT_D can be treated as a constant or could be based on a more complex model.

The most complex term to calculate in Equation (87) can be the differential loading, ΔY . To keep things simple, it can be straightforwardly evaluated at equilibrium conditions (ΔY_{eq}), in which case the DTMR would be $DTMR_{eq}$ (and the resulting COP would be COP_{eq}). For a more realistic evaluation, experimental data or heat and mass transfer modeling could be used to determine a more realistic ΔY . This is one of the strengths of the DTMR concept: it can be used for a quick and simple equilibrium calculation or for a much more detailed non-equilibrium calculation.

Evaluation of the remaining terms in Equation (87) is straightforward:

- Terms depending on heat exchanger design can be evaluated from heat exchanger geometry
- Terms depending only on working pair involve a simple adsorbent property ($C_{p,ads}$) and working pair property (L_{des})
- The term depending only on application is simply the driving temperature difference

To summarize, Equation (87) has been inserted into Equation (85). The results are shown in Equation (88). If the non-equilibrium differential loading (ΔY) and minimum loading (Y_{min}) are known, they can be used in place of the equilibrium values.

$$COP_{th} = \frac{L_{evap} - C_{P,liq} \Delta T_L}{L_{des} + \frac{\Delta T_D}{\Delta Y_{eq}} \left(\frac{\rho_{HTF} V_{HTF} C_{P,HTF} + \rho_{mat} V_{mat} C_{P,mat}}{\rho_{ads} V_{ads}} + C_{P,ads} + Y_{min,eq} C_{P,ref} \right)} \quad (88)$$

Comparing Equation (84) for absorption to Equation (88) for adsorption, the numerators are identical and the denominators are both the latent heat of desorption plus a sensible term. In each case that sensible term is proportional to the driving temperature

difference and inversely proportional to the differential loading. The difference is that, for absorption, the sensible term is proportional to the sorbent specific heat; while for adsorption, the sensible term is proportional to sum of four sensible elements, all with units of kJ per K per kg_{ads}:

- sorbent specific heat capacity
- retained refrigerant heat capacity
- heat exchanger material heat capacity [kJ/K] per unit mass of adsorbent
- heat transfer fluid heat capacity [kJ/K] per unit mass of adsorbent

One last note regarding the differences between absorption and adsorption COP expressions: if the adsorber heat exchanger had negligible HTF and material thermal mass, then the terms in parenthesis in Equation (88) would reduce to $C_{P,ads} + Y_{min}C_{P,ref}$. If a bulk C_P were used, as was done in the case of absorption with $C_{P,sol'n}$, then this would reduce to $C_{P,bulk}(1 + Y_{min})$, and the adsorption expression would be identical to the absorption expression. This shows that both the absorption and adsorption expressions account for the retained refrigerant specific heat, and the only difference lies in the need to cyclically sensibly heat additional components in the case of adsorption.

This discussion highlights one minor advantage of adsorption, which helps offset the need to cyclically heat the heat exchanger: the retained refrigerant is typically much lower than for absorption. Water-LiBr systems have retained refrigerant loading on the order of $Y_{min} \approx 0.6$ ($w_{abs,max} \approx 0.6$), and ammonia-water systems are on the order of $Y_{min} = 0.4$ ($w_{abs,max} \approx 0.7$). In contrast, values of $Y_{min} = 0.01$ to 0.1 are typical for adsorption systems. When $Y_{min} \approx 0$, that term can be neglected from the DTMR and COP calculations.

One more modification can be made to the adsorption COP expression to accommodate heat recovery. First, the effects of heat recovery need to be split into two

components. The first component is the isosteric or temperature-based heat recovery. It can be represented by a conventional heat exchanger effectiveness definition and is denoted ε_{HR}^{isost} . This type of heat recovery is present for all adsorption cycles using any method of heat recovery. It transfers sensible heat between adsorbers, and is defined as the fraction of the total adsorber HX desorption temperature swing (ΔT_D) which is accomplished by heat recovery.

The second component of heat recovery, which is only sometimes present, is the isobaric or variable-loading or latent heat recovery. It is denoted ε_{HR}^{isob} and is defined as the fraction of desorption which is powered by the heat of adsorption. This type of heat recovery involves desorption in the desorber powered by the heat of adsorption in the adsorber. It can most likely be encountered in cycles using thermal wave heat recovery. For most cycles and adsorbents under most operating conditions, $\varepsilon_{HR}^{isob}=0$.

Another way to think of these terms is that ε_{HR}^{isost} represents sensible heat recovery, and ε_{HR}^{isob} represents latent heat recovery. Equation (89) incorporates heat recovery into the expression for COP of an adsorption system.

$$COP_{th} = \frac{L_{evap} - C_{P,liq} \Delta T_L}{L_{des} (1 - \varepsilon_{HR}^{isob}) + \frac{\Delta T_D (1 - \varepsilon_{HR}^{isost})}{\Delta Y_{eq}} \left(\frac{\rho_{HTF} V_{HTF} C_{P,HTF} + \rho_{mat} V_{mat} C_{P,mat}}{\rho_{ads} V_{ads}} + C_{P,ads} + Y_{min,eq} C_{P,ref} \right)} \quad (89)$$

Restating in terms of DTMR, Equation (89) can be equivalently written as in Equation (90), which is Equation (85) modified to include heat recovery.

$$COP_{th} = \frac{L_{evap} - C_{P,liq} \Delta T_L}{L_{des} (1 - \varepsilon_{HR}^{isob}) + L_{des} (1 - \varepsilon_{HR}^{isost}) DTMR} \quad (90)$$

Note that perfect isosteric heat recovery can make the COP approach the limit of ψ^{-1} . The addition of isobaric heat recovery can boost the COP above that limit. Although it is useful to separate the two heat recoveries conceptually, they are not physically separate in practice. In a real system, isobaric heat recovery would be activated by the same mechanism as isosteric heat recovery following some threshold of isosteric recovery, and latent heat recovery would not be possible without sensible heat recovery.

Since the isosteric heat recovery term deals only with sensible heat, it can be defined based on temperature, as in a conventional heat exchanger effectiveness definition. The isobaric heat recovery term deals with latent heat of desorption, and thus is defined as the fraction of desorption heat provided from adsorption heat. This is only useful insofar as it isolates the effects of latent heat recovery to allow an explicit treatment of the sensible heat recovery.

Figure 166 illustrates these issues using $\Delta T_L = 20$ K and properties of the water/Z01 working pair ($L_{evap} = 2477$ kJ/kg, $L_{des} = 3000$ kJ/kg and $C_{p,liq} = 4.18$ kJ/kg-K). Both plots in the figure show contours of COP as a function of the two heat recovery effectivenesses. The left figure is for an extremely small DTMR of 0.1 and the right figure is for an extremely large DTMR of 10. The highest value contour reaches the Carnot COP; by the Second Law, no combination of heat recovery effectivenesses beyond this is physically possible. The lower left corner has value of COP_{min} , which is the COP without any heat recovery. The lower right corner has a value of COP equal to the ratio of latent heats ψ^{-1} (with an additional small penalty for non-zero refrigerant quality entering the evaporator).

Not shown in Figure 166 is the path that would be followed by actual heat recovery. Starting from the origin, initially heat recovery would be isosteric and the heat recovery path would follow the x-axis. Once the pressures in the adsorber chambers become equal, a vapor valve would open to bring them into mass-communication. From this point, the path would begin to rise off the x-axis through some roughly diagonally path. A Carnot system would proceed until intersecting the COP_{Ct} contour.

While approaching the COP_{Ct} is theoretically possible in both left and right cases, it is much more difficult with a large DTMR (on the right), where both heat recovery effectivenesses would need to approach one. For small DTMR (on the left), isobaric heat recovery is required to significantly boost the COP beyond that achievable without heat recovery, while with a large DTMR the isosteric heat recovery alone is effective. However, the large DTMR case is starting from a much lower base value of COP_{min} and would need large amounts of heat recovery to simply achieve the base COP of the small DTMR case.

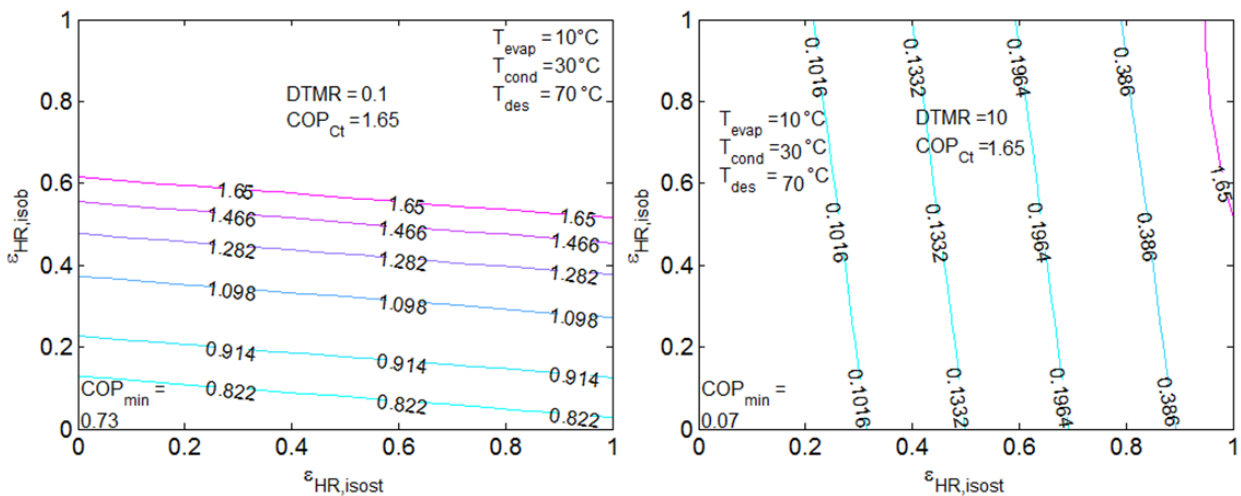


Figure 166: COP as a function of heat recovery effectivenesses

It is also important to note that the 2nd Law restricts the values of ϵ_{HR}^{isob} . The maximum possible value will be less than one in order to avoid exceeding the Carnot

limit. This must be true even in the ideal theoretical case where ψ^{-1} is greater than 1. This suggests that working pairs with a poor (low) value of ψ^{-1} have greater potential for isobaric heat recovery than working pairs with higher values of ψ^{-1} .

One more use of the DTMR and DTM is in expressing the COP as a function of cycle time. The dead thermal mass has units of kJ/K. Multiplying by ΔT_D [K] gives the sensible heat [kJ] that must be added each cycle, regardless of cycle time. Dividing this product by half cycle time [s] gives the average rate of sensible heat addition to the adsorber [kW]. Thus a rough estimate of cycle times that will result in the highest COP can be obtained from Equation (91) if the function $\Delta Y(\tau)$ is known. The cycle time with highest capacity can be obtained from the fact that capacity is proportional to $\Delta Y(\tau)/\tau$. Note that the difficulty in evaluation of this expression lies in the calculation of ΔY , which is a strong function of cycle duration. Since DTMR contains a ΔY term, it is a strong function of cycle time, and is written as $DTMR(\tau)$. On the other hand, DTM (the numerator of DTMR) can be treated as a constant.

$$COP_{th}(\tau) = \frac{\tau}{DTMR(\tau)} = \frac{m_{ads} L_{des} \Delta Y(\tau)}{\tau^{-1} DTM} \quad (91)$$

The simplest formulation of the relationship between differential loading and cycle time, denoted $\Delta Y(\tau)$, is to use a heat exchanger-bulk-averaged mass transfer coefficient, denoted h_m . This represents the mass transfer rate of refrigerant per unit of mass transfer driving force per unit area (for example, $[\text{kg}^1\text{s}^{-1}\text{m}^{-2}]$ per [driving force]). The driving force can be expressed in a variety of units. For the best engineering relevance, a driving force in differential pressure units is chosen, and the area is chosen to be the superficially apparent surface area of adsorbent (not the molecular-level surface

area, which is several orders of magnitude greater). The pressure difference is defined as the equilibrium vapor pressure of the adsorbent compared to the saturation pressure of pure refrigerant at the temperature of the adsorbent.

The bulk mass transfer coefficient was experimentally determined for the heat exchangers used in this experiment. Determination of the mass transfer coefficient requires measurement of the rate of ad/desorption of refrigerant mass under isothermal-isobaric conditions. Typically, material characterization experiments with such requirements are conducted using a balance or scale for mass measurements, and a small adsorbent sample placed inside an isothermal, pressure regulated vessel. However, this does not capture bulk-averaged properties for a whole heat exchanger.

A method was developed to measure the bulk mass transfer coefficient of the entire heat exchanger in situ in the fully-assembled operational heat pump. This required means to measure refrigerant mass transfer and to approximate isothermal-isobaric conditions. Refrigerant mass transfer was measured by condenser heat load. Isothermal-isobaric conditions were approximated by only opening the adsorber chamber to the condenser chamber for very short durations, on the order of 5-10 seconds. Then the chambers were re-isolated and held in isolation for about 600 seconds. This procedure was repeated until the cumulative open time was sufficient to fully adsorb/desorb the zeolite.

By this method, the value of h_m was calculated to be 6.5×10^{-6} in units of $[\text{kg}^1 \text{s}^{-1} \text{m}^{-2} \text{kPa}^{-1}]$ or $[\text{s}/\text{m}]$. Since each coated HX had an adsorbent substrate area of 16.7 m^2 , this means that an adsorber HX would transfer $1.1 \times 10^{-4} \text{ kg}_{\text{ref}}/\text{s}$ per kPa of equilibrium

differential pressure. For a typical ΔP_{equil} of 10 kPa, this is 1 g/s, which is just over 2 kW with the $h_{fg} = 2450$ kJ/kg for water refrigerant.

Evaluating the new analytical COP expressions for Z01 requires calculation of L_{des} for Z01 and DTMR for the particular heat exchanger on which it is coated in the experimental facility.

The latent heat of desorption for Z01 was determined by rearranging the Clausius-Clapeyron equation to yield latent heat, shown in Equation (92), where R_{ref} is the specific gas constant of the refrigerant and T is in units of Kelvin. The argument of the natural log has units of pressure, but the units are arbitrary since they cancel when taking the differential of the log. When evaluating the Clausius-Clapeyron equation for an adsorbent, the saturation pressure is really the equilibrium pressure of the adsorbent, evaluated at the given temperature and some specified adsorbate loading.

$$L = R_{ref} T^2 \left[\frac{\partial}{\partial T} (\ln(P)) \Big|_{sat} \right] \quad (92)$$

Using a finite difference method to evaluate the partial derivative, the Clausius-Clapeyron equation yields a value for L_{des} of 3.00 MJ/kg for Z01 zeolite at $T=315.15$ K (45°C) and $Y=0.10$ kg_{H₂O}/kg_{ads} (roughly half of Y_{max}).

Geometric measurements and CAD drawings were used to calculate the masses of constituents comprising the coated adsorber heat exchangers used in the experimental heat pump. The total measured mass of each heat exchanger is 11.52 kg without HTF (though the value can change depending on ambient humidity). The mass calculated from geometric measurements was practically identical at 11.51 kg without HTF (13.17 kg with HTF). For the moment ignoring the headers, the distribution of constituent masses,

and their corresponding thermal masses, is shown in Figure 167. Note that thermal mass is defined as the product of mass and specific heat, and thus has units of kJ/K.

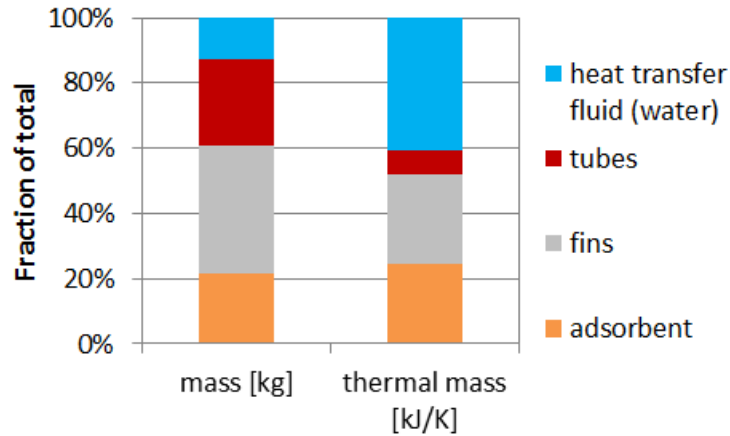


Figure 167: Relative contributions of heat exchanger constituents to mass and thermal mass of heat exchanger in isolation

A note of explanation is warranted on the inclusion of HTF in the thermal mass calculation. It may seem that, at the beginning of the desorption phase, the cool HTF in the heat exchanger will simply be expelled ahead of the incoming hot HTF, meaning that it never need be heated and does not contribute to thermal mass. However, as part of a closed loop, that HTF has to go back to the source of heat where it does need to be heated. Thus the HTF charge should be included in the thermal mass of the heat exchanger. In fact, all HTF should be included which lies between the switching valves that control the flow of either cool or hot HTF into/out of the heat exchanger (the “extended control volume”). The two control volumes (c.v.) are illustrated in Figure 168.

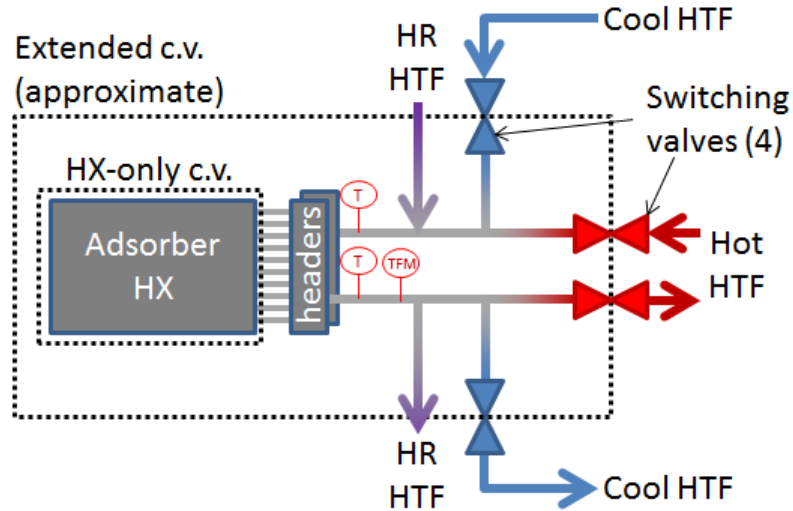


Figure 168: HX-only and extended control volumes for adsorber HX

The results of calculations for the extended control volume as exists on the prototype laboratory chiller are shown in Figure 169. Despite efforts to minimize it in construction, in this case the header and header-to-valve thermal masses account for nearly a quarter of the total. Clearly it is in the interest of the heat pump designer to minimize the header and pipe volumes between the heat exchanger flow passages and the HTF switching valves, in addition to minimizing the volume of the active heat exchange flow passages themselves. This can prove difficult as the plumbing needs to extend out of the vacuum chamber and may also incorporate tees and instrumentation before reaching a switching valve.

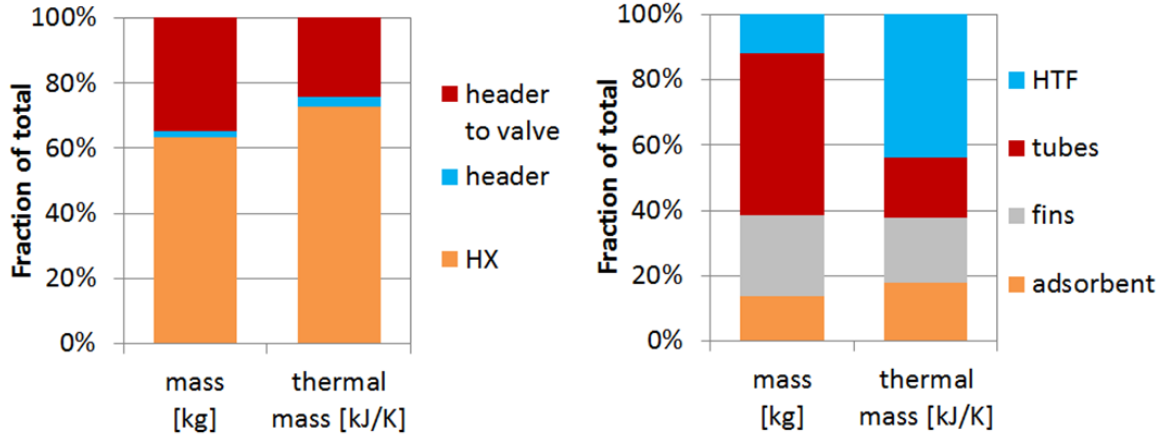


Figure 169: Relative contributions to mass and thermal mass of extended control volume

HTF should be excluded from thermal mass when an open loop is used. An example is using engine exhaust gas directly as a HTF, and expelling it to ambient after use. Another example is extracting geothermally heated water and dumping it downstream of the heat source after use.

Since the DTMR expression is entirely based on geometric parameters except for the ΔY and ΔT_D terms, it can be conveniently expressed with ΔY and ΔT_D explicit. It has been calculated for the prototype Z01-coated heat exchangers and the result is shown in Equation (93) for the heat exchanger without headers or connecting plumbing, and in Equation (94) for the extended control volume.

$$DTMR_{Z01,HX-only} = 0.00205 \frac{\Delta T_D}{\Delta Y} \quad (93)$$

$$DTMR_{Z01,extended} = 0.00275 \frac{\Delta T_D}{\Delta Y} \quad (94)$$

As seen in Figure 128, the ΔY for most practical experimental tests ranged from about 0.05 to 0.15. For a ΔT_D of 40 K, this gives a range of DTMR of about 0.74 to 2.23. In the best case without heat recovery and neglecting nonzero evaporator inlet vapor

quality, the COP would be expected to be lower than that predicted by $L_{evap}/L_{des} (\psi^{-1})$ by a factor of $1/(1+0.74)$ to $1/(1+2.23)$. For $\psi^{-1} = 0.82$, then the maximum COP would be 0.47.

Equation (85) can be evaluated semi-empirically by using measured ΔY for each experimental test. The result is shown in Figure 170. Since Equation (85) does not account for heat recovery, it is only accurate for tests without heat recovery. Figure 171 shows the fit of Equation (85) to the tests without heat recovery, in which 95.2% of 125 experimental results lie within 10% of the predicted value.

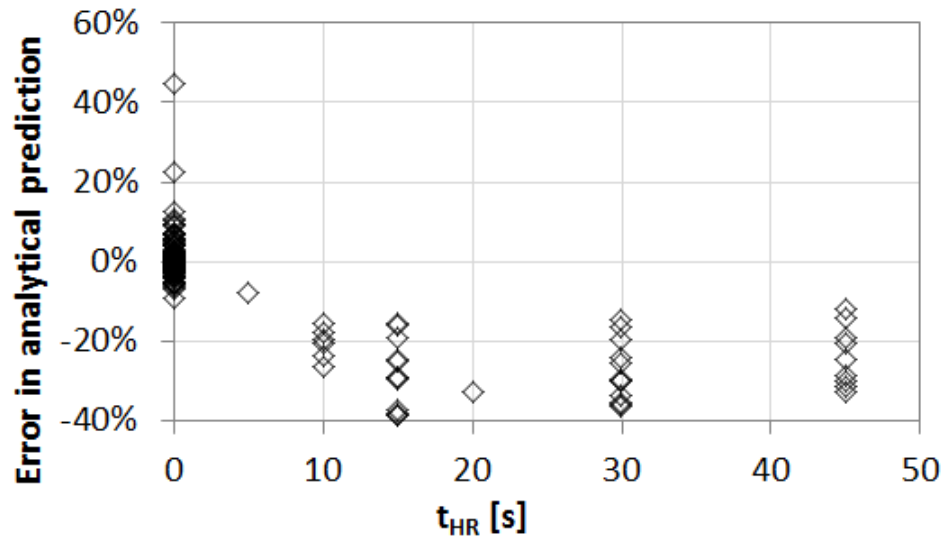


Figure 170: Analytical COP expression without heat recovery compared to all experimental results

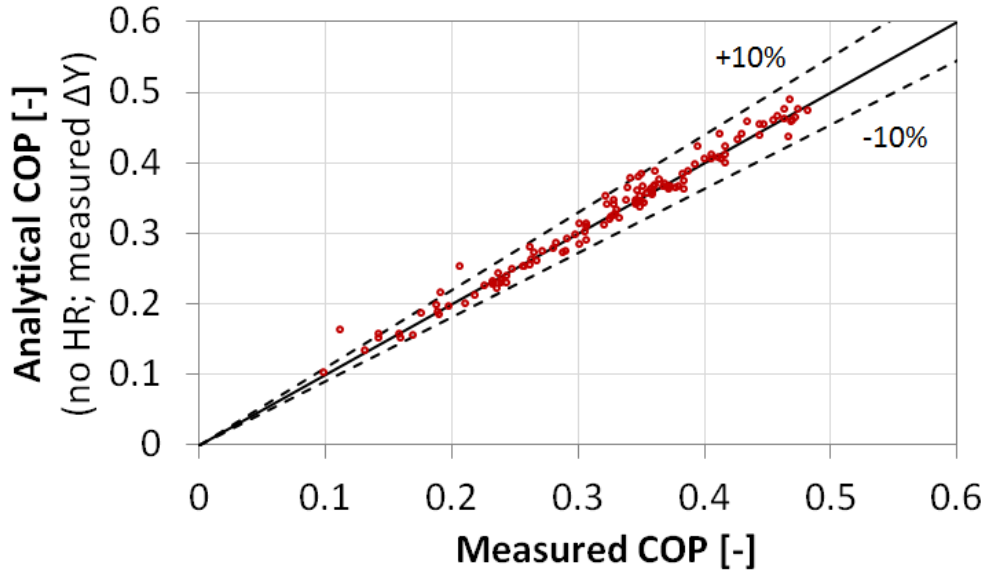


Figure 171: Analytical COP expression without heat recovery compared to experimental results without heat recovery

To capture the effects of heat recovery, Equation (90) must be used. Isobaric heat recovery was generally observed to be absent from heat recovery tests. Setting that to zero, a value of 0.40 for isosteric heat recovery effectiveness of any duration yields the fits shown in Figure 172 and Figure 173, where 92.3% of 170 experimental results are predicted within 10%.

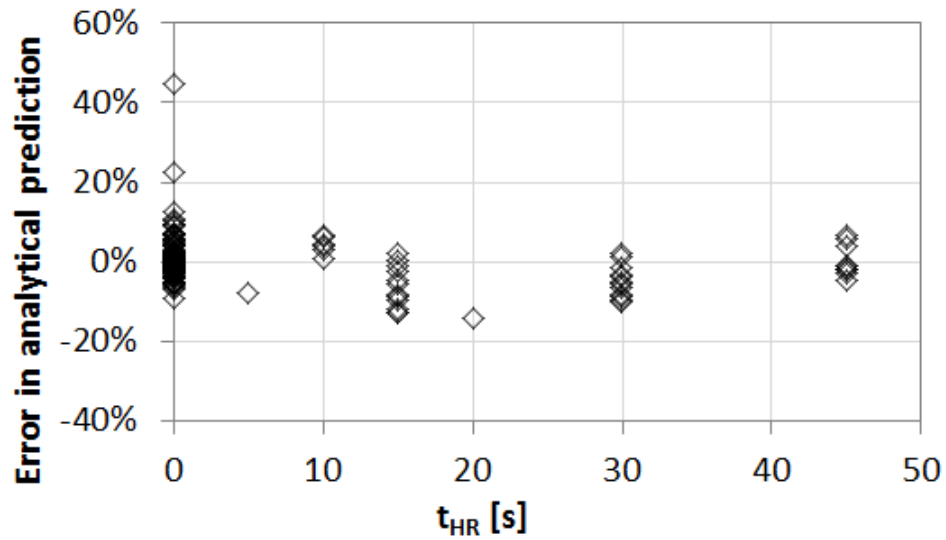


Figure 172: Analytical COP expression with 40% isosteric heat recovery effectiveness

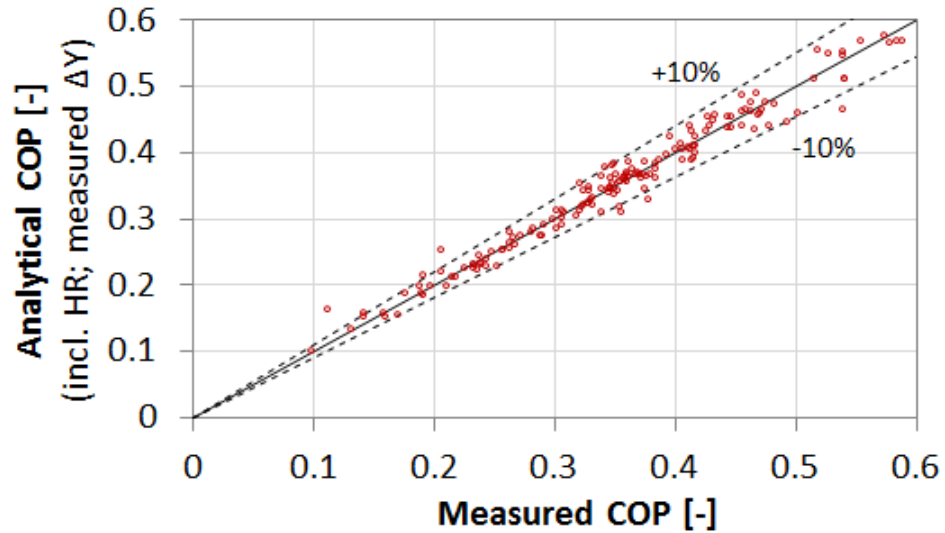


Figure 173: Analytical COP expression with 40% isosteric heat recovery effectiveness vs. 170 experimental results

Finally, it is important to point out the importance of deviation from equilibrium loading. If Equation (85) is evaluated using the ΔY_{equil} instead of $\Delta Y_{measured}$, the result is shown in Figure 174 and Figure 175. The accuracy generally improves as the duration of adsorption increases, since this gives the system a longer time to approach equilibrium. The COP predicted by the equilibrium assumption for Z01 is fairly constant due to the strong “S” shape of the isotherms (or equivalently, the tight clustering of isosteres in the Dühring diagram).

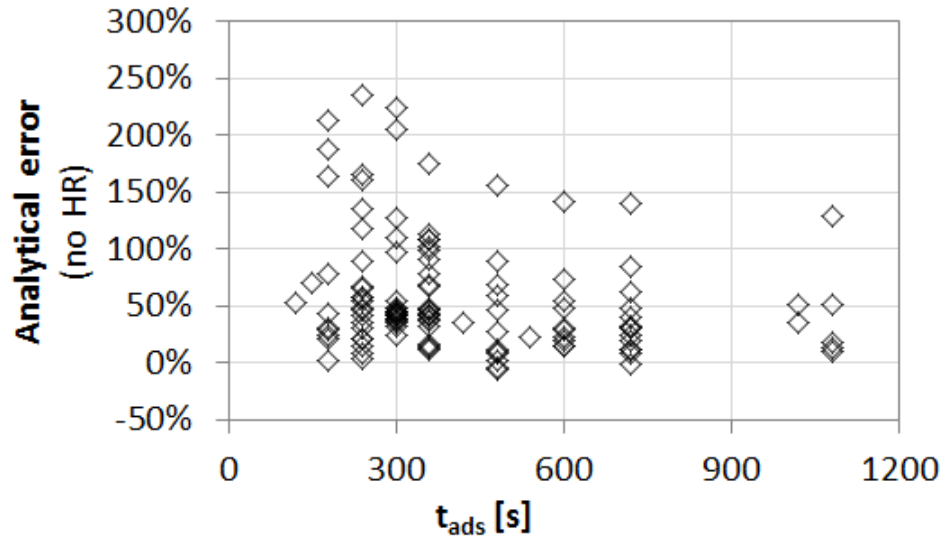


Figure 174: Analytical prediction error using the equilibrium assumption vs. adsorption duration

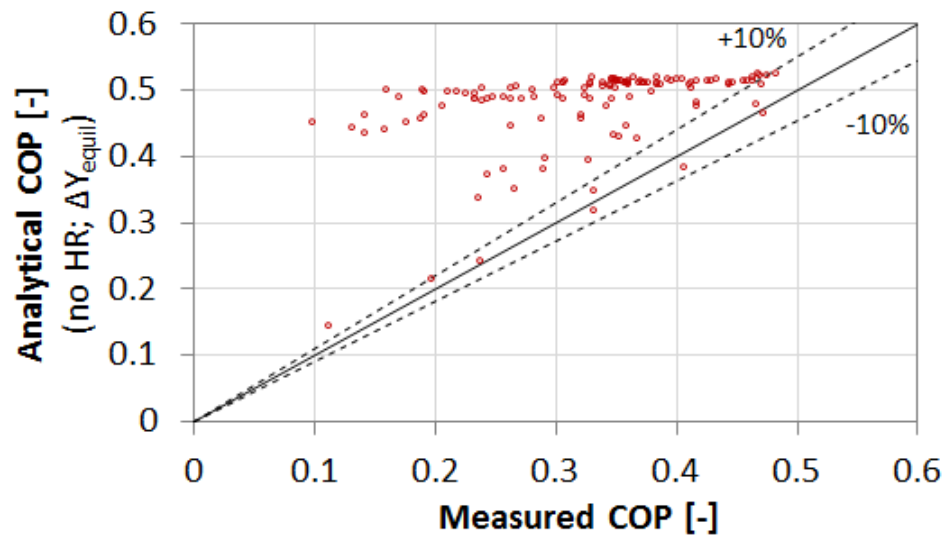


Figure 175: Analytical COP using the equilibrium assumption vs. measured COP

6.3 Adsorption heat pump: graphical approaches

Data on the equilibrium properties of the zeolite were provided by the manufacturer. Based on their data, a Dühring plot was constructed, as shown in Figure 176.

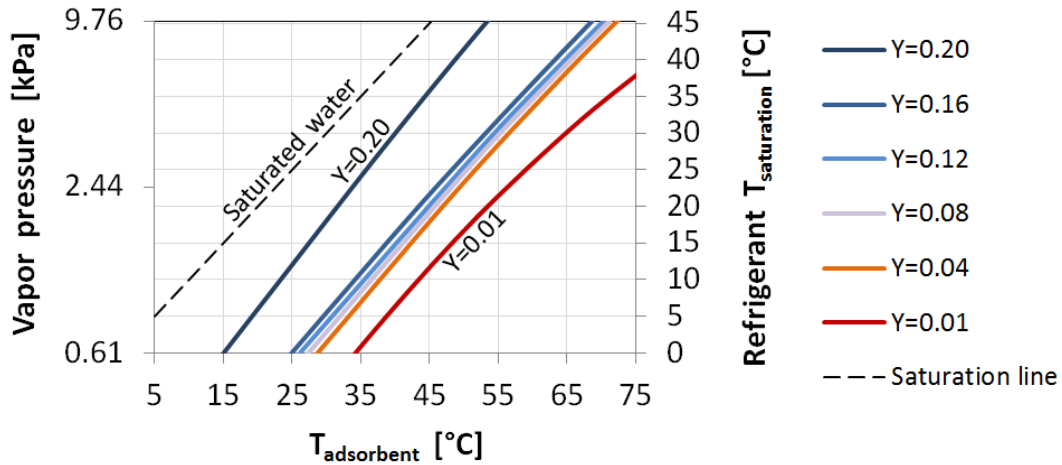


Figure 176: Dühring diagram for AQSOA FAM Z01 zeolite

Several useful observations can be made by inspection of the Dühring diagram by making use of three visually identifiable elements: (1) L_{des}/L_{evap} (relative isostere slope), denoted ψ , (2) $\Delta T_{dry-wet}$, and (3) $\Delta T_{wet-sat}$. The last two of these are illustrated in Figure 177. The relative isostere slope (ψ) is so named because the slope of a line in the Dühring diagram is proportional to the latent heat. Thus the isostere slope is proportional to L_{des} , the saturation line slope is proportional to L_{evap} , and the slope of the isostere relative to the saturation line is ψ . The term $\Delta T_{dry-wet}$ represents the temperature difference between a dry isostere and a wet isostere at constant pressure. It will generally have the same value when evaluated at any pressure. The term $\Delta T_{wet-sat}$ represents the temperature difference between a wet isostere and the saturation line at constant pressure. For the following analysis, it must be evaluated at the evaporator pressure.

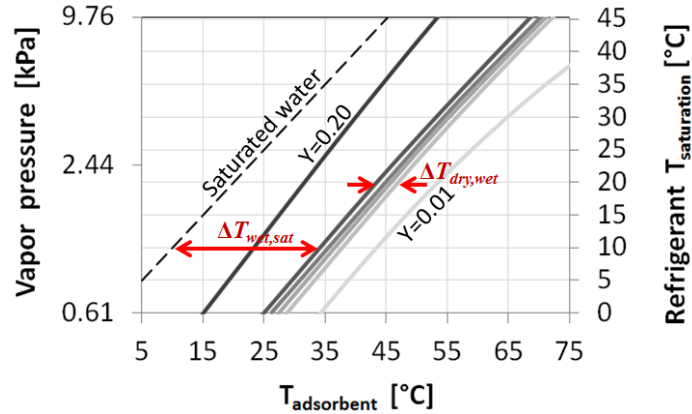


Figure 177: $\Delta T_{wet,sat}$ and $\Delta T_{dry,wet}$ on the Dühring diagram of Z01

The maximum temperature lift ($\Delta T_{L,max}$) can be estimated from the diagram as follows. Relatively complete adsorption requires that a high value of Y be achieved during adsorption. At the vapor pressure of saturated refrigerant in the evaporator (e.g. 10°C on the right y-axis), a Y of 0.16 corresponds to an adsorber temperature of just under 35°C. Since $T_{cond} \approx T_{ads}$ and temperature lift is $T_{cond} - T_{evap}$, and, slightly less than 25 K is the maximum temperature lift. Note that the outcome of this computation is equivalent to the horizontal distance from the saturated refrigerant line to the wet isostere. It could be said that, in order to have a large potential temperature lift, a working pair would have wet isosteres far to the right of the saturation line in a Dühring diagram. Since the slopes of the isosteres are steeper than the slope of the saturation line, the maximum temperature lift will be reduced as evaporator temperature increases, though this is a minor effect.

The minimum required driving temperature difference ($\Delta T_{D,min}$) can also be estimated from the diagram. Relatively complete desorption requires that, at the vapor pressure of saturated vapor in the condenser (e.g. 35°C on the right y-axis), a low value of Y must be achieved. For $Y=0.04$ this means an adsorber temperature of nearly 65°C. Since $T_{cond} \approx T_{ads}$ and ΔT_D is $T_{des} - T_{ads}$, a minimum ΔT_D of about 30 K is required. Note

that the outcome of this computation is equivalent to the horizontal distance from the saturated refrigerant line to the dry isostere. It could be said that, in order to have a low driving temperature, a working pair would have dry isosteres close to the saturation line in a Dühring diagram. A steeper isostere (relative to the saturation line slope) will reduce the ΔT_D for a given ΔT_L , but at the expense of lower COP.

Taking the above observations together, the relative driving temperature (defined as the quotient $\Delta T_D/\Delta T_L$) can be obtained by a ratio of horizontal differences, both starting from the refrigerant saturation line. The numerator is the distance extending to a dry isostere, and the denominator the distance to a wet isostere.

Since it will be shown later – see Equation (73) – that COP_{Ct} must be less than the relative driving temperature, it can be concluded that physical properties of a working pair could never be such that this ratio of distances exceeds the Carnot COP. Thus, assuming that isosteres have constant slope (constant L_{des}), the farther away from the saturation line that isosteres get, the wider apart the wet and dry isosteres must become.

This is relevant to the development of heat pumps for low driving temperature applications, because a low driving temperature at fixed temperature lift implies a low relative driving temperature. Getting the wet and dry isosteres to approach each other (making a more s-shaped isotherm and lowering the driving temperature) implies that the isosteres must also approach the saturation line (decreasing the achievable temperature lift).

Over 145 steady state evaluation points, the experimental adsorption system achieved the f_{Ct} values that were shown in Figure 127. Since the experimental adsorption

system achieves very reasonable values for f_{Ct} , there is little hope for any adsorbent to do much better than the Mitsubishi Plastic adsorbent for 70°C driving temperatures.

Another observation is that the narrowness of the intermediate isosteres ($Y=0.16$ to 0.04), which is related to the strong S-shape of isotherms in a plot of loading vs. relative pressure, is responsible for the property of low relative regeneration temperature.

Every adsorption cycle has the potential for isosteric heat recovery, but even perfect isosteric heat recovery can only bring the cycle to the ideal COP expressed by the inverse ratio of latent heats (ψ^{-1}), which is typically substantially below the Carnot COP. In order to improve on this, isobaric heat recovery would be required. However, isobaric heat recovery is much more difficult to achieve, see Tierney (2008).

In summary, the ideal working pair has conflicting characteristics:

- isosteres far to the right for high temperature lift
- isosteres not far to the right for low required driving temperature
- shallow isosteres (low ψ) for high COP
- steep isosteres (high ψ) for low ΔT_D relative to ΔT_L

These observations reinforce the idea that different working pairs are better suited to different applications. For the application of air conditioning with ICE coolant heat, the Z01 zeolite is very well suited, with prototype f_{Ct} experimentally approaching 0.4. It should be expected that an alternative adsorbent, if one were developed to have higher temperature lift abilities, for the same f_{Ct} , would have lower COP and/or higher required driving temperature difference. The above observations are summarized in Table 40.

Table 40: Summary of Dühring diagram visual interpretations

Heat pump property	Formula in terms of $\Delta T_{w,s}$, $\Delta T_{d,w}$ and ψ	Visual interpretation on Dühring diagram
$\Delta T_{D,min}$ – minimum driving temperature difference [K]	$\Delta T_{D,min} = \Delta T_{w,s} + \Delta T_L * (\psi - 1) + \Delta T_{d,w}$	horizontal distance from saturation line to <i>dry</i> isostere at <i>condenser</i> pressure
$\Delta T_{L,max}$ – maximum temperature lift [K]	$\Delta T_{L,max} = \Delta T_{w,s}$	horizontal distance from saturation line to <i>wet</i> isostere at <i>evaporator</i> pressure
$\Delta T_D / \Delta T_L$ – relative driving temperature [-]	quotient of previous two definitions	ratio of: (horizontal of distance from refrigerant saturation line to a <i>dry</i> isostere) to (horizontal distance from refrigerant saturation line to a <i>wet</i> isostere)
Carnot COP _{th} limit [-]	see above	approximately equal to the relative driving temperature (pessimistic by factor of 0.6 – 0.9)
COP limit without heat recovery [-]	$COP_{th,max} \text{ (no HR)} = \psi^{-1}$	ratio of isostere slope to saturated refrigerant slope

6.4 Adsorption heat pump: detailed equilibrium thermodynamic model

An equilibrium thermodynamic adsorption chiller model based on Anyanwu and Ogueke (2005) was carried out in Engineering Equation Solver. The results are detailed in Gluesenkamp et al. (2012c). This model was used to answer or estimate the following questions at the initial design phase:

- How much adsorbent is required to achieve the desired 2 kW of cooling capacity?
- What is the expected COP (how much heat do the adsorbers need to transfer)?
- What are the minimum T_{src} , minimum T_{CHW} , and maximum T_{rej} ?

The following assumptions were used in the model:

- Equilibrium is reached in each half cycle

- For capacity estimation, a fixed half cycle duration of 300 seconds is assumed (based on manufacturer recommendation)
- No heat recuperation or pressure recovery
- 3 K approach temperature in each heat exchanger
- No pressure drops in piping (later relaxed as shown in Chapter 4)
- C_p of dry adsorbent = $2 \text{ kJ}\cdot\text{kg}^{-1}\text{K}^{-1}$
- C_p of adsorber heat exchanger materials = $2 \text{ kJ}\cdot\text{kg}^{-1}\text{K}^{-1}$
- Dead mass ratio is 1:2 [kg/kg]
- No subcooling in the condenser
- Refrigerant leaving desorber is saturated at desorber temperature

The crux of the model is in the calculation of desorber heat input. This is given by Equation (95). The numerator represents the heat [kJ] added to the desorber each half cycle, with the half-cycle duration [s] in the denominator.

$$\dot{q} = \frac{q_{\text{evap}} + q_{\text{ret.ref,sens}} + q_{\text{gen.ref,sens}} + q_{\text{adsorbent,sens}} + q_{\text{metal,sens}}}{\tau} \quad (95)$$

A sample result with adsorber state point labels is shown in the Z01 Dühring diagram in Figure 178.

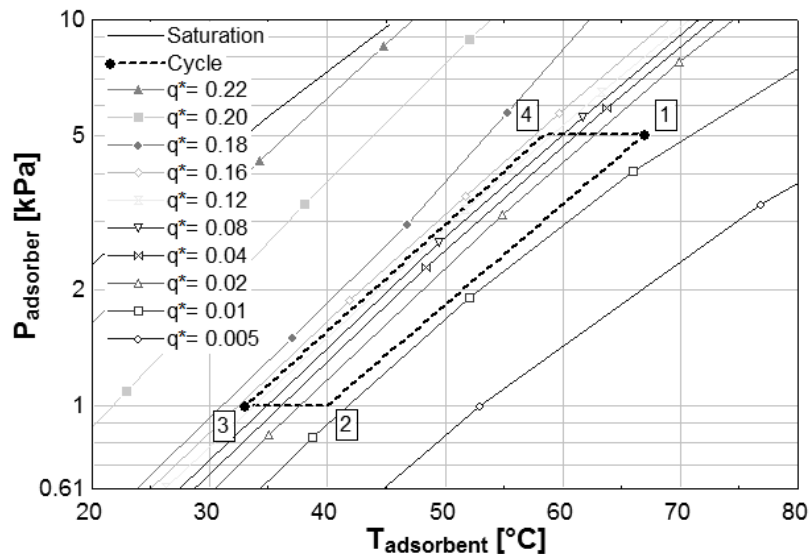


Figure 178: Equilibrium Dühring diagram for Z01 for $T_{\text{CHW}}/T_{\text{rej}}/T_{\text{src}} = 10/30/70^\circ\text{C}$

The COP, SCP and f_{Ct} are shown in Figure 179 to Figure 181 for a range of operating conditions, varying one external temperature at a time. It is expected that the COP and SCP are overestimated due to the equilibrium assumption, although performance gains by adding heat and pressure recovery should mitigate the overestimation.

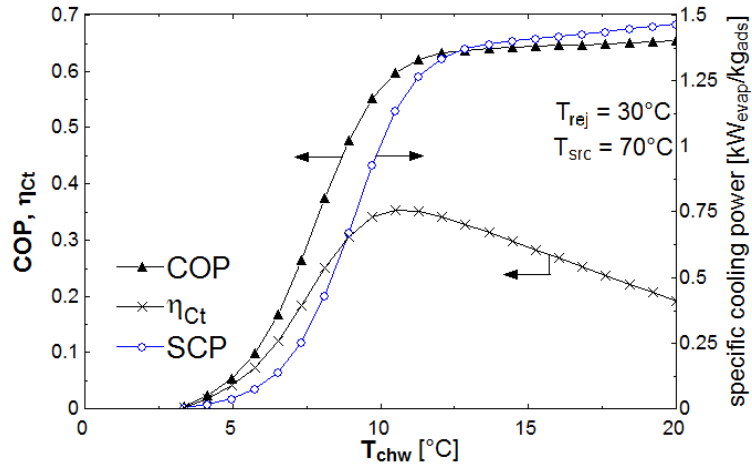


Figure 179: Effect of T_{CHW} on performance predicted by equilibrium model

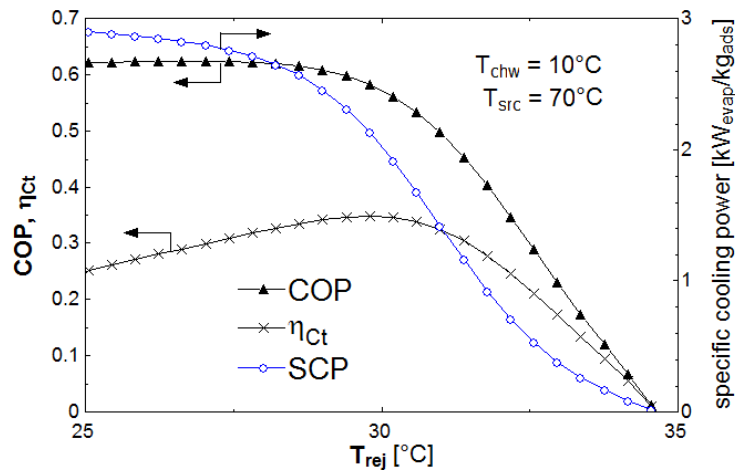


Figure 180: Effect of T_{rej} on performance predicted by equilibrium model

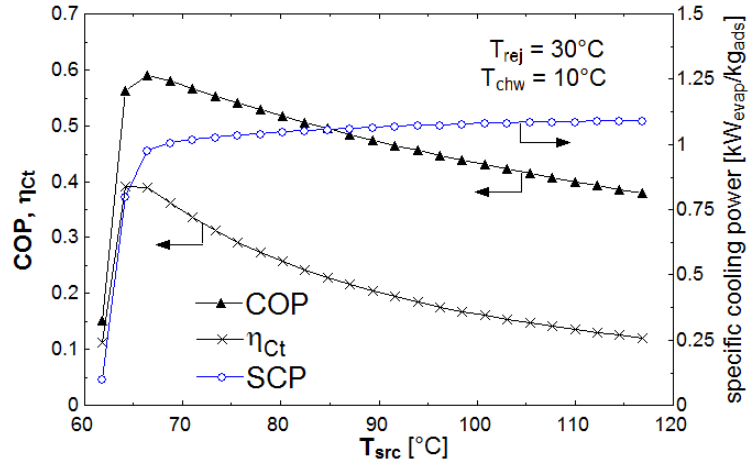


Figure 181: Effect of T_{src} on performance predicted by equilibrium model

The COP and SCP would vary with cycle time, an independent control variable not captured by this model. However, the model displays the expected COP and SCP trends with each temperature. As in Figure 178 and Equation (95), cooling capacity is related to the difference in isostere values between points 3 and 1. Lower evaporator temperatures hurt capacity by moving point 3 vertically down (to a lower isostere). Lower desorber temperatures hurt capacity by moving point 1 horizontally left (to a higher isostere). Higher adsorber temperatures hurt capacity by moving point 3 horizontally right (to a lower isostere), with higher condenser temperatures moving point 1 vertically up (to a higher isostere). This is all broadly consistent with the results in Figure 179 to Figure 181.

Although not modeled here, Figure 182 shows the state points in time that would form a framework for a model with pressure and heat recovery.

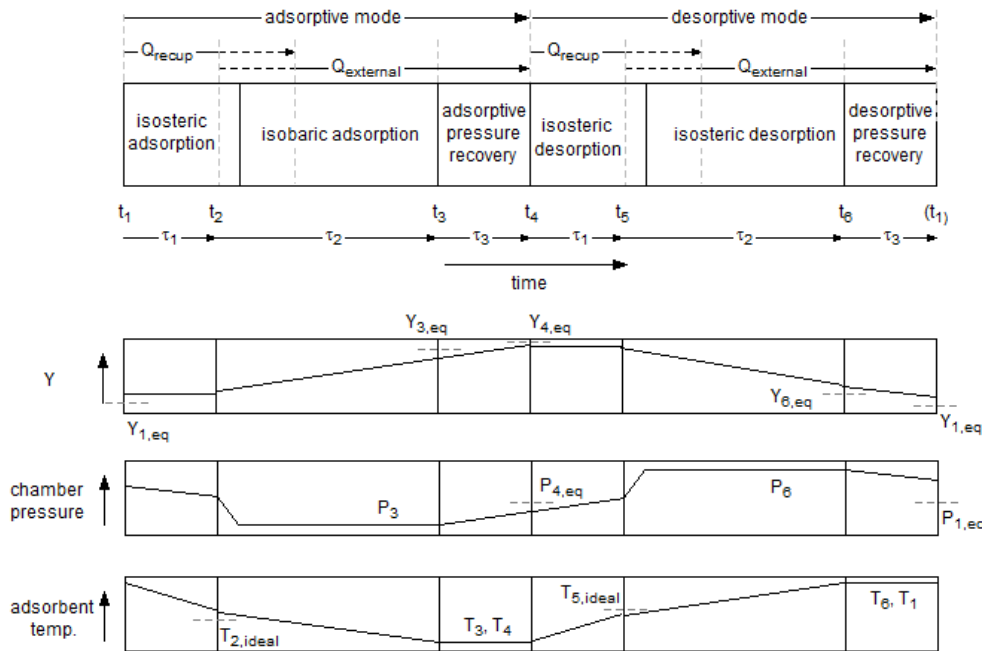


Figure 182: Illustration of state points (in time) for cycle with heat and pressure recovery

6.5 Adsorption heat pump: empirical model and validation

The development of an empirical model of the adsorption heat pump was described in Chapter 5. The algebraic form of the polynomial curve fits for the empirical model were shown in Equations (69) and (70), with coefficients shown in Table 34 and Table 35. This section presents results of the empirical model.

Figure 183, Figure 184 and Figure 185 show an overview for $T_{CHW} = 7, 13$ and 19°C , respectively. Those three figures share the same x-axis scale and y-axes scales to facilitate visual comparison. The figures show that, for a given heat rejection temperature, the chiller has a maximum cooling capacity, Q_{max} , which correspond to the relatively shorter adsorber and heat recovery duration $t_{ads,max}$. It also has a minimum continuous cooling capacity Q_{min} (below which the system would have to cycle on and off), corresponding to longer duration $t_{ads,min}$. The COP in the case of Q_{max} will be lower

than the COP for Q_{min} . Although not captured by the empirical model, the physical reason for this lower COP at higher capacity is because the shorter cycle duration results in a lower ΔY , and therefore larger DTMR.

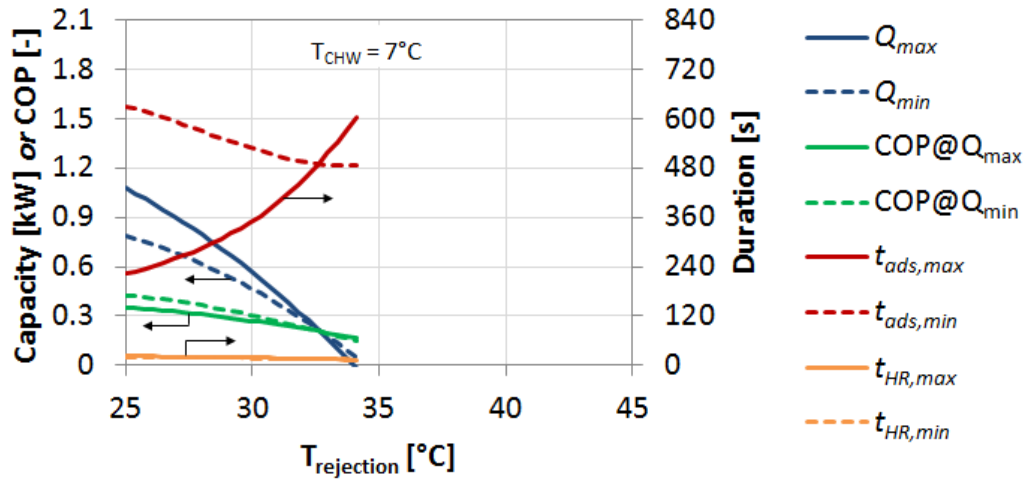


Figure 183: Empirical model results for $T_{CHW} = 7^\circ\text{C}$

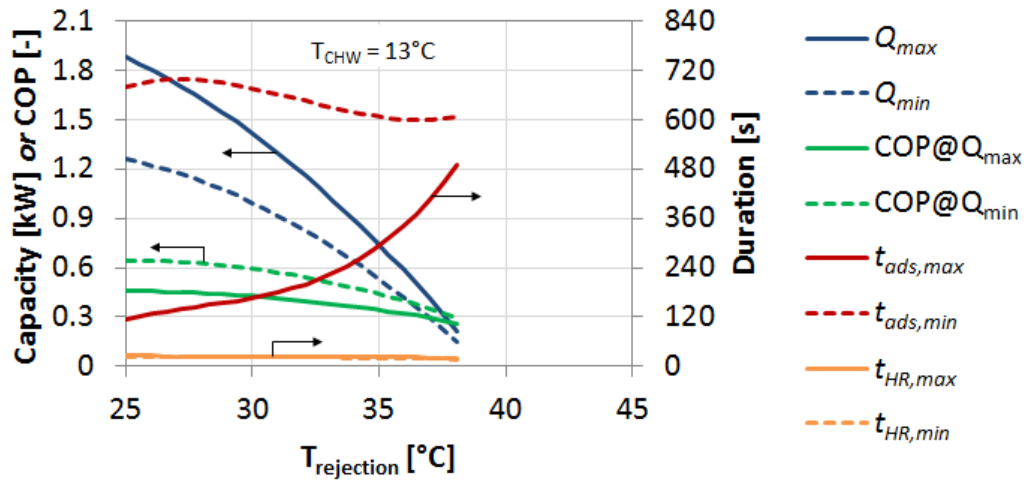


Figure 184: Empirical model results for $T_{CHW} = 13^\circ\text{C}$

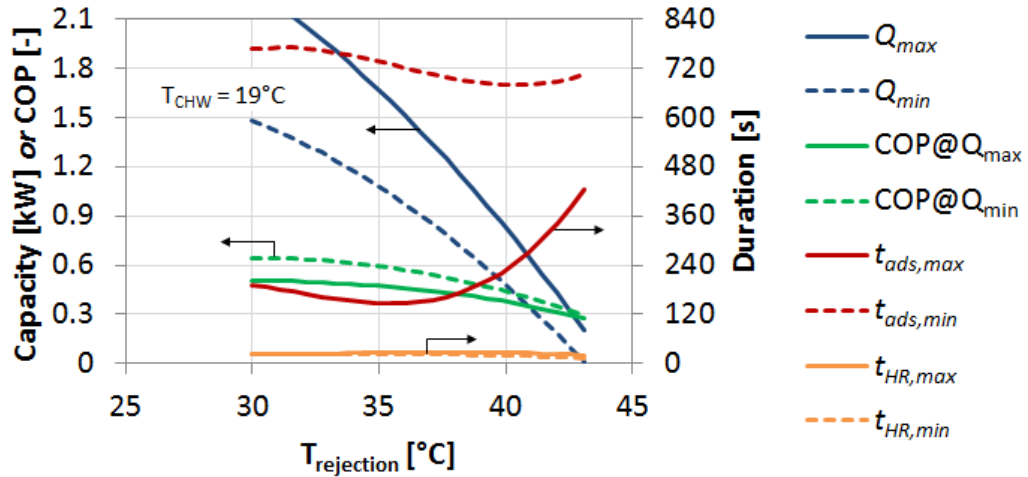


Figure 185: Empirical model results for $T_{\text{CHW}} = 19^{\circ}\text{C}$

Figure 186 shows the heat recovery time as a function of temperature lift for three chilled water temperatures and for Q_{min} and Q_{max} . There is relatively little variation in heat recovery duration for all conditions. This is likely due to the fact that heat recovery flow rate was fixed for all tests, and the HTF residence time (τ_{R}) through the adsorbers and associated piping at that flow rate corresponded to about 15-20 seconds. Thus the optimal heat recovery time was typically between about $0.9 \cdot \tau_{\text{R}}$ and $1.7 \cdot \tau_{\text{R}}$. This makes sense for the following reasons. If $t_{\text{HR}} > \tau_{\text{R}}$, this implies that cool HTF (originally in the adsorber) would be cycled back into the adsorber, lowering the pre-heating accomplished by heat recovery. If $t_{\text{HR}} < \tau_{\text{R}}$, not all of the hot desorber HTF would be brought into the adsorber to preheat it.

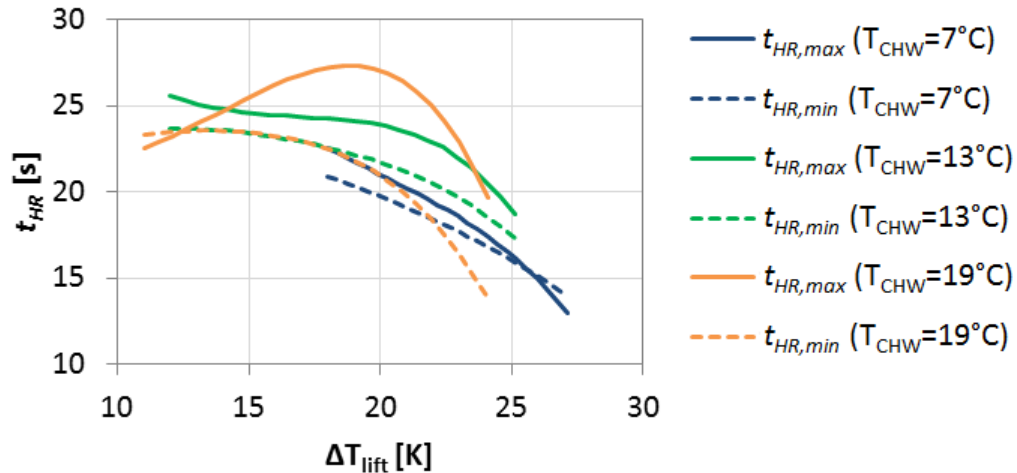


Figure 186: Heat recovery duration for maximum and minimum capacity from control strategy/empirical model

Furthermore, as borne out by the empirical control strategy results, having heat recovery generally made sense, even when maximum capacity was desired. This is because the HTF mass flow rate for heat recovery was greater than the flow rate for normal adsorption/desorption. Thus, although the inlet temperatures to the adsorber and desorber were less extreme in heat recovery than normal ad/desorption, the increase mass flow rate allowed a higher heat transfer.

An unexpected result that can be seen in Figure 186 was that heat recovery duration is longer for maximum capacity than for minimum capacity. This may be again due to the higher HTF mass flow rate during heat recovery.

Figure 187 shows adsorption time as a function of temperature lift for three chilled water temperatures and for Q_{min} and Q_{max} .

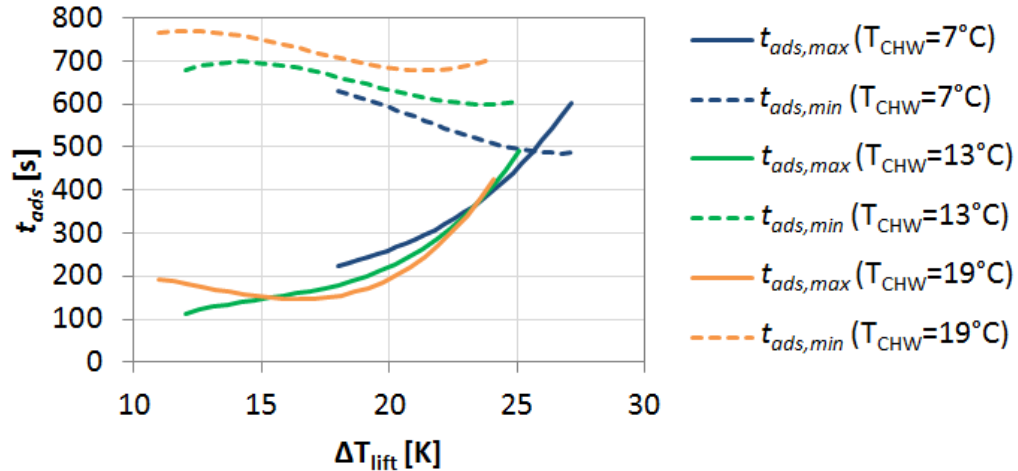


Figure 187: Adsorption duration for maximum and minimum capacity from control strategy/empirical model

Opposing trends can be observed, with durations generally increasing with temperature lift for maximum capacity, but decreasing for minimum capacity. Each is explained below. It is important to note that increasing temperature lift decreases the refrigerant mass flow driving potentials. Thus, Q_{min} and Q_{max} for a particular T_{CHW} will both decrease as ΔT_{lift} goes up.

Maximizing capacity is effectively maximizing the average refrigerant ad/desorption mass flow rate. This rate begins at zero at the beginning of an ad/desorption phase, rises to a maximum, and then decays over some time. Thus the duration of t_{ads} for maximum capacity will occur after the peak of refrigerant ad/desorption flow rate. As temperature lift increases, driving potentials for mass are lower and this maximum flow rate may take more time to develop as well as have a shallower peak with a more gradual decay.

To explain the decreasing adsorption time with higher temperature lift, recall from Section 5.4 that Q_{min} is here defined as the point at which further reducing the capacity would also decrease the COP. This means that the limiting factor for minimizing capacity is on maintaining COP. At long cycle times this is a balance between

convective/radiation heat losses (from desorber HX, piping and chamber) and capacity.

The adsorption time can be increased until the marginal increase in losses [kJ/cycle]

equals the marginal increase in capacity [kJ/cycle]. The duration at which this occurs will

get shorter for lower driving potentials (higher temperature lifts).

Chapter 7: Conclusions

Work presented in this thesis advances the understanding of when trigeneration makes sense at very small scales (<5 kW electric), and identifies the most promising opportunities for on-grid and off-grid trigeneration.

An analytical treatment of trigeneration provides guidance to the trigeneration research community. A discussion of matching prime movers and thermally driven equipment, and comparison with conventional technologies, highlights the promise of fuel cells as prime movers for trigeneration.

A unique micro trigeneration experimental facility was designed and constructed, capable of simulating residential building loads. A trigeneration system was built and installed in this facility, based around a commercial reciprocating engine-based micro CHP prime mover and a prototype adsorption chiller. The prototype chiller was designed, constructed and characterized as part of this work, and has the unique capability of being able to utilize reciprocating engine coolant heat at only 70°C to produce air conditioning, with higher efficiency than any preceding systems utilizing such low temperature waste heat. The chiller achieved efficiency nearly 40% of the Carnot limit. A control strategy for the full range of chiller operation was derived based on experimental data by utilizing Kriging metamodeling and non-dominated sorting. Along with the test facility developed as part of this thesis, the control strategy allowed evaluation of the full trigeneration system under a realistic 5-day residential test. The 5-day test used an hourly cooling profile based on a residential building model and a minutely DHW usage profile based on a statistical DHW model.

The experimental evaluation confirms the conclusions of the analytical treatment of trigeneration. Currently, adding an adsorption chiller to a combustion-based residential CHP system would not reduce primary energy consumption in a grid-connected context. However, this very same technology off the grid could reduce fuel consumption by up to 36%. Furthermore, residential trigeneration based on fuel cells with either adsorption chillers or other thermally driven technologies could save substantial energy on the grid.

This thesis describes separate sensible and latent cooling strategies that can reduce the temperature lift required of thermally driven chillers. This has been demonstrated to be useful for allowing operation at extreme ambient temperatures, and for facilitating low regeneration temperatures.

An analytical approach was also developed to predict the performance of adsorption cycles. This approach was successfully validated against experimental data for the prototype chiller.

7.1 Contributions

Contributions of this thesis are summarized as follows.

- Polygeneration design and performance evaluation
 - Development of dynamic experimental test facility capable of imposing realistic residential thermal loads for multi-day tests
 - Design, construction, experimental evaluation, and control strategy development for adsorption cooling cycle with novel zeolite
 - First realistic dynamic performance evaluation of residential trigeneration system
- Polygeneration modeling and validation
 - Semi-analytical expressions for energetic suitability of polygeneration systems

- Guidelines for trigeneration device matching (prime movers and chillers)
- Experimentally validated residential cogeneration model
- Experimentally validated analytical adsorption chiller model
- Enhancements to polygeneration performance
 - Development of novel separate sensible and latent cooling system to extend air-cooled absorption chiller operation, and enable low regeneration temperature adsorption chilling

Already published works include the following:

- 1) “Heat-activated cooling for small- and micro-CHP” (book chapter in *Small and Micro Combined Heat and Power Systems*, R. Beith, ed., Woodhead Publishing UK, 2011)
- 2) “High efficiency micro trigeneration systems” *Applied Thermal Engineering* (2011)
- 3) “High efficiency trigeneration for buildings” (European Conference on Polygeneration keynote, Spain 2011)
- 4) “Trends in absorption machines” (ISHPC keynote, Italy 2011)
- 5) “Preliminary design of a low regeneration temperature residential adsorption chiller” (ISHPC, Italy 2011)
- 6) “Air-cooled, single-effect, waste heat-driven water/LiBr absorption system for high ambient temperatures” (ISHPC, Italy 2011)
- 7) “Crystallization inhibitors for water/LiBr absorption chillers” (ISHPC, Italy 2011)

Invention disclosures related to these contributions are:

- 1) Radermacher, R., Gluesenkamp, K., Hwang, Y., Bush, J. (2012). *Utility cube*. University of Maryland Invention Disclosure PS-2012-066.
- 2) Horvath, C., Leighton, D., Gluesenkamp, K., Al-Abdulkarem, A., Hwang, Y., Radermacher, R. (2012). *Air-cooled absorber design*. University of Maryland Invention Disclosure PS-2012-013.
- 3) Gluesenkamp, K., Radermacher, R., Hwang, Y. (2010). *Cascade vapor compression and absorption cycles to achieve building air conditioning at*

high ambient temperature with air-cooled water/LiBr absorption heat pump. University of Maryland Invention Disclosure PS-2010-100.

- 4) Gluesenkamp, K., Radermacher, R., Hwang, Y. (2010). *Separate sensible and latent cooling for water/LiBr absorption heat pumps with small vapor compression system.* University of Maryland Invention Disclosure PS-2010-099.

Publications in development are:

- 1) “Thermally driven heat pumps for use in combined cooling heating and power.” Gluesenkamp, K., Hwang, Y., and Radermacher, R. (subchapter in IEA Annex 34 Handbook).
- 2) “Review and classification of separate sensible and latent cooling technologies.” Ling, J., Gluesenkamp, K., Hwang, Y., and Radermacher, R. (Target: *International Journal of Refrigeration*).
- 3) “Performance characterization and control strategy development for low regeneration temperature adsorption chiller.” Qian, S., Gluesenkamp, K., Hwang, Y., and Radermacher, R. (Target: *International Journal of Refrigeration*).
- 4) “Simulation studies of residential combined cooling heat and power and validation with experimental load-following data.” Qian, S., Hartsog, J., Gluesenkamp, K., Hwang, Y., and Radermacher, R. (Target: *International Journal of Refrigeration*).

Chapter 8: Recommendations for Future Work

This thesis established an experimental micro trigeneration facility and analyses of trigeneration systems and adsorption chillers. There are many ways that such a trigeneration system could be improved, including ways explicitly described in the thesis. There are also many opportunities for expanding analysis.

Experimental evaluation of CCHP

As pointed out in the thesis, the micro trigeneration systems based around fuel cells would have the most promising performance and ability to reduce energy consumption compared to a grid-driven VCS. The current adsorption chiller based on Z01 could be coupled to a LTPMEMFC, a single effect absorption chiller could be coupled to a HTPMEMFC, or a double effect absorption chiller could be coupled to a SOFC or MCFC.

Regarding the already-completed experimental evaluation of the SI-ICE-driven adsorption chiller, a mistake was made in implementation of the profile test. The heat recovery valve (HV9 in Figure 48) was inadvertently closed throughout the test. Re-running this test with heat recovery would boost the performance.

Experimental adsorption chiller

The chiller performance was characterized as a function of T_{cond} , T_{evap} , t_{ads} and t_{HR} . This characterization, and the resulting control strategy, was conducted at fixed HTF mass flow rates. There may be considerable room for improvement by allowing those flow rates to vary. Following a new DOE for these additional variables, the control strategy approach developed in this thesis could be readily applied to the new data.

Control strategy visualization would become difficult since more than two dimensions would be involved, but the methodology (and tools used in its implementation) is general enough to handle the additional dimensions.

Additional benefits could be realized in the prototype chiller by using smaller diameter piping between the adsorber HX headers and switching valves, to reduce the DTMR. Given the extremely high value of ECOP for the chiller, there is plenty of room to increase pumping power in order to reduce dead thermal mass.

For application of the adsorption chiller to applications other than an ICE with fixed coolant temperature, investigation of the effect of driving temperature would be beneficial. Higher driving temperatures would also make operation possible at higher ambient temperatures.

Adsorber HX optimization is another area with much room for improvement. The DTMR concept developed in this work would serve well as an optimization objective to be minimized.

Analysis of trigeneration

A very important consideration left out of this thesis is the energy cost savings of trigeneration systems. Due to the lower cost of natural gas vs. electricity (the “spark spread”), some trigeneration systems may reduce energy expenditures even more than primary energy consumption. The analytical expressions for PER of various systems could be readily modified to yield expressions for utility cost. Furthermore, the payback period of trigeneration systems must be favorable in order to have a chance of commercial implementation. This would require estimation of manufactured capital costs in addition to fuel/utility cost savings.

The assertion that all prime movers share a similar value of λ could be improved by surveying the overall fuel utilization factor actually achieved by products and prototypes of each prime mover type, and modeling the mechanisms of heat loss for each prime mover type to explain the differences.

Another element that would improve the analytical PER expressions is accounting for production of heat (such as DHW) as well as cooling and electricity. This would require one more term (f_{htg} in addition to f_{clg}) and would more accurately capture the benefits of trigeneration.

One more possibility for the analytical analysis would be to extend the analysis to include part load performance of components. This means relaxing the “infinite capacity, infinite turndown” assumption, which would necessarily complicate the expressions and introduce additional empirical terms. However, it would much better capture the drawbacks of trigeneration at extreme values of f_{clg} .

Analysis of adsorption cycle

This thesis experimentally estimated the bulk mass transfer coefficient for the adsorber HXs. The analysis of the adsorption cycle would benefit from a more detailed model of the adsorption using finite element tools or an analytical treatment. This would allow expression of differential loading as a function of cycle time. A time-dependent model of differential loading, whether empirical, analytical or finite element-based, combined with the analytical COP expression involving DTMR, would allow optimization of heat exchanger geometry to maximize COP and capacity, especially under adverse conditions. The current prototype comes close to the theoretical maximum COP value under favorable conditions, but there is much room for improvement in

capacity under all conditions, and for improving capacity and COP under less favorable conditions.

Simulation studies of trigeneration system

In this work an empirical adsorption chiller map was developed, and a transient CHP model has been developed in previous work (Bush, 2010). Building on these to create a transient system model of the trigeneration system would require the development of a prime mover control strategy for CCHP operation, and the addition of a hot water return port to middle of the stratified buffer tank component. The model could be validated against experimental data from the 5-day profile test presented in this thesis. This would enable parametric and sensitivity studies for different climate regions and different load profiles, and optimization of the capacity of prime mover and chiller. It would also be possible to substitute different prime movers and chillers.

Appendix

Alternate fuel energy calculation for instrumentation energy balance

In calculating the energy balance on the CHP engine, a convenient alternate method was developed using an adaptive heating value rather than the fixed, tabulated LHV or HHV heating values.

Conventionally, one would choose to use either the LHV or HHV of the fuel to calculate the energy into an engine. However, in calculating the energy flows out of the system, one would have to carefully choose the reference enthalpy for the exhaust flow calculation in order for the sum of all measured outputs to equal the measured fuel input.

Figure 188 illustrates the issue by plotting the enthalpy of ideal combustion products of methane and dry air under different sets of assumptions. HHV and LHV are both defined based on cooling ideal combustion products to 25°C (Turns, 2000). Each definition has a somewhat un-physical assumption about what happens to the H₂O product of combustion, as described presently.

The HHV definition assumes that all the water vapor generated by combustion is in the condensed phase, and thus the heat release vs. temperature follows the solid blue line in Figure 188. The dotted blue line shows the tabulated HHV value of 55,528 kJ/kg, and the two blue lines cross at the reference value of 25°C, as expected.

The LHV definition assumes that all the water vapor stays in the vapor phase even as the gases are cooled to 25°C. The heat release vs. temperature curve thus follows the solid red line in Figure 188. The dotted red line shows the tabulated LHV value of 50,016, and the two red lines cross at the reference value of 25°C, as expected.

For an actual moist flue gas stream, as cooling proceeds below the onset of condensation ($\sim 60^\circ\text{C}$ for stoichiometric complete methane/dry air combustion), *some* (viz. not all; not none) of the water condenses out. Specifically, the amount condensing out will follow the saturation pressure of water as a function of temperature. The black line in Figure 188 has been plotted by assuming that, beyond the onset of condensation, the partial pressure of water vapor in the exhaust equals the saturation pressure of water at the exhaust temperature. This corresponds to the actual heat that would be released as a function of temperature as ideal combustion products cool.

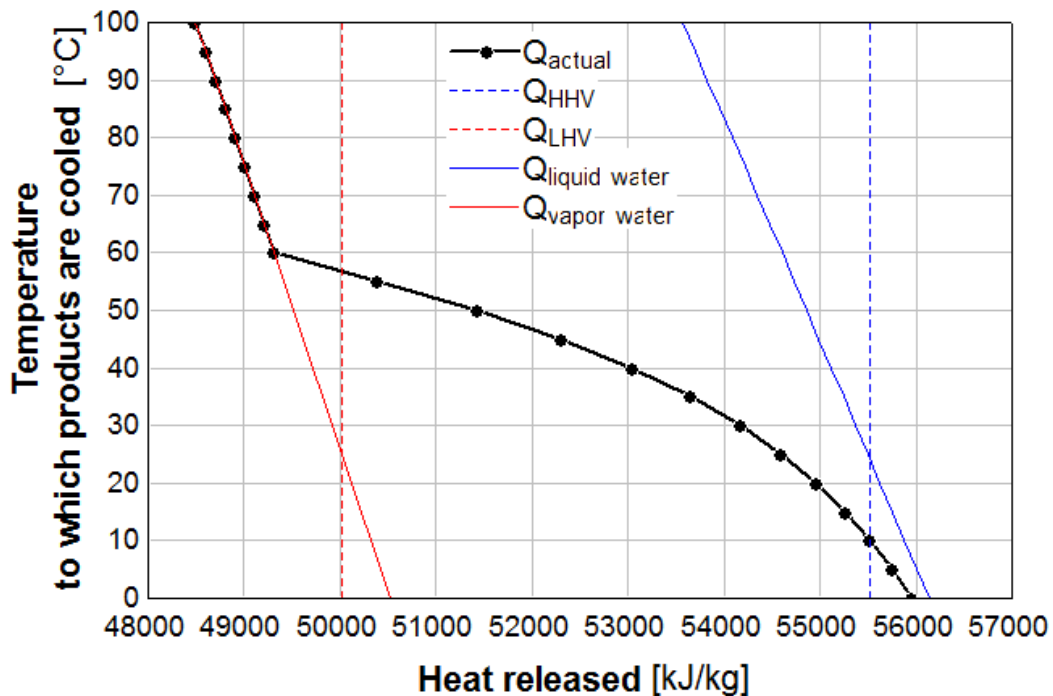


Figure 188: T-Q heating value diagram for stoichiometric complete combustion products of methane and dry air

Thus, the alternate method for conducting an instrumentation energy balance on a CHP engine (or condensing boiler/furnace) is to measure the temperature of exhaust gasses crossing the control volume boundary, and use the corresponding heat release (Q_{actual}) in Figure 188 to define the amount of fuel energy that entered the system. It is no longer necessary to decide on reference enthalpies for exhaust calculations.

Figure 188 would need to be adjusted for different fuel compositions. In addition, adjustment may be required for the humidity of non-dry combustion inlet air depending on the accuracy desired.

Glossary of key terminology

ΔT_{appr}	Approach temperature: a temperature difference between a fluid stream internal to a system and a fluid stream external to the system; the temperature difference between (1) the inlet of the external fluid and (2) the outlet of the internal fluid
ΔT_D	Driving temperature difference: the temperature difference between driving heat and heat rejection temperatures for a thermally-driven heat pump
ΔT_L	Temperature lift: the temperature difference across which a heat pump transfers heat (for buildings, typically this is the difference between indoor and outdoor temperatures)
ΔY	Differential loading: the difference in refrigerant mass ratio (Y) at the end of adsorption vs. end of desorption
ΔY_{eq}	Equilibrium differential loading: the difference in refrigerant mass ratio (Y) at the end of equilibrium adsorption vs. end of equilibrium desorption

References

- Abdelaziz, O. (2009) *Development of multi-scale, multi-physics, analysis capability and its application to novel heat exchanger design and optimization*, PhD thesis, University of Maryland, Department of Mechanical Engineering.
- Abdelaziz, O. (2011) 'Water-LiBr enabling technologies using chemical additives', in *American Society of Heating Refrigeration and Air Conditioning Engineers Winter Conference*, Las Vegas, Nevada, USA, 29 January – 2 February, 2011.
- Abdelaziz, O., Wang, K., Kisari, P. and Vineyard, E. (2010a) 'Crystallization temperature of aqueous LiBr solutions at low evaporation temperature', in *Road to Climate Friendly Chillers*, Cairo, Egypt, 30 September - 1 October, 2010.
- Abdelaziz, O., Wang, K., Kisari, P. and Vineyard, E. (2010b) 'Testing of crystallization temperature of a new working fluid for absorption heat pump systems', in *Road to Climate Friendly Chillers*, Cairo, Egypt, 30 September - 1 October, 2010.
- Alefeld, G. and Radermacher, R. (1994) *Heat conversion systems*, Boca Raton: CRC Press.
- American Society of Heating Refrigeration and Air Conditioning Engineers (2005) 'ASHRAE Handbook: Fundamentals'
- Anyanwu, E. E. and Ogueke, N. V. (2005) 'Thermodynamic design procedure for solid adsorption solar refrigerator', *Renewable Energy*, 30(1), 81-96.
- Bejan, A. (1982) *Entropy generation through heat and fluid flow*, New York: Wiley.
- Bush, J. (2010) *Modeling of combined heat and power unit and evaluation of system performance in building applications*, MS thesis, University of Maryland, Department of Mechanical Engineering.
- Chen, C. J., Wang, R. Z., Xia, Z. Z., Kiplagat, J. K. and Lu, Z. S. (2010) 'Study on a compact silica gel-water adsorption chiller without vacuum valves: Design and experimental study', *Applied Energy*, 87(8), 2673-2681.
- Ge, Y. T., Tassou, S. A., Chaer, I. and Suguartha, N. (2009) 'Performance evaluation of a tri-generation system with simulation and experiment', *Applied Energy*, 86(11), 2317-2326.
- Gluesenkamp, K. and Radermacher, R. (2011) 'Heat Activated Cooling Technologies for Small and Micro CHP Applications,' in Beith, R., ed. *Small and Micro CHP Systems*, Cambridge, UK: Woodhead Publishing Ltd.

- Gluesenkamp, K., Radermacher, R. and Hwang, Y. (2011a) 'Crystallization inhibitors for water/LiBr absorption chillers,' in *International Sorption Heat Pump Conference*, Padua, Italy, April 5-7, 2011.
- Gluesenkamp, K., Radermacher, R., and Hwang, Y., (2011b), 'High efficiency trigeneration systems for buildings,' in *European Conference on Polygeneration*, Tarragona, Spain, pp. 1-11.
- Gluesenkamp, K., Radermacher, R. and Hwang, Y., (2011c). 'Preliminary design of a low regeneration temperature residential adsorption chiller,' in *International Sorption Heat Pump Conference*, Padua, Italy, April 5-7, 2011.
- Gluesenkamp, K., Radermacher, R., and Hwang, Y., (2011d) 'Trends in absorption machines,' in *International Sorption Heat Pump Conference*, Padua, Italy, April 5-7, 2011.
- Gluesenkamp, K., Horvath, C., Radermacher, R. and Hwang, Y. (2011e) 'Air-cooled, single-effect, waste heat-driven water/LiBr absorption system for high ambient temperatures', in *International Sorption Heat Pump Conference*, Padua, Italy, April 5-7, 2011.
- Gluesenkamp, K., Hwang, Y., and Radermacher, R. (in press) 'High efficiency micro trigeneration systems,' *Applied Thermal Engineering*.
- Herold, K. E., Radermacher, R. and Klein, S. A. (1996) *Absorption Chillers and Heat Pumps*, Boca Raton, Fla.:CRC Press.
- Heywood, J. B. (1988) *Internal combustion engine fundamentals*, New York: McGraw-Hill.
- Huangfu, Y., Wu, J. Y., Wang, R. Z. and Xia, Z. Z. (2007) 'Experimental investigation of adsorption chiller for Micro-scale BCHP system application', *Energy and Buildings*, 39(2), 120-127.
- Incropera, F. P. (2007) *Fundamentals of heat and mass transfer*, 6th ed., Hoboken, NJ: John Wiley.
- Jordan, U., Vajen, K. (2001) 'Realistic domestic hot-water profiles in different time scales', developed within the scope of the *Solar Heating and Cooling Program of the International Energy Agency, Task 26: Solar Combisystems*.
- Kemp, I. C. (2007) *Pinch analysis and process integration : a user guide on process integration for the efficient use of energy*, 2nd ed., Oxford: Butterworth-Heinemann.

- Li, G., Aute, V., Azarm, S. (2010) 'An accumulative error based adaptive design of experiments for offline metamodeling', *Structural and Multidisciplinary Optimization*, 40, 137-155.
- Li, S. and Wu, J. Y. (2009) 'Theoretical research of a silica gel-water adsorption chiller in a micro combined cooling, heating and power (CCHP) system', *Applied Energy*, 86(6), 958-967.
- Meunier, F., Poyelle, F. and LeVan, M. D. (1997) 'Second-law analysis of adsorptive refrigeration cycles: The role of thermal coupling entropy production', *Applied Thermal Engineering*, 17(1), 43-55.
- Miguez, J. et al. (2004) 'Feasibility of a new domestic CHP trigeneration with heat pump: I. Design and development', *Applied Thermal Engineering*, 24(10), pp.1409-1419.
- Mitsubishi Plastics. (2008) 'Zeolitic water vapor adsorbent AQSOA', available at http://www.aaasaveenergy.com/products/001/pdf/AQSOA_1210E.pdf
- Mueller, A. (2009) *Analysis of residential building energy systems through transient simulation*, MS thesis, University of Maryland, Department of Mechanical Engineering.
- National Solar Radiation Database (2010) 'TMY3 weather data', available at http://rredc.nrel.gov/solar/old_data/nsrdb/1991-2005/data/tmy3/745940TY.csv
- 'NIST/SEMATECH e-Handbook of Statistical Methods', [online], available: <http://www.itl.nist.gov/div898/handbook/> [accessed March 2011]
- Petchers, N. (2003) *Combined heating, cooling and power handbook: technologies and applications: an integrated approach to energy resource optimization*, Lilburn, GA: Fairmont Press.
- Roques, J. F. and Thome, J. R. (2007) 'Falling Films on Arrays of Horizontal Tubes with R-134a, Part I: Boiling heat transfer results for four types of tubes', *Heat Transfer Engineering*, 28(5), 398-414.
- Roques, J. F. and Thome, J. R. (2007) 'Falling Films on Arrays of Horizontal Tubes with R-134a, Part II: Flow Visualization, Onset of Dryout, and Heat Transfer Predictions', *Heat Transfer Engineering*, 28(5), 415-434.
- Smith, M. and Few, P.C. (2001) 'Domestic-scale combined heat-and-power system incorporating a heat pump: analysis of a prototype plant', *Applied Energy*, 70(3), pp.215-232.
- Thomas, B. (2008) 'Benchmark testing of Micro-CHP units', *Applied Thermal Engineering*, 28(16), 2049-2054.

- Thome, J. R. (2009) *Wolverine Tube, Inc. Engineering Data Book III*, Wolverine Tube, Inc.
- Tierney, M. J. (2008) 'Feasibility of driving convective thermal wave chillers with low-grade heat', *Renewable Energy*, 33(9), 2097-2108.
- Turns, S. (2000) *An Introduction to Combustion*, Second Edition ed., McGraw Hill.
- UK Carbon Trust (2011). *Micro CHP Accelerator Final Report*
- US Energy Information Administration (2011). Annual Energy Outlook 2011, DOE/EIA-03 (April 2011).
- XProps™, Interfaces to NIST REFPROP Database, Version 2.0, 2012, Optimized Thermal Systems LLC., College Park, MD, www.optimizedthermalsystems.com
- Zogg, R. A., Feng, M. Y. and Westphalen, D. (2005) *Distributed Energy Program Report: Guide to Developing Air-Cooled LiBr Absorption for Combined Heat and Power Applications*, US Department of Energy, Energy Efficiency and Renewable Energy.
- Zogg, R. A. and Westphalen, D. (2006) 'Developing Air-Cooled LiBr Absorption for Light Commercial Combined Heat and Power Applications', *HVAC&R Research*, 12(3b), 731-747.

Bibliography

- Alefeld, G. and Radermacher, R. (1994) *Heat conversion systems*, Boca Raton: CRC Press.
- American Society of Heating Refrigeration and Air Conditioning Engineers (2005) 'ASHRAE Handbook: Fundamentals',
- American Society of Heating Refrigeration and Air Conditioning Engineers (2006) 'ASHRAE Handbook: Refrigeration',
- American Society of Heating Refrigeration and Air Conditioning Engineers (2008) 'ASHRAE Handbook: Systems',
- Angrisani, G., Minichiello, F., Roselli, C. and Sasso, M. 'Desiccant HVAC system driven by a micro-CHP: experimental analysis', *Energy and Buildings*, In Press, Accepted Manuscript.

- Anyanwu, E. E. (2003) 'Review of solid adsorption solar refrigerator I: an overview of the refrigeration cycle', *Energy Conversion and Management*, 44(2), 301-312.
- Anyanwu, E. E. (2004) 'Review of solid adsorption solar refrigeration II: An overview of the principles and theory', *Energy Conversion and Management*, 45(7-8), 1279-1295.
- Basmdjian, D. (1997) *The little adsorption book : a practical guide for engineers and scientists*, Boca Raton, Fla.: CRC Press.
- Bejan, A. (1982) *Entropy generation through heat and fluid flow*, New York: Wiley.
- Brundrett, G. W. (1987) *Handbook of dehumidification technology*, London ; Boston: Butterworths.
- Castro, J., Oliva, A., Carlos David, P.-S. and Oliet, C. (2008) *Recent developments in the design of a new air-cooled, hot-water-driven H₂O-LiBr absorption chiller*, New York City, NY, United states: Amer. Soc. Heating, Ref. Air-Conditioning Eng. Inc., 288-299.
- Castro, J., Oliva, A., Perez-Segarra, C. D. and Oliet, C. (2008) 'Modelling of the heat exchangers of a small capacity, hot water driven, air-cooled H₂O-LiBr absorption cooling machine', *International Journal of Refrigeration*, 31, 75-86.
- Cess, R., Kumar, I., Ostrach, S., Tiwari, S., Zaric, Z., and Zukauskas, A., *Advances in Heat Transfer, Volume 8*, J. P. Hartnett & T. F. Irvine, eds., Academic Press, 1972.
- Chunnanond, K. and Aphornratana, S. (2004a) 'An experimental investigation of a steam ejector refrigerator: the analysis of the pressure profile along the ejector', *Applied Thermal Engineering*, 24(2-3), 311-322.
- Chunnanond, K. and Aphornratana, S. (2004b) 'Ejectors: applications in refrigeration technology', *Renewable and Sustainable Energy Reviews*, 8(2), 129-155.
- Demir, H., Mobedi, M. and Ülkü, S. (2008) 'A review on adsorption heat pump: Problems and solutions', *Renewable and Sustainable Energy Reviews*, 12(9), 2381-2403.
- Dinçer, I. (2003) *Refrigeration Systems and Applications*, John Wiley and Sons.
- Godefroy, J., Boukhanouf, R. and Riffat, S. (2007) 'Design, testing and mathematical modelling of a small-scale CHP and cooling system (small CHP-ejector trigeneration)', *Applied Thermal Engineering*, 27(1), 68-77.
- Goodheart, K. A. (2000) *Low Firing Temperature Absorption Chiller System*, unpublished thesis University of Wisconsin-Madison.

- Gulen, S. C. (June, 2010) 'A proposed definition of CHP efficiency', *POWER Magazine*
- Henning, H.-M. (2007) *Solar-assisted air-conditioning in buildings : a handbook for planners*, 2nd rev. ed., Wien ; London: Springer.
- Henning, H.-M., Pagano, T., Mola, S. and Wiemken, E. (2007) 'Micro tri-generation system for indoor air conditioning in the Mediterranean climate', *Applied Thermal Engineering*, 27, 2188-2194.
- Huangfu, Y., Wu, J. Y., Wang, R. Z. and Xia, Z. Z. (2007) 'Experimental investigation of adsorption chiller for Micro-scale BCHP system application', *Energy and Buildings*, 39(2), 120-127.
- Hwang, Y., Radermacher, R., Al Alili, A. and Kubo, I. (2008) 'Review of Solar Cooling Technologies', 14(507-528).
- Jin, W., Cun Nan, L., Jian Hua, L., Si Chang, L. and Jun, C. (2009) *A New Air-Conditioning System of Liquid Desiccant and Evaporation Cooling*, translated by 1-4.
- Kim, D. S. and Ferreira, C. A. I. (2003) *Solar Absorption Cooling*.
- Kim, D. S. and Infante Ferreira, C. A. (2008) 'Solar refrigeration options - a state-of-the-art review', *International Journal of Refrigeration*, 31(1), 3-15.
- Kodama, A., Hirose, T. and Okano, H. (2003) *Low-temperature heat driven adsorptive desiccant cooling improved for the use in humid weather*, translated by Saha, B., Akisawa, A. and Koyama, S., Fukuoka, Japan.
- Kong, X. Q., Wang, R. Z. and Huang, X. H. (2004) 'Energy efficiency and economic feasibility of CCHP driven by Stirling engine', *Energy Conversion and Management*, 45(9-10), 1433-1442.
- Lambert, M. A. and Jones, B. J. (2005) 'Review of Regenerative Adsorption Heat Pumps', *Journal of Thermophysics and Heat Transfer* 19(4), 471-485.
- Liao, X. (2004) *The development of an air-cooled absorption chiller concept and its integration in CHP systems*, unpublished thesis (Text), University of Maryland.
- Mandegari, M. A. and Pahlavanzadeh, H. (2009) 'Introduction of a new definition for effectiveness of desiccant wheels', *Energy*, 34, 797-803.
- Mei, V. C., Chen, F. C., Lavan, Z., Collier, R. K. and Meckler, G. (1992) *An assessment of desiccant cooling and dehumidification technology*, Oak Ridge National Laboratory, US Department of Energy.

- Meunier, F., Poyelle, F. and LeVan, M. D. (1997) 'Second-law analysis of adsorptive refrigeration cycles: The role of thermal coupling entropy production', *Applied Thermal Engineering*, 17(1), 43-55.
- Meyer, A. J., Harms, T. M. and Dobson, R. T. (2009) 'Steam jet ejector cooling powered by waste or solar heat', *Renewable Energy*, 34(1), 297-306.
- Nayak, S. M. (2005) *Experimental and theoretical investigation of integrated engine generator - liquid desiccant system*, unpublished thesis (Text), University of Maryland.
- Nayak, S. M., Hwang, Y. and Radermacher, R. (2009) 'Performance characterization of gas engine generator integrated with a liquid desiccant dehumidification system', *Applied Thermal Engineering*, 29(2-3), 479-490.
- Ng, K. C., Chua, H. T., Chung, C. Y., Loke, C. H., Kashiwagi, T., Akisawa, A. and Saha, B. B. (2001) 'Experimental investigation of the silica gel-water adsorption isotherm characteristics', *Applied Thermal Engineering*, 21(16), 1631-1642.
- Nia, F. E., van Paassen, D. and Saidi, M. H. (2006) 'Modeling and simulation of desiccant wheel for air conditioning', *Energy and Buildings*, 38(10), 1230-1239.
- Niu, J. L. and Zhang, L. Z. (2002) 'Effects of wall thickness on the heat and moisture transfers in desiccant wheels for air dehumidification and enthalpy recovery', *International Communications in Heat and Mass Transfer*, 29(2), 255-268.
- Onovwiona, H. I. and Ugursal, V. I. (2006) 'Residential cogeneration systems: review of the current technology', *Renewable and Sustainable Energy Reviews*, 10(5), 389-431.
- Peltier, R. (February, 2010) 'Plant efficiency: begin with the right definitions', *POWER Magazine*
- Peltier, R. V. (2001) 'How efficient is 'efficiency'?', *POWER Magazine*, 145(2), 105.
- Petchers, N. (2003) *Combined heating, cooling & power handbook: technologies & applications: an integrated approach to energy resource optimization*, Lilburn, GA: Fairmont Press.
- Petrov, A. Y., Zaltash, A., Labinov, S. D., Rizy, D. T., Liao, X. and Radermacher, R. (2004) *Evaluation of different efficiency concepts of an integrated energy system (IES)*, translated by Anaheim, CA, United states: American Society of Mechanical Engineers, 347-356.

- Power Partners, I. (2010) 'Eco-Max Adsorption Chillers', [online], available: <http://www.eco-maxchillers.com/> [accessed
- Radermacher, R. and American Society of Mechanical Engineers. Advanced Energy Systems Division. (1994) *Proceedings of the International Absorption Heat Pump Conference : presented at the International Absorption Heat Pump Conference*, translated by New Orleans, Louisiana: American Society of Mechanical Engineers, viii, 534 p.
- Ruthven, D. M. (1984) *Principles of adsorption and adsorption processes*, New York: Wiley.
- Saha, B. B., Akisawa, A. and Koyama, S. (2003) *Proceedings of the International Seminar on Thermally Powered Sorption Technology : December 4-5, 2003, Chikushi Campus, Kyushu University, Fukuoka, Japan*
- Schinner Jr, E. N. and Radermacher, R. (1999) 'Performance analysis of a combined desiccant/absorption air-conditioning system', *HVAC and R Research*, 5, 77-84.
- Srikhirin, P., Aphornratana, S. and Chungpaibulpatana, S. (2001) 'A review of absorption refrigeration technologies', *Renewable and Sustainable Energy Reviews*, 5(4), 343-372.
- Sumathy, K., Huang, Z. C. and Li, Z. F. (2002) 'Solar absorption cooling with low grade heat source -- a strategy of development in South China', *Solar Energy*, 72(2), 155-165.
- Sumathy, K., Yeung, K. H. and Yong, L. (2003) 'Technology development in the solar adsorption refrigeration systems', *Progress in Energy and Combustion Science*, 29(4), 301-327.
- Sun, D.-W. (1999) 'Comparative study of the performance of an ejector refrigeration cycle operating with various refrigerants', *Energy Conversion and Management*, 40(8), 873-884.
- TIAX (2004) *Review of Thermally Activated Technologies. A Distributed Energy Program Report for the US DOE Office of Energy Efficiency and Renewable Energy* TIAX LLC.
- Wang, R. Z. (2001) 'Adsorption refrigeration research in Shanghai Jiao Tong University', *Renewable and Sustainable Energy Reviews*, 5(1), 1-37.
- Wu, D. W. and Wang, R. Z. (2006) 'Combined cooling, heating and power: A review', *Progress in Energy and Combustion Science*, 32(5-6), 459-495.

- Yang, R. T. (2003) *Adsorbents : fundamentals and applications*, Hoboken, N.J.: Wiley-Interscience.
- YapICI, R. and Ersoy, H. K. (2005) 'Performance characteristics of the ejector refrigeration system based on the constant area ejector flow model', *Energy Conversion and Management*, 46(18-19), 3117-3135.
- YapICI, R. and Yetisen, C. C. (2007) 'Experimental study on ejector refrigeration system powered by low grade heat', *Energy Conversion and Management*, 48(5), 1560-1568.
- Yong, L. and Wang, R. Z. (2007) 'Adsorption refrigeration: A survey of novel technologies', *Recent Patents on Engineering*, 1(1), 1-21.
- Zhang, X. J., Dai, Y. J. and Wang, R. Z. (2003) 'A simulation study of heat and mass transfer in a honeycombed rotary desiccant dehumidifier', *Applied Thermal Engineering*, 23(8), 989-1003.